

UNIVERSIDADE DE SÃO PAULO
ESCOLA POLITÉCNICA

CARLOS ALBERTO DA SILVA

**Corrosion in multiphase-flow pipelines: the impact on the oil and gas
industry**

São Paulo

2023

CARLOS ALBERTO DA SILVA

**Corrosion in multiphase-flow pipelines: the impact on the oil and gas
industry**

Original Version

Ph.D. Thesis submitted to the
Department of Metallurgical and
Materials Engineering of the
University of São Paulo to obtain the
title of Doctor in Science.

Concentration Area: Metallurgy and
Materials.

Supervisor: Dra. Zehbour Panossian.

São Paulo

2023

Catálogo-na-publicação

Da Silva, Carlos Alberto

Corrosion in multiphase-flow pipelines: the impact on the oil and gas industry.

Da Silva, Carlos A. -- Version Original -- São Paulo, 2023.

151 p.

Tese (Doutorado) – Escola Politécnica da Universidade de São Paulo.

Departamento de Engenharia Metalúrgica e de Materiais.

1. Multiphase flow, 2. Pipeline corrosion, 3. Carbon steel, 4. Wear, 5. Prediction model, 6. Emulsion. Universidade de São Paulo. Escola Politécnica.

Departamento de Engenharia Metalúrgica e de Materiais.

Philosophy separated from science when it asked the question, “ Which is the knowledge of the world and of life which enables man to live most happily?”

To beloved wife and daughter

Luciana & Zaila

ACKNOWLEDGEMENTS

My sincere acknowledgment to Professor Dra. Zehbour Panossian for her determination, attention and care during the development and supervision of this work. This gratitude is extended to Neusvaldo Lira for his collaboration and supervision during the project that enabled the elaboration of this Thesis.

I thank all the Corrosion and Protection Laboratory employees of the Technological Research Institute (LCP-IPT) who directly or indirectly participated in developing the various stages of this work.

I thank the Interdisciplinary Nucleus of Fluid Dynamics team at the Federal University of Rio de Janeiro for collaborating in designing the multiphase-flow loop. In particular to Professor Valter Aibe, Professor Juliana Loureiro and Laert.

I thank Repsol Sinopec for the investment in the project and for sharing information from the oil field, including discussions to define the test matrix and evaluate the results. In particular, I sincerely thank Gabriel Bassani from the research and development area.

I thank the National Petroleum Agency (ANP) for the investment in research, development, and technological innovation, which enabled the execution of the project that resulted in this Thesis.

Thanks to the teachers who contributed along this trajectory, particularly Professor Dr. André Tschiptschin, Professor Dr. Maria Elena Taqueda, Professor Dr. Idalina Vieira Aoki, Dr. Álvaro Augusto Oliveira Magalhães, and Dr. Javier Alejandro C. Velasco.

To friends like David Rodrigues, Henrique Pereira, Hamilton Lelis, Luís Varela, Tarcísio Henrique and Dra. Maria Helena. They helped me mature ideas, supported me, and contributed by feeding the discussions, encouraging the work, and the orientations, reflecting on the failures, and celebrating the successes. My thanks to all of them!

I thank my dear parents, Arlindo Augusto, and Maria Aparecida, for the best teachings, humility, and respect.

ABSTRACT

The present research aims to evaluate corrosion induced by multiphase flow in conditions similar to O&G production in pre-salt fields. The main focus was the corrosion of the uncoated carbon steel of rigid pipes used in risers and flowlines of wells that show a decline in productivity, which requires an increase in the injection of water and CO₂, called mature wells. A multiphase-flow loop was designed and built for experimental work with characteristics that better represent field conditions than traditional bench corrosion tests. Corrosion tests were carried out in this loop. A mixture of 80 % water cut was used to represent a mature well environment, composed of 20 % light oil (10 cP) or heavy oil (150 cP) plus 80 % solution with 15 % NaCl in deionized water. The tests were conducted at 40 °C under different partial pressures of CO₂ and H₂S balanced with N₂ to reach a total pressure of 2.5 bar. The flow of the gas phase and that of the liquid phase were also kept fixed. API 5L X80 carbon steel specimens were installed in pre-defined positions, and their corrosion rates were determined for different operating conditions of the loop. The influence of the position of the specimens in the loop (horizontal and inclined at 45° as well as the influence of the CO₂ partial pressure (sweet regime), the CO₂/H₂S ratio, and also the type of crude oil (light and heavy) in the corrosion process were studied. An investigative study was also conducted to understand the phenomena of cavitation, erosion, and corrosion. Statistical methods were used to treat the data obtained in the multiphase loop, which made it possible to obtain predictive models for the corrosion rate and flow characteristics. Forecasting models were vital as they allowed experimental planning for new tests in the multiphase corrosion loop. Finally, studies to evaluate the formation and stability of the emulsion were conducted to verify the impact of the emulsification process on corrosion.

Keywords: multiphase flow, pipeline corrosion, carbon steel, wear, prediction model, emulsion.

RESUMO

A pesquisa desenvolvida no presente estudo teve como objetivo avaliar a corrosão induzida por escoamento multifásico em condições que se aproximam das observadas na produção de óleo e gás nos campos do pré-sal. O foco principal foi a corrosão dos tubos rígidos de aço-carbono sem revestimento usados em *risers* e *flowlines* de poços que apresentam declínio de produtividade, o que requer aumento da injeção de água e CO₂, denominados de poços maduros. Para a condução dos trabalhos experimentais, foi projetado e construído um loop de escoamento multifásico com características que representam melhor as condições de campo, do que os ensaios de corrosão tradicionais de bancada. Os ensaios de corrosão foram realizadas nesse loop. Para representar um ambiente de poço maduro, foi utilizada uma mistura de 80 % de corte de água (*water cut*), composta por 20 % de óleo leve (10 cP) ou óleo pesado (150 cP) mais 80 % de solução a 15 % de cloreto de sódio em água deionizada. Os ensaios foram realizados a 40 °C sob diferentes pressões parciais de CO₂ e H₂S balanceadas com N₂ para atingir uma pressão total de 2,5 bar. Além da pressão total, a vazão da fase de gás e a da fase de líquido também foram mantidas fixas. Corpos de prova de aço-carbono API 5L X80 foram instalados em posições pré-definidas e as suas taxas de corrosão foram determinadas para diferentes condições de operação do loop. Foi estudada a influência da posição dos corpos de prova no loop (trecho horizontal e inclinada a 45°), a influência da pressão parcial CO₂ (*sweet regime*) e da relação CO₂/H₂S e, também, do tipo de óleo bruto (leve e pesado) no processo de corrosão. Em paralelo, foi conduzido um estudo investigativo com o objetivo de entender os fenômenos de cavitação, erosão e corrosão. Métodos estatísticos foram utilizados para tratamento dos dados obtidos no loop multifásico, o que possibilitou a obtenção de modelos preditivos para a taxa de corrosão e para as características do escoamento. Considerou-se importante a obtenção dos modelos de previsão, pois eles permitem o planejamento experimental dirigido para novos ensaios no loop de corrosão multifásico. Por fim, estudos para avaliação da formação e da estabilidade da emulsão foram conduzidos para verificar o impacto do processo de emulsificação na corrosão.

Palavras-chave: escoamento multifásico, corrosão de tubulação, aço-carbono, desgaste, modelo de previsão, emulsão.

FIGURE LIST

Figure 1 – Possible causes of pipeline corrosion	2
Figure 2 – Diagram showing the structure of the Ph.D. thesis.....	3
Figure 3 – Profitable pre-salt scenario for a 7800 MMBoe total production	6
Figure 4 - General arrangement of offshore production system components and infrastructure ...	8
Figure 5 – Subsea pipeline failure	13
Figure 6 – Corrosion regimes in CO ₂ /H ₂ S	17
Figure 7 – Corrosion rate (<i>CR</i>) and polarization resistance (<i>R_p</i>) of the studied low alloy steel exposed to CO ₂ /H ₂ S in sour regime according to Figure 6	18
Figure 8 – Corrosion rates were measured in pH 3 and 4 conditions	19
Figure 9 – Corrosion rate vs. <i>PCO₂/PH₂S</i> ratio (sweet regime according to Figure 6) for WL, ER and LPR.....	20
Figure 10 – Types of flow-induced corrosion	21
Figure 11 - Laminar and Turbulent Flow Velocity Profiles.....	23
Figure 12 - Three-phase gas-oil-water diagram for horizontal pipes (two-phase flow regimes for gas-oil (left border), gas-water (right border), and oil-water (lower border) flow). When all phases are present simultaneously, many more different flow regimes become possible.	24
Figure 13 - Flow pattern transition map with environment condition variation	26
Figure 14 – Schematic of a unit slug	28
Figure 15 - Adhesion force measurement method using an AFM.	29
Figure 16 - Topography images of a 30 μm × 30 μm area on the sample surface of four FeCO ₃ crystals scanned by applying different normal force: (a) 1.4 μN, (b) 8.4 μN, Crystal 2 is removed (c) 15 μN, (d) 22 μN, Crystals 1 and Cristal 3 are removed during the scanning. Crystal 4 cannot be removed by applying 30 μN which is the maximum value that the instrument can provide. ...	30
Figure 17 - (A) Schematic of a floating element WSS measurement system showing a sample measurement; (B) schematic diagram of WSS probe body.	32
Figure 18 - (A) Schematic design of bounded-channel flow cell; (B) schematic design of pipe flow loop with WSS.	33
Figure 19 - Specimen with a protrusion: specification and flow orientation (left: side view; right: top view).	34
Figure 20 – Specimen protrusion (A), flow velocity magnitude distribution (B), wall shear stress distribution (C), gauge pressure distribution (D).	35
Figure 21 - The dynamic viscosity changes as a function of WC. The emulsion was prepared by mixing oil and brine at a rotating velocity of 1200 rpm for 10 min.....	41
Figure 22 - 3D mapping of emulsion type	43
Figure 23 – Inversion point from normal to abnormal morphology (A+ → C+). Based on 3D map showing variation of emulsion.	44
Figure 24 – Compact separator (a) details of the section reduction in the separator entrance (b-c).....	47
Figure 25 – Software screen used showing the calculation of the flow properties (slug).....	49
Figure 26 - Software screen showing the parameters used and the results obtained for the flow frequency (slug).....	50

Figure 27 – Intermittent flow regime map	50
Figure 28 - Facilities layout for conceptual design (a) and (b).	51
Figure 29 - Corrosion multiphase loop as manufactured (a) and (b).	52
Figure 30 - Corrosion multiphase flow loop	53
Figure 31 – Emulsion box for conductivity determination	54
Figure 32 - Preliminary test to ensure a stable suspension during preparation and handling.	56
Figure 33 – O ₂ removal diagram in liquid preparation vessel.....	58
Figure 34 - O ₂ remove diagram in loop system.....	58
Figure 35 – Sensing module (a) and transduction and processing module (b) for flow measurements	60
Figure 36 - Loop monitoring screens (a) and process control (b) flow measurements.....	61
Figure 37 – Schematic drawing of specimen assembly WL into the bottom of the loop section.	63
Figure 38 - API carbon steel test specimen (a) loop test (b) RCE test.....	66
Figure 39 - Schematic view of the cavitation-erosion test equipment ¹²³	68
Figure 40 – Electrochemical cell diagram.....	68
Figure 41 - Emulsion test cell.....	69
Figure 42 – RCE test apparatus	71
Figure 43 – Schematic illustration of autoclave loading with brine and oil.....	72
Figure 44 – Vortex formation.....	73
Figure 45 – Microstructure of the longitudinal section of (a) API 5L X80 (ferrite + pearlite) and (b) API 5DP S (tempered martensite). Etchant: Nital 2 %.....	75
Figure 46 - Normal distribution for the LO tests.....	77
Figure 47 - Normal distribution for the HO tests.	78
Figure 48 - Multiphase flow-induced corrosion rate in the presence of CO ₂	79
Figure 49 - Multiphase flow-induced corrosion rate in the presence of CO ₂ with traces of H ₂ S.	79
Figure 50 – Corrosion rate (CR in mm/y) response surface analysis for LO (Equation 3).	94
Figure 51 - Corrosion rate (CR in mm/y) response surface analysis for HO (Equation 3).	96
Figure 52 – Cumulative mass loss for API 5L X80 and API 5DP S grade steels at 0° and 45° positions.	102
Figure 53 – Optical micrographs of the cross-section of API 5L X80 (a) and API 5DP S grade (b).	102
Figure 54 – XRD diffraction pattern of the surface of API 5L X80 steel test specimen a) 0° and b) 45° position.....	103
Figure 55 – Variation of the mass loss with cavitation-erosion testing time for API 5L X80 and API 5DP S grade.	105
Figure 56 – SEM surface images of the API 5L X80 carbon steel. (a) Before the cavitation tests (surface finishing obtained by grinding with ASTM 600 emery paper); (b) after 1 h testing; (c) after 3 h testing: wear marks, plastic deformation and some craters; (d) after 8 h testing: wear marks, craters and material detachment.	106
Figure 57 – SEM surface images of the API 5DP S grade. (a) Before the cavitation tests (surface finishing obtained by grinding with ASTM 600 emery paper); (b) after 2 h testing; (c) after 6 h	

testing: wear marks, plastic deformation and some craters; (d) after 10 h testing: wear marks, craters and material detachment and (e) after 16 h testing.....	107
Figure 58 - Cross-sectional SEM images of worn surface of API 5L X80 (a) and API 5DP S grade (b).	108
Figure 59 – OCP values of the API 5L X80 and API 5DP S grade specimens. Test conditions: 15 % of NaCl, 2 bar of CO ₂ partial pressure, 40 °C.....	109
Figure 60 – Potentiodynamic linear polarization curves of the API 5L X80 and API 5DP S grade specimens.	109
Figure 61 - Emulsion microstructures of (a) HO, (b) MO and (c) LO after the emulsion test with CO ₂ partial pressure of 2.0 bar, 80 % water cut stirred (1200 rpm) for 30 h at 40 °C. Stereomicroscope (Leica Fusion Optics M205C) images with a maximum magnification of 100x in 1.0x objective lens.....	111
Figure 62 – Visual appearance of the samples after emulsification test (a) HO (b) MO (c) LO and after analysis on the Turbiscan (a1) HO (b1) MO (c1) LO.	112
Figure 63 - TSI values of crude oil emulsions as a function of time at 40 °C.	113
Figure 64 – R_p (a) and estimated i_{corr} (b) for RCE tests in CO ₂ -brine solution (preliminary tests without oil).	117
Figure 65 – Corrosion rate calculated from weight loss measurement and estimated through the integration of the i_{corr} obtained in CO ₂ -brine solution (preliminary tests without oil).....	118
Figure 66 – Cathodic current densities for the cathodic potential of -0.87 V, SCE as a function of the square root of angular velocity (preliminary tests without crude oil).	119
Figure 67 – Optical Microscopy (OM) investigation of the surface of the specimen after the RCE tests in CO ₂ -brine solution (preliminary tests without oil).....	120
Figure 68 – R_p values with time of the RCE tests in CO ₂ -brine-LO, CO ₂ -brine-HO and CO ₂ -brine.....	120
Figure 69 – Surface images of WEs without cleaning (a) LO (b) HO, and (c) sample of the CO ₂ -brine-LO and (d) CO ₂ -brine-HO mixtures collected through the drain valve of the autoclave after 30 h of RCE tests.....	121
Figure 70 – Scheme of the emulsification process.....	122
Figure 71 – Corrosion rates calculated from weight loss measurements. For HO two values are presented: one considering the immersion time of 11 h (brine-wetting time) and the total test time of 30 h.	123
Figure 72 – Optical Microscopy (OM) analysis of the surface of the specimen after RCE test in (a) CO ₂ -brine-LO and (b) CO ₂ -brine-HO	124
Figure 73 – Main influencing factors on flow-induced corrosion.....	126
Figure 74 - Comparison between RCE test and loop multiphase-flow results for light and heavy crude oils and brine solution, CO ₂ partial pressure of 2 bar and 80 % WC + 20 %.	128
Figure 75 – Proposed multiphase slug flow 2D maps for (a) LO and (b) HO.....	129

TABLE LIST

Table 1 – Normal force, lateral force, cross-section area and stress values for removal of the nine FeCO ₃ crystals.	31
Table 2 – Validation tests for compact separator prototype built at the NIDF	48
Table 3 – Results of NaCl solution and WC preliminary tests using the device shown in Figure 31	55
Table 4 – Chemical composition (wt. %).	74
Table 5 – Mechanical properties.	74
Table 6 – Matrix of multiphase-flow loop tests.	75
Table 7 – Monitored parameters for tests performed with light oil.	76
Table 8 – Monitored parameters for performed with heavy oil.	76
Table 9 – Appearances of the surfaces of the specimens tested in the presence of LO and HO immediately after the tests.	80
Table 10 – SEM images and appearance of the surfaces of the specimens tested in LO after cleaning.	81
Table 11 – SEM images and appearance of the surfaces of the specimens tested in HO and after cleaning.	83
Table 12 – Multiphase flow loop tests.	88
Table 13 – Regression parameters for the multiple regression of CR.	90
Table 14 – Analysis of Variance for the CR regression.	91
Table 15 – Regression parameters for the Box-Cox transformation of CR (square root).	91
Table 16 – Analysis of Variance for the transformed CR regression (square root)	92
Table 17 – Regression parameters for the multiple regression of SBS.	97
Table 18 – Analysis of Variance for the SBS regression.	97
Table 19 – Regression parameters for the multiple regression of SBV	98
Table 20 – Analysis of Variance for the SBV regression.	98
Table 21 – Regression parameters for the multiple regression of SBF	98
Table 22 – Analysis of Variance for the SBF regression.	99
Table 23 – SEM images and appearances of the surface of the specimens tested in HO under CO ₂ partial pressure of 2 bar (the specimens were rinsed with isopropyl alcohol and pickled in Clarke’s solution)	101
Table 24 – Polarization resistance obtained directly from Figure 60	110

ACRONYM LIST

AFM	Atomic Force Microscopy
ANOVA	Analysis of variance
ANP	Agência Nacional de Petróleo ^a (ANP)
Avg.	Average
CAPEX	Capital Expenditures
CE	Carbon Equivalent
CFD	Computational Fluid Dynamic(s)
CRA(s)	Corrosion-Resistant Alloy(s)
CS	Carbon Steel
EDS	Energy Dispersive Spectroscopy
EIP	Emulsion Inversion Point
ER	Electrical Resistance Probes
ETP	Everhart Thornley Detector
FEG	Field Emission Gun
Fad	Adhesion force (s)
FIC	Flow-Induced Corrosion
FPSO	Floating Production, Storage and Offloading
GCL	Gas Carried by the Liquid
HIC	Hydrogen-Induced Cracking
HLD	Hydrophilic-Lipophilic Deviation
HO	Heavy Oil
HSE	Health, Safety and Environment
Lbody	Length of slug body
LCG	Liquid Carried by the Gas
Lfilm	Length of the stratified liquid film
Lmz	Length of mixing zone
LO	Light Oil

^a Brazilian Petroleum Agency.

LOM	Ligth Optical Microscope
LPR	Linear Polarization Resistance
Lslug	Length of Slug
MO	Medium Oil
NIDF	Interdisciplinary Center of Fluid Dynamics
O	Oil
OCP	Open Circuit Potential
OM	Optical Microscope
OPEX	Operational Expenditures
OV	Others Variables
O/W	Oil-in-water emulsion
O/W/O	Multiple emulsions
PIV	Particle Image Velocimetry
P&ID	Piping and Instrumentation Diagram
PSC	Production Share Contract
PSL	Product-Specification Levels
PT	Pressure Transmitter
R/T	Royalty and Tax
RCE	Rotating Cylinder Electrode
SARA	Classification methodology presented with the separation of the saturated (S), aromatic (A), resin (R) and asphaltenes (A') fractions
SCC	Sulfide Stress Cracking
SCRs	Steel Catenary Risers
SEM	Scanning Electron Microscopy
Semis	Semisubmersible(s)
SG	Spefic gravity
SP	Special Participation
SPARs	Surface Piercing Articulating Risers
SRB	Sulfide-Reducing Bacteria
SSC	Sulfide Stress Cracking
STDEV	Standard Deviation

TLPs	Tension Leg Platforms
TT	Temperature transmitter
TTRs	Top Tensioned Risers
UFRJ	Federal University of Rio de Janeiro
W	Water
WC	Water Cut
WL	Weight Loss
W/O	Water-in-oil emulsion
WSS	Wall Shear Stress
XRD	X-Ray Diffraction

SYMBOL LIST

α	Inclination
λ	Maximum likelihood estimation
μ	Oil dynamic viscosity
A	Area
CR	Corrosion Rate
d	Distance
DF	Degrees of freedom
ER	Electrical Resistance
f	Friction factor
F_S	Slug Frequency
F-value	Statistical test
K	Conductivity
L	Conductance
N_{Fr}	Froude Number
NR	Reynolds' number
(P_{CO_2}/P_{H_2S})	Partial Pressure ratio
P_{CO_2}	Partial CO ₂ pressure
P_{H_2S}	Partial H ₂ S pressure
P_{N_2}	N ₂ Partial Pressure
p-values	Statistical test
R	Resistance
R^2	Coefficient of determination
$R^2(\text{adj})$	Adjusted coefficient of determination
Ra	Average roughness
Rp	Polarization Resistance
SBF	Slug-Bubble Frequency
SBS	Slug-Bubble Size
SBV	Slug-Bubble Velocity
SE	Standard error of the coefficient

t-values	Statistical test
V_{sg}	Surface velocity of the gas phase
V_{sl}	Surface velocity of the liquid phase
x_1	Oil dynamic viscosity
x_2	Inclination
x_3	CO ₂ Partial Pressure
x_4	H ₂ S Partial Pressure
Wbreak	Water break

PUBLICATION LIST

The following publications listed below form an integral part of this thesis:

C. A. Silva, D. R. Filho, G. M. Nunes, G. S. Bassani, N. L. Almeida, e Z. Panossian, “**The design and development of a small-scale, multiphase flow loop for the study of corrosion in sour/sweet gas environments**”, in *Rio Pipeline Conference and Exhibition 2019*, 2019, p. 1–10.

C. A. Silva, D. R. Filho, G. M. Nunes, G. S. Bassani, N. L. Almeida, e Z. Panossian, “**Corrosion in multiphase slug flow loop in deep-water oil and gas exploitation**”, 2019, doi: 10.4043/29720-MS.

C. A. Silva, H. B. Pereira, M. E. S. Taqueda, e Z. Panossian, “**Prediction models for multiphase-flow-induced corrosion of API X80 steel in CO₂/H₂S environment**”, *Mater. Corros.*, p. 22, 2021, doi: 10.1002/maco.202112451.

C. A. Silva, L. B. Varela, F. Kolawole, A. P. Tschiptschin, e Z. Panossian, “**Multiphase-flow-induced corrosion and cavitation-erosion damages of API 5L X80 and API 5DP grade S steels**”, *Wear*, vol. 452–453, 2020, doi: 10.1016/j.wear.2020.203282.

C. A. Silva, D. R. Filho, M.H.A. Zanin, e Z. Panossian, “**Impact of Crude Oil Emulsion on Pipeline Corrosion**”, *J. Petrochemical Eng.*, vol. 1, n^o 1, p. 11–19, 2021, doi: 10.36959/901/249

C. A. Silva, D. R. Filho, T. Pimentel, Z. Panossian, “**Analysis of Crude Oil Effect for CO₂ Corrosion of Carbon Steel - a Rotating Cylinder Electrode Approach**,” vol. 6, no. 6, p. 21, 2023, doi: <https://dx.doi.org/10.2139/ssrn.4380157>.

CONTENTS

ACKNOWLEDGEMENTS	V
ABSTRACT	VI
RESUMO	VII
FIGURE LIST	VIII
TABLE LIST	XI
ACRONYM LIST	XII
SYMBOL LIST	XV
PUBLICATION LIST	XVII
CONTENTS	XVIII
CHAPTER 1 – INTRODUCTION	1
1.1 Background and industrial relevance	1
1.2 Objectives.....	2
1.3 Thesis structure	2
CHAPTER 2 – LITERATURE REVIEW	4
2.1. Upstream Market Overview	4
2.2. Offshore Industrial Scenario Overview	7
2.3. Subsea corrosion	12
2.4. Sweet corrosion.....	13
2.5. Sour corrosion	15
2.6. CO ₂ and H ₂ S corrosion	16
2.7. Flow-Induced Corrosion	20
2.8. Multiphase flow	25
2.8.1. Slug flow	27
2.8.2. Hydrodynamic effects	28
2.9. Emulsion	39

CHAPTER 3 – EQUIPMENT, MATERIALS AND METHODS	45
3.1 Multiphase flow loop testing.....	45
3.1.1 Concept, construction and operation of multiphase-flow corrosion loop	45
3.1.2 Compact separator	47
3.1.3 Preliminary tests for setup of operation parameters	52
3.1.4 Determining the composition of the liquid phase.....	53
3.1.5 Determining the agitation level in the preparation vessel to maintain homogeneity of the liquid phase.....	55
3.1.6 Oxygen removal procedure in the multiphase flow loop system	57
3.1.7 Sensing modules for multiphase flow	59
3.1.8 Flow Loop Monitoring System	61
3.1.9 Corrosion monitoring	62
3.1.10 Safety conditions for operation of the corrosion loop in multiphase flow	63
3.1.11 Installation site description.....	63
3.1.12 Security system components	64
3.2 Materials characterization and specimens preparations	64
3.2.1 Materials characterization	65
3.2.2 Specimen preparation	65
3.2.3 Corrosion rate from the mass loss measurement	66
3.3 Cavitation-erosion testing	67
3.3.1 Standard cavitation-erosion test	67
3.3.2 Electrochemical Test	68
3.4 Autoclave emulsion testing	69
3.4.1 Emulsification tests	69
3.4.2 Emulsion microstructure characterization	70
3.4.3 Analysis of emulsion instability by optical turbidimetry	70
3.5 Rotating cylinder electrode (RCE) testing	70

3.5.1	RCE test procedure.....	70
	CHAPTER 4 – EXPERIMENTAL RESULTS.....	74
4.1	Materials characterization	74
4.2	Results of Multiphase Flow Loop Testing	75
4.2.1	Monitored parameters.....	76
4.2.2	Test results.....	78
4.2.3	Discussion.....	86
4.2.4	Consolidation.....	87
4.3	Prediction models for multiphase-flow-induced corrosion of API X80 steel in CO ₂ /H ₂ S environment.....	87
4.3.1	Corrosion rate as a function of oil viscosity, pipe inclination and CO ₂ and H ₂ S partial pressure.....	90
4.3.2	Slug-bubble size, velocity, and frequency as a function of oil viscosity, pipe inclination and CO ₂ and H ₂ S partial pressure.....	97
4.3.3	Consolidation.....	100
4.4	Results of Cavitation-Erosion Testing	100
4.4.1	Multiphase Flow Loop Testing: comparing API 5L X80 with API 5DP S.....	101
4.4.2	Standard Cavitation-erosion Test	104
4.4.3	Electrochemical Test	108
4.4.4	Consolidation.....	110
4.5	Results of Autoclave Emulsion Testing	110
4.5.1	Results and discussion.....	111
4.5.2	Consolidation.....	114
4.6	Results of rotating cylinder electrode (RCE) testing.....	114
4.6.1.	RCE Preliminary tests: CO ₂ -brine solution without crude oil.....	116
4.6.2.	RCE with CO ₂ -brine-LO and CO ₂ -brine-HO mixtures.....	120
4.6.3.	Consolidation.....	124

CHAPTER 5 - GENERAL DISCUSSIONS.....	125
CHAPTER 6 - CONCLUSIONS.....	130
CHAPTER 7 - FUTURE WORK SUGGESTIONS.....	132
REFERENCES	133
ANNEX I	147
a) Parameters of crude oil fluids related to corrosion	147
b) SARA classification methodology	147
c) API gravity.....	147
d) Critical water break value (W_{break}) or emulsion inversion point (EIP)	148
APPENDIX I.....	149
a) Multiphase-flow validation of the sensors	149
b) Image of slug flow in the test of validation	149
APPENDIX II	151

CHAPTER 1 – INTRODUCTION

1.1 Background and industrial relevance

Corrosion has a very important impact on the Oil & Gas industry. On one side, this industry constitutes a significant part of the capital and operational expenditures (CAPEX and OPEX), whereas on the other side, it compromises the health and safety of the field personnel as well as the environment. It has been estimated that corrosion and scale formation accounts for 25 % of the operational safety incidents and for 8 % of the increase in CAPEX. The total spending on corrosion-related issues could be valued at around 33 % of the total OPEX for a single field. This way, corrosion can impose a significant cost penalty on the choice of material at the design stage. This cost is a consequence of poor corrosion control and awareness. On the other hand, of equal importance, corrosion costs present a potential impact on the control of health, safety, and environment (HSE). Therefore the corrosion management of Oil & Gas production is a topic of great relevance¹.

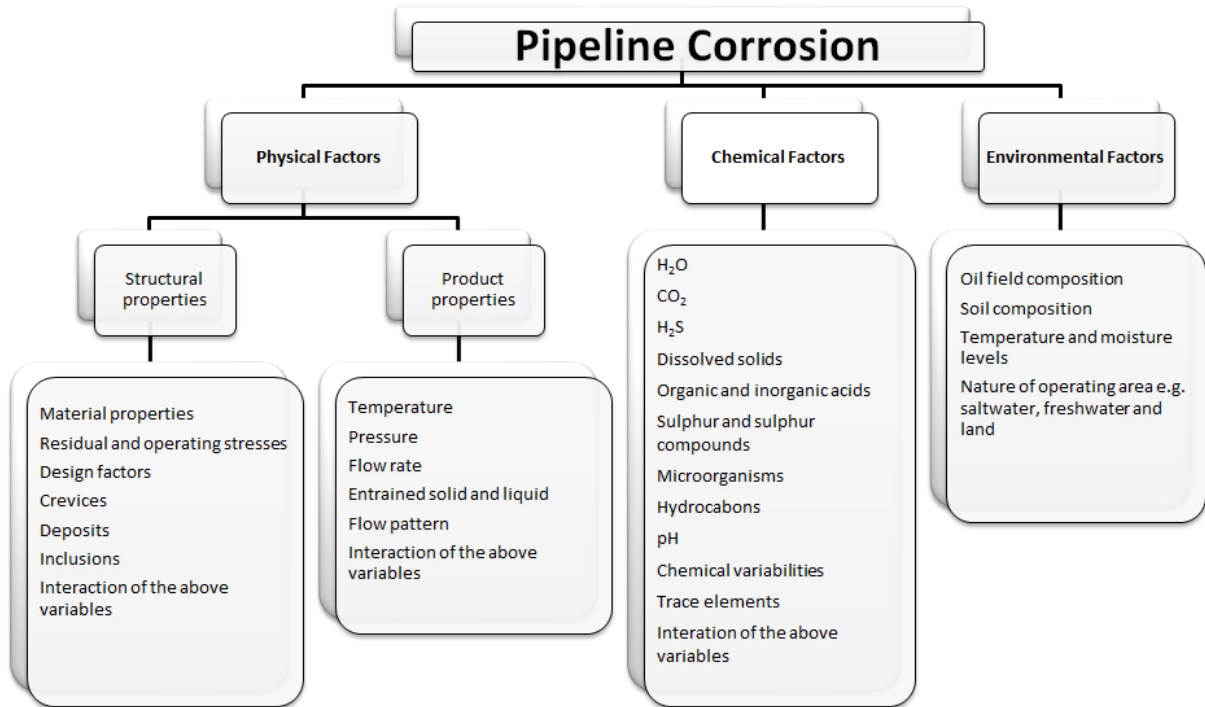
Carbon steel is the most commonly used material for pipelines in Oil & Gas production. This is due to its availability in the volume required, its relatively low price, and the possibility of easily satisfying mechanical and fabrication requirements. The increased water cut^b in the produced fluid, as a consequence of seawater injection, further aggravates the corrosion process and reduces the lifetime of the pipe material. The demand for oil has pushed the exploration to deeper fields, whose environment is extremely aggressive to the steel structures and equipment. The requirement to maintain production by injecting seawater needs to be balanced with the negative effects caused by this process on the corrosion resistance of carbon steel. The growing demand for reducing maintenance and operational costs has pushed the research to understand the mechanism of CO₂ corrosion of carbon steel in order to prevent its degradation.

Figure 1 shows the causes of pipeline corrosion, it is responsible for one-quarter to two-thirds of the total downtime in the Oil & Gas industry. Corrosion of pipelines can be attributed to numerous causes which are related to physical and chemical factors and includes both environmental conditions and the characteristics of the materials².

In this study, the interaction between physical, chemical and environmental factors will be addressed, with a focus on the parameters that involve corrosion in multiphase flow existing in Oil & Gas exploration.

^b Water cut is the ratio of produced water volume of the total of the produced liquid.

Figure 1 – Possible causes of pipeline corrosion



Source: Ossai, Boswell and Davies².

1.2 Objectives

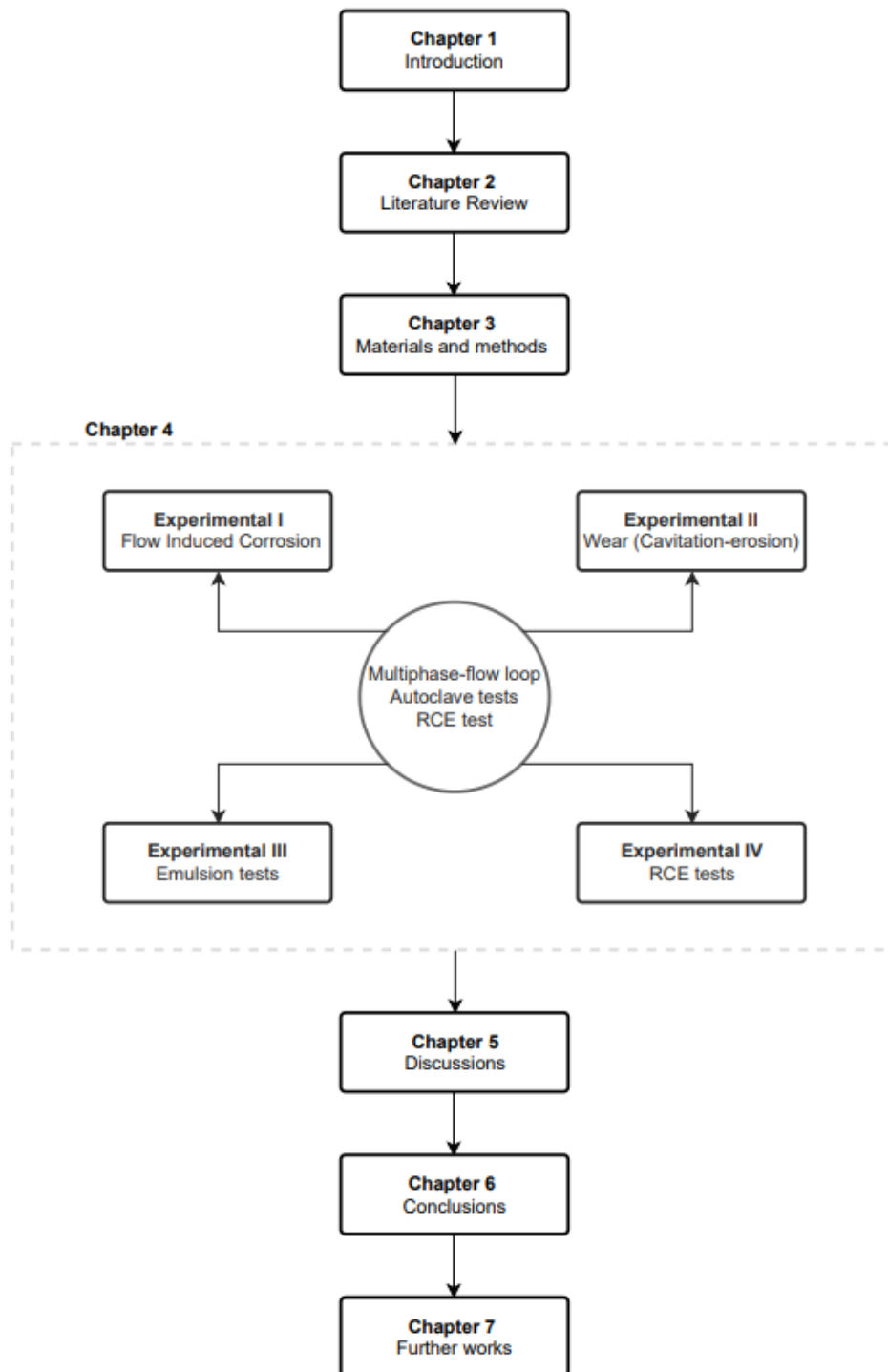
The main objective of this thesis was to study the corrosion induced by the multiphase flow (water, crude oil and CO₂/H₂S gas phases) of carbon-steel pipelines of mature wells of a pre-salt exploration condition. To achieve this objective, a specific corrosion multiphase-flow loop was projected and constructed. An additional objective was to understand the obtained higher corrosion rates with heavy oil which was not expected. This study was performed only under 2 bar of partial pressure of CO₂. Studies using CO₂/SO₂ as a gas phase will be performed in the future.

The corrosion loop was able to represent the corrosion phenomena and the hydrodynamic effects. The constructed loop is the only equipment with these characteristics in Brazil.

1.3 Thesis structure

The thesis is structured in 7 individual chapters. A diagram showing the individual chapters and their logical connections is shown in **Figure 2**. **Chapter 1** provides an introduction to the topic and the objectives of the project. **Chapter 2** presents a detailed literature review of the relevant pre-existing knowledge on the offshore market and industrial scenario overview, oil production well corrosion, multiphase flow and emulsion overview. A detailed overview of the fundamental aspects and experimental methods used in the current research are given in **Chapter 3**. **Chapter 4** presents the obtained results. **Chapter 5** presents a general discussion of the results, **Chapter 6** the main conclusions and **Chapter 7** the intended further works.

Figure 2 – Diagram showing the structure of the Ph.D. thesis



CHAPTER 2 – LITERATURE REVIEW

2.1. Upstream^c Market Overview

The world's demand for energy has led oil companies to expand their operations in cold environments such as offshore deep-water and onshore environments. In an offshore operation, subsea costs are the most significant of the whole project costs which generally include the capital expenditures (CAPEX) and operation expenditures (OPEX) of the subsea field development. The key costs of subsea CAPEX are related to the number of wells, water depth, pressure rating, temperature rating, material requirement and availability of an installation vessel³.

Nowadays, offshore production is responsible for about one-third of the global oil production and about a quarter of the world's natural gas supply. This scenario validates the risk of the operation itself. An important point is that offshore-production costs are roughly double of onshore-production costs due to the higher costs of installation and insulation of the former. For profitable production, the wells should produce roughly three times their costs.

An average onshore well may cost between US\$3 to US\$4 million and, an average shale-gas well, between US\$6 to US\$7 million including drilling, completion and fracturing. Deep-water wells cost significantly more, with a range of US\$75 to US\$175 million depending on the depth and the duration of the drilling. This means that a deep-water well should produce, on average, seven million barrels of oil to be profitable.

Deep-water reservoirs are usually prolific, with an annual decline rate of around 10 % and last for at least 20 years, sometimes 30 years, with typical host facility design life of 25 to 40 years. If a well operates for 10 years, it should produce 2000 barrels per day to be profitable. Such rates are on the low side for deep water, with most wells flowing 10 to 20 thousand barrels per day. The payback time for the best-producing wells in deep water is less than one year. While comparatively more productive deep-water wells present more risk due to their remoteness and cold and deep environment requiring a more thorough engineering design⁴.

Since 1997, Brazil has adopted a traditional Royalty and Tax (R/T) contract fiscal regime. According to Furtado, Gonçalves and Costa⁵, in this regime, the rent capture is done basically by royalty (5 % to 10 %), corporate tax (34 %) and special participation (SP) which depends on the petroleum field environment (onshore/offshore and water depth) and several other triggers, and it ranges from 0 % to 40 %.

However, after the discovery of pre-salt wells, the Brazilian authorities issued the new Production Share Contract (PSC) fiscal regime aimed at reducing the risk-reward balance. According to Smith *et al.*⁶, changes in the fiscal regime in the petroleum industry are common and, when done wisely, they can result in a more governmental rent capture without reducing

^c The upstream sector involves the exploration and extraction of crude oil and natural gas.

the levels of investment. In 2010, there have been two major fiscal regimes in Brazil: R/T and PSC.

The discovery of pre-salt in Brazil was announced by Petrobras in 2007. This represented a remarkable change in Brazil's position in the petroleum market. Soon, it was clear that this new geologic pre-salt province was much more prolific and had lower exploratory risks than other Brazilian geologic provinces³. In order to have an idea, it is worth mentioning that the pre-salt exploitation feasibility price is US\$56 per barrel, US\$8 corresponding to CAPEX, US\$10 to OPEX, US\$12 to the return from the entrepreneur and US\$26 from taxes and government participation⁷.

In Brazil, Furtado, Gonçalves and Costa⁵ performed an extensive analysis of the risk and attractiveness related to the fiscal regime, including the project, exploration and operation. They proposed a change of the auction methodology from a competitive bonus to a fixed and high bonus with a competitive profit-oil offer. In this way, the government was able to shift the desired companies' risk profile to a more aggressive one. The economic surplus share in the pre-salt province was adjusted without significant harm in the companies' profit: the government increased from 65 % to 68 % in the analyzed models based on the Libra prospect with volumes ranging from 800 MMBoe^d to 10,000 MMBoe.

The evaluation of CAPEX and OPEX for a petroleum upstream project is vital for deep-water reservoirs, given the need to optimize economic resources to make projects profitable^{5, 8}. **Figure 3** shows the pre-salt scenario for 7800 MMBoe total productions. After the first five years of exploitation, production starts, reaching its peak after 12 to 17 years of operation. At this stage of the project, CAPEX is the most intensive investment and, then, the project starts to demand more OPEX. In the period from 25 to 40 years, the necessity to save money for the abandonment and decommission stages becomes important.

Another point that impacts this assessment is the crude oil prices which change quickly in a response to new cycles, policy change and fluctuations in the world's markets. In recent auctions of the Agência Nacional de Petróleo^e (ANP), the interest in the pre-salt has been high among international oil companies. However, with the low oil price, a premium has been established on technologies which were able to reduce CAPEX and OPEX on the cost-side management⁹.

As mentioned, the impact of corrosion on the Oil & Gas industry is seen in terms of its effect on both capital and operational expenditures (CAPEX and OPEX) and on the control of health, safety and environment (HSE).

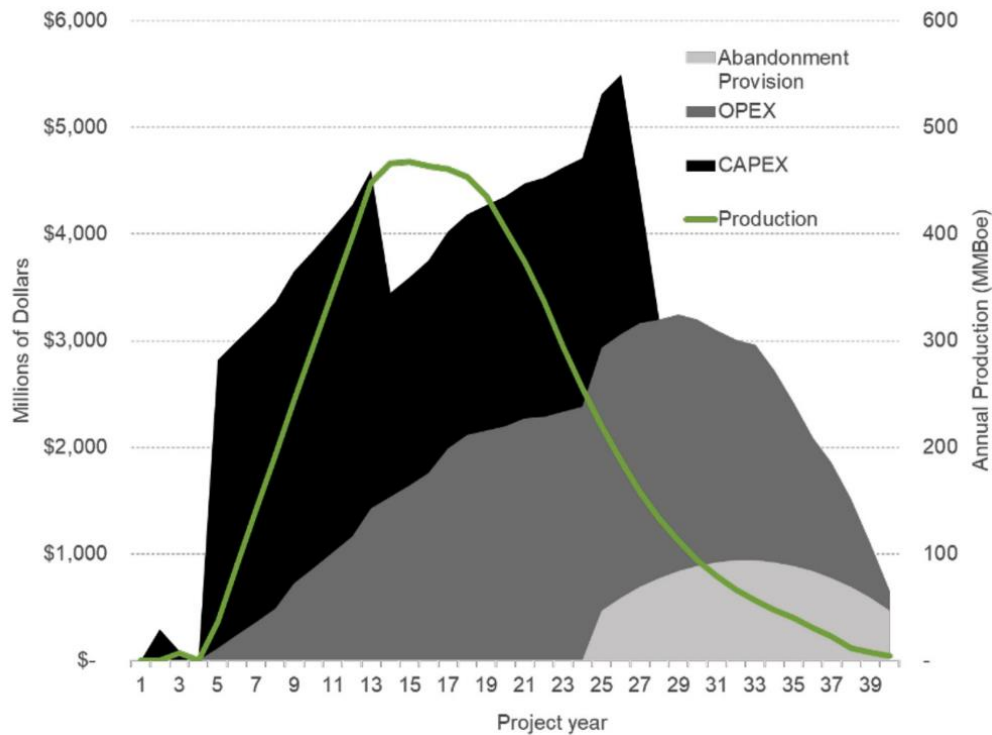
Beyond this point, we have growing populations that consume more energy which, in turn, increases the consumption of energy resources making them scarcer. They become harder to

^d MMBoe means Million Barrels of Oil Equivalent.

^e Brazilian Petroleum Agency.

extract. At the same time, forests are depleted, coal mines have become deeper, and oil has to be drilled in more complex environments. In other words, energy resource extraction experiences declining marginal returns.

Figure 3 – Profitable pre-salt scenario for a 7800 MMBoe total production



Source: Furtado, Gonçalves e Costa⁵.

The fuel coal, petroleum, and natural gas contribute to the sum of primary energy consumed worldwide and together, they thus represent about 88 % of the total. These fossil-fuel listed by the World Energy Council (1995) will be used by 2100, with the exception of the large resources of coal in Germany and the United Kingdom¹⁰. These data already justify all the attention given to studies on the exploration of these energy sources. To save energy, we need to know how to save materials.

In this context, O&G production corrosion challenges are not static phenomena. Fluid characteristics change over time, resulting in systems becoming less predictive for corrosion mitigation programs. Thus, methods based on technology and management can be considered corrosion prevention solutions.

The multiphase-flow metering and control are technologies that have a significant impact on the overall financial performance of pre-salt wells. For the ultra-deep-water environment, the return on investment of the use of multiphase-flow metering may be higher in Brazil than in other world areas because of the pre-salt flow rates, water salinity and CO₂ content which are higher and variable. To overcome these challenges, researchers recommend that further studies using multiphase-flow loops must be carried out by operators and manufacturers. They complement that, until today, there is not any multiphase-flow loop in the world that can

simulate the exact conditions of the pre-salt operational conditions. This may eventually represent a roadblock for the use of technologies which are in development⁹.

For the understanding and the study of the problem, several multiphase-flow loops have been built for corrosion tests in research institutions and petroleum companies. The multiphase flow loops show designs with variations even in the basic concept, using different pipe material and pumping systems and controls for simulating different field conditions, as described in several references^{11, 12, 21–30, 13, 31–40, 14, 41–50, 15, 51–60, 16, 61–70, 17, 71–78, 18–20}.

In general, the multiphase-flow loops are designed as closed loops and contain several functional parts. The corrosion rates, flow patterns and other flow parameters can be measured in the test section. The control of corrosion is an economic issue; however, the great challenge is to guarantee its effectiveness. Certainly, the use of corrosion-resistant alloys (CRAs) is an expensive alternative; an internal coating as an alternative is not technically easy to perform in the field and the use of inhibitors, although effective, requires attention regarding the chemical composition of the transported fluid which can affect their performance⁷⁹.

This research has focused on covering the correlation of parameters that show an influence on corrosion processes induced by flow regimes. The multiphase flow-induced erosion-corrosion in pipes was found mainly related to the interactions between the pipe surface and the fluid flowing along the surface⁸⁰.

From a practical point of view, multiphase-flow pipeline corrosion is a complex phenomenon and depends on crude-oil production conditions. In this way, the knowledge of the selection criteria for the piping system, risers and the structure configuration used in each well is important to provide technological solutions and flow assurance.

2.2. Offshore Industrial Scenario Overview

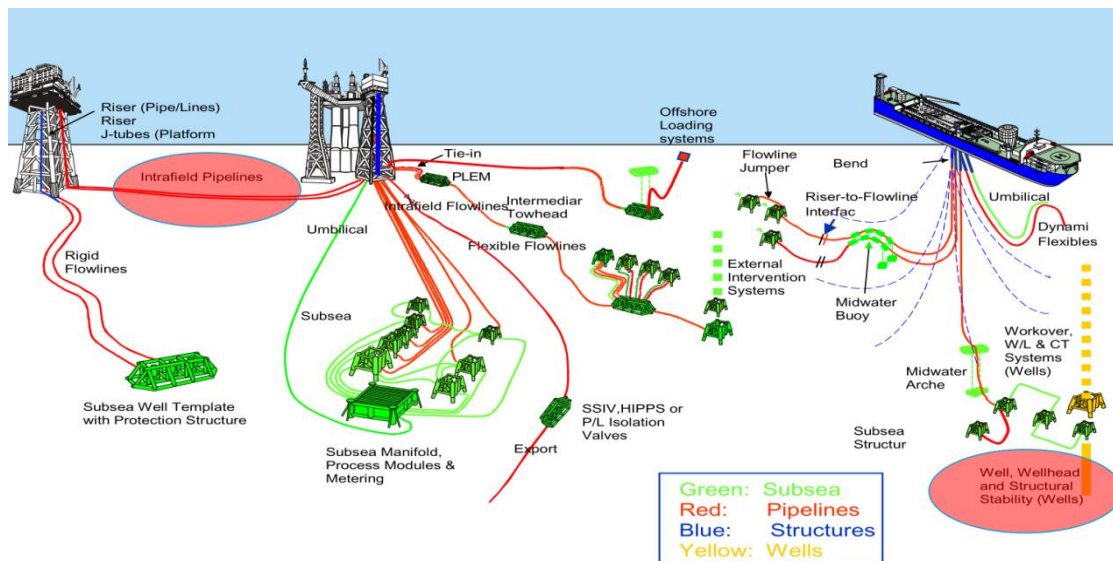
An overview of pipelines, riser designs and production system components used in offshore oil and gas exploration is the purpose of this topic and aims at showing the system complexity and the correlation of variables that may lead to multiphase-flow induced corrosion damages. An offshore production system consists of a completed well, a seabed wellhead, a subsea production tree, a subsea tie-in to flowline systems and subsea equipment and control facilities to operate the well. It can range in complexity from a single satellite well with flowlines linked to a fixed platform, to a Floating Production, Storage and Offloading (FPSO), or onshore facilities; or to several wells on a template or clustered around a manifold also linked to fixed or FPSO facilities or directly to onshore facilities⁸¹.

The system works in a simple way. From the reservoir, fluids are transported up through the production piping and into a wellhead before making their way to a processing platform. Basically, flowlines refer to the pipelines carrying hydrocarbon streams from the wellhead to the riser foot of the processing facility. There is another class of flowlines that are used to transfer fluids between platforms, manifolds and satellite wells, and to inject water and

chemicals. A general schematic arrangement of production system components and infrastructure is shown in **Figure 4**^{82, 81}.

The existing platforms can be used for several wells, extending their subsea production systems. For example, the geometry and the extension of a reservoir may be such that conventional directional drilling techniques are not able to cover its entire length, requiring the expansion of the subsea system of the main well.

Figure 4 - General arrangement of offshore production system components and infrastructure



Source: Cookingham⁸².

Water depth can also impact subsea field development. For shallow wells, limitations on subsea development can be derived from the height of the subsea structures. Christmas trees and other structures cannot be installed in water depths of less than 30 m. For these cases, jacket platforms consisting of dry trees can be used. The goal of subsea field development is to safely maximize economic gain using the most reliable, safe and cost-effective solution available at the time⁸².

Wells are clearly the center of all oil and gas operations both onshore and offshore. Wellheads may be located on the platform or at the mud line and, similarly, trees, which sit atop the wellhead, may be above or below the waterline. Dry-tree wells refer to trees above the waterline, whereas wet-tree wells refer to trees located on the seafloor. Dry-tree wells are accessible via a platform rig, whereas wet-tree wells require a mobile offshore drilling unit for interventions. Wet-tree wells are controlled using umbilicals from a nearby platform and route their production to the host via flowlines and up to platforms. Direct vertical access wells are a special type of subsea wells where the wellhead and the tree are located on the seafloor but they are accessible from a platform rig⁸³.

The infrastructure around the well is essential and depends on the requirement of each design. In shallow water, designs are relatively simple. If the field is large enough, a fixed platform is installed and wells are drilled and completed from the platform which usually processes the

oil production. For smaller reservoirs, a simple structure is installed around wellbores drilled from a jack-up rig and the production is directed back to a host platform for processing. In deep-water, multiple host and subsea layout configurations are possible and are designed based on their costs, risks and tradeoffs. Wet wells are used for marginal developments or in conjunction with a stand-alone facility. There is a variety of worldwide-used deep-water structures which include FPSOs, by far the most common, semisubmersibles (Semis), surface piercing articulating risers (SPARs), tension leg platforms (TLPs) and their varieties^{81, 83, 84}.

The primary purpose of the infrastructure is to hold the pieces of equipment in their position and to use them to exploit crude oil and to separate it into oil and gas streams for transportation. There are usually two exportation pipelines for oil and gas. But in some cases, there may be just one existing pipeline and in others, more than two. The number of flowlines and pipelines that board and depart from a structure depends on several factors such as the way of exploiting subsea wells and the type of platforms⁸³.

Umbilicals in the offshore industry are used for connections between the subsea equipment and platforms or FPSOs and enable the whole operation control. Umbilicals are made of steel and thermoplastic to be flexible and at the same time to resist operating conditions⁸⁵.

Pipeline construction costs are typically categorized according to material, services, engineering and inspection. The type of pipeline, the contractor, the installation requirements and the contracting strategy determine the way costs are categorized⁸⁶. Pipelines may be classified as rigid pipes, flexible lines, or pipe-in-pipe systems. All types are used in offshore applications, but rigid pipes and flexible lines are by far the most common in terms of covered distances. Rigid pipes are the least expensive and are considered the most reliable for long-term service⁸³.

The design of a pipeline is always in accordance with codes and specifications which define materials to use, working stresses, seismic loads, thermal expansion, other imposed internal or external loads, as well as fabrication and installation. In addition, other variables need to be observed as fluid(s) to be transported (oil/gas/solids, single/multiphase), length and required capacity, the environment (warm/cold climate, overland/buried/subsea, urban/countryside), and operational conditions (need for valves, compressors, pumps, emerges chambers, storage capacity)⁸⁷.

A fluid flow through a pipeline is generally categorized based on the fluid-phase condition: single-phase, two-phase and three-phase conditions. The single-phase condition is typical for export pipelines used to flow a single-phase hydrocarbon fluid, such as crude oil, dry gas and chemicals such as methanol and glycol lines⁸³.

A typical production fluid consists of water, oil and gas; oil and released gas; and gas and produced oil (condensate). In these cases, there is more than one-phase flow, i.e., multiphase flow. This mode of transportation is significantly more complex than one-phase flow^{83, 85}.

In the United States, oil and gas pipelines are constructed using pipe materials according to API Specification 5L, Line Pipe (API 5L) standards⁸⁵. API 5L provides requirements for the manufacture of seamless and welded pipes and consists of historical scientifically-validated criteria. Specification 5L is not a “how to” instructional manual, but rather a set of boundary limits and performance characteristics. There are two Product-Specification Levels (PSL): PSL 1 and PSL 2. PSL 1 is a standard quality level and PSL 2 applies tighter controls on chemical composition, mechanical properties and quality. PSL 2 has mandatory requirements for carbon equivalent, notch toughness, maximum yield strength and maximum tensile strength. Specification 5L also has annexes for supplemental requirements for fracture control in gas pipelines, sour services and offshore services⁸³.

Carbon steel (CS) is commonly used because of its good mechanical properties and cost-effectiveness in comparison with corrosion-resistant alloys (CRAs) but it is more sensitive to general corrosion in oil and gas environments. Iron carbonate and iron sulfide scale formation and also the use of chemical inhibitors help to reduce the corrosion rates of CS. However, a small amount of sand or other solid particles in the transported fluid can cause damage to the iron carbonate/sulfide scale or of the protective inhibitor film and consequently create a synergistic erosion-corrosion effect⁴⁹. Carbon steels used in offshore pipelines are low carbon-manganese alloys specified by a large number of characteristics which include chemical composition, mechanical properties, surface condition, grain size, hardenability and production process. Yield strength is a fundamental feature and is defined as the maximum stress the material can experience without failure. Strength is measured in units of force per area as thousand Newton per square meter (N/m^2) or pounds per square inch (ksi). The two-digit number following the “X” indicates the minimum yield strength (in ksi) of pipe steel⁸³. Currently, higher-strength steels for offshore projects are available; however, X80 is still the most used for pipelines. By increasing the strength of the steel, the cost per unit weight basis will increase, but the diameter and wall thickness of the pipeline may decrease, decreasing the total weight of the pipe and welding costs since less filler material is used⁸³.

Risers constitute the fluid transfer system, linking the seabed (drilling, production and import/export pipelines) to the platform of the facility. Production and water/gas injection risers connect the surface equipment to the wellheads at the seabed; export risers connect the processing equipment to seabed pipelines; and drilling risers are used to hold the drill string and serve as a conduit for drilling fluids between the surface and the wellhead. Risers are different from the pipelines and flowlines which are installed on the seabed and are subjected to a range of changing forces.

Ocean currents, water pressure, vessel motion and wave actions are the primary forces that risers encounter over their lifetimes and, therefore, must be designed to minimize fatigue damage. The riser design is one of the most complex in the deep-water production system, being highly dependent on the type of platform. Risers attached to fixed platforms are considerably different from risers attached to floating structures. There are three types of risers: rigid risers which include steel catenary risers (SCRs) and top-tensioned risers (TTRs),

flexible risers and hybrid risers that combine elements of rigid and flexible risers. The choice between flexible and rigid risers involves tradeoffs in cost and reliability.

SCRs were initially used as export lines on fixed platforms, attached to the outside of the structure, vertical at the top end and horizontal at the lower end. In this arrangement, the riser forms an extension of the flowlines which are hung from the platform in a catenary shape. In deep water, SCRs are free-hanging with no intermediate buoys or floating devices. SCRs are sensitive to waves and currents. Therefore, vortex-induced vibration-suppression devices such as helical stakes and fairings are used to reduce vibrations. SCRs are the most common riser types for export lines and wet trees.

TTRs are long circular cylinders used to link the seabed tree to a floating platform and are designed to provide direct access to wellheads on the platform. TTRs are held in tension at the surface and allow the riser to move axially or stroke relative to the platform. The risers often appear in a group arranged in a rectangular or circular array. TTRs are commonly used on TLPs and SPAR-dry-tree platforms. Flexible risers use flexible pipes in their configuration which depends on the water depth and the environment. Hybrid risers consist of a vertical bundle of steel pipes supported by external structures^{83, 85, 84}.

The design of a marine riser system will require consideration of several factors related to its functional suitability and long-term integrity. Considerations should be given to⁸⁵:

- consistency with Laws, Acts and Regulations;
- riser integrity: reliability, safety and risk;
- riser functional requirements;
- riser operational requirements;
- riser structural design criteria;
- materials;
- installation requirements;
- fabrication requirements;
- inspection and maintenance;
- engineering costs.

From an operational risk perspective, risers are susceptible to dynamic loads which can lead to failures. Due to its importance to oil and gas production, a structural riser failure can lead to severe financial losses to the operator. It results in a reduction or cessation of revenue by interrupting production; it may also lead to spillage and pollution and may even endanger lives. The following most probable external threats for those risers were determined: impacts, corrosion, overstress, fatigue, wear, material degradation and fire or explosion in the above-water sections⁸⁸.

A recommended practice for pipeline corrosion management has been compiled by British Petroleum which covers risers, transportation pipelines, trunk lines for multiphase fluids, flowlines and gathering lines, manifolds, catenary/dynamic risers, pig launchers and receivers. The practice includes the corrosion management policy and the risk-based inspection process.

It recommends a monitoring system which should provide warnings and alarms to responsible personnel when corrosion rates are high.

The implementation of corrosion management has been associated with a steady decrease in corrosion failures in offshore and onshore pipelines. Probabilistic assessment is used to estimate the probability of failure with time. It has been estimated that a corrosion management system has saved US\$3 million per year for an oil company in Nigeria. The implementation of a corrosion management system in Oman led to capital cost savings of US\$16 million and a rapid assessment of the implications of a rupture caused by internal corrosion. Integrated corrosion management systems have helped operators of gas-gathering projects in Australia to optimize resources used for inspection and maintenance and decrease the inspection work scope. The installation of such a system saved a Western Canadian gas processing unit between US\$300,000 and US\$3 million by decreasing corrosion rates so that a vessel which may have required replacement in 3.3 years could operate such that replacement would be needed in 36 years. The use of this best practice allows one to economically and safely produce and transport oil and gas⁴⁹.

2.3. Subsea corrosion

Subsea corrosion is becoming more a significant issue and, thus, can lead to economic and ecological disasters. In this context, the failure in the deep-sea structures (manifolds, flexible pipes, and flowlines) could be disastrous. Unlike onshore structures or even shallow-water structures, access to regular monitoring and repair is not an easy option, in terms of both cost and accessibility. Therefore corrosion management for subsea structures mostly relies on the estimation of corrosion rates. These corrosion rates themselves are calculated based on experimental research results and therefore, they are always limited in terms of their assumptions and applications.

Pipelines are commonly made of carbon steels which, as mentioned, present good mechanical properties, low cost and wider availability despite their relatively low corrosion resistance. In oil and gas exploration, the presence of highly corrosive agents such as CO₂, H₂S and chlorine compounds, which are dissolved in the fluids can accelerate the internal corrosion process of the pipeline^{89, 90}.

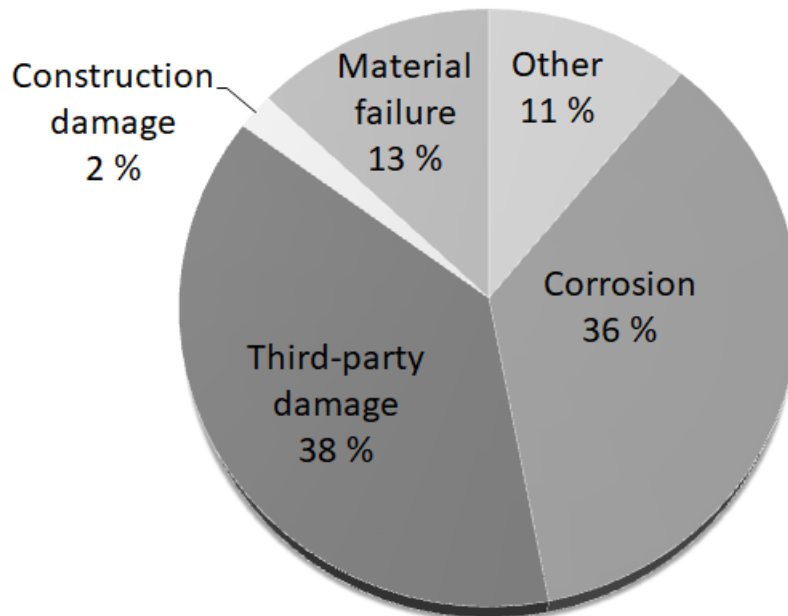
We can consider two categories of pipeline corrosion: internal corrosion caused by chemical agents, solids and fluid flow in pipelines; and external corrosion caused by ambient conditions of the subsea pipeline. For internal corrosion, the electrochemical process occurs due to the presence of contaminants such as carbon dioxide, hydrogen sulfide, and microbial community.

In the presence of CO₂, the internal corrosion starts locally, it develops slowly and its rate increases with the concentration of CO₂, temperature and pressure. H₂S-induced corrosion has four forms which depend on the environmental conditions of subsea pipelines: (i) sulfide pitting corrosion from the deposition of solid sulfide formed by the reaction of ferrous ion and

hydrogen sulfide; (ii) pitting attack at the cracking area of the sulfide film formed on the surface of pipelines; (iii) Sulfide Stress Cracking (SSC) and (iv) Hydrogen-Induced Cracking (HIC) and blistering occurring, in the pipeline due to atomic hydrogen diffusion in the pipeline. No less impacting, the microbiological corrosion results from the effects of sulfate-reducing bacteria (SRB) in the subsea pipeline. These bacteria flourish in water and oxidize fatty acids and generate CO₂, water and sulfide. Once sulfides are produced by SRB in the pipeline, microbiological corrosion acts similarly to a pitting attack in sour corrosion⁹¹.

Based on the literature review and incident data analysis, subsea pipeline failure can be grouped into four categories as shown in **Figure 5**. In this correlation the third-party damage and corrosion constitute the most important risk factors, accounting for 38 % and 36 % respectively⁹¹.

Figure 5 – Subsea pipeline failure



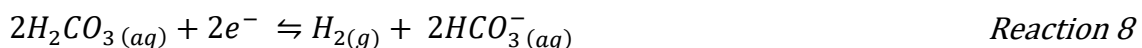
Source: Yang *et al.*⁹¹

In this work, in addition to the corrosion process caused by CO₂ and H₂S, the flow issues will be considered, because the high-velocity fluid flow may destroy the protective layer formed on the pipeline's internal surface. This fact accelerates corrosion processes⁹¹.

2.4. Sweet corrosion

Corrosion in carbon steel in CO₂-containing fluids depends on some parameters such as temperature, pressure, pH and steel composition. Researchers proposed a theoretical model for CO₂ corrosion in which the main focus was the factors influencing the formation of a protective iron-carbonate layer (FeCO₃) and the effect that this layer has on the overall

process of CO₂ corrosion. They suggest that corrosion rates are not associated with the thickness of the layer, but rather with their degree of homogeneity and the coverage on the metal surface. This layer may partially cover the surface and, consequently, may block just a part of the exposed metal or the layer may cover evenly the entire surface of the steel and may prevent further corrosion. Additionally, the processes occurring during corrosion under this layer at its interface with the metal may induce voids in the layer. The rate at which such voids appear determines the type of the layer, whether protective or not. The reactions which occur in systems containing CO₂ and that promote the formation of this layer are presented below³⁹:



It is possible to verify that the dissolution of CO₂ (**Reaction 1**) and the hydration of the dissolved CO₂ (**Reaction 2**) form carbonic acid. Then, the formation of bicarbonate and carbonate occurs in two steps (**Reaction 3**) followed by (**Reaction 4**). CO₂ corrosion is an electrochemical reaction with a global reaction (**Reaction 5**) leading to FeCO₃ formation, whereas the precipitation may form a protective or non-protective layer, depending on conditions such as flow velocity, pressure and temperature. The electrochemical reactions on the steel surface include the anodic dissolution of iron (**Reaction 6**) and two cathodic reactions (**Reaction 7** and **Reaction 8**).

The cathodic reactions are those of the reduction of protons and the direct reduction of carbonic acid. The corrosion rate of steel by CO₂ is determined by factors such as solution characteristics, flow rate, temperature, pressure and pH.

2.5. Sour corrosion

The presence of H₂S may lead to the formation of an iron-sulfide (FeS) layer. Studies have reported that, at a given temperature, the corrosion rate and the FeS-layer morphology depend on the amount of H₂S and the exposure conditions. In some cases, the iron-sulfide layer is protective; in other cases, it may not be protective, resulting in a localized attack. Understanding the mechanisms of the formation of the various forms of iron sulfide layers and their effect on the process of CO₂ corrosion are the main challenges in the prediction of CO₂/H₂S corrosion⁹².

The corrosion of carbon steel by CO₂ in the presence of H₂S is a great concern for oil refineries and natural-gas treatment facilities. Lately, this problem has become more important as the currently available oil reserves have a considerable amount of H₂S. Although there are many publications on the interaction of H₂S with low-carbon steels, the understanding of the H₂S effect on CO₂ corrosion is still limited because the nature of the interaction with carbon steel is complex. Additionally, elemental sulfur is often associated with high H₂S concentration and very little is known about the complex interactions in the presence of these species. It is known that H₂S may also lead to corrosion problems associated with sulfide stress cracking in the sour regime. In this study, these problems will not be addressed³⁹. When a small amount of H₂S is dissolved in an aqueous solution, a mild acid is produced and this acid may be treated as just another cathodic species. Additionally, the presence of H₂S may lead to the formation of various forms of iron-sulfide layers. The effect of this small concentration of H₂S on the corrosion of CO₂ was studied by maintaining constant other parameters such as pH, partial pressure of the gas phase and temperature, aiming at avoiding complex questions about the precipitation of FeS layers. Recent studies suggest that FeS layers, such as mackinawite, may be formed on the surface of the steel through solid-state reactions regardless of whether supersaturation over iron sulfide occurs. These FeS layers have two distinct and opposing effects on corrosion: they may inhibit corrosion (proportionally to the surface coverage) which is dominant at very low concentrations of H₂S, but also appear to have a corrosion acceleration effect at higher concentrations of H₂S, probably providing a larger surface area for the cathodic reaction. Researchers mention that, although H₂S is about three times more soluble in water than CO₂, the acid formed by the dissociation of H₂S is approximately three times weaker than the carbonic acid^{39, 93}. Thus, the effect of H₂S on decreasing the pH of the solution is almost the same as the CO₂ gas. The different reactions involved in the formation of FeS layers are described below⁶⁹:





It can be verified that, in the presence of H₂S, the chemical reactions begin with the dissolution and the dissociation of the dissolved H₂S followed by the dissociation of the HS⁻ ion.

2.6. CO₂ and H₂S corrosion

In the Oil & Gas industry, the most aggressive multiphase condition occurs when the fluid consists of seawater (aqueous phase), oil (organic phase) and the injected carbon dioxide (CO₂ gas phase), and the produced hydrogen sulfide (H₂S gas phase) under a slug-flow regime. The corrosion rates of carbon steel exposed to CO₂ and H₂S environments are generally estimated by prediction models based on experimental data obtained from laboratory tests, usually in the absence of hydrocarbons (organic phase). Several studies have been performed on the corrosivity of the aqueous phase which is dependent on the partial pressure of CO₂ and H₂S, temperature, flow pattern, water cut and composition of the produced water. The influence of these parameters on the carbon-steel corrosion mechanisms is also included in these studies. In general, the corrosion tests are conducted using loops which simulate the field production condition and are widely adopted to understand and identify the most representative field parameters influencing the corrosion process of carbon steel under a slug-flow regime^{17, 21, 64, 73, 75, 77, 94–99, 32, 100–105, 33, 35, 37, 38, 47, 57, 60}.

In general, the above-mentioned studies are focused on fluids containing a water phase and a gas phase, without an oil phase^{11, 12, 21–30, 13, 31–40, 14, 41–50, 15, 51–60, 16, 61–70, 17, 71–78, 18–20}. Some of them include a very light oil phase (below 2 cP). However, the water-oil-gas multiphase flow is the real condition of the oil and gas exploitation industry, especially for deep-water wells. Additionally, with the aging of wells, the pressure decreases and, thus, recovery methods such as CO₂ and water injection are commonly employed to maintain the pressure of the well.

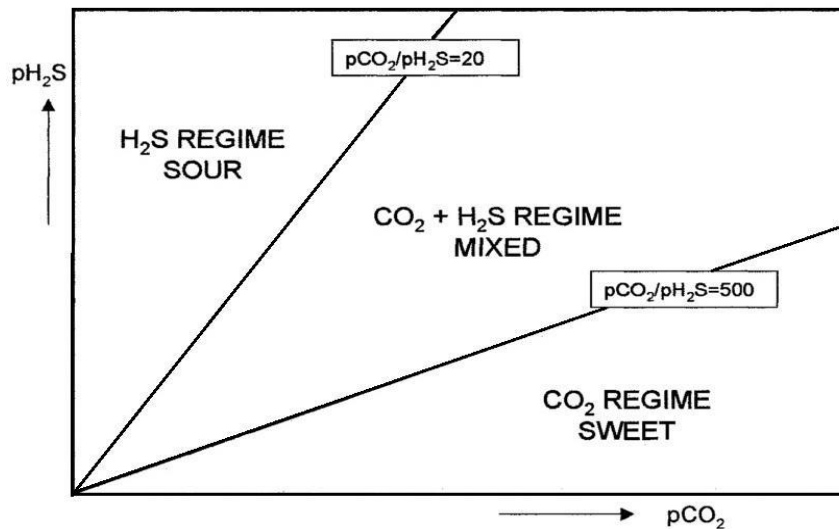
The use of CO₂ can increase the internal corrosion of carbon-steel pipes and equipment by reducing the pH of the aqueous phase, by emulsifying the oil and water mixture and by increasing the number of bubbles dispersed in the transported fluid. To understand the flow-induced corrosion mechanisms, this study focused on the analysis of the influence of chemical species on the electrochemical reactions as well as on the hydrodynamic effects.

Laboratory tests, described in the literature, allow the establishment of empirical correlations between the corrosion rate and specific exposure conditions. These correlations are thus used in corrosion prediction software which can help engineers design and monitor the life expectancies of industrial pipes. The majority of experimental studies found in the literature

address corrosion studies in a CO₂/H₂S environment limited to tests performed in autoclaves and glass cells. In these systems, a researcher produces test results which, despite their being useful in the understanding of corrosion mechanisms, are not able to produce multiphase-flow-regime results similar to those related to the conditions of pipelines in oil and gas exploitations. A small-scale corrosion loop provides a suitable environment for better reproducing hydrodynamic effects on the corrosion of pipe walls⁹⁵.

The simultaneous presence of CO₂ and H₂S in fluids promotes the formation of an aggressive environment which may lead to severe corrosion of carbon steel. There are a limited number of studies covering this area, particularly, when it is compared to the extensive literature available on corrosion in a CO₂-saturated environment. H₂S-related corrosion is a subject of great concern. Researchers report that H₂S-related corrosion is not widely studied in laboratory conditions because of the difficulty of working with H₂S. However, the need to understand the corrosion of CO₂ and H₂S has grown with the increase of the exploitation of deeper and more corrosive wells⁹⁵. Generally, three regimes in CO₂ and H₂S systems are considered based on H₂S concentration, as shown in the diagram of **Figure 6**. It can be verified that the “CO₂-H₂S regime mixed” condition adopted in this work were those limited to pressure ratios P_{CO_2}/P_{H_2S} of 100 and 400.

Figure 6 – Corrosion regimes in CO₂/H₂S



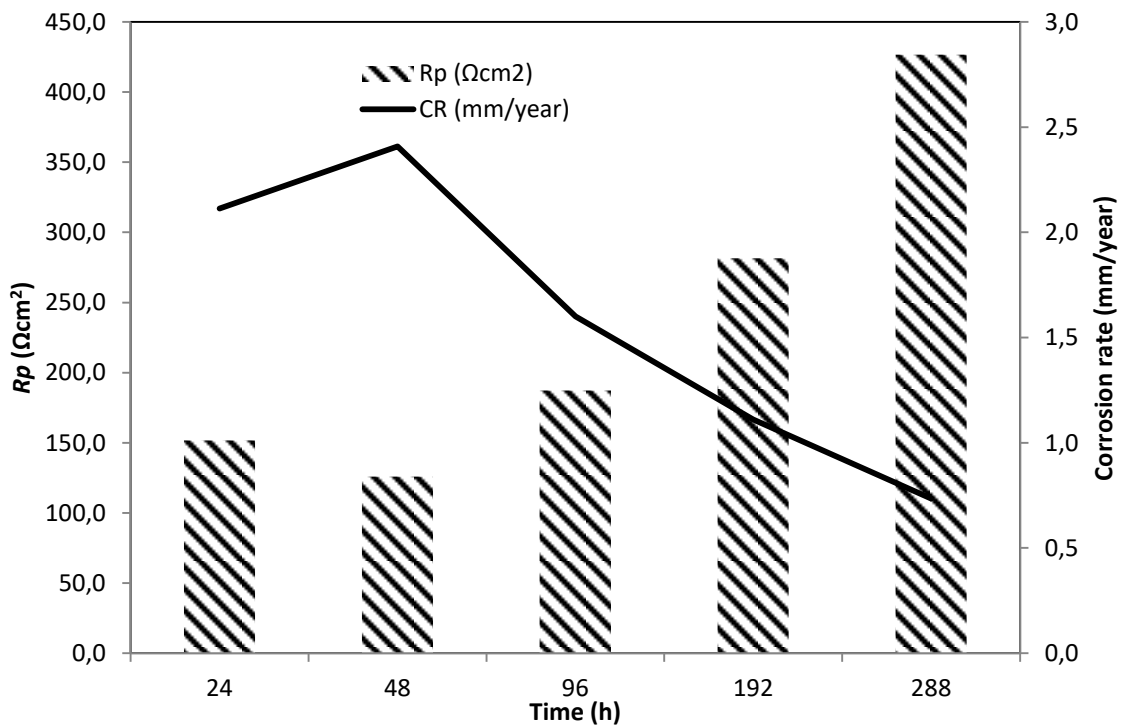
Source: Brown, Nestic and Pots^{69, 106, 107}

Studies have shown that the presence of H₂S can accelerate or inhibit the corrosion of carbon steel in a CO₂ environment, depending on the H₂S content and test conditions^{108,109,110,111,106}. However, the conditions, which were studied throughout this work, were not found in the literature. After an extensive review, some studies covering sour and sweet regimes shown in **Figure 6** were found which will be briefly cited to exemplify the complexity of the interactions of the environment containing both CO₂ and H₂S.

Wang *et al.*¹¹² performed corrosion tests in an autoclave by immersion of specimens of low alloy steel in a 3.5 % NaCl solution in the presence of a mixture of CO₂ and H₂S. During the

test, the solution was heated to 75 °C and the total pressure was adjusted to 12 bar with partial pressures of 0.9 bar H₂S, 6.4 bar CO₂ and 4.7 bar N₂ (P_{CO_2}/P_{H_2S} ratio of 7.1, corresponding to sour regime according to **Figure 6**). Five immersion times (24 h, 48 h, 96 h, 192 h and 288 h) were chosen to investigate the corrosion behavior of the studied steel. **Figure 7** presents the results of the corrosion rates (*CR*) and polarization resistance (*R_p*). Regarding the polarization resistance, we can observe that it increases *from* 24 h to 48 h, and then decreases continually up to 288 h. The corrosion rate presented an opposite behavior, as expected¹¹².

Figure 7 – Corrosion rate (*CR*) and polarization resistance (*R_p*) of the studied low alloy steel exposed to CO₂/H₂S in sour regime according to **Figure 6**



Source: plotted from Table 2 of Wang *et al.*^{108,109,112}

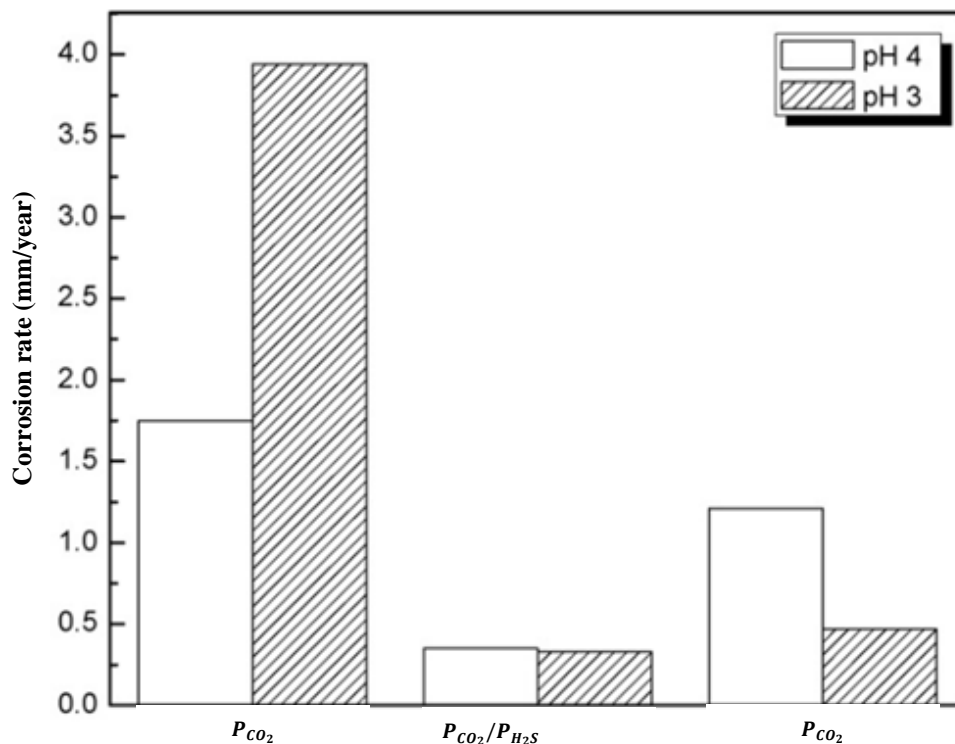
Choi, Nescic and Ling¹¹³ performed corrosion tests with carbon steel using a rotating cylinder electrode (RCE) at 1000 rpm in a glass cell (2 L). Measurements were taken and the tests were carried out in a 1 % NaCl solution at room temperature and a total pressure of 1 bar. Gas mass flow controllers were used to determine the flow rate of CO₂ and H₂S in the test cell. Before the carbon-steel sample was inserted into the solution, the solution was purged with CO₂ for 2 h, then adjusted to the desired pH value of 3 and 4 with the addition of an HCl solution or NaHCO₃ solution as appropriate.

Three stages were adopted as a test procedure to investigate the effect of H₂S on carbon-steel corrosion in CO₂ environments. In the first stage, only CO₂ was used, in the second stage, the tests were conducted with the sweet regime according to Figure 6 (P_{CO_2}/P_{H_2S} of 9.7×10^3), with a partial pressure of 0.97 bar of CO₂ and 10⁻⁴ bar of H₂S (100 ppm) and, in the third stage, just in the presence of CO₂.

During the experiment, instantaneous corrosion rates were monitored through Linear Polarization Resistance (LPR) measurements taken at regular time intervals. LPR measurements were performed over a range of ± 10 mV with respect to open circuit potential (OCP) and a scan rate of 0.166 mV/s.

Figure 8 shows a comparison between the results of the RCE tests at the end of each proposed stage. The corrosion rates of carbon steel were measured under pH 3 and 4 conditions. At pH 4, we can see that with the addition of a low concentration of H_2S (100 ppm) in the CO_2 environment, there is a reduction in the corrosion rate which corroborates with previous publications.

Figure 8 – Corrosion rates were measured in pH 3 and 4 conditions



Source: adapted from Choi, Nestic and Ling¹¹³

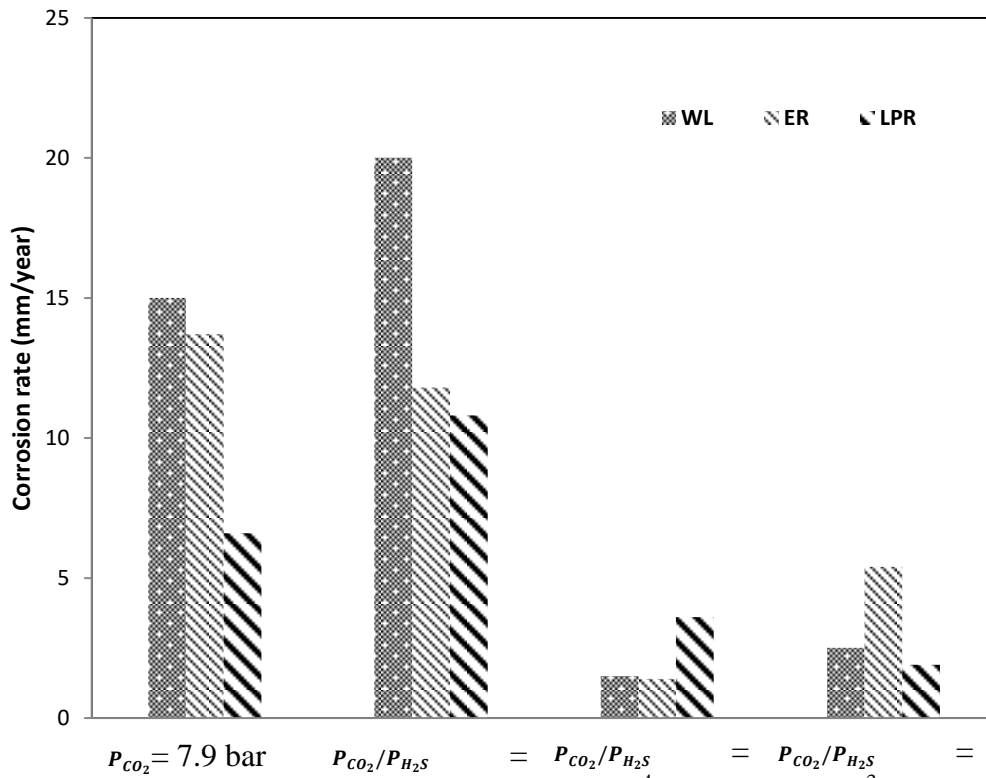
This inhibiting effect diminished when H_2S is removed from the system. However, at pH 3, while the addition of low-concentration H_2S also had an inhibitory effect, the corrosion rate reduction remained in the third stage even with the removal of H_2S from the system.

This CO_2/H_2S corrosion-inhibition process observed in an autoclave was also verified in studies carried out in a multiphase-flow loop with a superficial gas velocity (V_{sg}) of 3.0 m/s and a superficial liquid velocity (V_{sl}) of 1.0 m/s. Brown, Lee and Nestic¹⁰⁶ conducted experiments in a multiphase-flow loop using synthetic seawater at 60 °C for 24 h through weight-loss (WL) coupons, and LPR and *Electrical Resistance (ER)* sensors to measure corrosion rates.

The coupons and sensors were exposed to CO₂ partial pressure of 7.9 bar with H₂S partial pressure of 0 bar, 3.1x10⁻⁵ bar, 1,5x10⁻⁴ bar and 10⁻³ bar which correspond to P_{CO_2}/P_{H_2S} ratio of 0, 2.5x10⁵, 5.1x10⁴ and 7.6x10³, respectively (P_{CO_2}/P_{H_2S} corresponding to sweet regime according to **Figure 6**).

The obtained results are presented in **Figure 9**. We can observe that, for a very small addition of H₂S (P_{CO_2}/P_{H_2S} of 2.5x10⁵), the corrosion rate increases. Additional amounts of H₂S (P_{CO_2}/P_{H_2S} of 5.1x10⁴) causes a significant decrease in the corrosion rate.

Figure 9 – Corrosion rate vs. P_{CO_2}/P_{H_2S} ratio (sweet regime according to **Figure 6**) for WL, ER and LPR. ($P_{CO_2} = 7.9$ bar, pH = 4.0, $V_{sg} = 3.0$ m/s, and $V_{sl} = 1.0$ m/s.)



Source: adapted from Brown, Lee and Nesic¹⁰⁶.

As can be observed, in all discussed studies in both conditions (autoclaves and multiphase loop), the CO₂/H₂S mixed regime (**Figure 6**) in the presence of crude oil were not evaluated. These parameters are important conditions for correlations with the field.

2.7. Flow-Induced Corrosion

The concept of Flow-Induced Corrosion (FIC) is an interdisciplinary field and requires knowledge of material sciences, electrochemistry, inorganic chemistry, fluid dynamics, transport processes and an understanding of the mechanical effects involved.

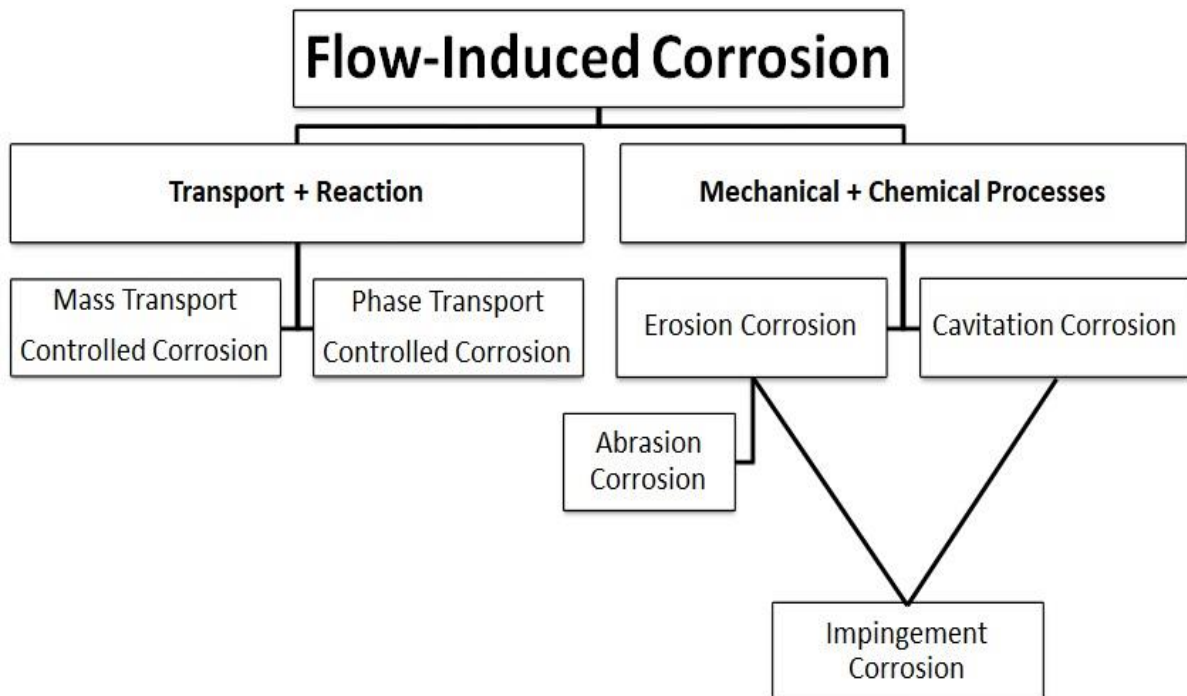
Low and moderate flow rates may be beneficial as they can eliminate the local accumulation of aggressive agents, thereby avoiding crevice and pitting corrosion. They may also enhance

the metal passivation or may increase the protective effect of inhibitors because of the improvement of the transport of the passivator agent or the inhibitor to the metal/environment boundary²⁴. On the other hand, the increase in flow rates may remove protecting layers of corrosion products enhancing corrosion processes.

Therefore, there are several mechanisms to describe the combined action of the flow and corrosion which results in four types of corrosion induced by the flow: mass-transport-controlled corrosion, phase-transport-controlled corrosion, erosion corrosion and cavitation corrosion²⁴.

Figure 10 shows a diagram illustrating the combined action of flow and corrosion mechanisms.

Figure 10 – Types of flow-induced corrosion



Source: Heitz²⁴

Mass-transport-controlled corrosion requires an increase in flow rates for transporting the oxidizing agent which promotes corrosion of a non-passivating metal such as carbon steel in an aerated solution.

Phase-transport-controlled corrosion requires wetting of the metal surface. This type of corrosion is dependent on the flow characteristics. The phase-transport-controlled corrosion produces a rough surface and it is generally observed in crude oil flow²⁴.

Erosion corrosion is characterized by the combined action of mechanical forces induced by the flow and by electrochemical and chemical processes²⁴. Concerning the mechanical portion, the action comprises the following types: shear stresses and pressure variations due to

high flow velocities, especially in turbulent flows and the impact of solid particles in multiphase flows. The problem is often to differentiate between erosion corrosion and corrosion controlled by mass transport because the hydrodynamics influence the moment of transport (mechanical action) and mass transport in the same way. Generally, erosion corrosion can be distinguished phenomenologically by the metal-surface appearance in the form of shallow pits, horseshoes or other local phenomena correlated with the direction of flow.

Cavitation corrosion can be easily distinguished from erosion-corrosion both by the phenomenology and the mechanism. The damage caused by cavitation corrosion appears as a set of deep, sharp craters on the surface of the metal²⁴.

In this work, the interaction of the liquid and gas phases with a pipe internal wall will be considered. As physical and mechanical effects are altered depending on the flow pattern, it is important to distinguish between single-phase and multiphase flow that is directly correlated with FIC. For a single-liquid-phase flow, the Reynolds number (N_R) can be used to determine whether the flow is fully laminar or turbulent. In a laminar flow, the fluid moves in smooth paths or layers, whereas, in a turbulent flow, the speed of the fluid at a point is continuously changing in both magnitude and direction⁸⁷.

For practical purposes, if the Reynolds number is less than 2000, the flow is laminar. If it is greater than 3500, the flow is turbulent. Flows with Reynolds numbers between 2000 and 3500 are sometimes referred to as transitional flows¹¹⁴.

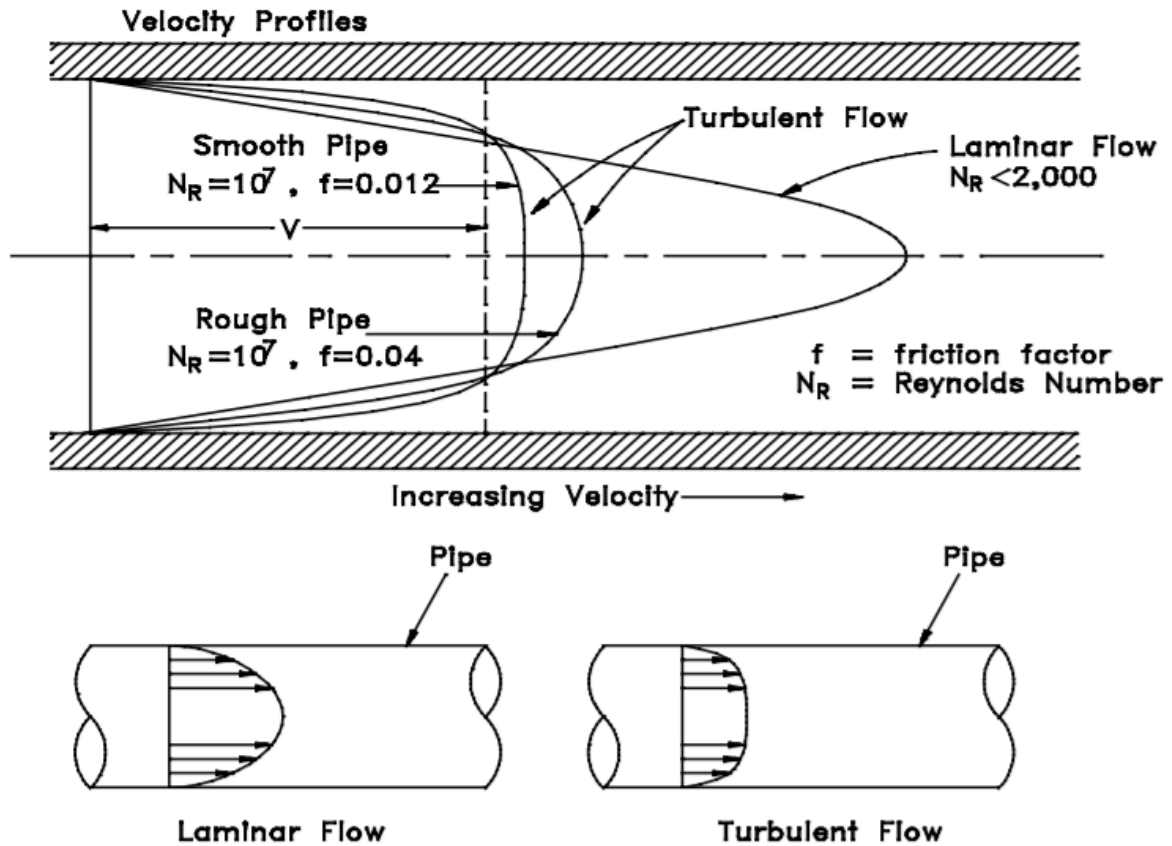
Figure 11 shows a simple diagram that represents laminar and turbulent single-phase flow. The laminar-flow and turbulent-flow regimes are important in the design and operation of any fluid system. The amount of fluid friction, which determines the amount of energy required to maintain the desired flow, depends upon the mode of flow¹¹⁴.

When fluid flows in a pipe, friction creates forces between the fluid moving at different velocities and the pipe wall. The closer the wall is to the fluid, the more it tends to slow down to zero velocity. The fluid in direct contact with the wall is stopped completely, and the closer to the center of the pipe, the higher the average velocity⁸⁷.

In general, pipe flow can be either laminar or turbulent, and the physics involved changes significantly when we go from one to the other. Closer inspection reveals that no such thing as completely turbulent pipe flow exists; there is always a laminar sub-layer closest to the pipe wall. On the other hand, even in a single-phase flow, pipe friction is a complex phenomenon and questionable friction calculations are surprisingly common⁸⁷.

Many of the flow problems are addressed by modeling. The first pipe flow models dealt with the single-phase flow of water or steam, though not both at the same time. Since many phenomena are multiphase, such single-phase models have their limitations. Early studies on transient two-phase flow were conducted in the nuclear industry, as it became mandatory to predict the transient flow behavior during potential accidents for licensing pressurized water reactors⁸⁷.

Figure 11 - Laminar and Turbulent Flow Velocity Profiles

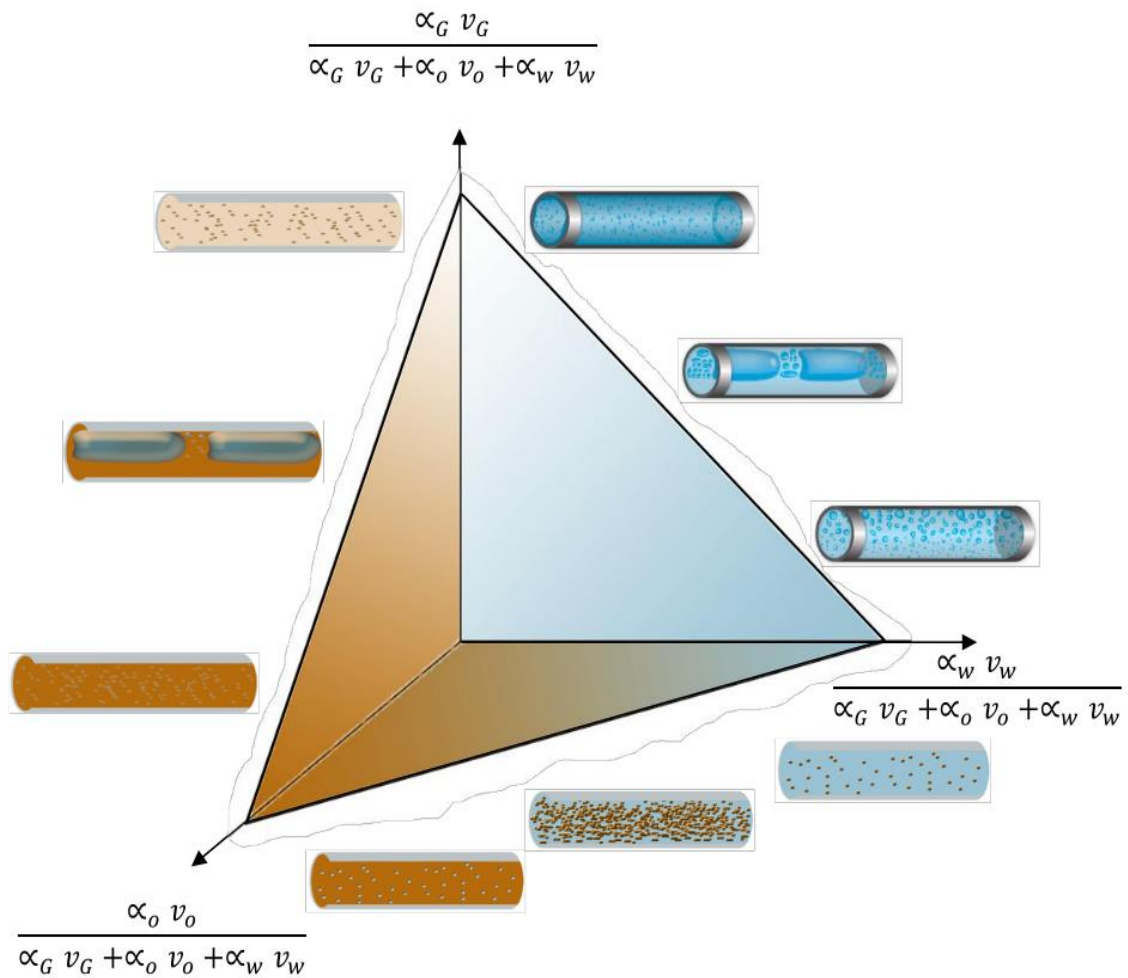


Source: DOE¹⁴.

The pipe-material selection is important, as are pipe overlay types. For this, it is essential to know the operation parameters such as temperature, pressure, flow pattern, and flow rates. In this system, the corrosion mechanism is very complex for some situations the flow simulation models can be used to calculate some of the parameters required as input to the corrosion simulation models. The same can be said about erosion: the flow model can be used to estimate the velocity of sand or other particles, and that is useful when we want to determine under which conditions particle or droplet erosion is likely to become a problem. For corrosion, we can observe greater damage with increased temperature and increased pressure. Higher speeds and turbulence conditions also intensify corrosion. Increased velocity tends to result in thinner protective films of iron-carbonate layers which reduce their protective capacity. In multiphase flowlines, production instability due to slugging is a major flow assurance concern. Slugging can occur due to periodical or randomized changes in the pressure of gas/liquid flows. Three conditions cause slugging: hydrodynamic, operational and terrain-induced slugging¹⁵. In **item 2.8.1** the flow pattern which causes slugging is described.

It is very difficult to illustrate the three-phase flow. **Figure 12** shows a diagram for three dimensions, one for each phase.

Figure 12 - Three-phase gas-oil-water diagram for horizontal pipes (two-phase flow regimes for gas-oil (left border), gas-water (right border), and oil-water (lower border) flow). When all phases are present simultaneously, many more different flow regimes become possible.



Source: Bratland, Ove ¹¹⁵.

The vertical axis is the gas superficial velocity as a fraction of the total superficial velocities, representing a pure gas flow. For pure liquid (oil-water) flow, which corresponds to a straight line in the oil-water plane, the gas fraction is zero. Similarly, if the water content is zero, our operation point will be located somewhere on a line in the gas-oil plane, and so on for zero oil content. Operation points inside the triangle will correspond to the three-phase flow¹¹⁵.

The plane of zero oil and water contents indicates gas-liquid flow regimes. The oil-water plane, the liquid-liquid mixture plane, can show a very interesting property in which the oil can occur as isolated droplets dispersed in a continuous water. In this case, when we increase the oil content, the flow can switch to the opposite situation called the inversion point. Thus, the viscosity of the dispersed phase tends to be similar to the continuous phase viscosity, which normally is much higher for oil than for water¹¹⁵. This phenomenon in a stable or unstable manner is known by the emulsification process.

2.8. Multiphase flow

In the field, the corrosion in the sour regime is almost always associated with a multiphase flow. A multiphase flow comprises two or more phases. The phases are named gas, liquid, or solid states. The term multiphase is also used to refer to the flow of two or more substances which are in the same phase, unmixed, but continuous or dispersed. In pipes, the different types of multiphase-flow patterns are presented as a function of the superficial velocities of the liquid phase and the gas phase. Measurements of shear-stress variations on the pipe wall over time can be made for different combinations of gas and liquid surface Reynolds numbers. These measurements represent the behavior of the shear stress of the wall as a function of the specific flow pattern. For example, the shear stress has no variation for a stratified-flow pattern. However, a variation in wavy, annular and plug-flow patterns is clearly observed for which the frequency at regular intervals is checked. The slug-flow pattern has as a principal characteristic its chaotic nature with irregular pulsation¹¹⁶.

As already mentioned, the fluid flow in flowlines is divided into three categories based on the fluid-phase condition⁸¹:

- single-phase flow: crude oil or dry-gas-transport flowlines, export flowlines, gas or water-injection flowlines, and chemical-service flowlines such as methanol, glycol and inhibitor lines, and others;
- two-phase flow: oil + released gas flowlines, gas + produced-oil droplet flowlines;
- three-phase flow (or multiphase flow): water + oil + gas, typical production flowlines.

Most oil wells produce both oil and gas and often contain produced water. Therefore, multiphase-flow transportation is common. This category of flow is currently receiving much attention throughout the Oil & Gas industry. The simultaneous transportation of crude oil, gas, seawater and sand can offer significant savings over the conventional, local-platform-based separation facilities. The possibility of hydrate formation, the increase in water content of the produced fluids, erosion, heat loss, and other factors create challenges to the hydraulic-design procedure⁸¹.

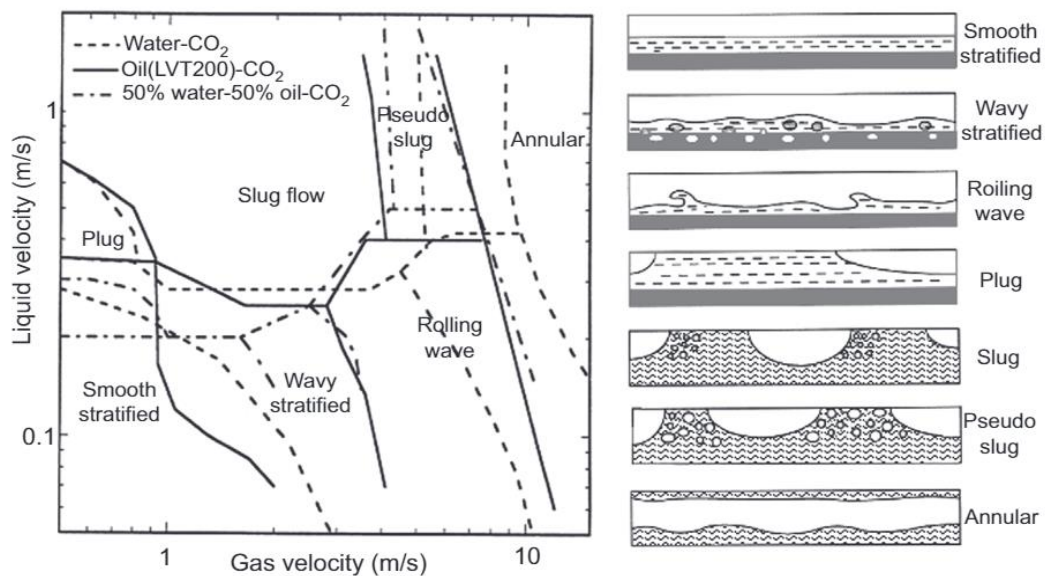
In many oil and gas productions with multiphase flowlines, the possibility of slugs or surges is one of the most important flow-assurance concerns and should be avoided. The multiphase flow in a pipeline is usually studied by the flow regime and the corresponding flow rate. The flow-regime description is not simply an identification of laminar or turbulent flow for a single flow, the relative quantities of the phases and the topology of the interfaces must be described.

The change in flow regime occurs because of the magnitudes of the forces that act on the fluids. Parameters such as turbulence, inertia and surface tension forces are susceptible to variations in flow rates, pipe diameter, inclination angle and fluid properties of the phases. Another important factor is the liquid holdup which is defined as the ratio of the volume of a

pipe segment occupied by liquid to the volume of the pipe segment. Understanding flow-pattern hydrodynamics can help us to design better and define which parameters involved with the multiphase flow will influence significantly the corrosion rate⁸¹.

In the field, corrosion in the CO₂-containing environment is almost always associated with a multiphase flow. In pipelines (flowlines), the different types of multiphase-flow patterns can be represented in **Figure 13**, depending on the surface velocities of the liquid, water cut and gas phases. The transition lines that delimit the boundaries between these patterns are observed. This delimitation is a function of flow rates, physical properties and pipe orientation^{47, 49}.

Figure 13 - Flow pattern transition map with environment condition variation



Source: El-Sherik⁴⁹.

The evolution of slugs is very sensitive to the pipe inclination in such a way that changing the inclination by less than a degree may be sufficient to change the balance causing a flow-regime transition. In the slug flow, both the gas and liquid phases contribute to the pressure gradient. The gas phase in a slug flow exists as large bubbles which are separated by slugs of liquid. The velocity of the gas bubbles is greater than that of the liquid slugs.

As already mentioned, water cut is the ratio of produced water to the volume of the total of the produced liquid. CO₂ corrosion is mainly caused by the presence of water in contact with the steel surface. The severity of the CO₂ corrosion is proportional to the time during which the steel surface is wetted by the water phase. Thus, the water cut is an important factor in influencing the corrosion rate. However, the effect of the water cut cannot be separated from the flow velocity and the flow regime.

Researchers proposed that no corrosion occurs if the water cut is less than 30 %. The corrosion rates do not just depend on water cut but also on the superficial gas velocity, superficial liquid velocity and inclination angles, among other factors⁶⁶. Liquid velocity is

usually limited because of erosion effects at fittings. Erosion damage can occur in flowlines in a multiphase-flow regime because of the continuous impingement of high-velocity liquid droplets. The damage is almost always confined to places where the flow direction is changed, such as elbows, tees, manifolds, valves, risers and so on. The erosional velocity is defined as the bulk fluid velocity which will result in the removal of corrosion product scales, corrosion inhibitor films and/or other protective scales presented on the internal surface of a pipeline.

In recent years, the corrosion problem with CO₂/H₂S has become more important as the available reserves of oil possess a considerable amount of H₂S. Although the interaction of H₂S with low-carbon steels has been published by various authors, understanding of the effect of H₂S on CO₂ corrosion is still limited because the nature of the interaction with carbon steel is complicated^{45,63,65}. The steel corrosion in environments containing CO₂ and H₂S can be briefly related to flow factors, to the chemical characteristics of the environment, to the metallurgical characteristics of the steel, or the biological activity in the ^{45,63,65}.

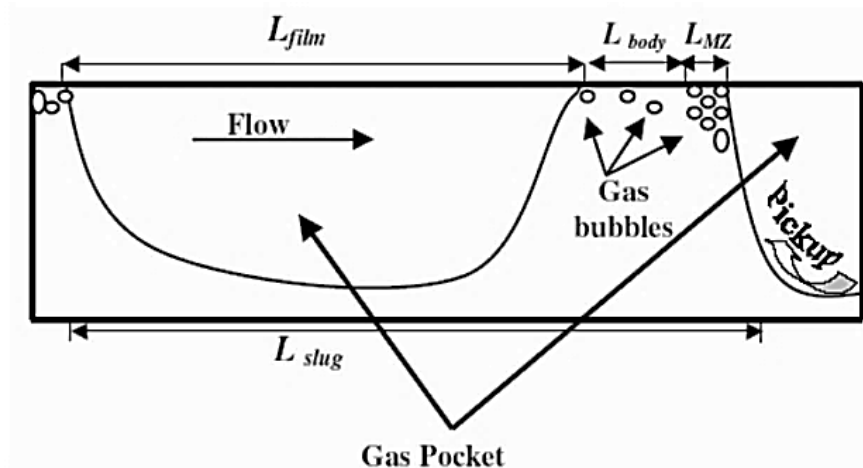
2.8.1. Slug flow

The characteristics of a slug length (average length and length distribution) were for many years predicted using literature models. Over the last ten years, much effort has been invested by academic researchers and by oil companies. Researches were developed to improve the ways of predicting frequency, average slug length and length distribution¹⁹.

Methods to predict the slug frequency and the slug length have been studied since 1989 for usage in almost horizontal systems¹⁹. Recent successes in the methodology have announced the implementation of methods in multiphase-flow lines with higher slopes, deeper water and longer lengths. These methods, in turn, need to be explored to take into account these new operating environments¹⁹. In these new fields, the slug is a flow pattern associated with a pressure loss compared to other flow patterns. The slug is usually accompanied by a pressure drop when compared to other flow patterns. The pressure drop can be divided into three components: a portion of friction, a portion of acceleration and another of gravitation. The total pressure drop due to friction is a function of the contact between the pipe wall and the liquid phase ($L_{slug} + L_{body} + L_{MZ}$ of **Figure 14**). The pressure drops resulting from the acceleration portion have origin in a motion gradient between the liquid film in contact with the pipe wall related to the slug which moves with a greater speed. For the flow in inclined pipes, gravity imposes resistance to the flow direction and the work performed to meet the upward flow against the action of gravity is what physically results in the gravitational pressure drop³⁸.

The hydrodynamic effects influence the corrosion-inhibition capacity of FeCO₃ protective layers. Thus, multiphase flow systems are used to evaluate the performance of these layers because the turbulence in these systems is higher than in single-phase systems. For example, gas transport is often under multiphase-flow conditions. In addition, there are water and even solid particles, such as sand, which promote complex multiphase-flow patterns¹¹⁷.

Figure 14 – Schematic of a unit slug



Source: Daas and Munroe³⁸.

2.8.2. Hydrodynamic effects

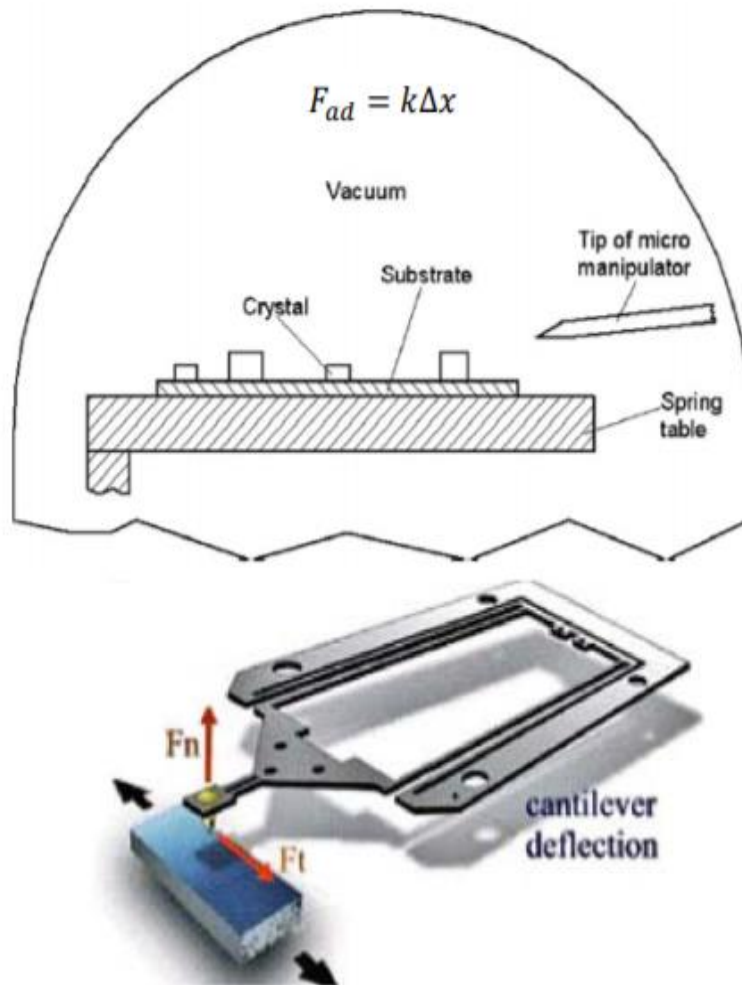
Depending on the operational conditions, the multiphase flow can develop different flow regimes. In horizontal pipes, the flow patterns become more complex due to the force of gravity which causes an asymmetric distribution of the phases. One of the most common and turbulent flow regimes is a slug one. Many efforts have been made to measure the shear stress in the horizontal flow of the slug in pipelines.

Researchers reported that the critical wall shear stress (WSS) in a horizontal pipe could reach a value of 260 Pa. In such conditions, a thinner layer of FeCO_3 is formed at high flow rates. In extreme conditions, the flow rates are so high that they can even mechanically remove the protective layers resulting in increased surface damage and high corrosion rates³⁹. This type of surface damage is treated as corrosion associated with the flow.

Researchers¹¹⁸ conducted loop testing in a CO_2 -free aqueous solution with the presence of light oil and performed measurements of shear stresses on the surface of the pipe walls (WSS). These stresses are promoted by mechanical forces exerted by a slug flow. As a result, researchers¹¹⁸ found at the top of the pipe the highest WSS, in the order of 102 Pa, and they verified that these values were two to four times larger than the values found at the bottom of the pipe¹¹⁸.

The same research group presented a detailed study of the influence of WSS on the removal of the corrosion product layer (FeCO_3) under the action of the flow. The researchers produced an iron carbonate layer on API X65 steel and subjected the FeCO_3 crystals of that layer to tangential forces (lateral force) using adhesion force (F_{ad}) measurement method using an atomic force microscopy (AFM) as show in **Figure 15**.

Figure 15 - Adhesion force measurement method using an AFM.

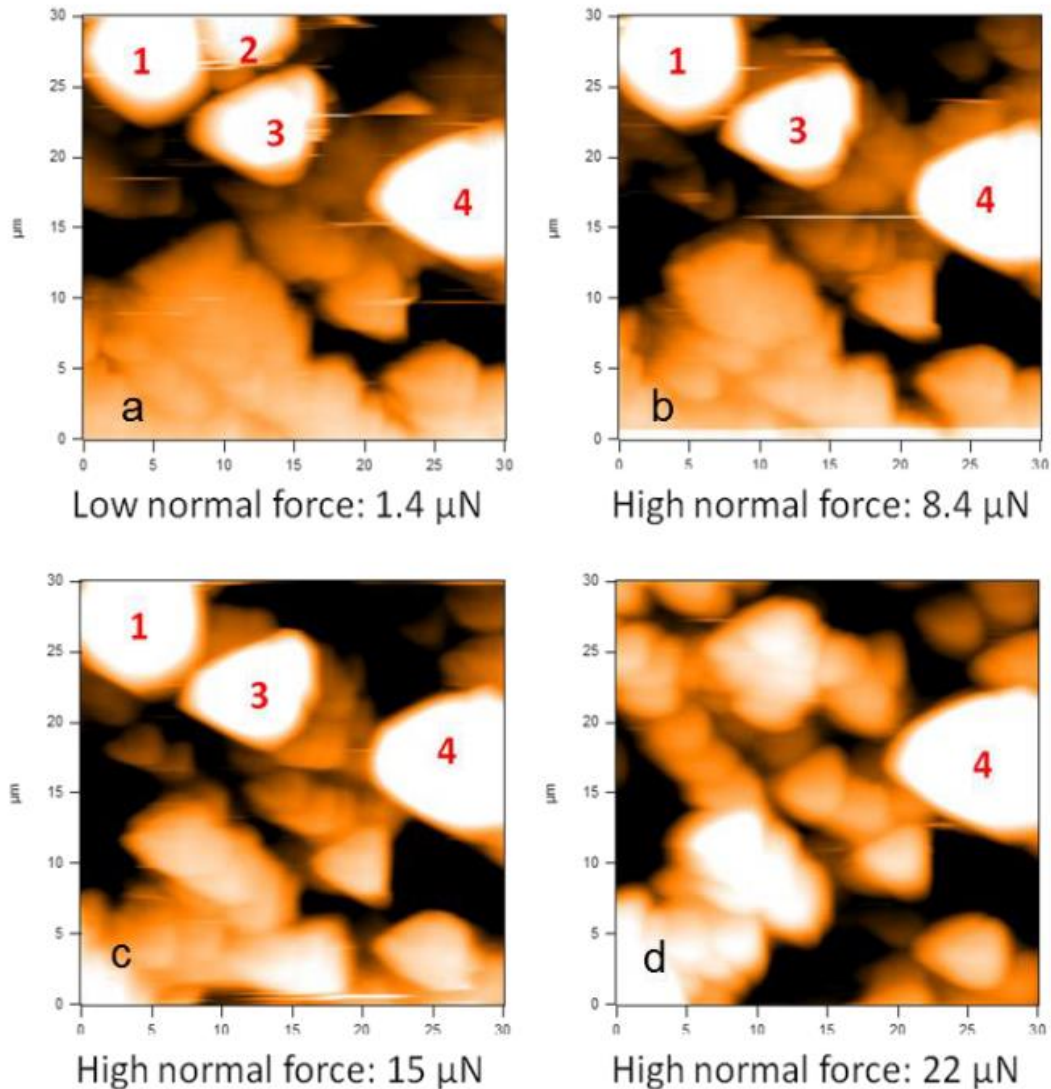


Source: Roquette, Rodrigo¹¹⁹.

Figure 16 shows details of the measurements. Four FeCO_3 crystals are numbered and highlighted with white color. Their width and length are approximately $5\ \mu\text{m}$ to $10\ \mu\text{m}$ which are consistent with the dimensions of FeCO_3 shown in SEM images. AFM measurements suggest that the height of FeCO_3 crystals is approximately $2\ \mu\text{m}$ to $3\ \mu\text{m}$, which is significantly larger than the measured steel surface roughness ($200\ \text{nm}$).

Therefore, individual FeCO_3 crystals could be detected by the AFM scanning probe. At the beginning of the test, the four FeCO_3 crystals were imaged by using a low normal force of $1.4\ \mu\text{N}$ (**Figure 16a**). **Crystal 2** was first removed by increasing the applied normal force up to $8.4\ \mu\text{N}$ (**Figure 16b**), while the other three crystals resisted this force. When the force reached $22\ \mu\text{N}$, **Crystals 1** and **Crystals 3** were removed by the probe (**Figure 16d**). **Crystal 4** was still intact even after applying a maximum normal force of $30\ \mu\text{N}$. This analysis was carried out with nine FeCO_3 crystals removed using the same procedure. The obtained normal force values were from $0.7\ \mu\text{N}$ to $25\ \mu\text{N}$ ¹²⁰.

Figure 16 - Topography images of a $30\ \mu\text{m} \times 30\ \mu\text{m}$ area on the sample surface of four FeCO_3 crystals scanned by applying different normal force: (a) $1.4\ \mu\text{N}$, (b) $8.4\ \mu\text{N}$, Crystal 2 is removed (c) $15\ \mu\text{N}$, (d) $22\ \mu\text{N}$, Crystals 1 and Cristal 3 are removed during the scanning. Crystal 4 cannot be removed by applying $30\ \mu\text{N}$ which is the maximum value that the instrument can provide.



Source: Wei Li, Yao Xiong *et al.*¹²⁰.

This indicates that the adhesion force between the FeCO_3 crystals and steel surface varies at least one order of magnitude and it is expected to be dependent on the size, shape, and surface contact area of each crystal. Cross-section areas of crystals were measured and it was found that the normal forces leading to the removal of crystals were related to the cross-section area of crystals. Larger crystals exhibited higher adhesion and required higher removal forces¹²⁰.

The normal force, however, is not a measure of the direct interaction between the scanning probe and the crystal. A calculation of lateral force which is the actual force responsible for removing FeCO_3 crystals is required. Based on the area of crystals, the authors calculated the lateral stress values. The obtained results are shown in **Table 1**. The researchers took into

account the error from the use of a cross-section area which is smaller than the real contact area and estimated that the lateral stress values are of the order of 0.1 MPa to 10 MPa.

Table 1 – Normal force, lateral force, cross-section area and stress values for removal of the nine FeCO₃ crystals.

Crystal	Normal force (μN)	Lateral force (μN)	Area (μm^2)	WSS (MPa)
1	21	1526	140	11
2	24	1755	180	10
3	0.7	51	87	0.6
4	4.7	283	87	3
5	8.4	565	39	14
6	22	1602	92	17
7	22	1602	97	16
8	25	1831	138	13
9	12	840	50	17

Source: Wei Li, Yao Xiong *et al.*¹²⁰.

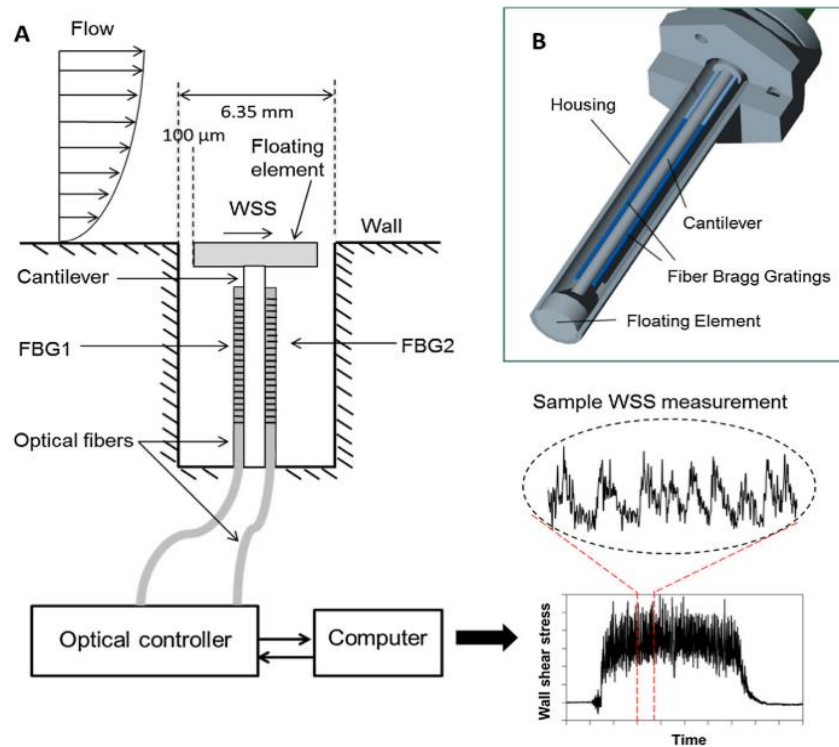
When researchers compared the results for single-phase and two-phase flow WSS measurements, the floating element sensor method was successfully used to measure WSS (see **Figure 17**). It was found that in the slug flow regime, which is considered to be one of the most violent multiphase-flow regimes, the highest WSS occurs on the top of the pipe when the slug passes. It is speculated that the water layer at the bottom of the pipe in the slug flow regime can dampen the impact of the slugs. Therefore, a much smaller WSS value is found at the bottom of the pipe when the slug passes. In this study, for ambient pressure and horizontal gas-liquid two-phase flow, the highest WSS recorded was approximately 100 Pa in magnitude. On the other hand in the AFM measurement, the calculated lateral stress required to remove FeCO₃ crystals is of at least 1 MPa magnitudes¹²⁰.

The researchers conclude that differences of at least 3 to 4 orders of magnitude indicate that the removal of FeCO₃ layer solely by WSS exerted by fluid flow is unlikely. Clearly one must search for other explanations.

It is important to highlight that the authors did not mention any test performed with crude oil or the possibility of emulsification of the liquid phase, which can alter the entire behavior of the flow and interactions between phases. An extensive literature review was performed, and no studies of multiphase-flow tests using crude oil were found.

Another hypothesis for flow-induced corrosion is the cavitation model associated with a slug-pattern multiphase flow in which dispersed bubbles collapse on the pipe wall promoting damages whose intensity is related to the density of these bubbles.

Figure 17 - (A) Schematic of a floating element WSS measurement system showing a sample measurement; (B) schematic diagram of WSS probe body.



Source: Wei Li, B.F.M. Pots *et al.*^{118,121}.

We can define cavitation by the formation and rapid collapse of cavities or bubbles of vapor or gas within a liquid resulting from mechanical or hydrodynamic forces¹²².

Wei Li¹²¹ noted that the WSS measured in a typical multiphase flow pipe is several orders of magnitude less than the stresses required to remove inhibitor films or layers of corrosion product from the steel surface. Therefore, purely mechanical removal of these layers by WSS alone is unlikely. For this reason, the author considered the hypothesis that the geometric irregularity of the surface could locally lead to high instantaneous hydrodynamic stresses and interfere with the corrosion processes. To assess this hypothesis, the author established two fronts of analysis, one experimental and the other by Computational Fluid Dynamics (CFD) simulation. Flow experiments were performed in two loops: bounded-channel flow (**Figure 18a**) and pipe flow (**Figure 18b**). The investigation was conducted in the following conditions: 1 % NaCl, pH 5, 0.97 bar CO₂, 25 °C, 720 ppmv inhibitor, 16 m/s, 4 day test duration, API X65 steel, O₂ < 2 ppb.

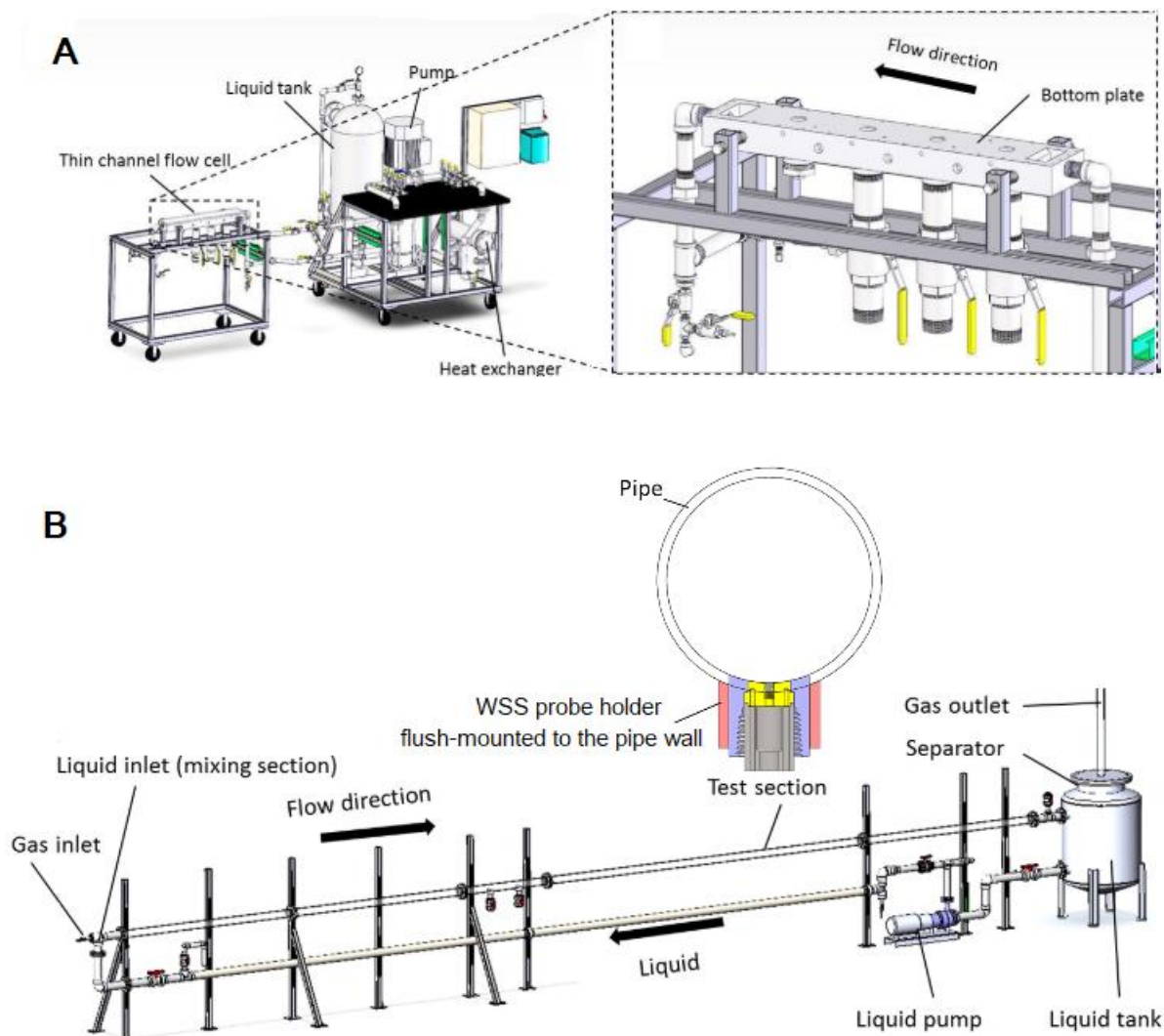
In the bounded-channel flow (**Figure 18a**), experiments were performed with a well-defined flow channel test section named thin channel flow cell. In this system, due to the high flow velocity, high shear stress of the wall was expected¹²¹.

In the pipe-flow loop (**Figure 18b**), single-phase and two-phase horizontal-flow tests were performed. In these experiments, flow recordings synchronized with the WSS measurements

were performed. This allowed the author to observe and record flow events, such as the passage of a slug, to be correlated with WSS data¹²¹.

CFD was used to perform the analysis involving fluid flow. The CFD results supplemented the experimental results of WSS measurements in flow systems, allowing the author to estimate local hydrodynamic properties that are often not easy to obtain through experimental measurements¹²¹. According to the author, to validate WSS measurements made by the flush-mounted probes, the measured values were compared to empirical well-known single-phase correlations and CFD simulations¹²¹.

Figure 18 - (A) Schematic design of bounded-channel flow cell; (B) schematic design of pipe flow loop with WSS.



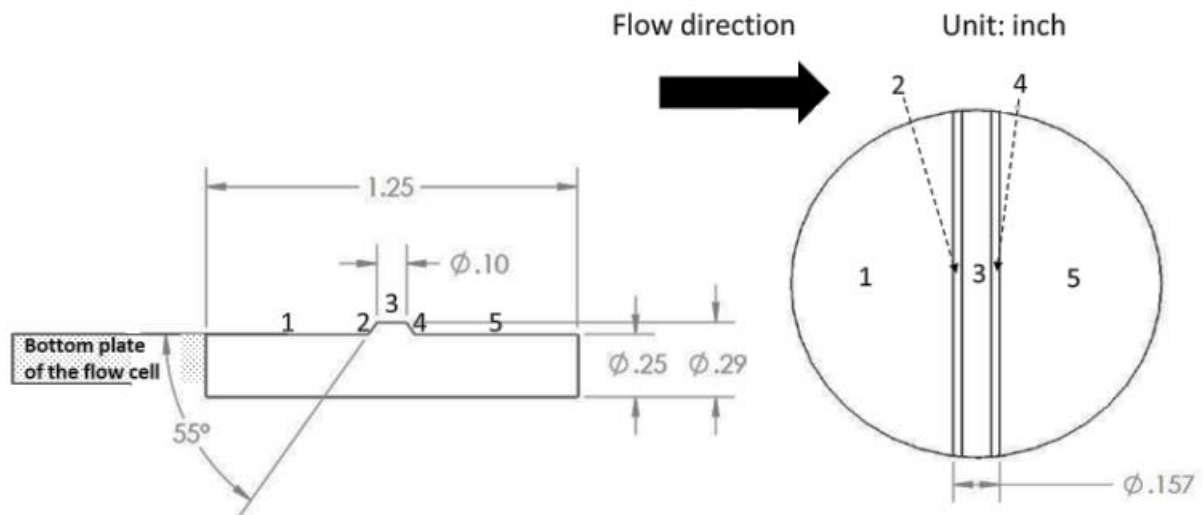
Source: Wei Li, B.F.M. Pots *et al.*^{118, 121}.

During the WSS measurements in the slug flow test, Wei Li¹²¹ observed that the flow velocity profile in the liquid slug body was highly non-uniform and that the highest WSS occurred on the top of the pipe when the slug front passed with the maximum flow velocity.

The maximum WSS value was about 2 to 4 times higher than the calculated mean WSS value from empirical correlations. The author suggested that these results may guide future work for slug modeling involving the removal of corrosion inhibitor films and corrosion product layers.

For a final check, another experiment with inhibitors was conducted using a specimen made of the API 5L X65 carbon steel with a trapezoidal-prism-shaped protrusion on the cylindrical base, as shown in **Figure 19**. This specimen was assembled in the bounded-channel flow to have the cylindrical wall was flush to the bottom surface of the flow cell and the protrusion directly subjected to the flow action (**Figure 18a**), similar to a weld bead of an in-service pipeline. The evaluation was made in 5 numbered regions on the surface as shown in **Figure 19**: 1 (upstream flat surface), 2 (leading edge, upstream slope), 3 (top surface of protrusion), 4 (leading edge, downstream slope), 5 (downstream flat)¹²¹.

Figure 19 - Specimen with a protrusion: specification and flow orientation (left: side view; right: top view).



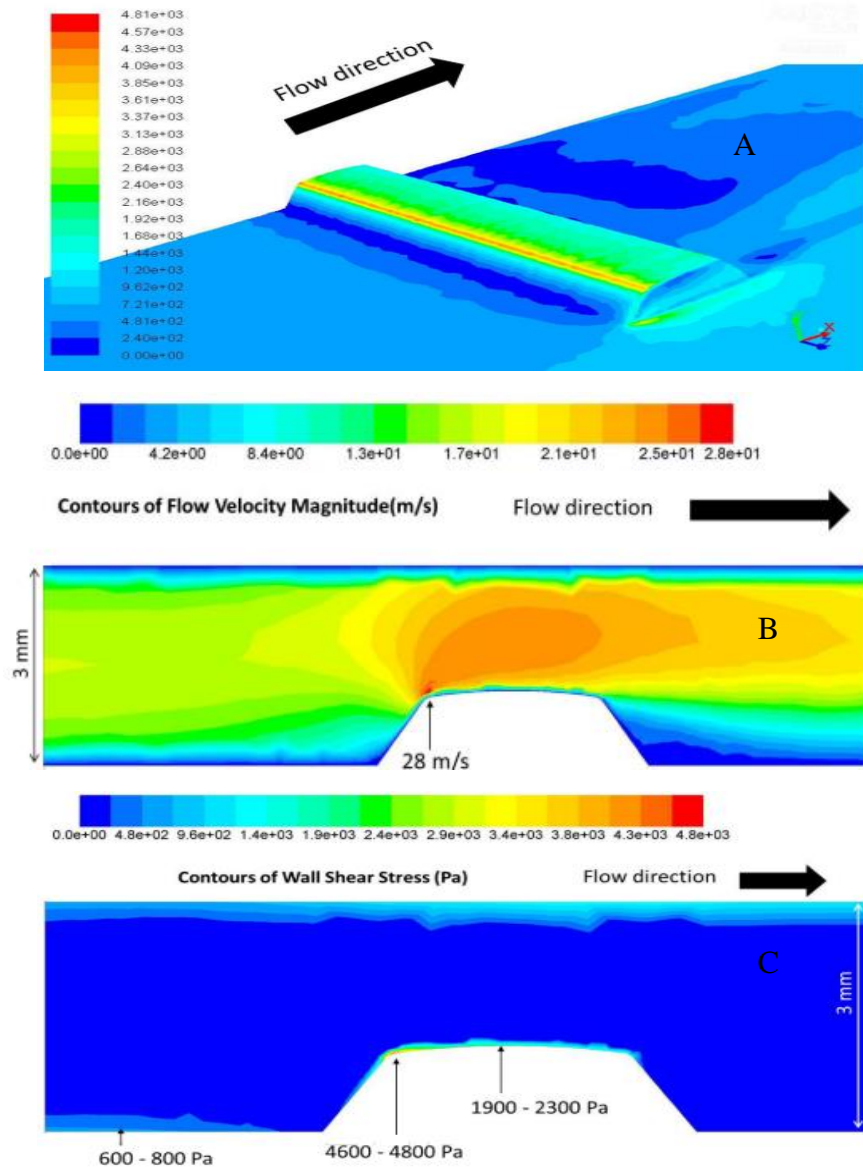
Source: Wei Li¹²¹.

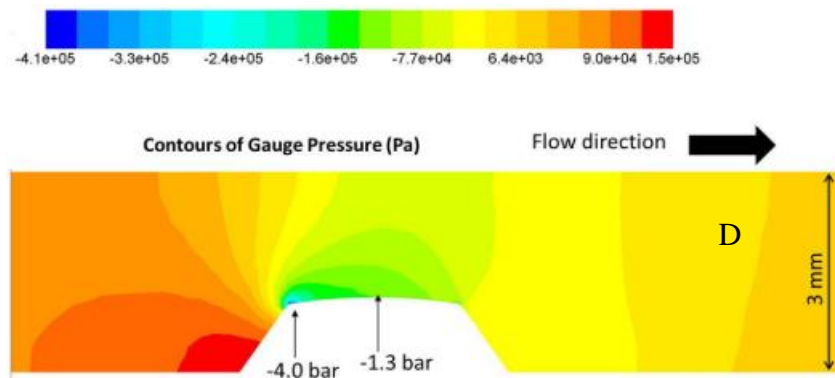
The flat surface of the specimen (1 upstream and 5 downstream) analysis indicated uniform corrosion. A series of small pits were observed from the upstream leading edge (2) to the protrusion top-flat surface (3). Several dip pits were found in the middle of region 3. The pit depths were around 140 μm to 150 μm depending on the chemical parameters of the environment¹²¹. CFD simulation was deemed a suitable diagnostic tool to analyze the hydrodynamic conditions around the protrusion of the studied specimen. The exact geometry of the channel flow cell with the specimen with protrusion was constructed for the computer simulation. The specimen protrusion, flow velocity magnitude distribution, wall shear stress distribution and pressure distribution along the flow direction are shown in **Figure 20^f**. As a result of the simulation, Wei Li¹²¹ observed that WSS values of the upstream flat surface (1)

^f Pressure values represent pressure differences. Therefore, a negative value means a decrease in pressure, and a positive value an increase.

were within the range of 600 Pa to 800 Pa (**Figure 20c**). On the upstream leading edge (2), a sudden increase of WSS up to approximately 4000 Pa to 4800 Pa was observed, while, on the middle of the protrusion top flat surface (3), the WSS values were within the range of 1900 Pa to 2300 Pa. The author considered that these values were unlikely to remove inhibitors.

Figure 20 – Specimen protrusion (A), flow velocity magnitude distribution (B), wall shear stress distribution (C), gauge pressure distribution (D).





Source: Wei Li¹²¹.

A pressure decrease of approximately -4.0 bar as found at the upstream leading edge (2) as shown in **Figure 20d**.

The pressure on the middle of the top-flat surface of the protrusion (3) quickly recovered up to -1.3 bar. The author supposed that the pressure fluctuation led to a cavitation process. The collapsed bubbles generated significantly high mechanical stresses that removed locally the corrosion products and induced localized corrosion: pitting corrosion was observed between the upstream leading edge and the top-flat surface (3) of the protrusion¹²¹.

The researcher reiterates that the collapsed cavitation bubbles may generate significantly high stresses that locally remove inhibitor molecules from the steel surface. The mechanical impacts of collapsing bubbles onto the surface can reach values in order of magnitudes of MPa or even GPa. They found that the protrusion of the specimen into the flow stream changed the local hydrodynamic conditions and caused cavitation in a highly turbulent flow system, reaching WSS values up to 4.8 kPa in the studied flow conditions¹²¹.

The material resistance against hydrodynamic effects (cavitation corrosion) promoted by a multiphase flow can be verified by standard cavitation and erosion tests that qualify the steel resistance to cavitation in comparison to other materials¹²³.

Researchers proposed a theoretical model for CO₂ corrosion in which the main focus was the factors that influence the formation of a protective iron carbonate layer (FeCO₃) and the effect of this layer on the overall process of CO₂ corrosion. They suggest that corrosion rates are not associated with the thickness of the layer but rather with their degree of coverage or homogeneity on the metal surface. This layer may partially cover the steel surface and consequently may block just a part of the exposed metal or may evenly cover the entire surface of the steel and may prevent further dissolution. The rate at which voids appear determines the type of layer, whether protective or not⁹². The reactions which occur in systems containing CO₂ and that promote the formation of this layer were presented in **Reaction 1, Reaction 2, Reaction 3, Reaction 4, Reaction 5, Reaction 6, Reaction 7 and Reaction 8**.

As already explained, we can observe since the dissolution and hydration of CO_2 to form carbonic acid until CO_2 corrosion leading to the formation of FeCO_3 . The protective or non-protective characteristic of this FeCO_3 layer depends on operational conditions such as the flow velocity, pressure and temperature, pressure and pH. Lee³⁹ reported that, in general, the flow affects the CO_2 corrosion of steel by mass transport processes.

Depending on the environmental conditions, rarely may the turbulence be beneficial for the protective behavior of the layer of corrosion products. In the two-phase or multiphase flow (turbulent flow), the liquid phase, in the form of slugs or small drops, can impulsively be directed towards the inner wall surface creating high rates of dissolution and transportation as well as high mechanical forces which result in an increased corrosion rate since the mass transport is the rate-determining factor³⁹.

Nevertheless, when conditions favor the formation of a FeCO_3 protective layer, the transportation of species in a turbulent flow affects the concentration of the species on the surface and, consequently, of the FeCO_3 precipitation rate.

Under these conditions, a thinner layer of FeCO_3 is formed at high flow rates. Under more aggressive conditions, the high flow rates may remove the protective layer increasing the surface damage and the corrosion rate³⁹. The suitability of corrosion loop tests that simulate these conditions of turbulence flow is considered fundamental for understanding and monitoring all the stages of the corrosion processes. An in-depth analysis of the results obtained from loop tests may give information that, in turn, can be used for significant improvements to the operational conditions of oil production and extraction. The tests performed in our laboratory seek to simulate the slug pattern of a multiphase flow found in a well. The slug is usually accompanied by a pressure drop when compared to other flow patterns.

As previously mentioned, the flow affects CO_2 corrosion through the mass transport processes. A turbulent flow accelerates the transport of species to and from the metal surface resulting in an increased corrosion rate since transport is the rate-determining factor³⁹. Authors³⁹ also reported that the processes occurring during corrosion under this layer, at their interface with the metal, may induce voids or holes in the layer.

Therefore, the void or hole formation rate is a significant parameter in determining what kind of layer is formed. When those characteristics are observed, its morphology may be recognized based on the density, porosity, and thickness to know whether it may act as a protective barrier⁹². A thinner protective layer of FeCO_3 is formed at high flow rates. However, the FeCO_3 layer can be mechanically removed at very high flow rates, promoting increased surface damage and corrosion rates³⁹. This surface damage is treated as corrosion associated with the flow.

Corrosion models associated with the effects of the flow are classified into four types: mass transport, phase transport, corrosion erosion, and corrosion cavitation³⁰. The cavitation model can be associated with the slug-pattern multiphase flow in which dispersed bubbles collapse

and act on the internal surface of the pipes, promoting damages whose intensity is related to the density of these bubbles. Researchers conducted loop tests in a CO₂-free aqueous phase with oil and performed measurements of shear stresses on the surface of the pipe (WSS, Wall Shear Stress)¹¹⁸. These stresses are caused by mechanical forces exerted by the standard slug flow. As a result, they discovered that the highest WSS, about 102 Pa, was found at the top side of the pipe and these values were two to four times larger than values found at the pipe's bottom side¹¹⁸. In general, the pipes subjected to multiphase flow operate with several flow patterns and, in Oil & Gas industry, mostly result in a slug flow pattern. This pattern of flow increases the effects of corrosion and erosion resulting in rates much higher than those promoted in other flow regimes¹²⁴. Researchers observed that the gas phase in a slug flow is entrained in the form of dispersed bubbles as shown in **Figure 14**.

They identified a mechanism that causes an increase in the corrosion process in the slug pattern in which the flow pushes dispersed bubbles toward the bottom of the pipe. Thus, they established a correlation between the rate of corrosion and the amount of gas at the bottom of the pipe. Besides, they found craters at the surface of protective layers due to the collapse of the gas bubbles at the bottom of the pipe¹²⁴. The impact of the dispersed gas bubbles may cause their collapse on the pipe walls causing a cavitation-like effect that can remove the protective layers causing degradation. The combination of layer removal with the shear stress due to rolling motion and the impact of the bubbles on the pipe wall results in an increase in the corrosion/erosion rates. This fact occurs only under a slug-flow regime¹²⁴.

The selection of materials for Oil & Gas transportation is not always done with an emphasis on corrosion resistance but on mechanical properties, the simplicity of manufacturing and low cost. Due to high mass-loss rates resulting from internal corrosion, the knowledge of the corrosion resistance of API 5L 65, X70 and X80 steels used in pipelines for sweet service is necessary⁹².

In addition to the corrosion processes, the effects of the flow in the drilling pipe are also generally ignored. However, at the ends of a threaded pipe, there is a sudden change in the flow direction due to the variation of the pipe sections.

The vortex formed in the threaded region may even lead to cavitation accelerating the erosion and corrosion processes. Therefore, it is necessary to analyze the failure mechanism of the drill pipe from the perspective of corrosion associated with the flow. In the literature, the analysis of a failure mechanism in multiphase flows in the connecting regions of the drilling pipes is done based on the Eulerian-Lagrangian method and the discrete phase model which confirms the existence of corrosion associated with a flow⁸⁰.

In this work, the resistance of the materials to the hydrodynamic effects associated with cavitation promoted by the multiphase flow was studied. In addition of the tests using the multiphase-flow loop, standard cavitation-erosion tests¹²³ were performed aiming at comparing the resistance to cavitation-erosion of the API 5L X80 steel and the API 5DP grade used in drill pipes^{125, 126}.

In this context, the study to compare the resistance of carbon steel to cavitation-erosion may permit the understanding of corrosion mechanisms associated with the flow and may promote a better material selection. To achieve this goal, efforts are required in technological development.

As already mentioned, in general, the tubes subjected to multiphase flow operate in the worst flow regime (slug) which, as mentioned, causes an increase in erosion/corrosion effects, resulting in corrosion rates much higher than those promoted in other flow regimes¹²⁴. The researchers observed that the gas phase in the slug flow was in the form of bubble pulses. It was concluded that these pulses definitely contribute to the increase in corrosion intensity. In the slug pattern, the pulses that drag the gas bubbles were directed to the bottom wall of a tube.

Thus, they established a correlation between the corrosion rate and the amount of gas in that region¹²⁴. Gas-bubble pulses impacting the pipe wall can collapse, causing a cavitation-like effect that can remove the protective layer causing degradation and reducing their protective performance.

The combination of the layer removal, the shear stress due to rolling motion and the impact of the bubbles on the pipe wall results in an increase in the erosion/corrosion rates unique to the slug flow¹²⁴.

2.9. Emulsion

Emulsions are dispersions with one liquid phase in another and can exhibit stability in the presence of surfactants, macromolecules and solid particles adsorbed at the interface of both. At least two immiscible liquid phases must be present to form an emulsion. Therefore, it is important to know the behavior of a system constituted by a surfactant and two immiscible liquids, generally referred to as oil (O) and water (W)^{127,128,27}.

There are three types of emulsions: water-in-oil (W/O) emulsion, oil-in-water (O/W) emulsion and multiple emulsions^{128,79}. In emulsion studies, the focus is on interparticle forces or colloid interactions and the emulsion stability in terms of demulsification. The work (thermodynamic) for emulsification can be defined as the product between the interfacial tension and the variation of the area generated by the process. This energy must remain stored for some time until the system follows the natural path of minimizing it by decreasing the interfacial area and consequent destruction of the dispersion. Despite their thermodynamic instability, many emulsions are kinetically stable and do not change for long periods. This happens because the barrier potential, which prevents aggregation of the particles, is high¹²⁸.

Oil wells produce single-phase crude oil at first, but it is common for water to occur after some production time. The water content can be as high as 90 % or more before the well becomes uneconomical and is shut down. Under these conditions, the two liquids can form emulsions with high viscosity. The result can be a gel with non-Newtonian properties, and its transportation can be as difficult as a very viscous oil. Predicting whether such emulsions are

likely to occur and evaluating whether they can cause serious problems typically involve both chemical analysis and flow calculations¹¹⁵.

The presence of CO₂ can change the properties of crude oil. The solubility of CO₂ in crude oil is often much greater than in water. Incorporating CO₂ can induce an expansion in the volume of crude oil. The viscosity of crude oil decreases enormously with increasing pressure and temperature. It should also be noted that, in W/O emulsions, a lower viscosity can lead to easier separation of phases a condition that increases the risk of corrosion¹⁶⁵.

In Brazil, about 20 % of the oil reserves comprise heavy oil with a viscosity ranging from 20 cP to 400 cP under reservoir conditions. The extraction of heavy oil is more complex and more expensive than that of light oil because the challenges are greater; the refining is more difficult, and the generated derivatives are of lower added value. A significant portion of Brazilian reserves is located in deep or ultra-deep waters. A greater depth of the well tube can result in higher partial pressure of CO₂. Therefore, heavy oils associated with high CO₂ partial pressure may indicate a higher corrosion risk for pipelines and equipment of deeper wells¹⁶⁵.

In this scenario, the flow assurance in production is a crucial factor considering the high pressures and low temperatures. The main challenges are to reduce production losses by improving operational practices to properly handle highly viscous emulsions, hydrates and paraffin depositions. Characterizing of W/O type emulsions is important to improve confidence in prediction of the necessary pressures for the flow of emulsions formed mainly by heavy and viscous oils. These problems are aggravated when the fields operate in low temperatures and reach mature ages^{166,167}.

In the Oil & Gas industry, centrifugal pumps are widely employed to lift fluids from wells to topside facilities. Nowadays, it is estimated that approximately 10 % of the oil supply in the world is produced with centrifugal pumping installations. In these systems, the high shear and turbulence also can promote the breakup of the phases into small drops, producing dispersions and emulsions, which can be O/W or W/O types¹⁶⁸.

Many variables can influence the emulsification process. For instance, phase viscosity is an important factor since it is related to the efficiency of the stirring process. It is well known that if the difference in the viscosity between the water phase and the oil is high, the emulsification process could be considerably changed. A change in the phase viscosity ratio can produce a change in an emulsion standard inversion line⁹⁹. The increase in emulsion viscosity is due to a large number of small water droplets often leading to increasing the cost of the operation condition¹²⁹.

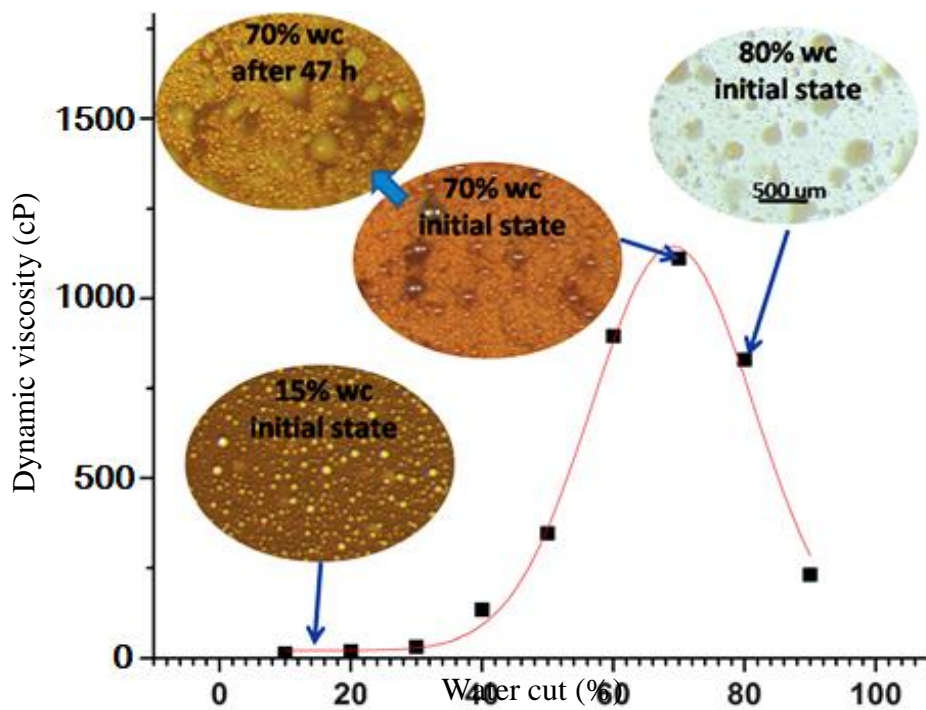
Using specific emulsification tests, it is possible to better understand the phenomenology of emulsions⁹⁹. This knowledge can be used for corrosion assessment and management of pipelines carrying brine-oil mixtures.

In general, two important factors cause emulsion formation in the petroleum industry: turbulent flows and pressure changes in choke valves and other valves during crude oil

extraction. Therefore, the cost of transportation and pumping of crude oil as well as the corrosion risks of the crude-oil processing equipment increase. This is one of the biggest problems in the petroleum industry, especially for mature oil fields for which the water quantity accompanying crude oil extraction is high¹²⁹.

Ming Wang *et al.*¹³⁰ cited in their study that an emulsion can also undergo a phase inversion in which the dispersed phase becomes the continuous phase and the continuous phase becomes the dispersed phase. Emulsion inversion point (EIP) consists of a change from O/W to W/O, with the characteristic of an increase in the total pressure gradient, leading to significant pressure loss in the oil production system and explains the decrease observed in the dynamic viscosity after a peak in **Figure 21**. However, the authors found that the peak pressure gradient did not occur in the high-viscosity oil flow, nor did the pressure gradient gradually decrease after the phase inversion. One aspect that may explain the non-occurrence of the peak pressure gradient is the lack of formation of emulsified droplets of water in oil. In more viscous oil, water is likely to be present in the form of large, deformable and coalescent drops which are entrained by the viscous oil. High-viscosity oil retains more water and forms an emulsion more easily¹³⁰. The emulsion formation, in turn, further increases the viscosity. Consequently, the frictional and gravitational force components increase, promoting an increase in the shear stress on the pipe surface. Using specific emulsification tests, it is possible to improve the understanding of the phenomenology of emulsions¹²⁸.

Figure 21 - The dynamic viscosity changes as a function of WC. The emulsion was prepared by mixing oil and brine at a rotating velocity of 1200 rpm for 10 min.



Source: adapted from Ming Wang *et al.*¹³⁰

The water/oil ratio (WOR) and surfactant–oil–water (SOW) blend are important parameters influencing emulsion type and inversion point. To determine the inversion point in systems with the water, oil and surfactants, experimentally, the mixture is emulsified according to a typical standard procedure with a turbulent stirring and its conductivity is measured. When the aqueous phase contains some electrolyte, the emulsion conduct electricity only if the aqueous phase is continuous¹²⁸.

Sjöblom¹²⁸ presents a 3D map for the qualitative treatment of all conditions in which emulsion inversion occurs and shows typical emulsion-inversion surface shapes in **Figure 22**. Although a 3D map is an approximation, it is a significant improvement because it allows interpretations and predictions of the relative position of a system to an emulsion inversion point.

The map shows three axes: hydrophilic-lipophilic deviation (HLD), water fraction (Water) and other variables (OV). The definition of the hydrophilic–lipophilic deviation (HLD) concept considers the effect of system salinity and temperature, surfactant characteristics, oil type, and alcohol added to the system. This HLD concept is applied to design new surfactant molecules used in specific formulation conditions¹³¹.

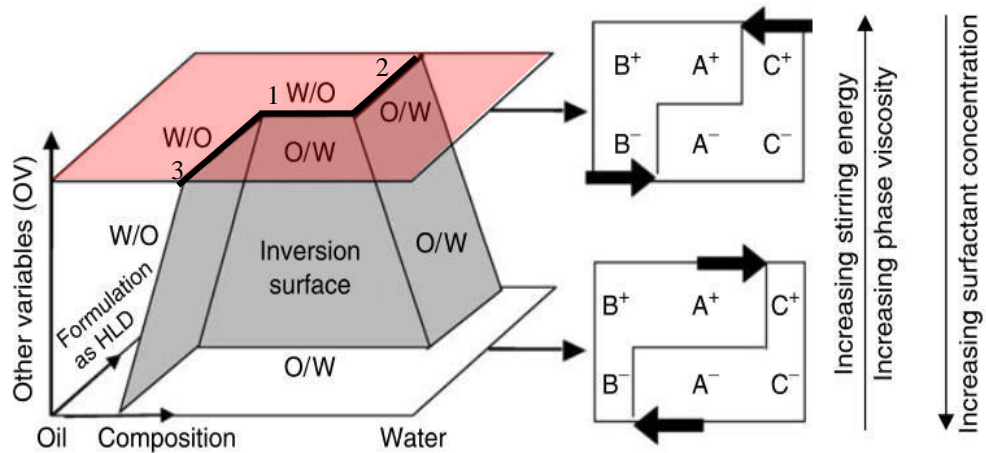
In **Figure 22**, the bold lines (1, 2 and 3) of the red surface correspond to the standard inversion point. The inversion line is the frontier which separates the water (continuous phase) from the oil (continuous phase).

The horizontal bold line 1 (HLD=0) corresponds to an optimum formulation for transporting petroleum in an enhanced oil recovery technique. The bold vertical lines 2 and 3 are defined as the above region with about 30 % of W (HLD>0) and the below region with about 30 % of O (HLD<0), respectively. In this way, it is possible to present the inversion in a staggered manner with six regions labeled: A, B, C to indicate the WOR, with (+) or (-) sign according to the HLD value, above and below respectively¹²⁸.

Bancroft's rule⁸ applies in regions where the emulsion type is normal which are A+, B+ for W/O and A-, C- for O/W. Abnormal emulsion types are those in which the morphology is imposed by WOR as in the regions (C+ and B-). Abnormal regions are associated with the presence of multiple morphologies, ie w/O/W in C+ and o/W/O in B-, the lowercase letter indicates the dispersed droplets¹²⁸.

⁸ The Bancroft rule states: "The phase in which the stabilizing agent is more soluble will be the continuous phase." This means that water-soluble surfactants tend to give oil-in-water emulsions and oil-soluble surfactants give water-in-oil emulsions¹²⁸.

Figure 22 - 3D mapping of emulsion type



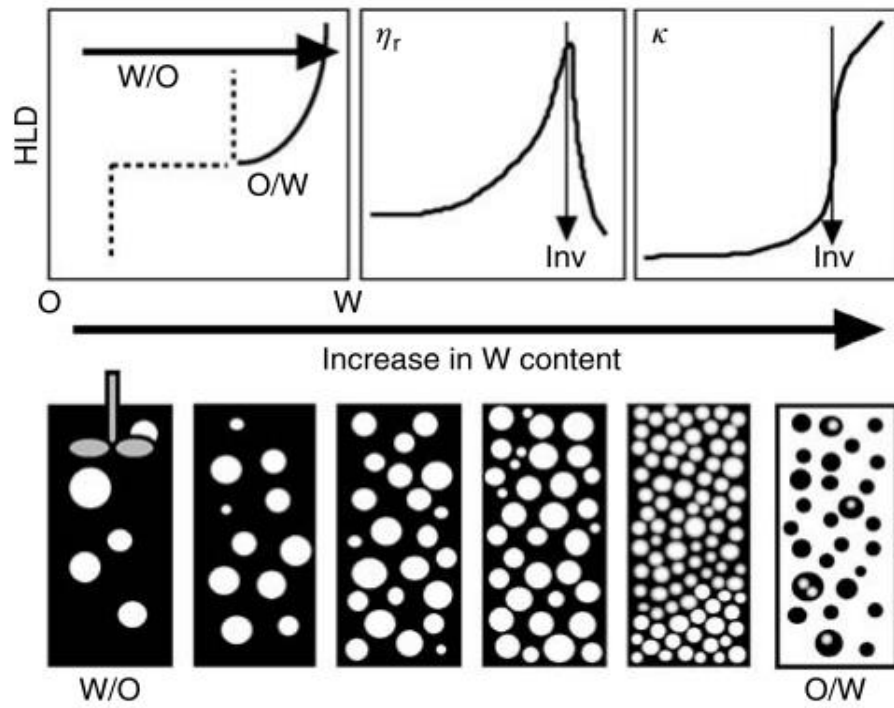
Source: adapted from Sjöblom¹²⁸.

Sjöblom¹²⁸ shows some illustrations of the application of the 3D map. One of them, shown in **Figure 23**, presents an example of the inversion point from a normal (A⁺) to a multiple abnormal emulsion (C⁺). This inversion occurs when water is added to W/O emulsion in HLD > 0 conditions in the presence of a specific surfactant concentration.

As illustrated in **Figure 23**, as we increased the amount of water under stirring, the water dispersed in drops and became more numerous and closer to each other. As the critical limit of water content is reached, for example, between 65 % to 70 %, the drop coalescence does not occur because the emulsion is stable (A⁺). When the water content continues to increase, depending on the applied shear and the surfactant performance, the droplets would coalesce, becoming a continuous phase, resulting in the emulsion inverting into an abnormal O/W (C⁺) sometimes with some residual droplets¹²⁸.

This example of inversion of the emulsion of the W/O to O/W shows that the experimental conditions as the degree of stirring, the fraction of W/O, and the surfactant concentration define the variation of the emulsion in relation to the viscosity, conductivity and distribution of drops¹²⁸.

Figure 23 – Inversion point from normal to abnormal morphology ($A^+ \rightarrow C^+$). Based on 3D map showing variation of emulsion.



Source: Sjöblom¹²⁸.

CHAPTER 3 – EQUIPMENT, MATERIALS AND METHODS

As the main objective of this thesis was to study the corrosion induced by the multiphase flow, a specific corrosion multiphase-flow loop was projected and constructed. Therefore, initially, this topic is presented. Then, the materials used as test specimens are presented including characterization tests and specimen preparation. For the tests in which corrosion rates were obtained from mass loss measurements, the adopted procedure was described. Finally, the specific experimental devices for cavitation-erosion tests, emulsion formation tests, and rotating cylinder tests are presented.

3.1 Multiphase flow loop testing

In this item, all parts of the design, construction and operation of the multiphase loop for corrosion studies will be covered. The concept adopted considered the need to carry out simultaneous tests both in the horizontal 0° and in the 45° inclined direction and produce an intermittent flow pattern with recirculation of the phases. Additionally, for the loop design, we considered controlling the partial pressure of the gases, the average pressure of the system, the flow rates of each phase and the average temperatures.

3.1.1 Concept, construction and operation of multiphase-flow corrosion loop

The multiphase flow corrosion loop was fabricated from AISI 316L austenitic stainless-steel tubes with a nominal diameter of 38.1 mm for a working pressure of up to 10 bar and of a temperature up to 100 °C. The inner surface of the tubing which was in contact with the medium, including the test sections, was coated with epoxy. In the literature, authors have developed experiments on loops with different designs, using materials and pumping systems and different controls^{17, 21, 64, 73, 75, 77, 94–99, 32, 100–105, 33, 35, 37, 38, 47, 57, 60.}

The conceptual design of the intermittent flow loop and the definition of operating conditions required prototyping steps on a laboratory scale before defining the final design and construction. Preliminary tests and calculations with simulation with flow model were carried out using practical tests with water and airflow to evaluate the operating conditions and the conditions for the formation of the intermittent flow. Part of these tests was conducted on specific prototypes built at the Interdisciplinary Center of Fluid Dynamics (NIDF) of the Science and the Technology Center of the Federal University of Rio de Janeiro (UFRJ).

The concept is to produce flow with recirculation of the phases controlling the partial pressure of the gases, the average pressure of the system, the flows of each phase and the average temperatures of the phases. With the open circuit loop and recirculation, only phenomena due to corrosion and hydrodynamic effects are expected to occur. In the present study, two complementary strategies were used to guarantee the correct dimensioning of the diameter and the flow of the liquid and gas phases. First, four empirical correlations were used based on the literature to determine the slug frequency. Then, a real-scale experiment, with horizontal and inclined tubing of an internal diameter of 38.1 mm, was set up in which the values of bubble frequency in the horizontal section were determined using a resistive sensor.

As a result, it was observed that the bubble frequency was slightly above the range predicted in the model and also that the flow rates were sufficient to exceed the minimum value of 1 Hz.

The test analyses allowed determining the range for loop design with flow rates for the liquid from 1 m³/h to 8 m³/h, and the gas from 2 m³/h to 15 m³/h, resulting in a frequency in the range from 1 Hz up to more than 5 Hz. The influence of the dynamic viscosity of the liquid phase on the flow pattern, in both horizontal and inclined sections with multiphase mixtures (water + oil + gas), was verified only in the tests after the steel loop construction. After defining the conceptual design and the operating limits, we moved on to the stage of manufacturing design and installation infrastructure.

In the literature, it was stated that the fluid flow influences the corrosion process mainly through the transport of mass involved in the corrosion by CO₂ and H₂S. At high flow rates of the distinct phases, which occur, there is greater turbulence and a more effective mixing in the solution. Depending on the conditions of the medium, such turbulence may or may not be beneficial to the formation of the protective layer of corrosion products. The turbulent flow accelerates the transport of species to the metal surface and away from it which can increase the corrosion rate since the transport is determinant in the corrosion rate control³⁹.

The presence of CO₂ and/or H₂S may lead to the formation of iron carbonate (FeCO₃) or iron sulfide (FeS) layers, respectively. Studies have reported that, at a given temperature, the corrosion rate and the FeS layer morphology depend on the amount of H₂S and the exposure conditions. In some cases, the iron sulfide layer may not be protective and it may result in a localized attack. Understanding the mechanisms of the formation of the various forms of iron sulfide layers and their effect on the corrosion process of CO₂ are the main challenges in the prediction of CO₂/H₂S corrosion⁹².

Laboratory tests, described in the literature, allow the establishment of empirical correlations between the corrosion rate and specific exposure conditions. These correlations are, thus, used in corrosion-prediction software that can help an engineer design and monitor the useful-life expectancies of industrial pipes. Most experimental studies in the literature address corrosion studies in a CO₂/H₂S environment limited to tests performed in autoclaves and glass cells. In these systems, a researcher produces test results which, despite their being useful in the understanding of corrosion mechanisms, can not give multiphase-flow regime results similar to those related to the conditions of pipelines in oil and gas exploitations¹³². A small-scale corrosion loop provides a suitable environment for better reproducing hydrodynamic effects on the corrosion of pipe walls. Therefore, the suitability of corrosion loop tests, which simulate these turbulent conditions, is considered fundamental to understanding and monitoring all stages of the corrosion-multiphase flow test for in-depth analysis of system variables which can lead to significant improvements in oil production and extraction.

In this case, the challenge was to determine a conceptual design of the flow loop in a compact and modular way that would allow reaching the multiphase flow pattern with recirculation to generate less waste disposal.

3.1.2 Compact separator

Among the essential equipment in the system, the phase separator stands out. The function of this equipment is to separate the liquid and gaseous phases to maintain recirculation conditions in the system. Typically, liquid/gas separators used by the Oil & Gas industry are manufactured for large volumes and the manufacturers are owners of the technologies. In this project, in partnership with NIDF, a multiphase flow loop was developed, including a compact separator to be installed within a small physical space available for the equipment assembly. The separator consists of a vertical tube with an inclined tangential inlet and two outlets, one at the top for the gas and the other at the bottom for the liquid (Figure 25a). The working principle is gravitational, as are separators in general. The difference is in the tangential inlet flow provided by the reduction of area (flow rate = velocity x area) to a sufficient degree to generate a centripetal force in one order of magnitude greater than that of gravity.

The combination of these forces increases the thrust on the gas, increasing the separation efficiency compared to a conventional gravitational separator. **Figure 24** illustrates the design of the compact separator built at UFRJ and **Table 2** presents the results of the validation tests performed. In each of the ten tests performed, the operating conditions and the separation efficiency regarding the amount of liquid carried by the gas (LCG) and the amount of gas carried by the liquid (GCL) were monitored. Because the separator used in the experiment was transparent, it was possible to observe the separation efficiency by visual inspection and, thus, determine the point of excessive LCG.

Figure 24 – Compact separator (a) details of the section reduction in the separator entrance (b-c).

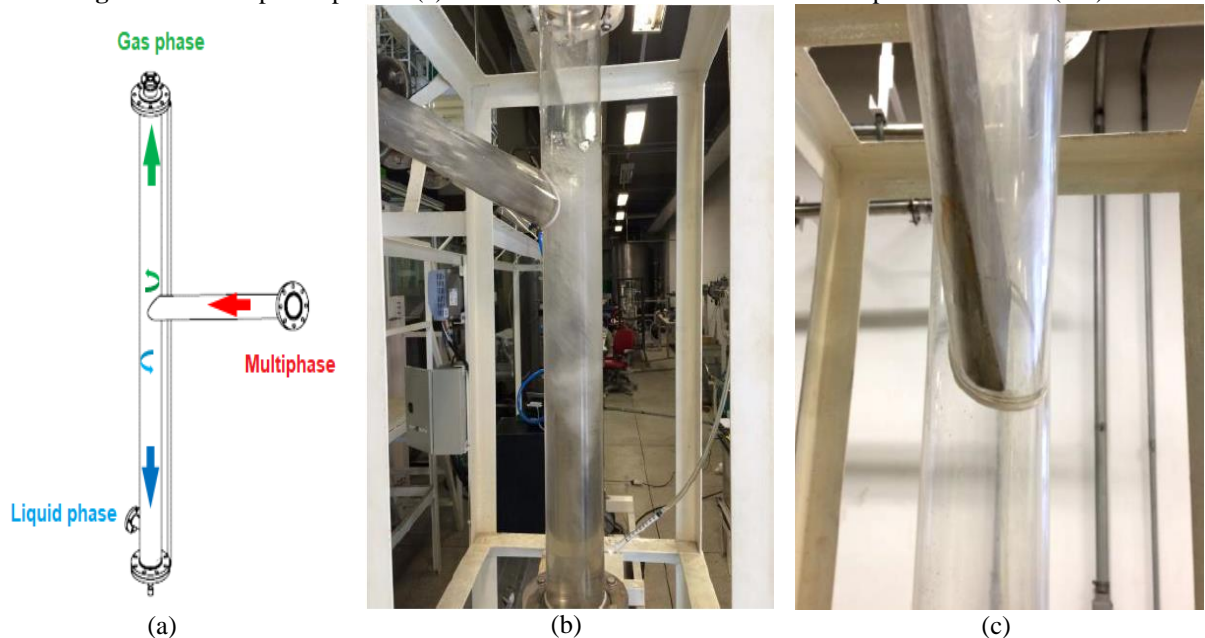


Table 2 shows that, under specific gas and liquid flow conditions, excessive liquid entrainment, in the form of small droplets, occurred through the upper outlet. Visually, in any of the tests, no significant amount of air was being charged to the liquid outlet.

However, that whenever the liquid flow was increased, it was necessary to open the valve that restricted the lower outlet to maintain the height of the water column below the entry point.

In the literature, laboratory and field data are used to develop multiphase flow models. Six parameters, considered the most important, are used in these models: total length, maximum diameter, inclination, operating pressure, length of the test section and type of fluid¹². In this work, a software of the UFRJ was used for this purpose.

Table 2 –Validation tests for compact separator prototype built at the NIDF

Test	Liquid flow rates (m ³ /h)	Gas flow rates (m ³ /h)	Results
1	5.0	6.7	Normal separation
2	5.0	11.6	Normal separation
3	6.0	6.2	Normal separation
4	6.0	11.4	Normal separation
5	6.0	12.0	Excess LCG
6	8.0	6.1	Normal separation
7	8.0	10.0	Normal separation
8	8.0	11.0	Excess LCG
9	10.0	6.1	Normal separation
10	10.0	8.5	Excess LCG

Figure 25 illustrates the input parameters used and calculation models, and **Figure 26** the selected parameters and the results obtained for the flow frequency (slug).

Thus, two complementary strategies were used to guarantee the correct dimensioning of the diameter and the flow of the liquid and gaseous phases.

First, four empirical correlations available in the literature for the frequencies of bubbles were used. Second, a prototype was mounted for a full-scale test using horizontal and inclined acrylic tubes with an internal diameter of 38.10 mm for the circulation of a biphasic mixture (water + air).

Values of the frequency of the gas bubbles in the horizontal section were experimentally determined using a resistive senso. At the end of the test, it was observed that the frequency of bubbles was slightly higher than the range predicted in the model and the flow rates were sufficient to exceed the minimum value of 1 Hz.

These analyzes made it possible to determine in the loop design the flow ranges for the liquid (1 m³/h to 8 m³/h) and gas (2 m³/h to 15 m³/h), resulting in a frequency in the range of 0.4 Hz to 5 Hz.

The influence of the dynamic viscosity of the liquid phase in the pattern flow, both in the horizontal and in the inclined section, with multiphase mixtures (water + oil + gas), was verified only in the tests after the loop was manufactured.

Figure 25 – Software screen used showing the calculation of the flow properties (slug).

Slug Properties Calculator

Air/Water Slug Properties

Laboratory of Multiphase Flows

Parameters

Pipe Diameter (D) [m]:

Liquid Mass Flow Rate (Wl) [kg/s]:

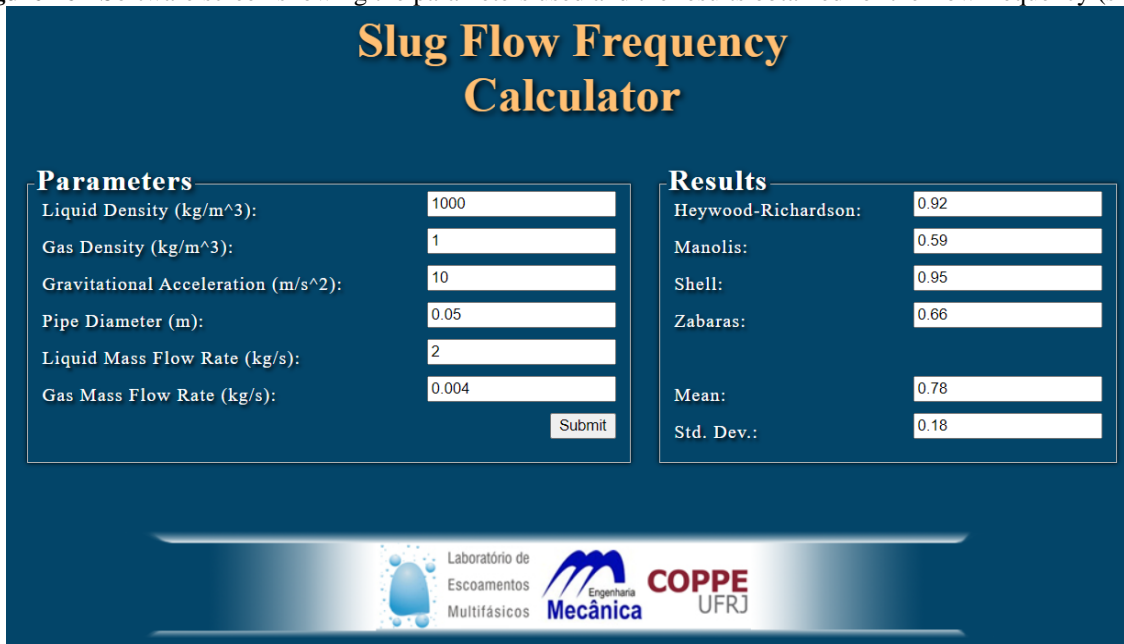
Gas Mass Flow Rate (Wg) [kg/s]:

Slug Frequency (v) [Hz]: Zabarras (2000) Cook and Behnia (2000)

Results

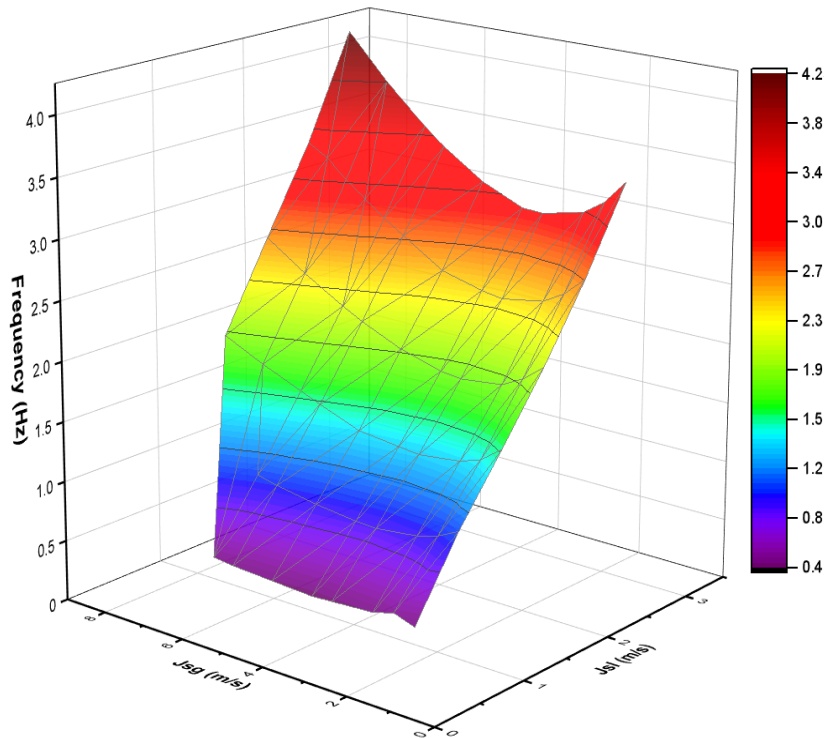
	Orell (2005)	Dukler and Hubbard (1975)
Slug Unit Length (lu) [m]	0.44	0.40
Slug Length (ls) [m]	0.34	0.26
Mixing Vortex Length (lm) [m]	--	0.00
Liquid Film Length (lf) [m]	0.10	0.13
Slug Translational Velocity (ut) [m/s]	1.78	1.59
Slug Liquid Velocity (us) [m/s]	1.29	1.29
Liquid Film Velocity (uf) [m/s]	0.07	0.89
Gas Velocity (ug) [m/s]	1.77	--
Slug Liquid Holdup (Hs) []	0.98	0.99
Liquid Film Holdup (Hf) []	0.28	0.43
Slug Unit Head Loss (Δpu) [Pa]	362.37	263.55
Slug Head Loss (Δps) [Pa]	361.79	263.55
Slug Liquid Head Loss (Δpl) [Pa]	361.79	143.13
Mixing Vortex Head Loss (Δpm) [Pa]	--	120.42
Liquid Film Head Loss (Δpf) [Pa]	0.59	--
Slug Frequency (v) [Hz]	4.03	4.03
Slug Mass Pickup Rate (x) [kg/s]	--	0.09
Slug Reynolds Number (Res) []	23168.63	25038.97

Figure 26 - Software screen showing the parameters used and the results obtained for the flow frequency (slug).



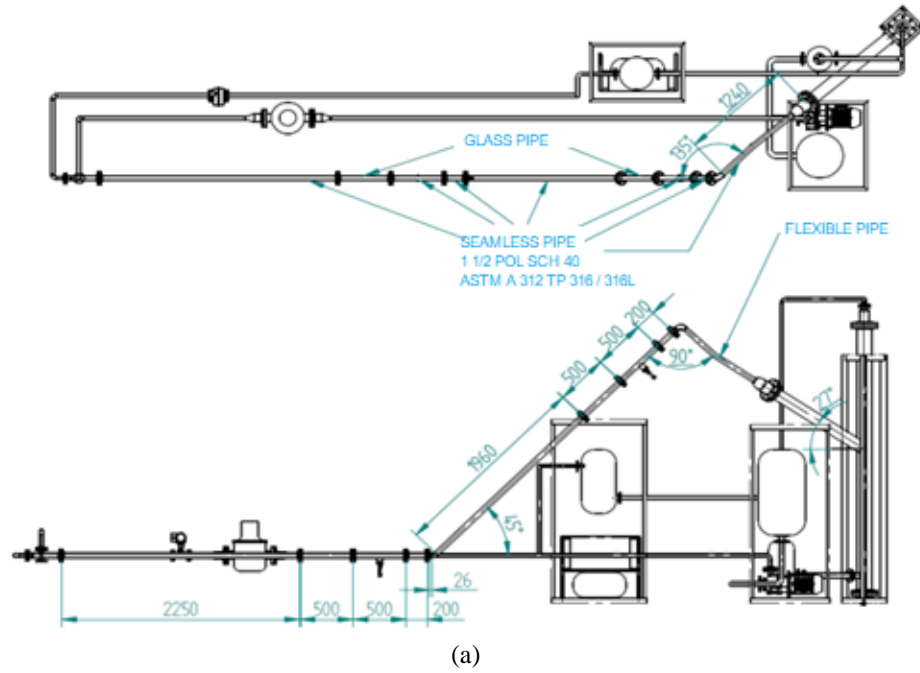
Based on the tests using the prototype, it was possible to define a frequency map as a function of the surface velocities of the liquid phases (J_{sl}) for water with a density of 1025 kg/m^3 and surface velocities of the gas phase (J_{sg}), considering air density of 2.4 kg/m^3 . **Figure 27** is the map obtained. This map was used as a reference to define the flow rates for multiphase flow with water, oil and gases in the manufactured loop.

Figure 27 – Intermittent flow regime map

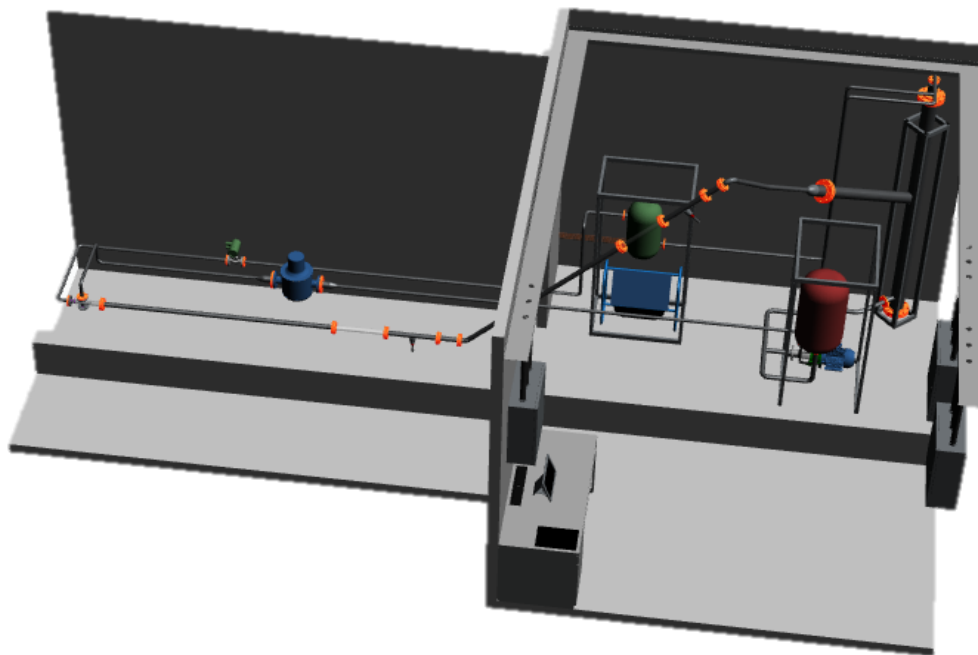


With the definitions of the conceptual design, we moved on to the manufacturing design and installation infrastructure stage to establish the methodology and the operating procedure. **Figure 28** and **Figure 29** show the layout and images of the fabricated loop.

Figure 28 - Facilities layout for conceptual design (a) and (b).



(a)



(b)

Figure 29 - Corrosion multiphase loop as manufactured (a) and (b).



(a)

(b)

3.1.3 Preliminary tests for setup of operation parameters

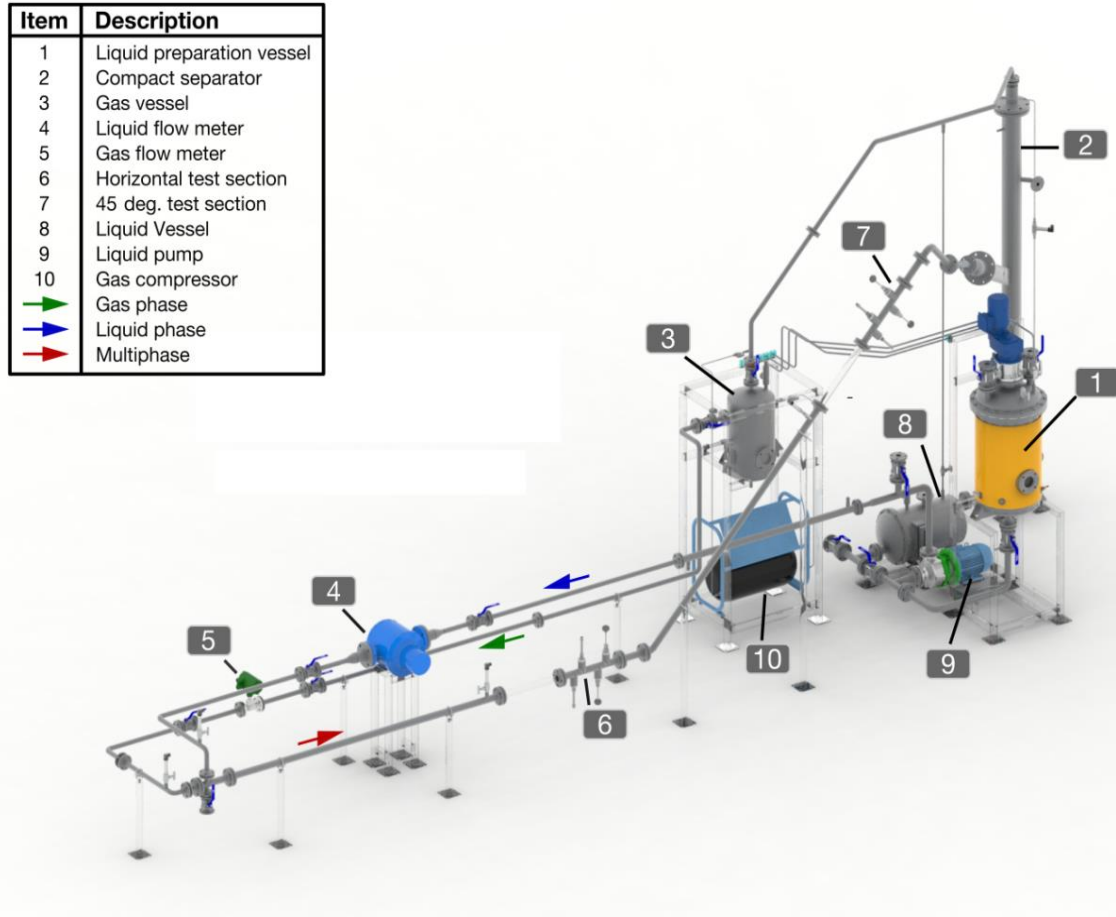
The schematic itemized drawing of the loop is shown in **Figure 30**. It is possible to observe the position loop components and understand the steps of the preparation procedure to be described, which is the first stage of the tests in the loop.

The saline solution is directly in the “liquid phase preparation vessel” (**Figure 30**, item 1) that has a capacity of 200 L. For each test, 48 L of saline solution were prepared. The concentration of NaCl in the saline solution was defined after carrying out preliminary tests, and the following composition was established: 15 % sodium chloride, 0.017 % acetic acid and 0.038 % sodium bicarbonate (all in mass fraction) in deionized water. Acetic acid was added as a buffer to control pH variations.

After the preparation of the saline solution, oil (12 L) was added, in the proportion of 80 % of the saline solution and 20 % of oil (light or heavy) in mass fraction. In the Oil & Gas industry, this type of mixture is called water cut, and is expressed as a percentage of water in the mixture and indicated as follows WC 80. Preliminary tests were carried out to determine the

level of agitation necessary to maintain a homogeneous liquid phase in the preparation vessel to facilitate and optimize pumping.

Figure 30 - Corrosion multiphase flow loop



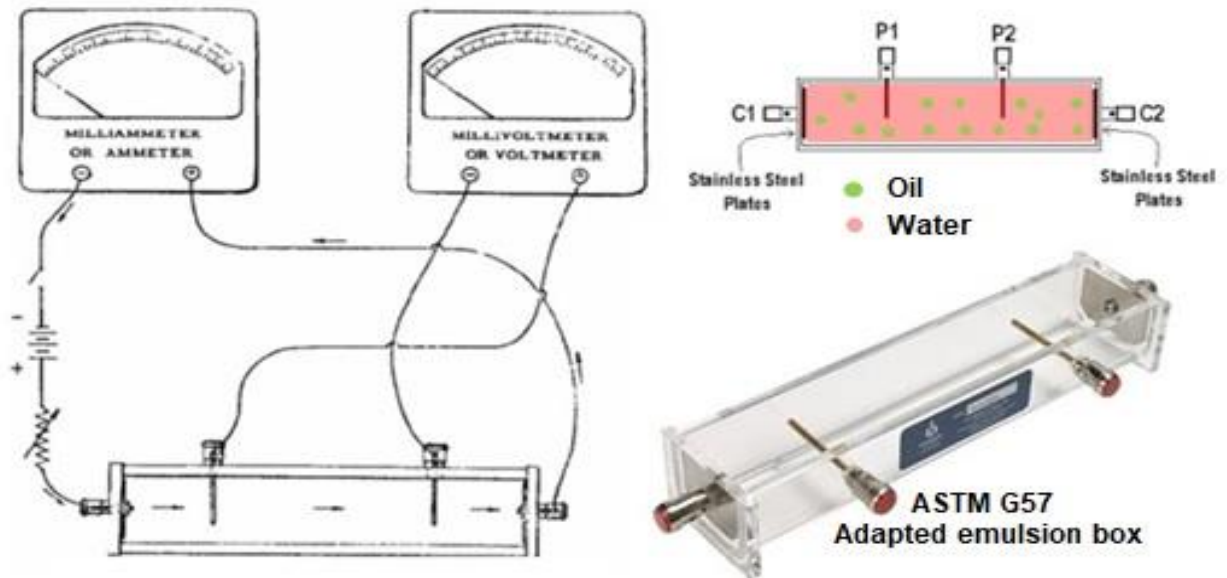
3.1.4 Determining the composition of the liquid phase

The NaCl concentration initially proposed was 20 % (mass fraction). To verify the operation of all instrumentation employed in the loop, a test was conducted with a biphasic mixture (NaCl solution and N₂) without the presence of oil (WC 100). Under these conditions, the signals from the sensing module were dispersed along the pipeline and lost in the grounding system of the loop structure. After the end of this test, the conductivity of the 20 % NaCl solution was measured with a bench conductivity meter. A value of about 200 mS/cm was obtained. It was concluded that this solution is highly conductive, making it impossible for the flow sensors to function correctly, since a solution with this degree of salinity when flowing through the loop pipe, presented a behavior similar to that of a conductive wire.

A test matrix was set up, including mixtures with oil which represent the field conditions in the decommissioning phase, shown in **Table 3**. The oil used in this matrix was light (10 cP at 40°C), due to its low viscosity which facilitated the obtaining of homogeneous mixtures. More details on the crude oil used in this work are provided in **Erro! Fonte de referência não encontrada.**

The conductivity of oil and water mixtures could not be measured by the bench conductivity meter because it is not suitable for oil mixtures; it was decided to mount a device shown in **Figure 31** for this purpose.

Figure 31 – Emulsion box for conductivity determination



This device was developed based on Wenner's four electrodes recommended by ASTM G57. As **Figure 31** shows, the method requires inner (P1 and P2) and outer (C1 and C2) electrodes equidistantly placed along a straight line in the oil/brine mixture to a depth not exceeding 5 % of the minimum separation of the electrodes.

A voltage is impressed between the outer electrodes (C1 and C2), causing current to flow, and the voltage drop between the inner electrodes is measured using a sensitive voltmeter. The resistance can be measured directly, and the resistivity can be calculated. For the measurements, the mixtures were subjected to manual agitation for a few minutes until the formation of a homogeneous mixture.

This mixture was quickly transferred to the emulsion box (**Figure 31**), and then the resistance ($R=1/L$) was measured and the conductivity (K) was obtained using **Equation 1**.

Equation 1

$$K = L \frac{d}{A}$$

where: L is the conductance, d is distance between P1 to P2 and A is the area of C1 and C2.

The results obtained are shown in **Table 3**. It can be seen that the mixture with a solution with 15 % NaCl and WC 80 was the one that presented the lowest conductivity among the matrix mixtures.

A reduction in the concentration of NaCl conferred insulating properties. It was not considered to include values less than WC 80 in the matrix because it would not represent the mentioned field conditions.

Table 3 – Results of NaCl solution and WC preliminary tests using the device shown in **Figure 31**.

Preliminary test conditions	NaCl (%)	Water cut (%)	Mixture conductivity (mS/cm)
A	20	100	205
B	15	100	174
C	10	100	131
D	5	100	75
E	20	95	124
F	20	80	98
G	15	90	101
H	15	80	76
I	10	80	Insulating

3.1.5 Determining the agitation level in the preparation vessel to maintain homogeneity of the liquid phase

To homogenize the liquid phase (water and oil), it is necessary to keep the mixture stirring in the preparation vessel. This is because the mixture formed in WC 80 is unstable, t. s., in the absence of minimal agitation, phase separation occurs. Therefore, a test matrix was prepared with the mixture presented in **item 3.1.4** to define the appropriate agitation intensity in the preparation vessel.

Another aspect considered in the preliminary tests was the investigation of the behavior of the liquid phase (water and oil). Researchers present in their studies results that correlate the formation of liquid phase emulsions during oil exploration to the WC and to the hydrodynamic effects (agitation). They inform that the characteristic of the mixture alters the values of dynamic viscosity, increasing or decreasing, mainly due to the WC, which is associated with the operation stage of the well^{27, 35, 37, 133}.

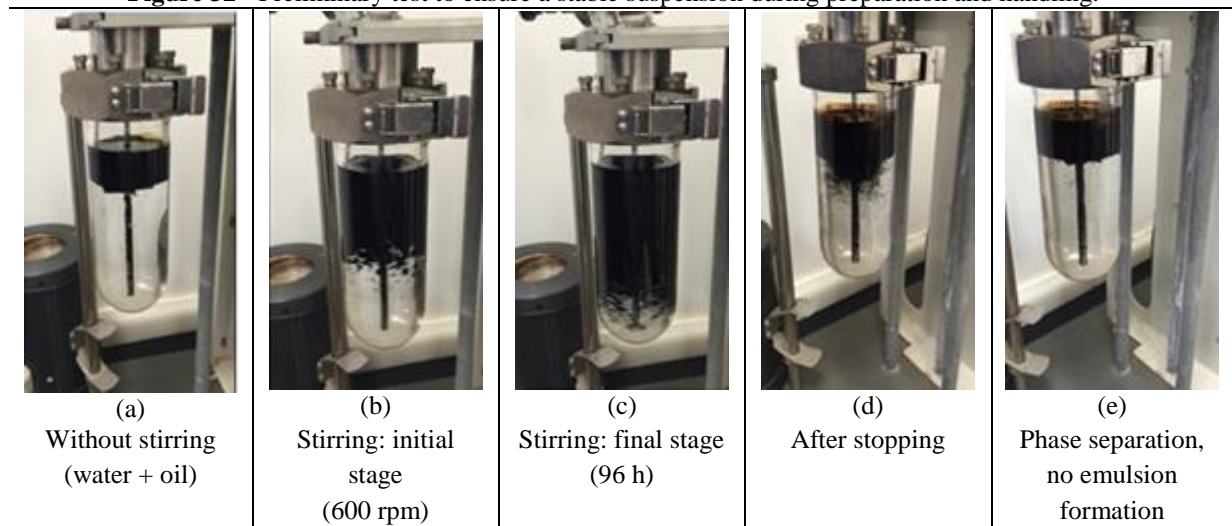
This association was also discussed in 2015 by Ming Wang *et al.*¹³⁰ through **Figure 21**, illustrating the results of tests with the variation of the WC. They observed that there is a tendency for the dynamic viscosity values to increase as the water fraction (WC) increases in the system and then decreases. WC 70 corresponds to the highest viscosity value and, at this point, there is the formation of a water-in-oil emulsion. With WC values greater than 70 %, the emulsion becomes composed of the oil-in-water emulsion, in which the viscosity decreases again.

It is known that the measurement of the viscosity are an advisable practice for the correlations of corrosion and flow effects. Einstein's rheological model of 1906 and 1911, for example, already suggested that the effective viscosity of a water-in-oil emulsion is greater than the viscosity of the separate pure oil.

As, in the preparation vessel (**Figure 30**, number 1), the objective was to form a stable mixture under agitation, but not emulsion, the preliminary tests were carried out using 300 rpm and 400 rpm, values well below that adopted by Ming Wang *et al.*¹³⁰. The liquid phase used in these tests was the saline solution already defined (15 % sodium chloride, 0.017 % acetic acid and 0.038 % sodium bicarbonate) and WC 80 and heavy oil (150 cP at 40 °C) for 96 h. We opted to carry out the tests with heavy oil because a higher level of agitation is necessary for heavy oils to obtain a homogeneous mixture. The 96 h period was adopted to be sure of the applicability of the results in the loop tests that were performed adopting a 30 h period.

Figure 32 shows the test performed with constant agitation of 600 rpm at different times. At the test beginning, in **Figure 32a**, there is agitation, and, thus water and oil are separated. When the stirring begins (**Figure 32b**), water and oil are mixed. The amount of mixed phase established in the level shown **Figure 32c**. After 96 h, agitation was interrupted (**Figure 32d**) and rapid separation of water and oil was observed, returning to the initial state (**Figure 32e**).

Figure 32 - Preliminary test to ensure a stable suspension during preparation and handling.



Oil viscosity measurements before and after the test showed 150 cP and 154 cP, respectively. It can be seen that there was a negligible increase in the viscosity, a fact that may be associated with the presence of a small amount of water dispersed in the oil after the test.

With the result of the preliminary suspension tests (water + oil), it was possible to observe the rapid separation after the agitator stopped showing that there will be no emulsion formation in the preparation vessel and, therefore, there will not be large changes in dynamic viscosity in the initial phase of the tests in the loop. Thus, the degree of agitation of a maximum of 400 rpm was established for the liquid phase preparation vessel (**Figure 30** number 1), during the entire O₂ removal procedure.

3.1.6 Oxygen removal procedure in the multiphase flow loop system

The removal of dissolved oxygen (O_2) from the liquid and gaseous phases is necessary to guarantee a medium with no oxygen (<10 ppb) and promote the tests under the action of CO_2 and H_2S gases with N_2 flask in established proportions.

This removal was done in two stages: the first was the removal of oxygen from the liquid phase in the preparation vessel; and the second, was the removal of oxygen in the entire empty loop circuit (piping, separator and auxiliary vessels). The first stage, as illustrated in the schematic diagram in **Figure 33**, started with the injection of nitrogen (N_2) at a higher pressure than that existing inside the liquid phase preparation vessel (**Figure 30**, number 1).

Before starting the N_2 injection, all valves were kept in the closed position. Then, valves V2 and V3 were opened and maintained in this position. The internal pressure in the vessel was raised to 1 bar. At this point, the V5 valve was opened to the “½ open” position. The concentration of O_2 dissolved in the gaseous environment expelled at the outlet of the V5 valve was measured by an optical sensor (model Mettler Toledo InPro6970i) installed in a closed chamber between the liquid phase preparation vessel and the gas washer. Then, the liquid phase preparation vessel was closed, the temperature of the liquid phase was raised to 40 °C and the mixture was kept under stirring (between 350 rpm and 400 rpm) until the start of it is pumping.

The flow rates of the N_2 inlet and the gases expelled from the vessel were maintained until the O_2 content measured in the chamber reached the expected value (<10 ppb). The time for this step varied with the type of oil (light or heavy) at an average of 12 h. Once the minimum pre-established O_2 value was reached, the pressure of the vessel (**Figure 30**, number 1) was relieved by the breather valve V4 and V5 communicated with the gas scrubber. This purging of N_2 was performed to lower the volume and pressure of the gas inside the vessel, enabling the start of the second stage.

The pressure vessel was kept on hold while the second stage was being carried out. During the execution of the second stage, a minimum positive pressure was maintained in the preparation vessel, preventing the entry of O_2 .

Then the second stage started, with oxygen removal activities from the loop. First, the specimens were positioned at 0° and 45° and the test section of the loop was set up. To avoid leakage, a tightness test was carried out with N_2 in the entire piping system. This test consisted of raising the pressure in the loop to 3 bar with N_2 and maintaining this condition for 2 h. During this period, when leaks were detected in the connections and joints, with the use of Snoop leak detector liquid, the tightness of the joint was redone at the proper torque until it was watertight. In the case of a failure, the joint was replaced. The oxygen removal procedure was initiated when there was no reduction in the pressure measured in the system, at least for 2 h.

Figure 33 – O₂ removal diagram in liquid preparation vessel

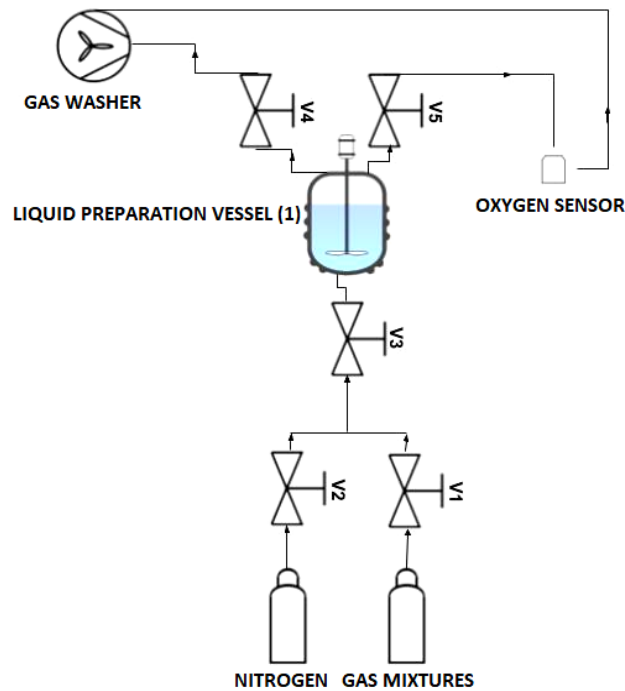
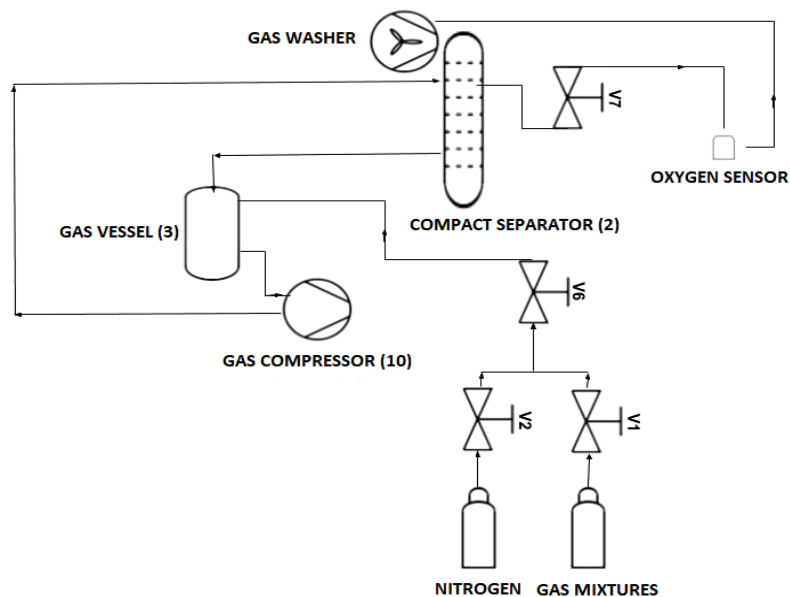


Figure 34 shows the scheme of valves used for this step. This procedure was initiated with the pressure and the volume of N₂ operating during the leak test (3 bar) in the system. In this condition, the gas compressor was turned on (**Figure 30**, number 10) causing the N₂ to circulate to drag the O₂ throughout the system. At that time, all of the valves shown in **Figure 34** were in the closed position. The compressor was activated to flow N₂ gas with an average gas flow of 10 m³/h, from upstream, suctioning the gas from the lung vessel and pressurizing the gas downstream in the compact multiphase separator.

Figure 34 - O₂ remove diagram in loop system



Then, the valves V2, V6 and V7 were opened and the O₂ concentration was monitored by the same sensor mounted in the closed chamber until reaching values below 10 ppb. This operation, aided by the compressor, took an average of 2 h to reach deflation. When levels below 10 ppb of O₂ were obtained, valve V2 was closed and valve V7 was opened to the “½ open” position.

From this point, as well as carried out in the liquid phase preparation vessel, the pressure and volume of gas in the loop were reduced to a minimum. Then, valve V1 was opened until the pressure in the loop reached the test pressure of 2.5 bar. The constant monitoring of the O₂ content indicated the desired operating conditions. During this process, the heat exchanger was activated to increase the temperature of the gas flowing in the loop to 40 °C, which was the test temperature. All variables are monitored, and the data obtained is stored and controlled by an application and control loop developed for the operation of the loop.

Once the loop was equalized (pressure and temperature) and the bleeding procedures were completed, all inlet and outlet valves were closed and the loop was ready to start the tests.

Remembering that the liquid phase was in the preparation vessel (**Figure 30**, number 1) and the gas phase in the loop, it became necessary to produce a pressure differential between the two systems (vessel and loop). For this, the V7 valve located in the compact separator (**Figure 30**, number 2) was opened, promoting a decrease in the pressure of the loop. Then, the drain from the preparation vessel was opened to drain the liquid phase to the pump. Immediately, the pump was started which allowed flow increase, controlled by the frequency inverter until reaching a flow rate of 3.5 m³/h. Then, the V7 valve was closed and the compressor was started.

If necessary, the partial pressure could be corrected with the combined opening and closing of valves V1, V6 and V7 featuring an open system^h with phase separation and recirculation. At that moment, the gas phase flow reached 8 m³/h and the liquid phase flow 3.5 m³/h. This relationship allowed the surface velocities of the phases in a multiphase mixture to reach the values necessary to obtain the intermittent flow pattern, slug pattern, developed in the horizontal and inclined test sections according to the loop design.

3.1.7 Sensing modules for multiphase flow

While the loop was in operation, multiphase flow measurements were made by sensors positioned upstream of both 0° and 45° test sections. **Figure 35** presents the illustrations of the sensing modules (a) and the transduction module and measurement processing (b). These modules were developed exclusively for monitoring the corrosion loop of this project. The working principle of the slug sensor is conductivity.

Two sensors and an emitter were installed at each sensing module shown in **Figure 35**.

^h Open system is defined with unlimited gas injection in the loop in order to maintain constant partial pressure of CO₂ and H₂S during the tests.

The variations in the conductivity of the medium captured by each sensor give information about the phase passing through. We have conductivity very close to zero for the gas phase and a much higher conductivity for the liquid phase. The gap between these two signals is measured to obtain the speed of the slug. The slug pass frequency is the inverse of the time between the noses of two successive Taylor bubbles. The size of the bubble is obtained as a function of the speed and the time width of the signal.

Figure 35 – Sensing module (a) and transduction and processing module (b) for flow measurements

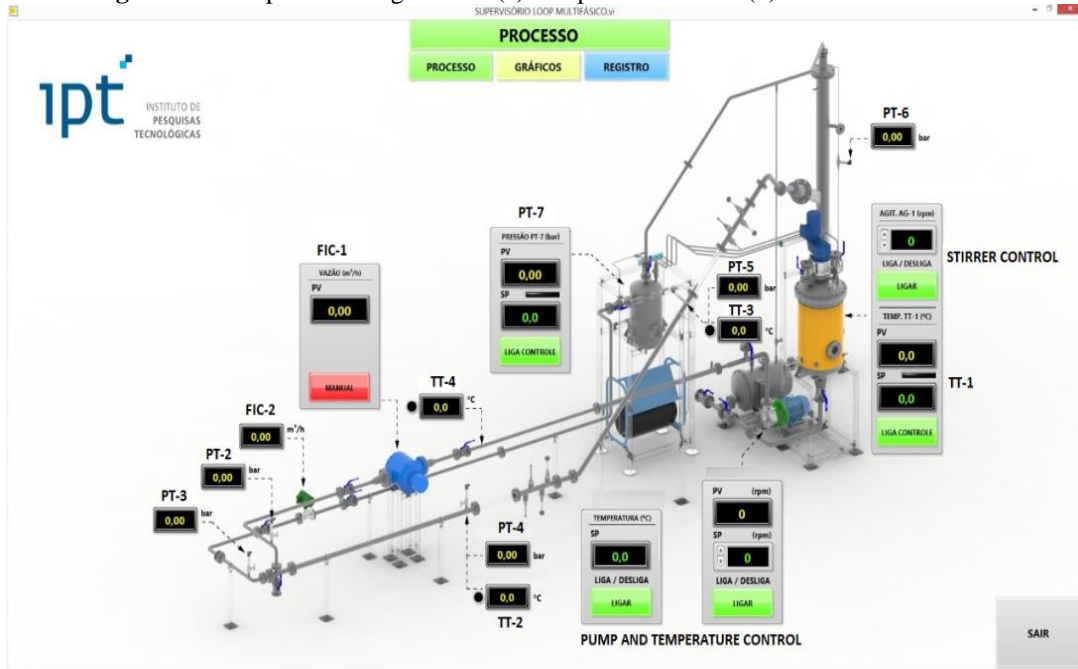


The dimensional characteristics of a slug were predicted for many years using literature models. In the last ten years, much effort has been invested by researchers, oil companies and research institutes to develop improved ways of predicting frequency, average slug length and length distribution¹⁹.

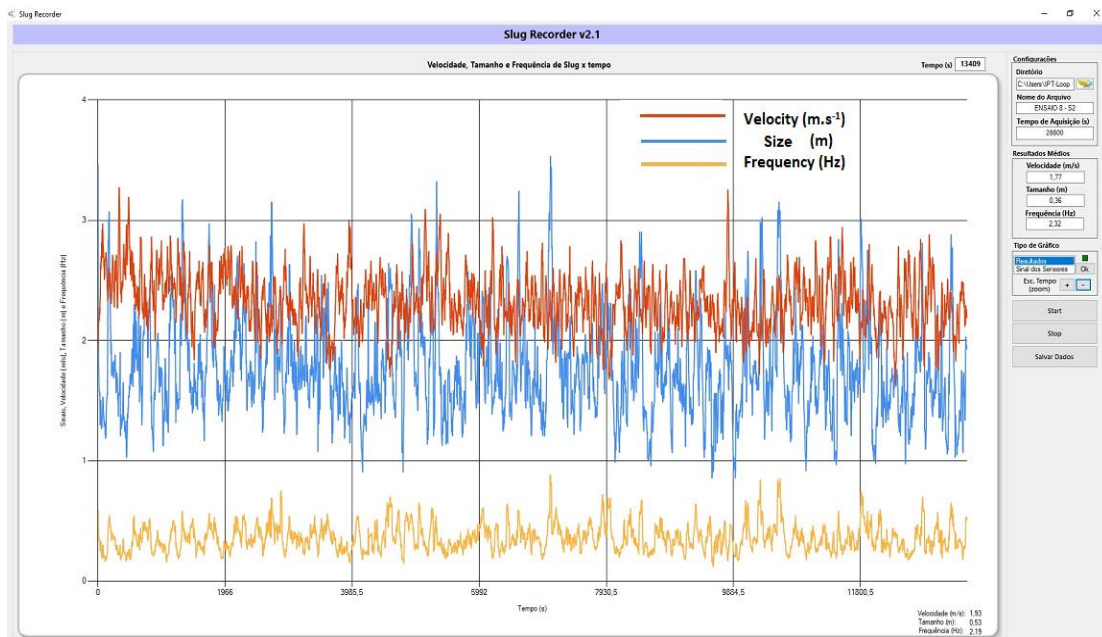
Based on the simulation of the flow pattern Taylor bubbles were produced and the validation of the sensors was carried out with tests measured by the particle image velocimetry (PIV) technique, the results are presented in **appendix I**.

The application developed for the control and monitoring of the loop also stored the measurements made by the flow meters and pressure and temperature sensors distributed at specific points. **Figure 36** presents the process control screen (Instruments Diagram to Multiphase flow loop) (a) and the real-time measurement screen of the slug sensor (b).

Figure 36 - Loop monitoring screens (a) and process control (b) flow measurements.



(a)



(b)

3.1.8 Flow Loop Monitoring System

During loop operation, the multiphase-flow parameters were monitored by two sensors positioned upstream of both 0° and 45° test sections. **Figure 35** shows the sensor and the transducer used for monitoring flow pattern parameters, i.e., the Taylor bubble frequency, the bubble size and the bubble velocity.

The operating principle of the sensor was based on fluid conductivity. For each transducer, two sensors were installed. The conductivity differences between the liquid phase (signal 1) and the gas phase (signal 2) were captured by each sensor and transmitted to the transducer that processes the received data and gives the desired flow pattern parameters. The conductivity of the gas phase is very close to zero and the conductivity of the liquid phase is much higher, about 80 $\mu\text{S}/\text{cm}$.

For the slug-velocity determination, the time elapsed between the two signals was measured. The frequency of bubble passages is the inverse of the time between the signals of two successive Taylor bubbles.

The size of the bubble was obtained from the speed and the time elapsed between signals. An applicative was developed to help to control, to monitor the loop and also to store the measurements made by flow meters and pressure and temperature sensors distributed at pre-selected points.

Measurement solutions are studying for application the latest electrical process tomography technology that uses arrays of electrodes to provide real-time images and volumetric data of what is going inside the loop system in 2D and 3D formats. Beyond the wall shear stress sensor, mounts flush with a pipe wall enabling direct measurement of wall shear stress, flow rate and viscosity of liquids during flowing or mixing without process flow interruption.

3.1.9 Corrosion monitoring

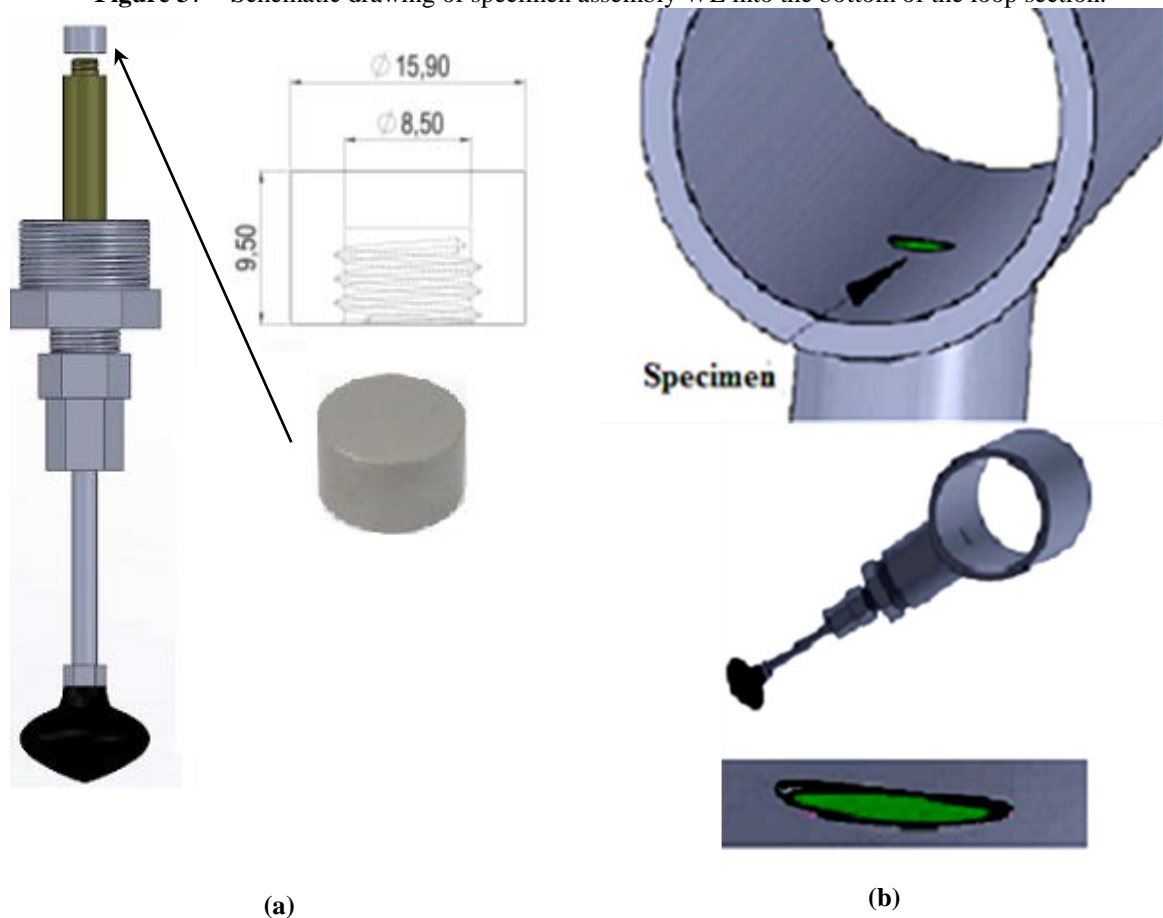
The configuration and the experimental operation of the multiphase flow loop was done in such a way to include horizontal (0°) and inclined (45°) test sections. Based on this concept, the skid assembly allows an interchangeable system with various possible configurations to simulate different industrial processes with compatible instrumentation.

The standard configuration for corrosion measurement was composed of weight loss probes (WL) and flow detection sensors for horizontal and inclined pipeline flows. In each of the multiphase-test sections, all probes were installed at the bottom of the pipe.

The test specimens (WL) and their holders were made according to **Figure 37**. In these tests, the disc-type and the ring-type specimens were fixed in support made of a high-performance polymer to guarantee the necessary mechanical resistance to the multiphase flow and also to allow the electrical insulation between the specimen and the pipe, avoiding corrosion by a galvanic coupling.

WL was length adjustable to the probe to permit their insertion into the bottom of the sections of the loop so that their flat circular surfaces exhibit maximum tangential alignment with the pipe minimizing hydrodynamic effects.

Figure 37 – Schematic drawing of specimen assembly WL into the bottom of the loop section.



3.1.10 Safety conditions for operation of the corrosion loop in multiphase flow

The IPT laboratory where the corrosion loop was installed has a safety system designed to prepare both the installation site of the equipment as well as the infrastructure for the gas transport tubes and the installed instrumentation.

When using hazardous gases, many safety steps must be taken into account during the initial design phase for a research facility to be safer. For example, the definition of the system installation site, piping material, instrumentation, safety systems, and operational procedures should be considered during construction.

3.1.11 Installation site description

The laboratory occupies an area of 50 m², with two access doors to the test loop with exhaust distributed at two suction points connecting the exhaust system with the gas washer. The building was designed and constructed to meet the explosion-proof condition. Every electrical installation has a grounding protection system and an electric power generator, guaranteeing operation and maneuvers in the event of a power failure. In the region where the corrosion loop was assembled, a containment basin (capacity greater than 10 times the loop volume) was built to retain possible leaks.

The infrastructure has a chemical pump with high flow, allowing quick removal of the liquid contained in the containment basin. In this way, the laboratory presents all the required conditions for gas exhaustion and liquid disposal demand.

However, containment alone does not effectively prevent the risks of the test medium. For this reason, monitoring and signaling instrumentation (visual and audible) were installed to detect air toxicity. Adequate training was offered to professionals who operated the corrosion loop.

3.1.12 Security system components

An operation of the corrosion loop with H₂S and CO₂ gases requires a proper design and the correct selection of tubes, derivations, and valves for handling gases, mainly of the pressure reduction and control system for injection in the loop. The gas phase valves were manufactured in AISI 316 stainless steel with a working pressure above 200 bar, a CO₂ pipe was manufactured with copper alloy and the H₂S was manufactured in AISI 316 stainless steel, both able to withstand pressures of up to 400 bar.

The pressure regulators were equipped with internal sintered filters to guarantee the retention of solid particles in the gas line to avoid component failure. Washers and valves were used in the seals and these were published for daily tests to check the tightness of the system.

The instrumentation for the testing laboratory in the loop comprised relief valves for safety by thermal expansion positioned in the lung vessels of the gas phase and preparation of the liquid phase (**Figure 30**), with discharge pressure (setpoint) adjusted to 6 bar, reminding that the vessels were designed to operate at 10 bar.

The laboratory was equipped with H₂S detection sensors (Opus z Sienger model) connected with light and an audible alarm at the laboratory entrance before access to the loop. The sensor triggers alarms for gas concentrations in the H₂S environment below 10 ppm. To access the laboratory, professionals must wear necessary personal protective equipment such as a suitable mask and a pocket-sized H₂S sensor (Pro Gasbadge model). The loop operates in an open circuit, with phase recirculation (liquid + gas).

This project conception aimed at reducing environmental impacts by reducing waste for disposal. After each test, the loop was cleaned with biodegradable detergent (Accell Clean Multipurpose) in two stages: the first cleaning step used a served detergent solution followed by cleaning with a new detergent solution. When the solution served reached saturation, it was discarded properly.

3.2 Materials characterization and specimens preparations

In this study, two grades of API carbon steel pipes were used to prepare the specimens used for the experimental tests: API 5L X80 and API 5DP S. The first was used in all experimental tests and the second was used only for the tests related to the cavitation-erosion study. Both

grades were characterized in terms of chemical composition, microstructure and mechanical properties (tensile strength and hardness).

3.2.1 Materials characterization

The chemical composition analyses of both grades were performed by optical spectrometry and via combustion. Optical spectrometry was carried out at an ambient temperature of 21 °C and relative humidity of 69 %, using the Optical Emission Spectrometer Brand ARL Model 3460, according to ASTM E 415/2017 and/or ASTM A 751/2014a and/or ASTM E 1086/2014 standards. The reported standard deviation of the results presented in **Chapter 4** is predominantly associated with the non-uniformities of the tested sample. The analyses via combustion (carbon and sulfur) were carried out at an ambient temperature of 21 °C and relative humidity of 68 %, using a carbon and sulfur Analyzer, LECO Model CS 230.

The microstructural analyses of the specimens were carried out using a Light Optical Microscope (LOM), Olympus BX51M in a bright field and a Field Emission Gun Scanning Electron Microscopy (FEG-SEM), Inspect-F50, operating at 20 kV, with an Everhart Thornley Detector – ETD and a working distance of 10 mm. For these analyses, the steel specimens were submitted to metallographic preparation and were etched with Nital (2 %) for about 10 s. Before the metallographic preparation the surface of the steel specimens was nickel-plated to protect them from bulging during the polishing.

The tensile tests were carried out on two specimens extracted in the longitudinal direction of the pipe samples. The thickness was machined to make it parallel and eliminate surface irregularities resulting from tube curvature. The specimens were machined according to Table D.2 of ISO 6892 with a width of 20 mm and a thickness of 9.4 mm. The starting length of the elongation base (L₀) was 80 mm. The test method followed the ISO 6892, having been led on Instron 300 DX equipment.

The hardness tests were carried out on the test specimens on the Brinell scale with a 5 mm sphere and a load of 750 kgf. The results presented in **Chapter 4** represent the average of five impressions and the respective confidence interval 95 %.

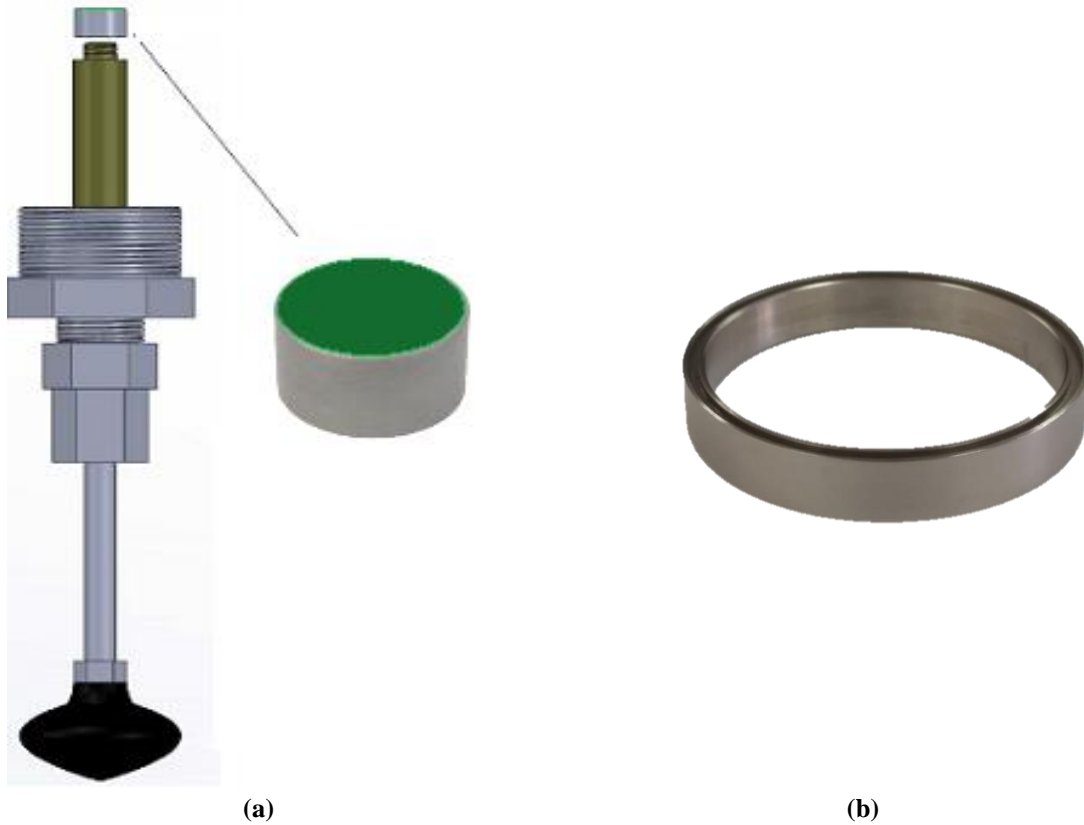
The X-Ray diffraction (XRD) was used to determine the composition of the corrosion-product layers formed during the tests, using Bruker D2 Phaser and Softwares Bruker: Diffraction Measurement e Diffraction Eva. The instrument was operated at 30 kV and 10 mA with Cu-K α radiation ($\lambda = 0.15406$ nm).

3.2.2 Specimen preparation

The test specimens used in the multiphase-flow loop test (**Figure 38a**) were machined from the steel pipe samples to obtain a straight cylinder cup with diameter dimensions of 15.90 mm by 9.5 mm in height and a total surface area of 1,99 cm². For the cavitation-erosion tests, the same type of specimens were used.

For the Rotating Cylinder Electrode (RCE) test (**Figure 38b**), the working electrodes were also machined to obtain a hollow cylinder with an outer diameter of 80 mm and a width of 10 mm, giving a total surface area of 25,13 cm².

Figure 38 - API carbon steel test specimen (a) loop test (b) RCE test.



Before the experiments, the specimens were sandblasted with a glass microsphere (105 μm to 210 μm), promoting a medium roughness (R_a) of 0.45 μm .

This was followed by degreasing in acetone, rinsing with isopropyl alcohol and air-drying. After testing, the samples were retrieved, rinsed with isopropyl alcohol and placed in a desiccator. No additional preparation procedure was used. The surface of the tested specimens were analyzed using energy dispersive X-ray spectroscopy (EDS) or X-ray diffraction (XRD).

For the cavitation-erosion tests, the surface finishing was obtained by grinding with ASTM 600 emery paper.

3.2.3 Corrosion rate from the mass loss measurement

For the multiphase-flow loop tests, cavitation-erosion tests and Rotating Cylinder Electrode tests (RCE), the specimens were weighed before the tests (m_1).

After testing, the samples were rinsed with isopropyl alcohol and dried. For the cavitation-erosion tests the specimen was weighed, and the mass loss was calculated.

For the multiphase-flow loop tests and for RCE tests, the specimens were immersed in Clarke's solution (a combination of hydrochloric acid and inhibitors) for the removal of corrosion products and weighed again (m_2). Then, the mass loss was calculated.

For the multiphase-flow loop tests, the mass loss was used as the test result.

For the RCE tests, corrosion rates were calculated by the following equation¹³⁴:

$$CR = \frac{8.76 \times 10^4 (m_1 - m_2)}{S \times \rho \times t}$$

Where CR is the corrosion rate (mm/year), m_1 and m_2 (g) are the mass of the specimen before and after the removal of corrosion products by the Clake solution, respectively. S (cm²) is the exposed area of the specimens, ρ (g/cm³) is the steel density and t (h) is the testing time.

3.3 Cavitation-erosion testing

In this item, the objective was to establish a performance classification based on the mass loss of API 5L X80 and 5DP S steel drill pipes caused by multiphase-flow-induced corrosion and cavitation. Multiphase-flow-loop tests were conducted using a mixture of 20 % heavy oil (150 cP) + 80 % deionized water, containing 15 % of sodium chloride, at 40 °C under a partial CO₂ pressure of 2.0 bar. Cavitation-erosion tests were performed in deionized water at 40 °C with a horn vibration frequency of 20 kHz. The corrosion and wear resistance was evaluated by measurements of accumulated mass loss, Scanning Electron Microscopy, X-ray Dispersive Energy and X-Ray Diffraction.

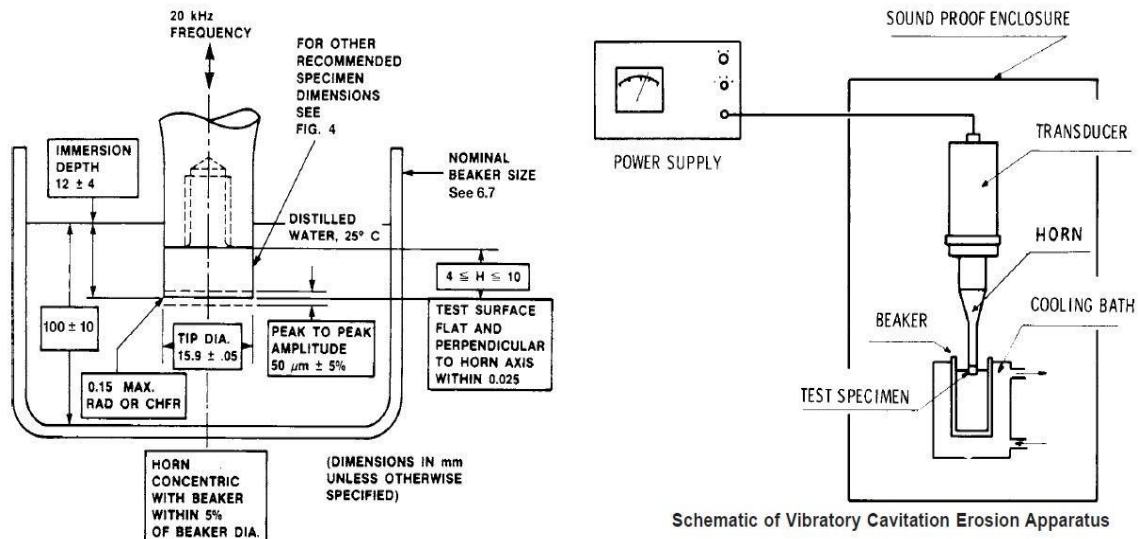
3.3.1 Standard cavitation-erosion test

Cavitation-erosion tests were carried out according to the ASTM G32 standard¹²³. The specimens were maintained 0.5 mm apart from the vibrating horn, as shown in **Figure 39**. The cavitation-erosion tests were conducted in deionized water at 40 °C, to obtain results just related to wear without the influence of the corrosion process.

The vibration frequency of the horn was 20 kHz with a 50 μm peak-to-peak displacement amplitude. The tests were conducted for 30 h with periodical interruptions for registering the dimensions and the mass losses aiming at the obtention of time-variation curves of the cumulative mass loss for both tests.

Each point in the mass loss curves presented in **Chapter 4** corresponds to the average mass loss for each specimen of the three tests performed under the same conditions. Additional cavitation-erosion tests were carried out to identify the wear mechanisms and to assess the evolution of the damage at the surface of the specimens. The surface of the specimens was analyzed by SEM.

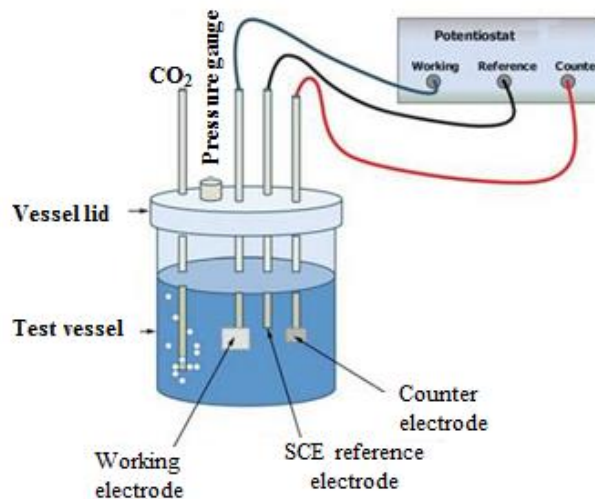
Figure 39 - Schematic view of the cavitation-erosion test equipment¹²³.



3.3.2 Electrochemical Test

Electrochemical tests were carried out without the influence of the wear using deionized water containing 15 % of sodium chloride. The CO₂ partial pressure was maintained at 2.0 bar, the total pressure at 2.5 bar (N₂ balanced) and the temperature at 40 °C. The electrochemical vessel was designed as shown in **Figure 40**.

Figure 40 – Electrochemical cell diagram.



The measurements were performed using a saturated calomel (SCE) reference electrode facing the working electrode. Before each experiment, the working electrodes were abraded with a 600 grit silicon carbide paper, rinsed and sonicated in isopropanol for 5 min. After inserting the working electrode into the test vessel, the solution was purged using dry N₂ gas

up to the point dissolved oxygen content in the experiment was < 10 ppb. Then, the open circuit potential (OCP) was monitored for 50 min or up to a steady-state was reached. The potentiodynamic linear polarization curves were obtained by sweeping the potentials from -20 mV to $+20$ mV around the OCP value at 0.167 mV/s scan rate.

3.4 Autoclave emulsion testing

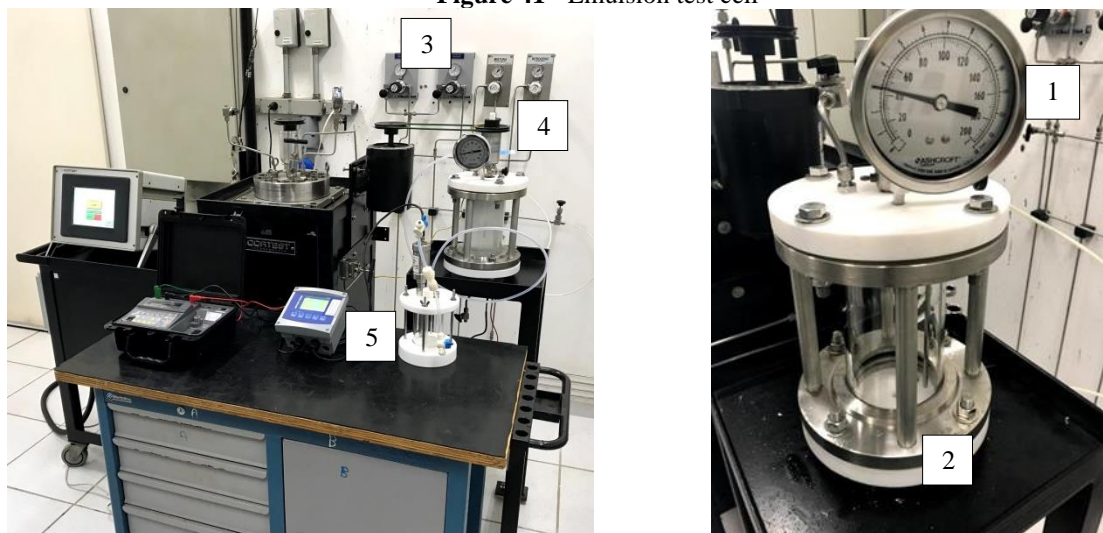
The objective of this item was to study the effect of emulsion formation on steel corrosion in a sweet environment in a laboratory scale. Field experience shows that improper sizing of pipelines in the petroleum industry is often caused by a lack of understanding of three-phase flows which are characterized by a gas phase flowing together with a brine-oil liquid phase.

3.4.1 Emulsification tests

Tests were conducted with the light oil and the heavy oil used in the multiphase-flow test plus a medium crude oil, all of them with a water cut of 80 % at 40 °C for 30 h, under stirring, with a CO_2 pressure of 2.0 bar. For stirring the mixture, an impeller with a rotation of 1200 rpm was used. The adopted stirring represents the mean values of the rotation of the electric motor of the centrifugal pump used in the multiphase-flow corrosion loop^{135,22}.

Figure 41 shows the emulsion test cell (2) which holds up to 3 bar pressure. As can be seen, the cell is provided by gas inlets and outlets (3) to perform conditions similar to those observed in the loop with constant test gas pressure. The system pressure was checked by a manometer (1) and a rotor with magnetic coupling (4) was coupled in order to transmit 1200 rpm to the impeller mounted inside the pressure vessel which was manufactured from a borosilicate tube with Teflon flanges at both ends (2). For guaranteeing the efficiency of O_2 removal, an optical sensor (5) model Mettler Toledo InPro6970i was used. A maximum limit of the oxygen of 10 ppb was adopted. A thermostat with an internal bath was used to maintain the test temperature at 40 °C for 30 h.

Figure 41 - Emulsion test cell



3.4.2 Emulsion microstructure characterization

The microstructures of obtained emulsions both in the loop test and in the emulsion test cell were obtained through a stereomicroscope examination (Leica Fusion Optics M205C).

3.4.3 Analysis of emulsion instability by optical turbidimetry

As emulsions are thermodynamically unstable systems, the dispersed phase can coalesce and flocculate. The formed floccules can sediment or float at the surface. All these processes directly influence the turbidity and the opacity of the emulsion. In this case, it is important to define which destabilization mechanisms are taking place. Thus, immediately after the emulsification cell test is done, the optical turbidimetry studies were performed based on a multiple light scattering method by a TURBISCAN Lab Expert analyzer to monitor the optical properties which allow a more reliable and accurate analysis.

The Turbiscan takes readings at various pre-programmed time intervals and superimposes the curves on a graph to show the emulsion's destabilization. In this work, the scans were scheduled to be done for one day for each hour continuously at 40 °C.

The final result of this analysis is presented by two different graphs, one by a transmitted light (T) profile and the other by a backscattered light (BS) profile. A sample was previously collected from the emulsion cell and placed in a quartz glass cell. The measurements were done by scanning vertically the sample bottle up to the height of 50 mm, for 24 h.

3.5 Rotating cylinder electrode (RCE) testing

The objective of this item was to confirm and to understand one of the results obtained in the multiphase-flow loop tests: a higher corrosion rates in the presence of heavy oil under a partial pressure of 2 bar of CO₂. Higher corrosion rates with heavy oil are not expected according to the literature⁷⁹.

Field experience shows that improper sizing of pipelines in the petroleum industry is often caused by a lack of understanding of three-phase flows which are characterized by a gas phase flowing together with a brine-oil liquid phase. Therefore, understanding the reason for these unexpected results was considered important.

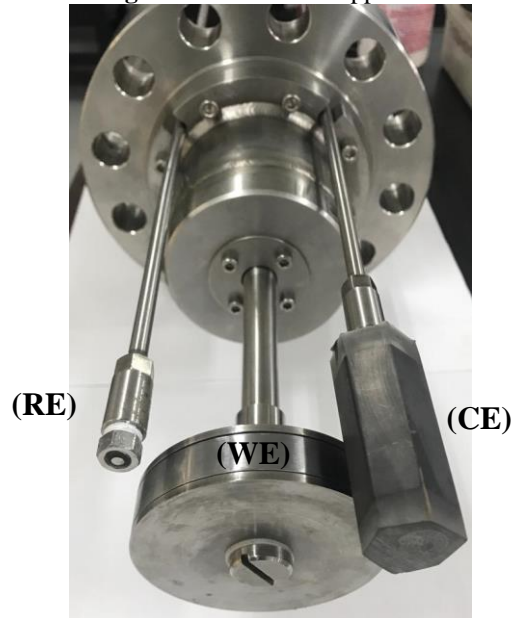
3.5.1 RCE test procedure

The test condition adopted in the RCE tests was the same as the multiphase loop test in which the highest corrosion rate was obtained: brine solution containing 15 % NaCl and 5.5 pH, a temperature of 40 °C and a partial pressure of 2.0 bar of CO₂.

Tests were performed with and without the presence of light crude oil (LO) and heavy crude oil (HO) with a WC of 80 %. For all tests, the open circuit potential (OCP) was monitored, and potentiodynamic linear polarization curves were obtained for estimating the polarization resistance (R_p).

Figure 42 shows the apparatus developed to perform the corrosion experiments conducted with RCE. As one of the objectives of the study was to monitor the system over time, the design of the apparatus focuses on it. Information from the literature^{136,137,138,139} contributed to the design and assembly of the test apparatus.

Figure 42 – RCE test apparatus



RE – Reference Electrode
WE – Work Electrode
CE – Counter Electrode

The test cell consisted of a 5 L autoclave equipped with a saturated calomel reference electrode (SCE) with a platinum electronic bridge (RE) developed in previous work¹⁴⁰; a rotating cylindrical work electrode (WE) made of carbon steel API 5L X80 with 1 cm external diameter and 1 cm height (total exposed area of 25 cm²); and a graphite counter electrode (CE) of 36 cm² area.

A cylindrical counter electrode was not used to envelop the entire working electrode because a graphite cylinder was not available. To overcome this problem, an attempt was made to use a stainless steel cylinder. However, in exploratory tests with CO₂-brine solution + crude oil, it was verified that the internal surface of the stainless steel CE was covered by an oil film, causing a loss of electrical signal in a short time. The signal loss did not occur with the graphite counter electrode, as the adherence of the studied oils was lower on graphite.

The tests were carried out in three different environments:

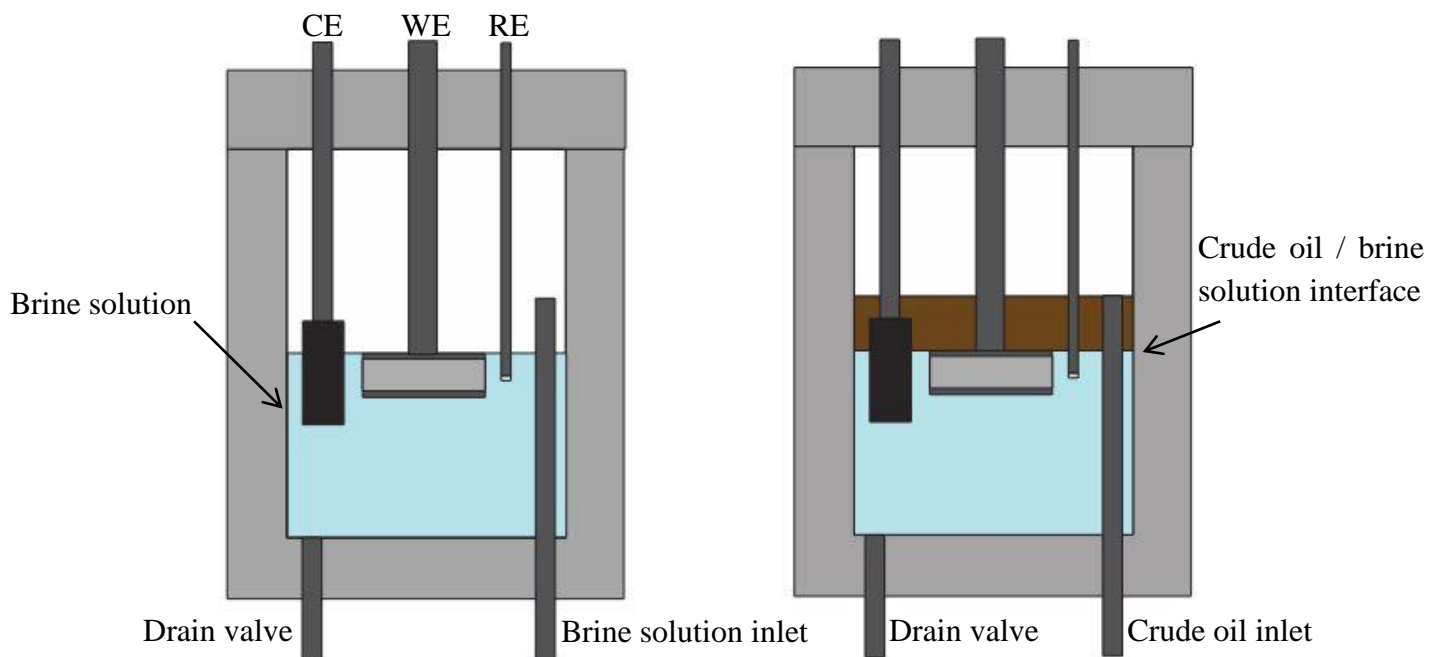
- **CO₂-brine solution:** preliminary tests to validate the experimental apparatus;
- **CO₂-brine-LO and CO₂-brine-HO mixtures:** tests to compare the results among the crude oils and verify the higher aggressiveness of the heavy crude oil.

All the electrodes were installed in the autoclave. Then the autoclave was closed and purged with N₂. In another container, the O₂ of the brine solution was removed with N₂ until a concentration of less than 10 ppb of O₂ was reached. Then, the autoclave was loaded with the deaerated brine solution already saturated with CO₂. This procedure was similar to that adopted in the corrosion loop tests¹²⁷.

For tests with crude oils, the transfer of the brine solution was carried out to prevent the contact of the oil phase with the WE surface before the measurements to avoid errors in the interpretation of results. The simplified scheme is shown in

Figure 43. First, the brine solution was loaded through the inlet tube installed at the bottom of the autoclave until covering the entire WE surface (**Figure 43a**). Then, the oil was loaded using the same inlet tube (**Figure 43b**). Finally, the autoclave was pressurized with 2.0 bar of CO₂.

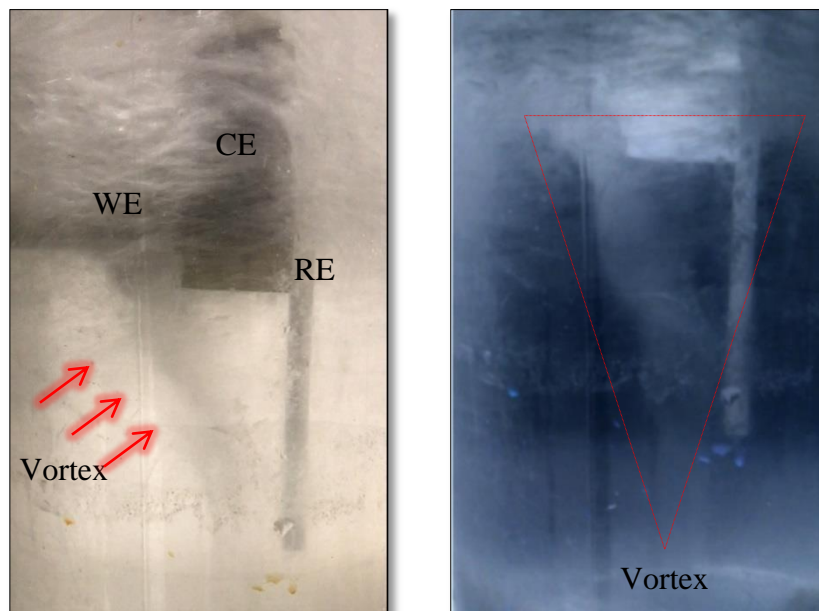
Figure 43 – Schematic illustration of autoclave loading with brine and oil



A vortex was formed around the WE when the rotation was started, as shown in **Figure 44**. In the tests carried out with oil, the formation of the vortex pushed the supernatant oil downwards, partially covering the surface of the WE. The mixing of the oil/brine solution occurred by different mechanisms, as described in the results. For the preliminary tests, three conditions were adopted: without agitation and with RCE rotation velocities of 537 rpm and 1200 rpm. These values were estimated from loop test conditions¹⁴¹. For this, the average velocity of the multiphase flow (2.2 m/s) and the velocity of the liquid pump (1200 rpm) monitored in the corrosion tests in the loop¹⁴² were considered. The calculation is presented in **appendix II**.

For all tests, the monitoring of the open circuit potential (OCP) was started after the stabilization of all test conditions (temperature, CO₂ partial pressure and degree of agitation). During OCP monitoring, linear polarizations of ± 20 mV around OCP were performed every 30 min, with a sweep rate of 0.167 mV/s, to determine the polarization resistance (R_p). The total test duration was 30 h. In the preliminary tests without crude oil, after 30 h, a cathodic polarization curve was obtained starting from + 20 mV vs OCP up to - 1.2 V vs SCE, in an attempt to determine the cathodic current limit for each degree of agitation. In the tests with crude oil (CO₂-brine-crude oil), after 30 h, the WEs were cleaned and weighed. The weight loss was used to estimate the corrosion rate. All the electrochemical measurements were carried out with a Gamry potentiostat/galvanostat/ZRA (Reference 600).

Figure 44 – Vortex formation



CHAPTER 4 – EXPERIMENTAL RESULTS

4.1 Materials characterization

API 5L X80 and API 5DP S steel were used to prepare the test specimens. Both steel grades were characterized by chemical composition, microstructure and mechanical properties (tensile strength and hardness). **Table 4** shows the materials' chemical composition.

Table 4 – Chemical composition (wt. %).

Element (%)	API 5L X 80	API 5DP S grade
Carbon (C)	0.073 ± 0.01	0.29 ± 0.01
Silicon (Si)	-	0.27 ± 0.01
Manganese (Mn)	1.63 ± 0.01	0.78 ± 0.01
Phosphorus (P)	0.012 ± 0.001	0.004 ± 0.001
Sulfur (S)	0.01	0.003 ± 0.001
Chromium (Cr)	-	1.16 ± 0.02
Molybdenum (Mo)	-	0.45 ± 0.01
Nickel (Ni)	-	0.028 ± 0.001
Copper (Cu)	-	0.029 ± 0.001
Aluminum (Al)	-	0.039 ± 0.002
Niobium (Nb)	0.058 ± 0.004	-
Titanium (Ti)	0.026 ± 0.001	-
Vanadium (V)	0.036 ± 0.001	0.045 ± 0.0001

Table 5 shows the mechanical properties of API 5L X80 and API 5DP S grade steels.

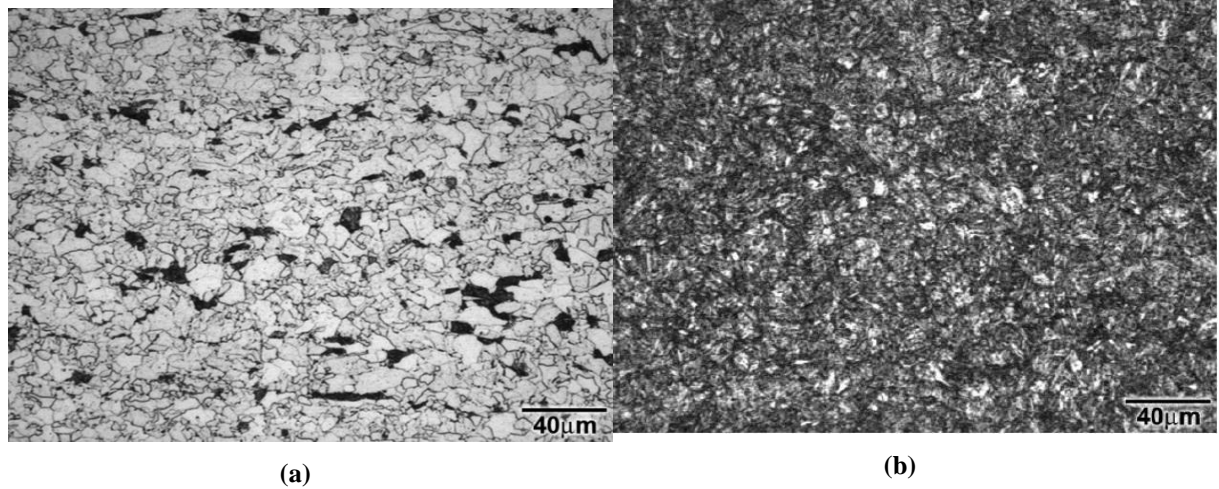
The mechanical properties and chemical composition of both materials are within the ANSI/API Specification 5L and 5DP standards.

Figure 45a displays the API 5L X80 microstructure, revealing ferrite (white area) and pearlite (black region). **Figure 45b** shows a tempered martensite microstructure for API 5DP S grade steel.

Table 5 – Mechanical properties.

Materials	API 5L X80	API 5DP S grade
Yield Strength (MPa)	555	1120
Ultimate tensile strength (MPa)	635	1218
Strain (%)	21.4	16
Hardness (HV)	245	382

Figure 45 – Microstructure of the longitudinal section of (a) API 5L X80 (ferrite + pearlite) and (b) API 5DP S (tempered martensite). Etchant: Nital 2 %.



4.2 Results of Multiphase Flow Loop Testing

The operation of the multiphase flow loop, the liquid phase preparation, and the control of temperature and pressure were established through preliminary tests described in **Chapter 3**.

The test matrix was defined based on the saline water + oil suspension and the degree of agitation of the liquid phase preparation vessel capable of causing a stable oil suspension in the water. The maximum conductivity limit and the agitation range were set at 80 mS/cm and 600 rpm, respectively. This condition was necessary to ensure the proper functioning of the slug flow sensors and the proportion of the liquid phase during the tests. The pressure, temperature, pH, oxygen concentration and sodium chloride concentration are presented in **Table 6**. This table also shows the ratio of the mixtures proposed in the test matrix composed of five tests for light oil (LO) and heavy oil (HO). Gas mixtures are also indicated in **Table 6**.

Table 6 – Matrix of multiphase-flow loop tests.

Controlled Parameters								
Dynamic viscosity LO / HO	NaCl (%)	pH	Flow pattern	Pipe inclination (°)	Pressure/ Temperature (bar /°C)	WC (%)	Flow rate liquid phase (m ³ /h)	Flow rate gas phase (m ³ /h)
10 cP / 150 cP	15	5.5	Slug	0 and 45	2.5 / 40	80	3.5	9.0
Partial pressure in gas phase (LO)				Partial pressure in gas phase (HO)				
Tests	P_{N_2}	P_{CO_2}	P_{H_2S}	Tests	P_{N_2}	P_{CO_2}	P_{H_2S}	
T1	2.0	0.5	0.0	T1	0.0	0.5	0.0	
T2	0.5	2.0	0.0	T2	0.5	2.0	0.0	
T3	1.995	0.5	0.05	T3	1.995	0.5	0.005	
T4	0.495	2.0	0.05	T4	0.495	2.0	0.005	

The gases were specified and obtained with ready-mix bottling in appropriate cylinders in proportions of CO₂ and H₂S balanced with nitrogen (N₂). Each test condition mentioned in the matrix of **Table 6** lasted 30 h.

4.2.1 Monitored parameters

Table 7 and **Table 8** show the mean values of the monitored parameters near the test section of each proposed condition for LO and HO, respectively. By identifying the size of the bubble passing through the sensing module as a measure close to the film length shown in **Figure 14**, the velocity was calculated by the inflow and outflow time of the bubble and the frequency was calculated by the number of bubbles passing through the sensor in a unit of time (Hz).

Table 7 – Monitored parameters for tests performed with light oil.

Light oil		Monitored slug data						Process data			
		Size (m)		Velocity (m/s)		Frequency (Hz)		Pressure (bar)		Temperature (°C)	
		Avg.	STDE V	Avg.	STDE V	Avg.	STDE V	Avg.	STDE V	Avg.	STDE V
T1	0°	0.44	0.34	1.44	0.38	2.90	0.43	2.61	0.19	39.3	2.0
	45°	0.47	0.17	1.94	0.42	2.47	0.29	2.54	0.19	37.7	1.8
T2	0°	0.43	0.17	1.38	0.26	2.91	0.49	2.61	0.15	39.4	2.3
	45°	0.69	0.21	1.31	0.28	2.06	0.31	2.54	0.14	37.9	1.8
T3	0°	0.74	0.39	2.82	0.59	3.07	0.72	2.64	0.08	38.70	0.59
	45°	0.75	0.17	2.77	0.74	2.75	0.69	2.55	0.08	37.02	0.56
T4	0°	1.01	0.26	2.76	0.55	2.16	0.27	2.63	0.06	42.08	0.70
	45°	0.93	0.25	3.55	0.77	2.59	0.41	2.56	0.06	39.95	0.64

Table 8 – Monitored parameters for performed with heavy oil.

Heavy oil		Monitored slug data						Process data			
		Size (m)		Velocity (m/s)		Frequency (Hz)		Pressure (bar)		Temperature (°C)	
		Avg.	STDE V	Avg.	STDE V	Avg.	STDE V	Avg.	STDE V	Avg.	STDE V
T1	0°	0.94	0.75	2.23	0.67	3.22	0.60	2.31	0.27	41.3	1.1
	45°	0.40	0.25	1.82	0.45	2.83	0.82	2.17	0.28	41.2	1.1
T2	0°	0.50	0.22	2.06	0.42	3.35	0.70	2.49	0.24	40.6	2.5
	45°	0.40	0.13	2.07	0.61	2.73	0.73	2.40	0.25	40.1	2.9
T3	0°	0.51	0.22	2.19	0.50	3.33	0.55	2.72	0.08	43.1	2.7
	45°	0.48	0.19	2.64	0.69	4.10	0.74	2.59	0.08	41.2	2.3
T4	0°	0.75	0.23	2.53	0.60	2.87	0.60	2.47	0.15	42.0	2.6
	45°	0.34	0.10	2.31	0.64	3.14	0.89	2.36	0.14	40.3	2.0

Thus, the calculated values do not exactly represent the actual frequency but may serve as a good reference to explain mainly the hydrodynamic effects. The obtained mean frequency values are within the predicted values in the conceptual design (1 Hz to 5 Hz).

To verify the flow behavior in the LO and HO tests, a distribution of the average slug size as a function of the pipe diameter was plotted to simplify the understanding of the parameters monitored during the tests. The results are shown in **Figure 46** and **Figure 47**. Observing the graphs of the average slug size in the first two conditions (without H₂S) for the light oil, an increase in the average size of the bubbles can be seen with the increase in the partial pressure of CO₂ at the test position 45°. The mean bubble size values at the 0° position were smaller than at the 45° position. In the third and fourth test conditions (with H₂S), there was also an increase in the size of the bubbles with the increase in the partial pressure of CO₂ at the two test positions 0° and 45°. We can also verify that there is a tendency to increase the size of the bubbles with the addition of H₂S for the two positions 0° and 45°.

For the heavy oil, we observed that with the increase in the partial pressure of CO₂ and the presence of H₂S, the size of the bubbles at the 0° position became larger. On the other hand, the size distribution is similar for the first and second conditions.

Figure 46 - Normal distribution for the LO tests.

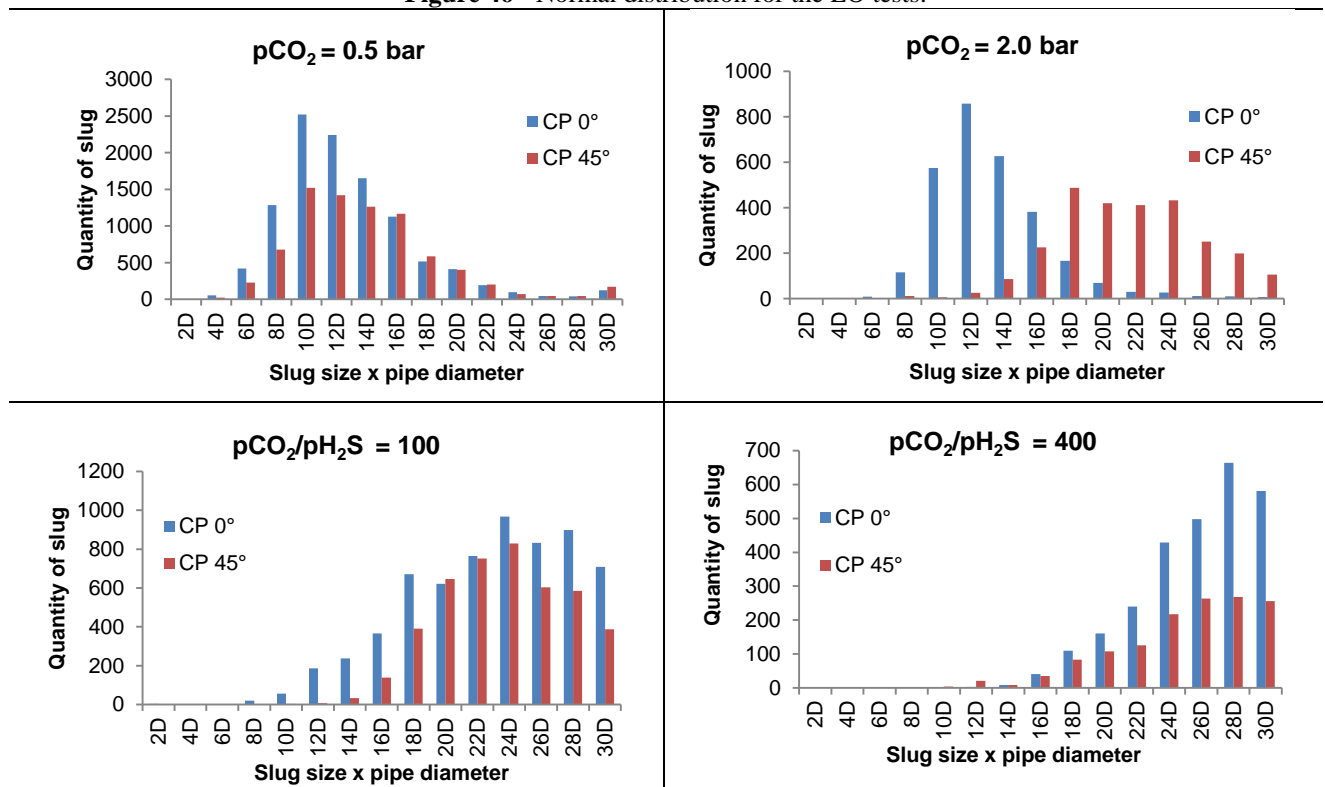
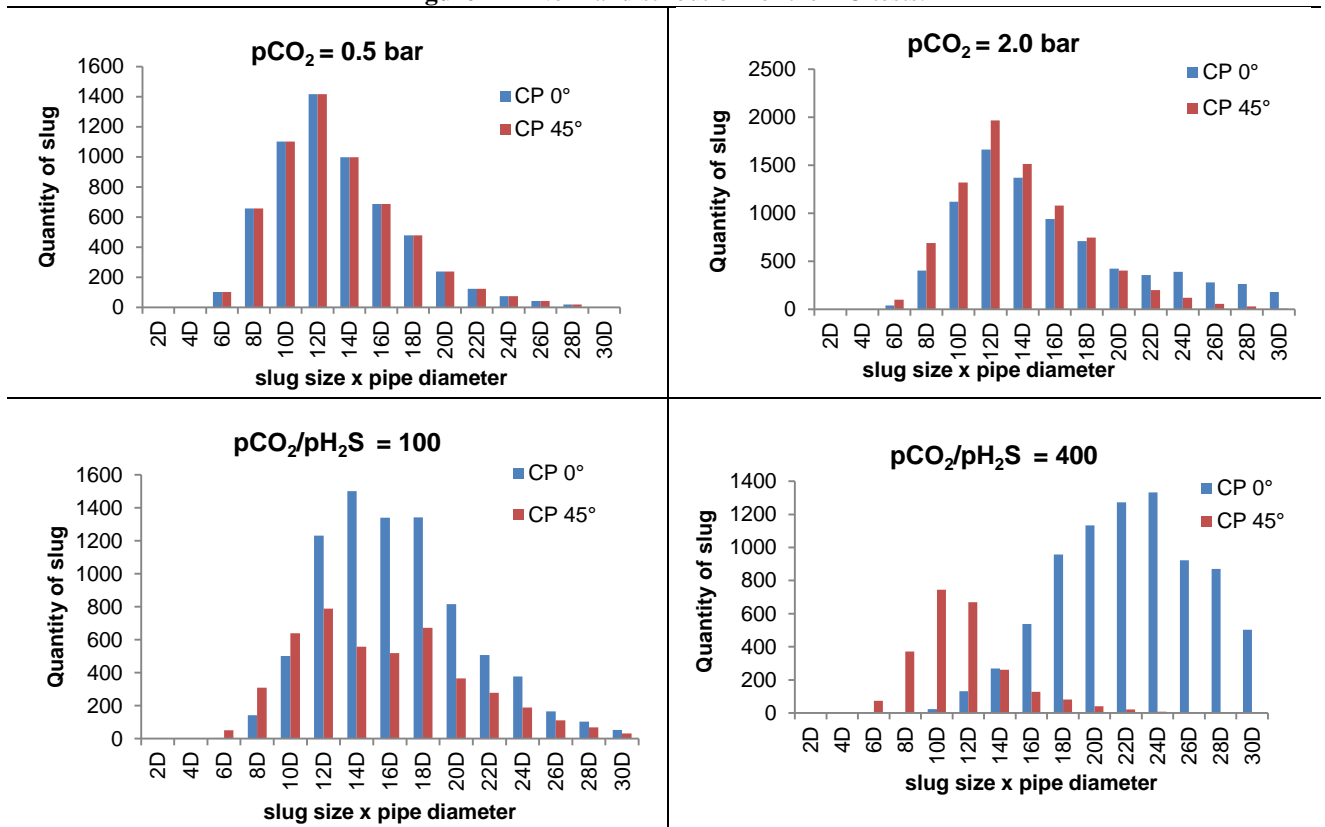


Figure 47 - Normal distribution for the HO tests.



4.2.2 Test results

After 30 h of tests, the loop was emptied and the test specimens were removed. The visual observation of the specimens and the liquid phase of the tested environment showed an emulsion formation for all test conditions of the test matrix. The test specimens were cleaned as described in Chapter 3, and the weight loss was determined.

The obtained weight loss measurements in CO_2 and CO_2/H_2S containing environments are presented in **Figure 48** and **Figure 49**, respectively.

Figure 48 shows that, in a CO_2 -containing environment, as expected, the higher the partial pressure of CO_2 , the higher the weight loss for both tested oils. However, the weight loss was significantly higher in heavy oil than in light oil, which is unexpected.

Comparing the weight loss at horizontal (0°) and inclined (45°) positions of the tests performed with the light oil, higher values for the inclined position were verified. For tests performed with heavy oil, the weight loss values were higher for the horizontal than the inclined position. This behavior was maintained even with the increase of the CO_2 partial pressure.

A significant difference was observed when H_2S was added to the tested environment (**Figure 49**). The influence of the type of oil was also noticed; however, in this case, higher values were obtained with light oil, but the differences among the oils were lower. The influence of

the position of the test specimens was also different. In the presence of H₂S, the weight loss was higher at the horizontal (0°) than at the inclined (45°) for both crude oils.

Figure 48 - Multiphase flow-induced corrosion rate in the presence of CO₂.

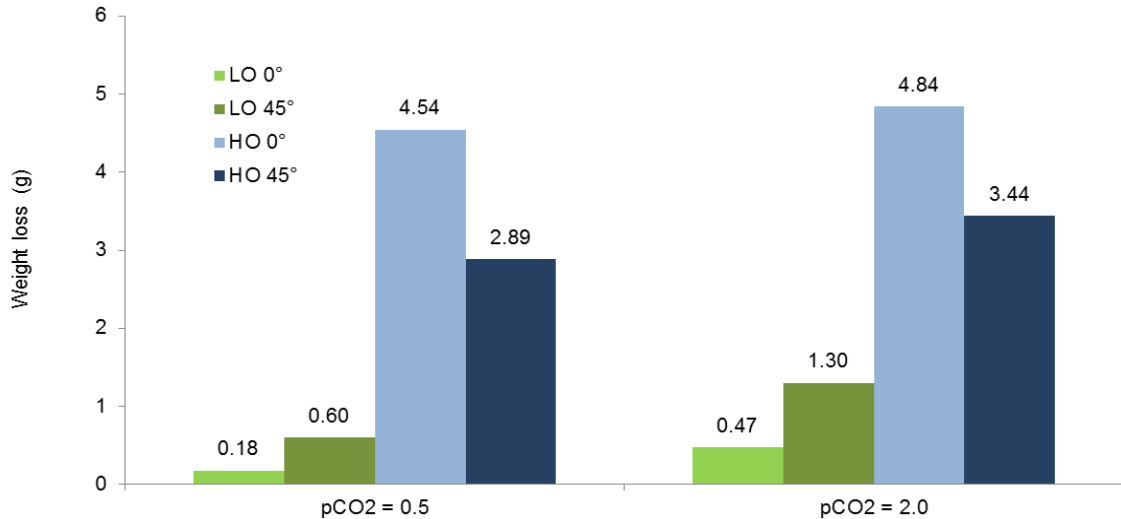


Figure 49 - Multiphase flow-induced corrosion rate in the presence of CO₂ with traces of H₂S.

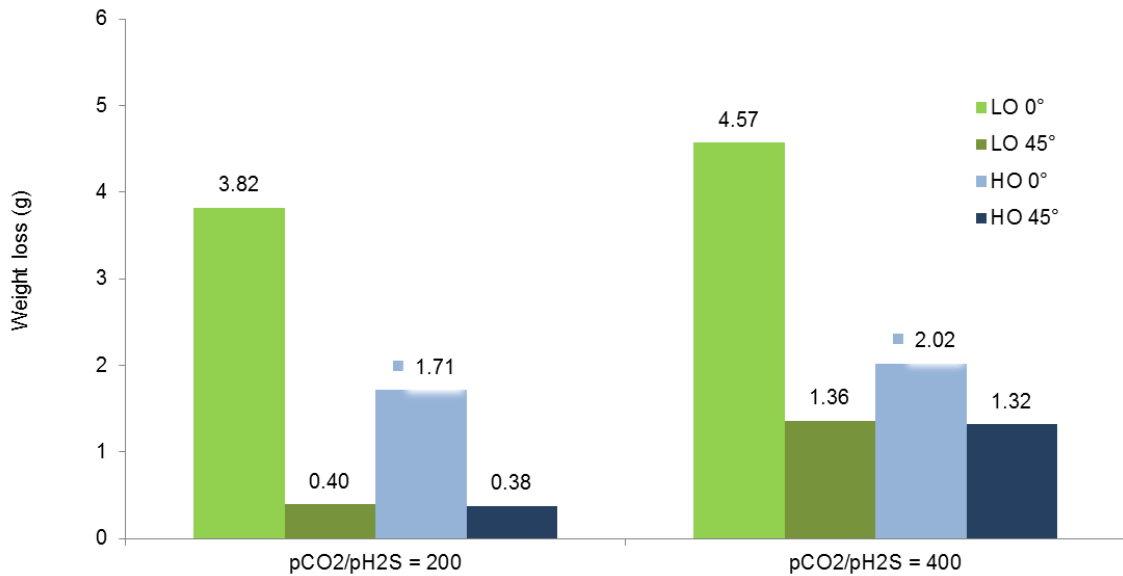


Table 9 shows the surface appearance of the specimens immediately after the tests in light and heavy oil.

Table 10 and **Table 11** show SEM and optical microscopic (OM) images of specimens tested in light and heavy oil, respectively. The specimens' surfaces were previously degreased by rinsing with isopropyl alcohol and dried. SEM images were also obtained after additional pickling in Clarke's solution.

Table 9 – Appearances of the surfaces of the specimens tested in the presence of LO and HO immediately after the tests.

T1 test (0.5 bar CO ₂ containing environment)			
0°	45°	0°	45°
LO	LO	HO	HO
			
T2 test (2 bar CO ₂ containing environment)			
0°	45°	0°	45°
LO	LO	HO	HO
			
T3 test (CO ₂ /H ₂ S = 100 containing environment)			
0°	45°	0°	45°
LO	LO	HO	HO
			
T4 test (CO ₂ /H ₂ S = 400 containing environment)			
0°	45°	0°	45°
LO	LO	HO	HO
			

Table 10 – SEM images and appearance of the surfaces of the specimens tested in LO after cleaning.

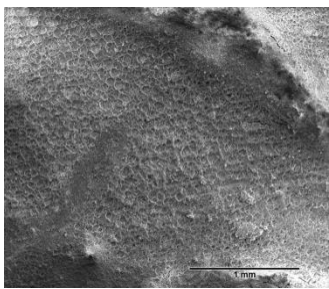
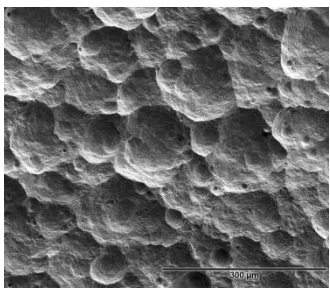

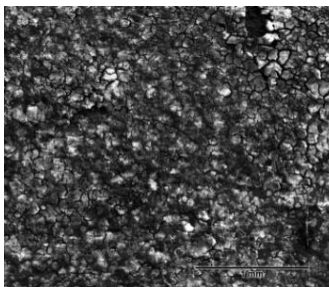
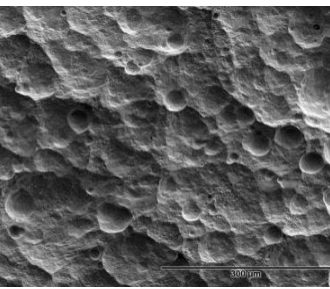

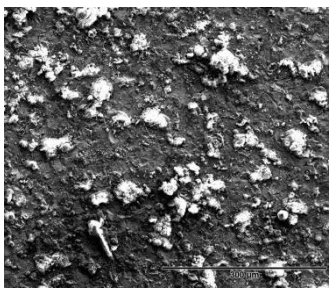
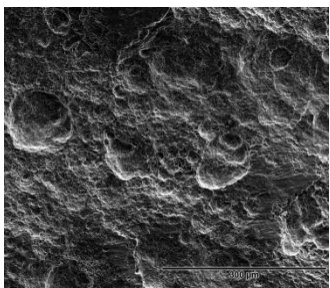

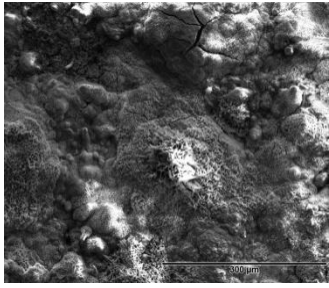
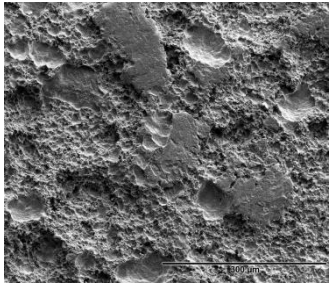

Position	SEM		OM
	After rinsing with isopropyl alcohol and dried	After pickling in Clarke's solution (most attacked region)	After pickling in Clarke's solution
T1 (0.5 bar CO ₂)			
0°	 (a)	 (b)	 (c)
45°	 (d)	 (e)	 (f)
T2 (2 bar CO ₂)			
0°	 (g)	 (h)	 (i)
45°	 (j)	 (k)	 (l)
T3 (pCO ₂ /pH ₂ S=100)			

Table 10 – SEM images and appearance of the surfaces of the specimens tested in LO after cleaning.

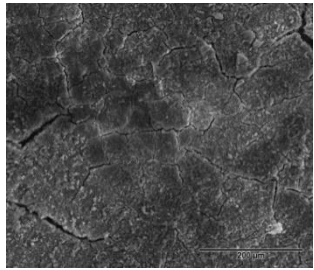
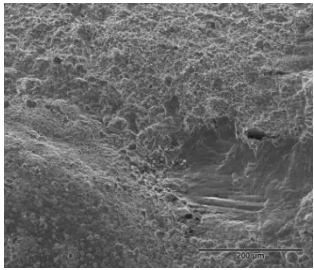

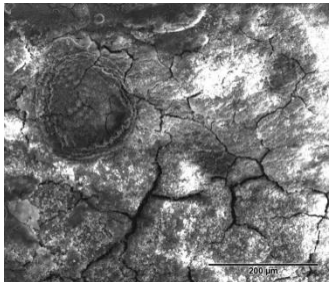
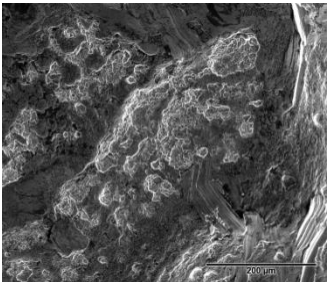

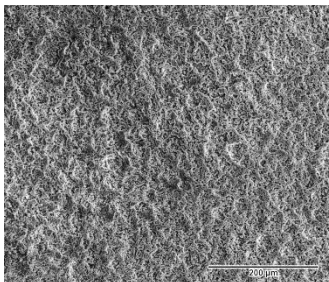
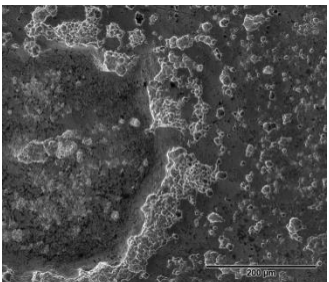

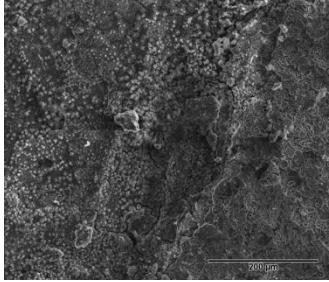
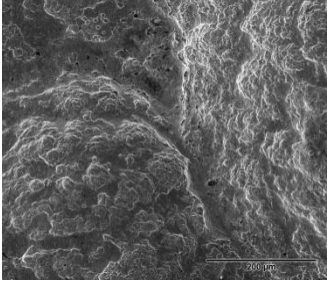

Position	SEM		OM
	After rinsing with isopropyl alcohol and dried	After pickling in Clarke's solution (most attacked region)	After pickling in Clarke's solution
0°	 (m)	 (n)	 (o)
45°	 (p)	 (q)	 (r)
T4 (pCO ₂ /pH ₂ S=400)			
0°	 (s)	 (t)	 (u)
45°	 (v)	 (x)	 (z)

Table 11 – SEM images and appearance of the surfaces of the specimens tested in HO and after cleaning.

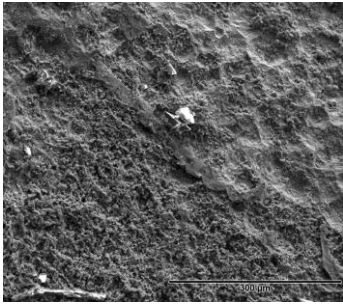
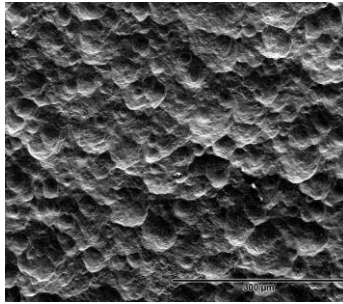

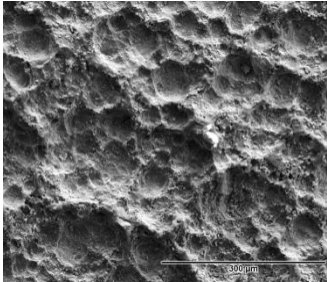
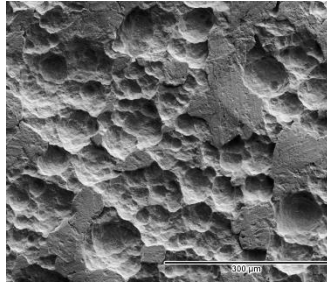

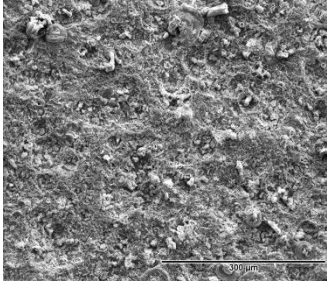
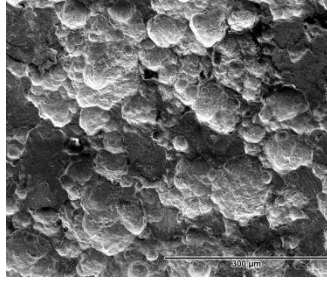

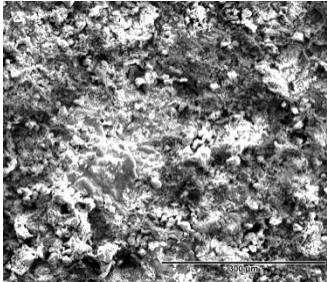
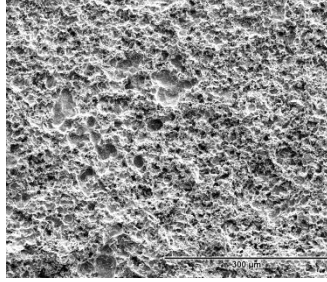

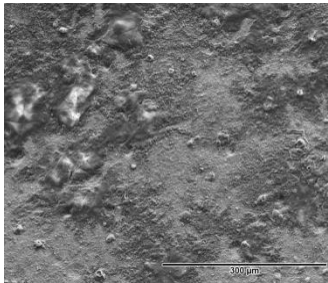
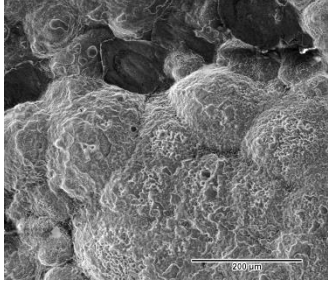

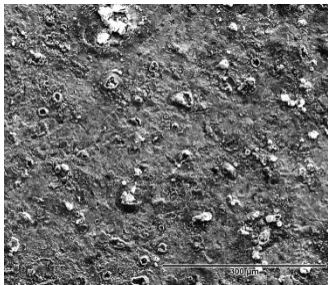
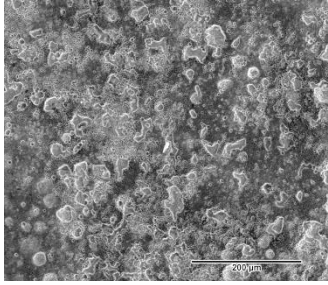

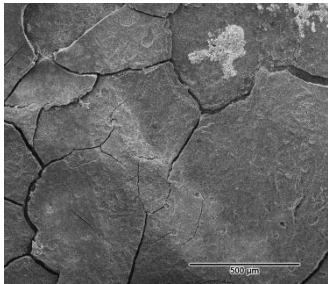
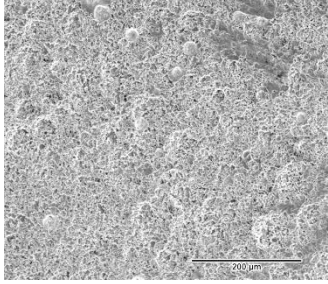

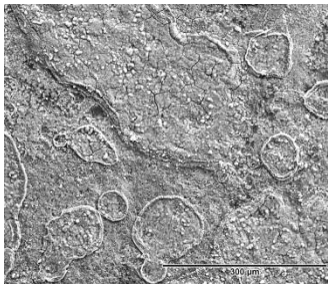
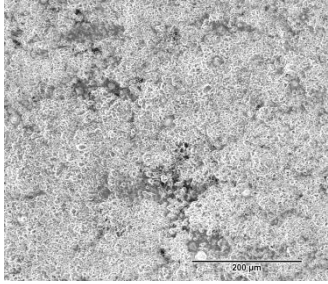

Position	SEM		OM
	After rinsing with isopropyl alcohol and dried	After pickling in Clarke's solution (most attacked region)	After pickling in Clarke's solution
T1 (0.5 bar CO ₂)			
0°	 (a)	 (b)	 (c)
45°	 (d)	 (e)	 (f)
T2 (2 bar CO ₂)			
0°	 (g)	 (h)	 (i)
45°	 (j)	 (k)	 (l)
T3 (pCO ₂ /pH ₂ S=100)			

Table 11 – SEM images and appearance of the surfaces of the specimens tested in HO and after cleaning.

Position	SEM		OM
	After rinsing with isopropyl alcohol and dried	After pickling in Clarke's solution (most attacked region)	After pickling in Clarke's solution
0°	 (m)	 (n)	 (o)
45°	 (p)	 (q)	 (r)
T4 (pCO ₂ /pH ₂ S=400)			
0°	 (s)	 (t)	 (u)
45°	 (v)	 (x)	 (z)

For light oil tests in the CO₂-containing environment, no oily film was observed on the specimen surfaces (**Table 9**). After cleaning in isopropyl alcohol, it was found that the surface of the specimens had been attacked non-uniformly at the horizontal position (0°) and more

uniformly at the inclined position (OM images of **Table 10**). In the CO₂/H₂S-containing environment, a non-adhered oily film was observed on the surface of the specimens (**Table 9**). After cleaning in isopropyl alcohol, it was found that the surface of the specimens had been attacked non-uniformly at both positions (OM images of **Table 10**).

A detailed observation of the SEM images of **Table 10** (after cleaning in isopropyl alcohol) shows that a thin, non-adherent layer was formed on all specimens tested in light oil. EDS analyses of the specimens' surface were conducted in the areas with the most deposited products. The detected elements carbon, sulfur, chlorine, and sodium come from the solution, and iron, aluminum, silicon, manganese, copper, molybdenum, titanium, and vanadium come from the tested steel. Chromium and nickel come from the stainless-steel components used in the loop construction. XRD analyses were performed only on the **T3** test specimens, both at the horizontal (0°) and inclined (45°) positions, because they were the only ones tested in the light oil that presented sufficient corrosion products. The results obtained from this analysis were NaCl from the test solution, iron from the test specimen material, and akaganeite (β-eOOH), typical iron oxide formed in environments with chlorides. SEM images obtained after pickling the specimens tested in the CO₂-containing environment (**Table 10**) show the presence of concavities typical of the strong hydrodynamic effect associated with corrosion at both horizontal and inclined positions.

For heavy oil tests in the CO₂-containing environment, an oily tick film was observed on the surface of all specimens (**Table 9**). After removing this film in isopropyl alcohol, significant surface damage was observed on the surface of specimens tested in CO₂ and CO₂/H₂S-containing environments (OM images of **Table 11**). In the presence of the CO₂-containing environment, the surface attack was more uniform; however, the thickness loss was so high at the horizontal (0°) position that the useful thickness of the specimen was consumed, confirming the highly increased mass loss of **Figure 48**.

From **Table 11** (heavy oil), the SEM images of the specimen surfaces, obtained after the removal of the oil film in isopropyl alcohol, allowed showing a few products deposited on most of the surface of the specimens in a non-homogeneous manner. EDS analyses of the specimens' surfaces were performed in the areas with the most deposited products. The results showed the presence of elements such as sodium, chlorine and sulfur that came from the test environment. Iron, aluminum, silicon, manganese, copper, molybdenum, titanium, and vanadium, which are elements from the API 5L X80 steel, were also detected. The detected chromium and nickel are derived from part of the AISI 316 stainless-steel components used for the loop construction.

From the images obtained of the pickled surface of the specimens tested in the CO₂-containing environment with HO (**Table 11**), the same concavities as for the LO were detected, indicating the strong hydrodynamic effect associated with corrosion at both horizontal and inclined positions.

4.2.3 Discussion

The evaluation of the corrosion process influenced by the multiphase flow is a complex matter, especially when we adopt conditions representative of those observed in the field, including the use of crude oil in the experiments, as in the case of this work. The current practices in laboratory studies involve using an aqueous phase without crude oil. Probably, for this reason, several significant and unexpected results were obtained in the tests performed in the constructed multiphase-flow loop.

In the presence of CO₂, the results showed extremely high weight loss for the HO, much higher than for the LO, which is unexpected. Another unexpected result was the differences in the influence of the horizontal and inclined positions: a higher weight loss was observed at the 45° position for the LO. In contrast, a significantly higher weight loss for the HO was observed at the 0° position. A hypothesis can be made based only on the results of the LO attributing the higher weight loss at the inclined position to the distribution of the gravitational forces, the friction, and the acceleration involved in the slug flow pattern. However, this explanation cannot be applied to the HO.

Another point of attention related to the results obtained in tests conducted in the CO₂-containing environment was the presence of concavities on all surfaces of the tested specimens. In this case, such surface damages may be attributed to the collapse of the dispersed bubbles characteristic of the slug flow pattern. The density of those dispersed bubbles increases with increasing CO₂ partial pressure. This fact explains the higher weight loss for the higher partial pressure value. This observation is in agreement with the literature reports^{38, 24, 39, 117}.

Finally, the presence of the oily tick film with HO and the absence of visible oily film with LO on the surface of the specimens tested in the CO₂-containing environment indicate a difference in emulsion formation processes worth to be studied.

Therefore, we conducted additional studies to understand these unexpected results obtained in the CO₂-containing environment and to confirm the strong hydrodynamic effect associated with corrosion and the possibility of different emulsion formation processes with the LO and HO.

The influence of the oil type was also noticed in the CO₂ and H₂S-contained environments. Higher weight loss values were obtained for the tests with LO because the weight loss values of the specimens tested with this oil increased in the presence of H₂S, and with the HO, these values decreased, resulting in higher corrosion rates for the tests with LO. Additionally the influence of the specimen position also changed in the presence of H₂S. Both crude oils presented higher corrosion rate at the 0° position.

All the differences observed in the presence of H₂S revealed that different mechanisms might act in the absence and presence of H₂S. Therefore, complementary studies are also necessary

to understand the influence of H₂S. However, specific studies on this topic were not carried out in this work and will be considered for future projects.

4.2.4 Consolidation

Unexpected results and interesting behavior were obtained in tests conducted with the multiphase-flow loop in the CO₂-containing environment, which were: significantly higher corrosion rate of API 5L X80 steel grade in the presence of HO than LO; higher weight loss at the horizontal position with HO, in contrast to the lower values with LO at the same position; formation of concavities on the specimen surfaces in all tested conditions; and the formation of emulsion with both oils. To understand all these results, specific studies were developed as follows:

- corrosion-erosion testing to verify the cavitation and erosion resistance of the tested API 5L X80 steel grade in comparison with the API 5DP S, a high cavitation-erosion resistant steel grade (**item 4.4**);
- autoclave emulsion testing to verify the type of emulsion formation processes of the two tested oils, which may explain the unexpected high weight loss values obtained in the presence of heavy oil (**item 4.5**);
- the rotating cylinder electrode tests accompanied with electrochemical measurements attempting to elucidate the influence of the type of emulsion formation on the weight loss of the API 5L X80 steel grade in the presence of LO and HO (**item 4.6**).

Additionally, prediction models for the multiphase-flow loop under the studied conditions were obtained to facilitate the establishment of test matrixes for future studies within the range of the test conditions established in the present work (**item 4.3**).

A significant difference was observed when H₂S was added to the CO₂-containing environment. The weight loss values of tests with LO increased and with HO decreased in the presence of H₂S; the horizontal position presented the highest weight loss with LO and with HO; and emulsion formation occurred with both oils. This work did not conduct specific studies to understand these differences and will be considered for future projects.

4.3 Prediction models for multiphase-flow-induced corrosion of API X80 steel in CO₂/H₂S environment

The main objective of this topic is to establish models that can predict corrosion intensity based on the experimental results obtained from multiphase-flow loop tests, according to **item 4.2**.

The experimental data were analyzed using multiple regression and Box-Cox transformation for linear regression. These equations allowed for making damage predictions and optimizing of matrix parameters for the loop tests. The following symbols were used in the statistical analyses:

μ	Oil dynamic viscosity (cP)
α	Inclination (°)
p	CO ₂ partial pressure (bar)
P_{H_2S}	H ₂ S partial pressure (bar)
P_{N_2}	N ₂ partial pressure (bar)
CR	Corrosion rate (mm/year)
SBS	Slug-Bubble Size (m)
SBV	Slug-Bubble Velocity (m/s)
SBF	Slug-Bubble Frequency (Hz)

Table 12 presents all the results of the loop test matrix again. In this case, the weight loss values were converted in the corrosion rates in mm/year. The independent variables were codified to facilitate the statistical analyses, as shown at the end of **Table 12**.

Table 12 – Multiphase flow loop tests.

Experimental results of the test matrix, in original units of variables									
Dynamic viscosity LO/HO	NaCl (%)	Flow pattern	Pipe inclination (°)	Pressure / Temperature (bar /°C)		WC (%)	Flow rate liquid phase (m ³ /h)	Flow rate gas phase (m ³ /h)	
10 cP / 150 cP	15	Slug	0° e 45°	2.5 / 40		80	3.5	9.0	
Test code	CR	μ	α	SBS	SBV	SBF	P_{N_2}	P_{CO_2}	P_{H_2S}
LOT1	1.27	10	0	0.295	1.955	2.849	2.5	0.0	0.0
	4.63		45	0.386	1.882	3.204			
LOT2	9.25	10	0	0.275	1.896	2.680	2.0	0.5	0.0
	30.7		45	0.716	3.101	3.605			
LOT3	24.46	10	0	0.444	1.437	2.904	0.5	2.0	0.0
	66.92		45	0.887	2.226	3.206			
LOT4	178.39	10	0	0.474	1.941	2.474	1.995	0.5	0.005
	109.91		45	0.397	1.822	2.826			
LOT5	112.27	10	0	0.432	1.377	2.912	0.495	2.0	0.005
	77.22		45	0.497	2.063	3.354			
HOT1	104.86	150	0	0.687	1.309	2.063	2.5	0.0	0.0
	31.83		45	0.404	2.073	2.730			
HOT2	218.76	150	0	0.955	2.744	2.215	2.0	0.5	0.0
	139.13		45	0.506	2.188	3.335			
HOT3	251.66	150	0	0.753	2.897	2.364	0.5	2.0	0.0
	178.06		45	0.476	2.640	4.095			
HOT4	93.34	150	0	1.121	3.007	2.229	1.995	0.5	0.005

Experimental results of the test matrix, in original units of variables										
Dynamic viscosity LO/HO	NaCl (%)	Flow pattern	Pipe inclination (°)	Pressure / Temperature (bar /°C)			WC (%)	Flow rate liquid phase (m ³ /h)	Flow rate gas phase (m ³ /h)	
10 cP / 150 cP	15	Slug	0° e 45°	2.5 / 40			80	3.5	9.0	
Test code	CR	μ	α	SBS	SBV	SBF	P_{N_2}	P_{CO_2}	P_{H_2S}	
	20.51		45	0.749	2.527	2.875				
HOT5	107.02	150	0	0.992	3.737	2.326	0.495	2.0	0.005	
	69.65		45	0.336	2.311	3.136				
Coded units of variables										
Original unit of variables	μ (cP)		α (°)		P_{CO_2} (bar)			P_{H_2S} (bar)		
Coding	$x_1 = (\mu - 80)/70$		$x_2 = (\alpha - 22.5)/22.5$		$x_3 = P_{CO_2} - 1$			$x_4 = (P_{H_2S} - 0.0025)/0.0025$		
Levels	10	150	0	45	0	0.5	2	0	0.005	
Coded variables	-1	+1	-1	+1	-1	-0.5	1	-1	+1	

The investigation was carried out using Multiple Regression to determine the relationship of the dependent variables (response variables) to independent variables (input variables), whose analysis was made from two tables resulting from the Multiple Regression, the first with the regression parameters and the second with the analysis of variance. The table with the regression parameters shows important columns that describe the prediction model, the standard error of each coefficient, and the p-value, which gives the significance level for each model term.

Generally, the term is considered significant for a p-value less than or equal to 0.05, i.e., the null hypothesis is rejected. If the p-value exceeds 0.10, the term should be removed from the model¹⁴³.

The regression ANOVA indicates the importance of the parameters to the model based on the residual error. The analysis includes the determination coefficients presented as R^2 and R^2 (*adj*). These values indicate the proportion of process variability that the model contemplates. R^2 (*adj*) is adjusted for degrees of freedom (*DF*), i.e., it considers the sample size.

The multiphase-loop test results were statistically analyzed to estimate the principal and two-factor interaction effects in the test conditions. The response variables were the corrosion rate, slug-bubble size, velocity, and frequency. The independent variables selected were the dynamic viscosity of the oil (x_1 codified), the inclination of the tube where corrosion coupons were installed (x_2 codified), and CO₂ (x_3 codified) and H₂S (x_4 codified) partial pressures. For these analyses, multiple regression and Box-Cox transformation methods were applied using the Minitab 19 software (academic version)^{144, 145}.

The Box-Cox transformation procedure is often used to modify the distributional shape of the response variable so that the residuals are normally distributed. This is done so that tests and confidence limits, which require normality, can more appropriately be used.

Attention should be paid to data that contain outliers that this technique may not adequately adjust¹⁴⁵. The advantages of the transformation can be observed by a decrease in values of the mean squares, maintaining the same *DF* for the analysis of variance of the untransformed and reciprocally transformed models. To show the effect of transformation, the *F-values* must be compared. The *F-value* is the statistic test used to determine whether the term is associated with the response from the model¹⁴⁶.

For the Box-Cox transformation, the lambda (λ) values is used for the maximum likelihood estimation. Typically, the interval for this parameter is set from -1 to +1. Several regressions were performed with different λ to determine its optimum value. In this study, the best λ was 0.5. It is desired that the transformation simplifies the model and makes it more relevant and interpretable.

4.3.1 Corrosion rate as a function of oil viscosity, pipe inclination and CO₂ and H₂S partial pressure

The analysis of multiple regressions, using the codified independent variables, for predicting the corrosion rate is presented in **Table 13** and **Table 14**. This model gave an R^2 of 94.11 % and $R^2(adj)$ of 86.01 %, which are the percentage of variation in the response that the model explains.

The analysis of the coefficient presented in **Table 13** is usually an excellent way to assess the practical significance of a term's effect on the response variable. Using the measures of the standard error of the coefficient (*SE*), we can define the precision of the estimated value. The smaller the standard error, the more precise the estimated value. Therefore, by dividing the coefficient by its standard error, we obtain the *t-value*. The closer *t-values* are to zero, the lower the significance of the coefficient values. The *p-values* are related to the *t-values* and can also be used to verify the significance of the terms. The analysis of variance (*ANOVA*) of the model is shown in **Table 14**.

Table 13 – Regression parameters for the multiple regression of CR

Coefficients				
Terms	Coefficient	SE Coefficient	t-value	p-value
Constant	130.4	16.1	8.12	0.000039
x_1	20.14	6.23	3.23	0.012002
x_2	-20.28	6.23	-3.26	0.011609
x_3	34.0	10.7	3.20	0.012704
x_4	-6.10	7.18	-0.85	0.420697 (*)
x_3^2	-53.5	23.2	-2.31	0.049591

Table 13 – Regression parameters for the multiple regression of CR

Coefficients				
Terms	Coefficient	SE Coefficient	t-value	p-value
x_1x_2	-15.01	6.10	-2.46	0.039159
x_1x_3	22.86	7.51	3.04	0.015991
x_1x_4	-49.26	6.41	-7.68	0.000059
x_2x_3	7.05	7.51	0.94	0.375637 ^(*)
x_2x_4	-8.20	6.41	-1.28	0.236887 ^(*)
x_3x_4	-13.27	9.09	-1.46	0.182267 ^(*)

^(*) No statistically significant because the p-values are higher than the minimum acceptable value of 0.10.

Table 14 – Analysis of Variance for the CR regression.

ANOVA	DF	Sum of Squares (Adjusted)	Mean Square (Adjusted)	F-value	p-value
Regression	11	94936	8630.5	11.62	0.000922
Error	8	5944	743.0	-	-
Total	19	100880	-	-	-

Therefore, in **Equation 2**, the terms which presented a p-values higher than 0.1 (**Table 13**) were removed.

Equation 2

$$CR = 130.4 + 20.14x_1 - 20.28x_2 + 34x_3 - 53.5x_3^2 - 15.01x_1x_2 + 22.86x_1x_3 - 49.26x_1x_4$$

Thus, the Box-Cox transformation was used to obtain a better fit for the statistical model. This procedure finds the appropriate Box-Cox power transformation for a dataset containing a pair of variables that should be analyzed by multiple regression.

Table 15 and **Table 16** present the square root Box-Cox transformation. **Equation 3** was built considering the same procedure adopted in **Equation 2**. This model showed the optimum value of λ of 0.5.

The coefficients of determination for the model were R^2 of 95.62 % and $R^2(adj)$ 89.59 %, indicating an improvement in the model's fit that represents around 90 % of of the variability accounted for by the coefficients.

Table 15 – Regression parameters for the Box-Cox transformation of CR (square root).

Coefficients				
Terms	Coefficient	SE Coefficient	t-Value	p-Value
Constant	11.15	0.80	13.92	0.000001
x_1	1.27	0.31	4.09	0.003492

Table 15 – Regression parameters for the Box-Cox transformation of *CR* (square root).

Coefficients				
Terms	Coefficient	SE Coefficient	t-Value	p-Value
x_2	-0.90	0.31	-2.90	0.019948
x_3	2.30	0.53	4.33	0.002502
x_4	0.06	0.36	0.17	0.869040 ^(*)
x_3^2	-3.40	1.16	-2.95	0.018539
x_1x_2	-0.97	0.30	-3.18	0.013051
x_1x_3	0.68	0.38	1.82	0.106417 ^(*)
x_1x_4	-2.73	0.32	-8.54	0.000027
x_2x_3	0.54	0.38	1.44	0.186754 ^(*)
x_2x_4	-0.71	0.32	-2.22	0.056961
x_3x_4	-0.59	0.45	-1.31	0.226792 ^(*)

^(*)No statistically significant because the p-values are higher than the minimum acceptable value of 0.10.

Table 16 – Analysis of Variance for the transformed *CR* regression (square root)

ANOVA	DF	Sum of Squares (Adjusted)	Mean Square (Adjusted)	F-value	p-value
Regression	11	322.63	29.33	15.86	0.000299
Error	8	14.80	1.85	-	-
Total	19	337.43	-	-	-

Equation 3

$$CR^{0.5} = 11.15 + 1.27x_1 - 0.90x_2 + 2.30x_3 - 3.40x_3^2 - 0.97x_1x_2 - 2.73x_1x_4 - 0.71x_2x_4$$

The *CR*-transformed regression (**Table 16**) is a better fit because its *F-value* is higher than the *CR* regression (**Table 14**). The transformation effects can also be observed in the reduction of the *p-value* of the *ANOVA* regression.

Thus, the transformation fulfilled its objective of improving the association with the model's response and adjusting the data distribution with a slight improvement in average variance.

From , we conclude that the individual effect of CO₂ partial pressure (x_3) is the term that promotes more impact on the *CR*. For this quadratic equation, we can observe in the vertex of its parabola a maximum value because the term is negative.

For a complete analysis, response surfaces were built for the test conditions with light ($x_1 = -1$) and heavy ($x_1 = +1$) oil in the absence and presence of H₂S (x_4). For all response surfaces shown in **Figure 50** and **Figure 51**, the y-axis was the inclination variation (x_2) and the x-axis was the variation of the CO₂ partial pressure (x_3). Analyzing the response surfaces

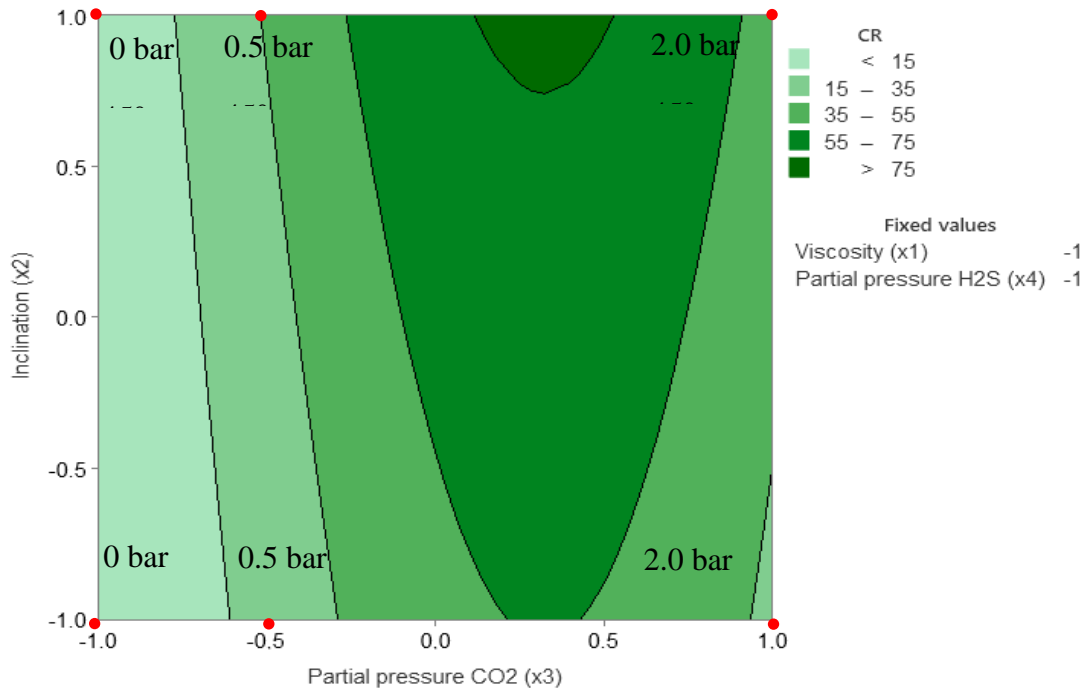
for LO with and without H₂S (**Figure 50**), we can see that the model predicts an increase in the corrosion rate as a function of the CO₂ partial pressure^{16, 66, 75} up to a region in which the corrosion rate values are maximum.

After that region, the corrosion rates fall again. The increase in the initial corrosion rate observed is related to the increase in CO₂ pressure. Most probably, the maximum region occurs due to the precipitation of iron carbonate which, at the end of that region, begins to assume adherent protective characteristics, being able to withstand the shear forces resulting from the flow of the fluid. From that moment on, the corrosion rate decreases. In the absence of H₂S, the model indicates that the region of maximum corrosion rate (75 mm/year) occurs for an inclination close to 45°.

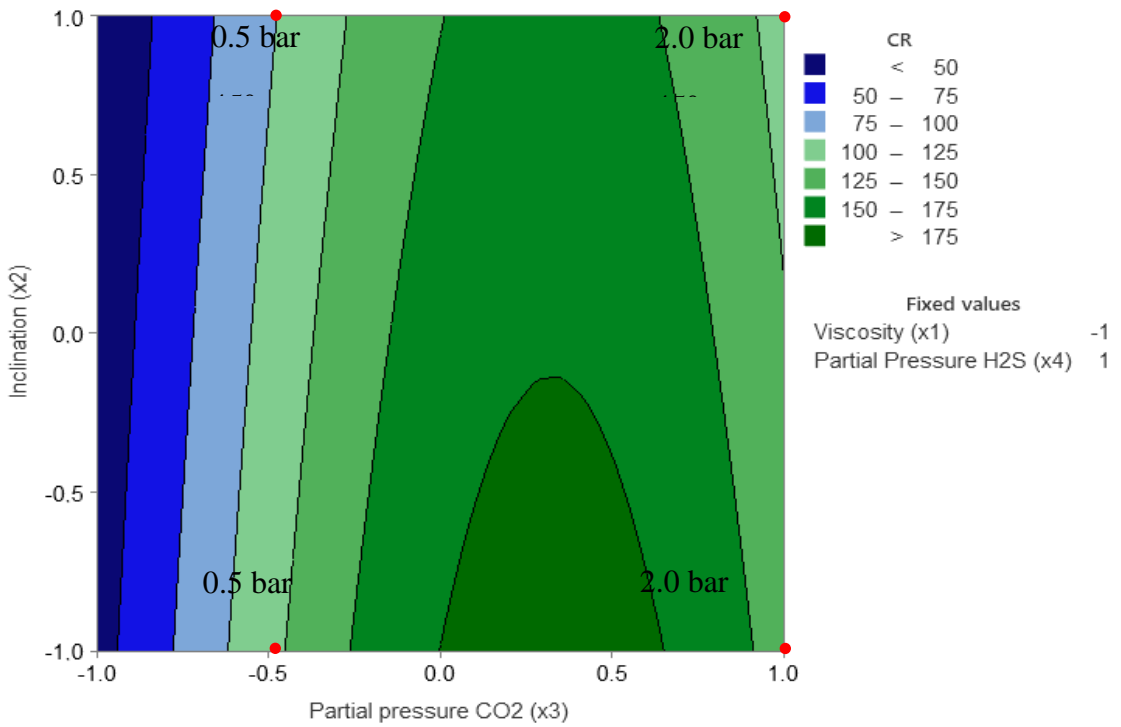
On the other hand, in the presence of H₂S, the values of the maximum corrosion rate correspond to a broader region and reach values greater than 175 mm/year for an inclination close to 0°. To understand the predictions of the highest corrosion rates of the model in the presence of H₂S, it is necessary to mention that there is a competition between the action of H₂S and CO₂ gases^{147, 69}.

H₂S has more favorable kinetics, i.e., greater reaction velocity with iron, quickly forming a layer of iron sulfide on the steel surface and a layer of iron carbonate. According to some authors, corrosion rates can increase in these conditions because the iron sulfide layer, with weak adhesion, facilitates the flow in removing the layers^{106, 95, 148}. Other authors mention that a reduction in corrosion rates is observed when H₂S is added to a CO₂-containing aqueous solution. This reduction was associated with the competition between the formation of FeS and FeCO₃ corrosion product layers^{39, 113}.

Figure 50 – Corrosion rate (CR in mm/y) response surface analysis for LO (Equation 3).
Without H₂S



With H₂S



The same analysis performed previously can be done for the response surfaces of the tests performed with HO shown in **Figure 51**. Analyzing the results without and with H₂S, we can again observe the initial increase in the corrosion rate with the increase in the partial CO₂ pressure followed by a region of maximum corrosion rate.

Without H₂S, the model indicates a broad maximum region with corrosion rates greater than 250 mm/year at 0°. However, in the presence of H₂S, the region of maximum corrosion rate showed a smaller area and lower corrosion rates (> 150 mm/year) at 0°. In general, the corrosion rates decreased in the presence of H₂S, in contrast to the tendency observed with the LO (**Figure 50**). This behavior was already highlighted in **Item 4.2**.

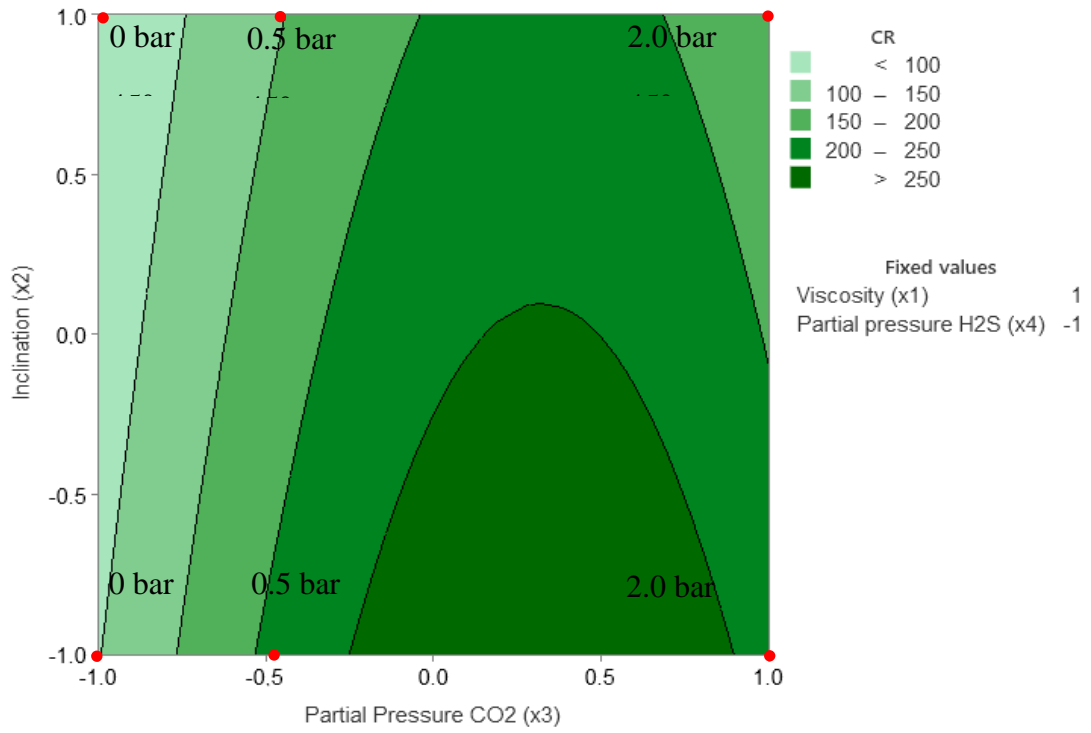
The analysis of this behavior is complex, and justifications for this result have not been found in the consulted literature. Many studies have been conducted using multiphase loops with two-phase environments (water and gas or water, gas, and soluble oils). However, studies in three-phase environments using crude oil and water cut 80 % have not been found¹⁴⁹.

Therefore, the clarification of the antagonistic influence of H₂S in a CO₂-containing environment increasing the corrosion rate in the presence of LO and decreasing it in the presence of HO needs to be studied in detail.

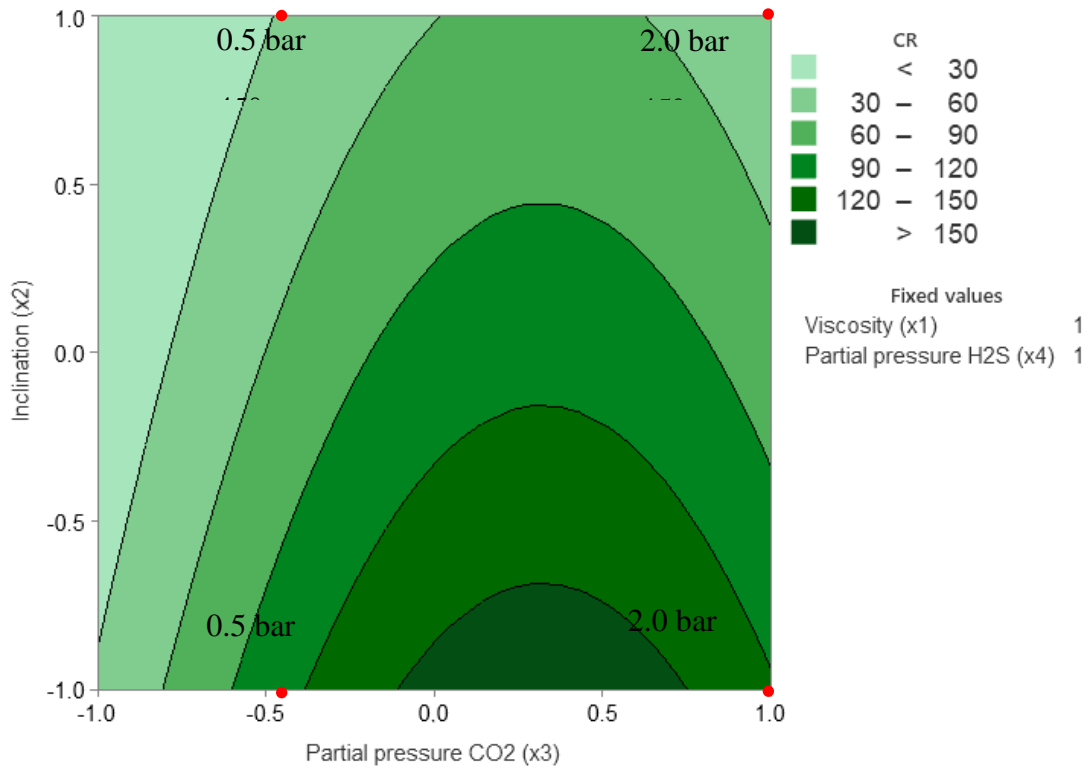
As can be seen, in general, the experimental values obtained using the constructed multiphase loop were reflected on the response surfaces. It can be seen that the corrosion rates predicted by the model are adjusted satisfactorily, but in the experimental data, the maximum region predicted by the model is not detected.

Therefore, the most crucial consideration of the model is the ability to predict regions such as the maximum corrosion rates which represent conditions not considered in the experimental matrix. In this way, the response surfaces from the model can be used as a guide for future experiments.

Figure 51 - Corrosion rate (CR in mm/y) response surface analysis for HO (Equation 3).
Without H₂S



With H₂S



4.3.2 Slug-bubble size, velocity, and frequency as a function of oil viscosity, pipe inclination and CO₂ and H₂S partial pressure

The results of the multiple regression for the flow parameters: slug-bubble size, velocity, and frequency obtained from the performed tests (**Table 12**), adopting the same procedure for *CR*, are presented in **Table 17** and **Table 18**; **Table 19**, **Table 20** and **Table 22**, respectively.

Equation 4, **Equation 5** and **Equation 6** represent the flow parameters models. In each of these equations, the terms with *p-values* higher than 0.10 were removed.

Table 17 – Regression parameters for the multiple regression of *SBS*

($R^2 = 92.8\%$, $R^2_{(adj)} = 82.9\%$).

Coefficients				
Terms	Coefficient	SE Coefficient	t-Value	p-Value
Constant	0.71	0.06	11.69	0.00
x_1	0.12	0.02	5.20	0.00
x_2	-0.07	0.02	-2.84	0.02
x_3	0.05	0.04	1.21	0.26 ^(*)
x_4	0.01	0.03	0.42	0.69 ^(*)
x_3^2	-0.16	0.09	-1.83	0.11 ^(*)
x_1x_2	-0.15	0.02	-6.47	0.00
x_1x_3	-0.08	0.03	-2.84	0.02
x_1x_4	0.07	0.02	2.94	0.02
x_2x_3	0.02	0.03	0.66	0.53 ^(*)
x_2x_4	-0.07	0.02	-2.77	0.02
x_3x_4	-0.05	0.03	-1.43	0.19 ^(*)

^(*)No statistically significant because the *p-values* are higher than the minimum acceptable value of 0.10.

Table 18 – Analysis of Variance for the *SBS* regression

ANOVA	DF	Sum of Squares (Adjusted)	Mean Square (Adjusted)	F-value	p-value
Regression	11	1.11	0.10	9.38	0.00
Error	8	0.09	0.01	-	-
Total	19	1.19	-	-	-

Equation 4

$$SBS = 0.714 + 0.1232x_1 - 0.0672x_2 - 0.15x_1x_2 - 0.0811x_1x_3 + 0.718x_1x_4 - 0.0675x_2x_4$$

Table 19 – Regression parameters for the multiple regression of *SBV*
 ($R^2 = 80.2\%$, $R^2_{(adj)} = 53.0\%$).

Coefficients				
Terms	Coefficient	SE Coefficient	t-Value	p-Value
Constant	2.75	0.25	10.90	0.00
x_1	0.32	0.10	3.27	0.01
x_2	0.00	0.10	-0.05	0.96 ^(*)
x_3	0.32	0.17	1.94	0.09
x_4	-0.04	0.11	-0.36	0.73 ^(*)
x_3^2	-0.74	0.36	-2.03	0.08
x_1x_2	-0.22	0.10	-2.32	0.05
x_1x_3	0.24	0.12	2.07	0.07
x_1x_4	0.17	0.10	1.65	0.14 ^(*)
x_2x_3	-0.02	0.12	-0.18	0.86 ^(*)
x_2x_4	-0.16	0.10	-1.56	0.16 ^(*)
x_3x_4	0.08	0.14	0.54	0.61 ^(*)

^(*)No statistically significant because the p-values are higher than the minimum acceptable value of 0.10.

Table 20 – Analysis of Variance for the *SBV* regression.

ANOVA	DF	Sum of Squares (Adjusted)	Mean Square (Adjusted)	F-value	p-value
Regression	11	5.94	0.54	2.95	0.07
Error	8	1.47	0.18	-	-
Total	19	7.41	-	-	-

Equation 5

$$SBV = 2.75 + 0.3199x_1 + 0.324x_3 - 0.738x_3^2 - 0.221x_1x_2 - 0.244x_1x_3$$

Table 21 – Regression parameters for the multiple regression of *SBF*
 ($\lambda = -3$ and $g = 2.82601$ is the geometric mean of *SBF*, $R^2 = 95.0\%$, $R^2_{(adj)} = 88.1\%$).

Coefficients				
Terms	Coefficient	SE Coefficient	t-Value	p-Value
Constant	20.28	0.12	174.20	0.00
x_1	-0.23	0.05	-5.07	0.00
x_2	0.39	0.05	8.69	0.00
x_3	0.26	0.08	3.35	0.01
x_4	-0.10	0.05	-2.01	0.08
x_3^2	-0.18	0.17	-1.08	0.31 ^(*)

Table 21 – Regression parameters for the multiple regression of *SBF*
 ($\lambda = -3$ and $g = 2.82601$ is the geometric mean of *SBF*, $R^2 = 95.0\%$, $R^2_{(adj)} = 88.1\%$).

Coefficients				
Terms	Coefficient	SE Coefficient	t-Value	p-Value
x_1x_2	0.21	0.04	4.73	0.00
x_1x_3	0.08	0.05	1.49	0.17 ^(*)
x_1x_4	0.03	0.05	0.66	0.53 ^(*)
x_2x_3	-0.03	0.05	-0.58	0.58 ^(*)
x_2x_4	-0.04	0.05	-0.78	0.46 ^(*)
x_3x_4	0.06	0.07	0.89	0.40 ^(*)

(*) No statistically significant because the p-values are higher than the minimum acceptable value of 0.10.

Table 22 – Analysis of Variance for the *SBF* regression.

ANOVA	DF	Sum of Squares (Adjusted)	Mean Square (Adjusted)	F-value	p-value
Regression	11	5.93	0.54	13.81	0.0005
Error	8	0.31	0.04	-	-
Total	19	6.24	-	-	-

Equation 6

$$\frac{SBF^{\lambda-1}}{(\lambda g)^{\lambda-1}} = 20.279 - 0.2289x_1 + 0.3923x_2 + 0.2585x_3 - 0.1048x_4 + 0.2089x_1x_2$$

For **Equation 4** and **Equation 5** models, the Box-Cox transformation was not necessary because their optimum value of λ of 1.0. For **Equation 4 (SBS)**, the R^2 and $R^2_{(adj)}$ of this model were 92.8 % and 82.9 %, respectively, which means that the model explains much of the variability of the process.

However, for **Equation 5 (SBV)**, the model does not explain the variability of the process as $R^2_{(adj)}$ (53.0 %) is much lower than R^2 (80.2 %). This is attributed to the difficulty in measuring all interaction complexity for multiphase flow which, in general, is a consequence of a chaotic condition of the flow. According to the literature, for these complex flows, a statistical description is required with definition of average properties of the mixture as: averages in the volume, in the area, time averages, or a combination of these^{150,151,152}. The instrumentation used in the experimental tests was not able to obtain such average properties and should be improved.

For **Equation 6 (SBF)** model, the transformation ($Y'=1/Y^3$) was performed and optimum value of λ of -3 was obtained. The determination coefficient adjusted was around 88 % of the variability of the accounted by the coefficients.

Despite the good statistical response of the bubble size and the frequency of the slug flow, we did not discuss the correlation with the experimental results because the three flow dependent variables are interdependent.

4.3.3 Consolidation

Using multiple regression and Box-Cox transformation, it was possible to perform four prediction models based on the initial results of the multiphase-flow loop experimental tests.

The corrosion rate model showed good correlations with the experimental test data. In addition, the model was able to show some important experimental conditions not explored in the experimental test matrix, which demonstrates the model's predictive power.

For the flow-related parameter models (bubble slug size, velocity and frequency), the performance of the prediction was compromised by the type of instrumentation used. The models showed relatively high adjusted determination coefficients (above 80 %) for bubble slug size and frequency. However, for the bubble slug velocity, this parameter was around 0.5. As the dependent variables (slug-bubble size, velocity, and frequency) are interdependent, we did not analyze the model data. We decided to improve the experimental instrumentation, mainly for flow pattern characterization, for better statistical sensitivity.

Finally, new studies can emerge from these results to modify the test matrix, varying test conditions, pipe material, and design concept, correlating them with the mechanisms of corrosion rate.

4.4 Results of Cavitation-Erosion Testing

In this topic, the resistance of the materials to the hydrodynamic effects associated with cavitation promoted by the multiphase flow was studied. Standard cavitation-erosion tests¹²³ were performed to compare the resistance to cavitation-erosion of the API 5L X80 steel and the API 5DP grade used in drill pipes^{125, 126}.

The selection of materials for O&G transportation is not always done with an emphasis on corrosion resistance but on mechanical properties, the simplicity of manufacturing and low cost. Due to high mass-loss rates resulting from internal corrosion, the knowledge of the corrosion resistance of different steel grade used in pipelines for sweet service is necessary⁹².

In the literature, the analysis of a failure mechanism in multiphase flows in the connecting regions of the drilling pipes is done based on the Eulerian-Lagrangian method and the discrete phase model, which confirms the existence of corrosion associated with a flow⁸⁰.

In this context, comparing the resistance of carbon steel API 5L X80 with a high cavitation-erosion resistant steel, such as API 5DP S steel grade, may permit the understanding of corrosion mechanisms associated with the flow and may promote better material selection.

To better compare the steel grades, multiphase-flow loop tests were performed also for the API 5DP S steel grade in the same conditions described in **item 4.2** for API 5L X80, focusing on the CO₂-containing environment with HO under a partial CO₂ pressure of 2.0 bar.

4.4.1 Multiphase Flow Loop Testing: comparing API 5L X80 with API 5DP S

Table 23 shows the surface images of API 5DP S grade specimens after the loop tests together with API 5L X80 grade results already presented in **Table 11** (T2 test).

As highlighted in **Item 4.2**, the intensity of the API 5L X80 steel degradation under multiphase flow at 0° was so high that the useful thickness of the specimen was consumed. The same level of degradation was not observed for 45°. Degradation was also observed for API 5DP S steel but with much less intensity. It is worth mentioning that, after rinsing with isopropyl alcohol, the surface of the API 5DP S steel presented a minor amount of corrosion products.

Table 23 – SEM images and appearances of the surface of the specimens tested in HO under CO₂ partial pressure of 2 bar (the specimens were rinsed with isopropyl alcohol and pickled in Clarke’s solution)

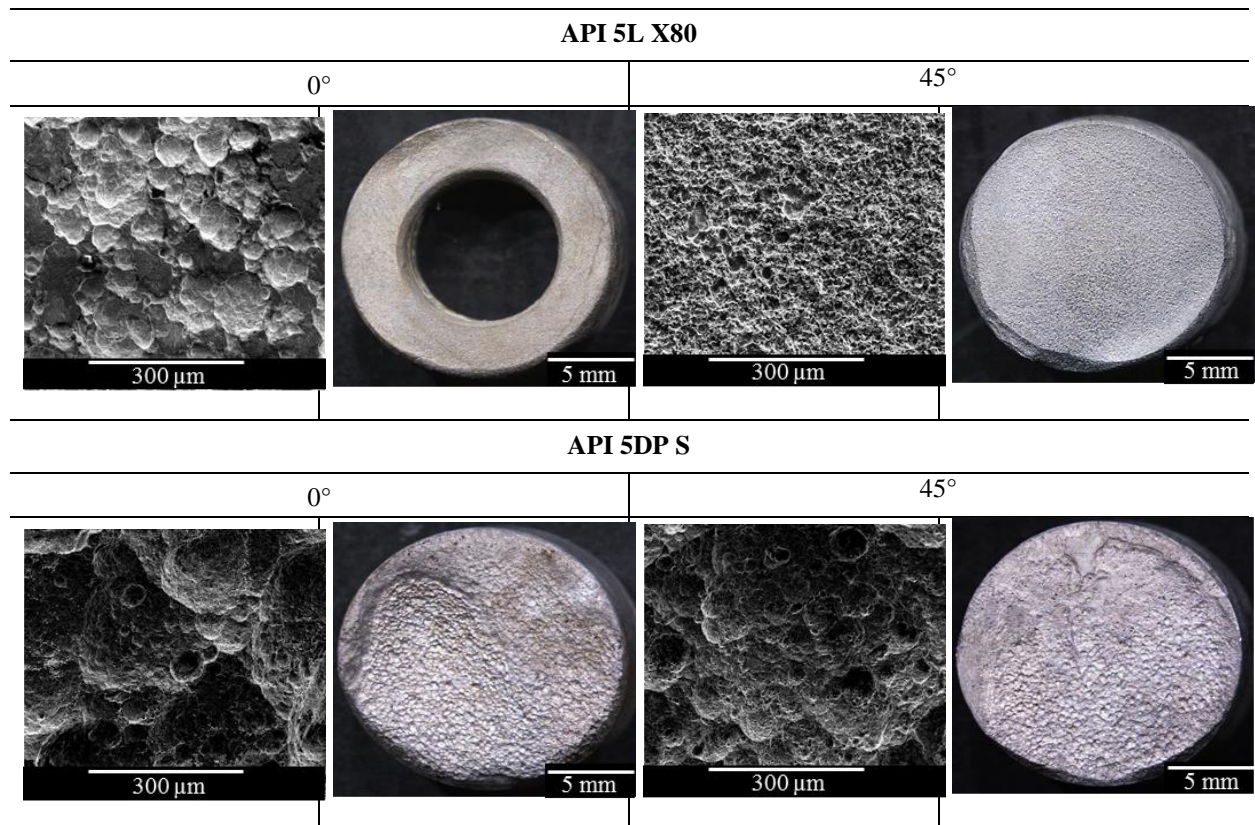


Figure 52 summarizes the cumulative mass loss at 0° and 45° incidence angles for API 5L X80 and API 5DP S steel specimens. The superior degradation resistance of the API 5DP S grade horizontal and inclined position is seen in this figure.

Figure 52 – Cumulative mass loss for API 5L X80 and API 5DP S grade steels at 0° and 45° positions.

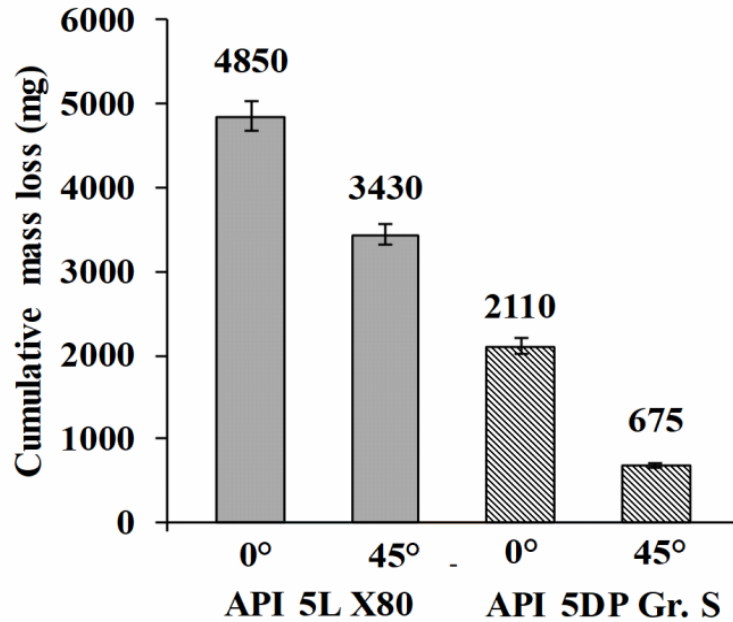
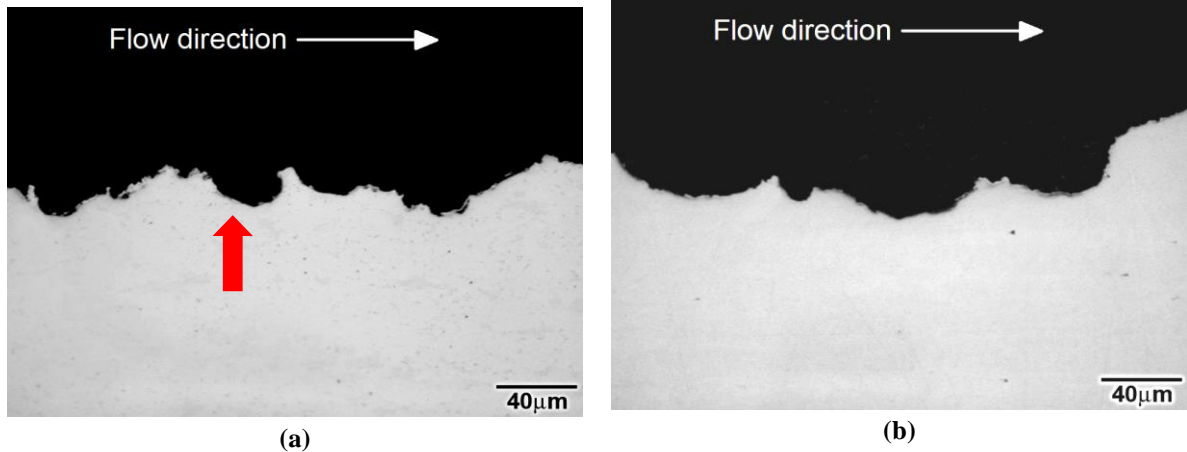


Figure 53 shows the cross-sectional micrograph of the specimens in a longitudinal section of the corroded surface. These images suggest that multiphase flow produced material detachment in the downstream direction, probably due to the combined action of corrosion and wear. The concavity shape signed with a red arrow in Figure 53a is typical for corrosion-erosion. This behavior has been reported in the literature⁸⁹.

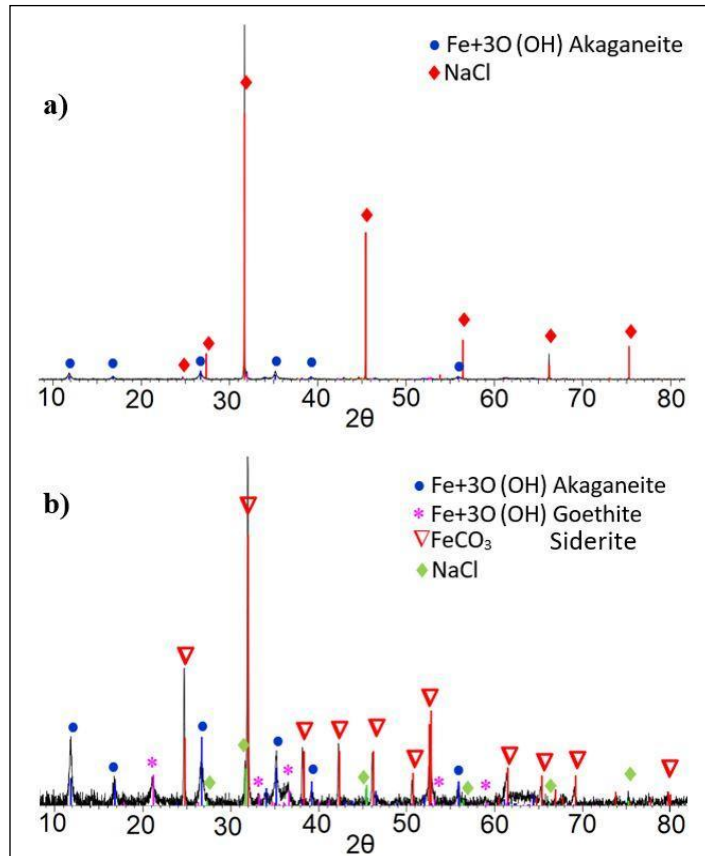
Figure 53 – Optical micrographs of the cross-section of API 5L X80 (a) and API 5DP S grade (b).



This result suggests that the multiphase flow produced intense wall shear stresses at the horizontal position, removing the protective FeCO_3 layer. It is essential to mention that, for API 5DP S, the FeCO_3 was not detected, probably because of the reduced amount of corrosion product, which was observed with the naked eye just after rinsing the tested specimens with isopropyl alcohol. Figure 54 shows XRD patterns taken at the surface of API 5L X80 specimens tested at horizontal (0°) and inclined (45°) positions. NaCl, coming from

the testing solution, was detected on the surface of the specimens tested at the horizontal position. In contrast, siderite (FeCO_3) was detected in some regions at the surface of specimens tested at 45° position with minor amounts of NaCl. This result suggests that the multiphase flow produced intense wall shear stresses at the horizontal position, removing the protective FeCO_3 layer. It is essential to mention that, for API 5DP S, the FeCO_3 was not detected, probably because of the reduced amount of corrosion product, which was observed with the naked eye just after rinsing the tested specimens with isopropyl alcohol.

Figure 54 – XRD diffraction pattern of the surface of API 5L X80 steel test specimen **a)** 0° and **b)** 45° position.



There are several mechanisms to describe the synergistic action of flow and corrosion which results in flow-induced corrosion. In some cases, intensified flow eliminates the local accumulation of aggressive agents on the metal surface, avoiding pitting and crevice corrosion. In other cases, the intensified flow enhances passivation due to a continuous supply of oxidizing agents promoting the formation of a protective layer. In some cases, high flow rates promote the removal of protective corrosion layers, exposing a clean metal surface to the corrosive environment, and causing severe corrosion. In the present study, a set of deep, sharp-edged craters formed on the metal surface show that the last-mentioned mechanism took place⁸⁹. For the studied conditions, it is expected that an iron carbonate layer formed as the primary corrosion product which may reduce the degradation processes if the test condition will not remove it from the metallic surface. bubble-collapsing phenomena open

holes in the iron carbonate films and promote flow-induced corrosion. As this compound was not detected especially at the horizontal condition, it is reasonable to suppose that the slug flow conditions enhanced the corrosion processes.

Flow-induced localized corrosion enhanced by micro-turbulence leads to an increase of oxide layer surface roughness and a thinning down and growth of porosity of the barrier oxidized layer, promoting layer degradation. The localized attack will be concentrated on this site and the formation of a further barrier layer will be limited by the flow velocity. According to references^{153, 154}, in the absence of a flow effect, a protective barrier layer would be formed inside the pores of the iron carbonate layer, reducing the corrosion rate. This is not observed for a high flow rate. Thus, we can suggest that API 5L X80 steel, which presents a typical ferrite-pearlite microstructure in its original structure, underwent increased corrosion due to the selective dissolution of the ferritic phase, maintaining the iron carbide intact, causing a galvanic coupling effect. This increased the surface availability for the cathodic reaction and the formation of a thick porous layer was enhanced. In contrast, the Cr containing API 5DP S steel presents a tempered martensite microstructure. As reported in the literature¹⁵⁵, for low-alloy martensitic steels exposed to CO₂, Cr promotes the formation of compact and self-repairable Cr-rich compounds. For instance, a compact inner layer of FeCO₃ crystals and Cr-rich compounds improves corrosion resistance. Furthermore, the presence of Cr-rich carbides distributed in the martensite and the galvanic coupling between the carbides and substrate can build up a compact inner layer when immersed in a corrosive solution¹⁵⁵.

4.4.2 Standard Cavitation-erosion Test

Figure 55 presents the mass loss variation as a function of time for the API 5L X80 and API 5DP S steels submitted to cavitation-erosion tests. Each point corresponds to the average of the three tests performed under the same conditions.

As observed in **Figure 55**, the variation in cumulative mass loss with testing time for both materials exhibited typical stages of a material submitted to a cavitation-erosion test: (a) incubation stage, where the mass loss was negligible compared to longer testing times. The observed incubation periods were 9 h and 3 h for the API 5DP S and API 5L X80 steels, respectively. The acceleration stage starts after the incubation period, where the cumulative mass loss increases rapidly.

From **Figure 55**, it can also be observed that the API 5DP S grade showed better cavitation resistance than API 5L X80. After 30 h of testing, the API 5DP S grade and API 5L X80 carbon steel lost 13 mg and 60 mg, respectively.

Despite the API 5L X80 being widely used for pipelines in the oil industry, the cavitation-erosion test results indicate the instability and limited applicability in a condition where the multiphase flow also produces cavitation-erosion damages. The API 5DP S grade steel reveals a higher cavitation-erosion resistance, being more indicated for cavitation-erosion requirements.

Figure 55 – Variation of the mass loss with cavitation-erosion testing time for API 5L X80 and API 5DP S grade.

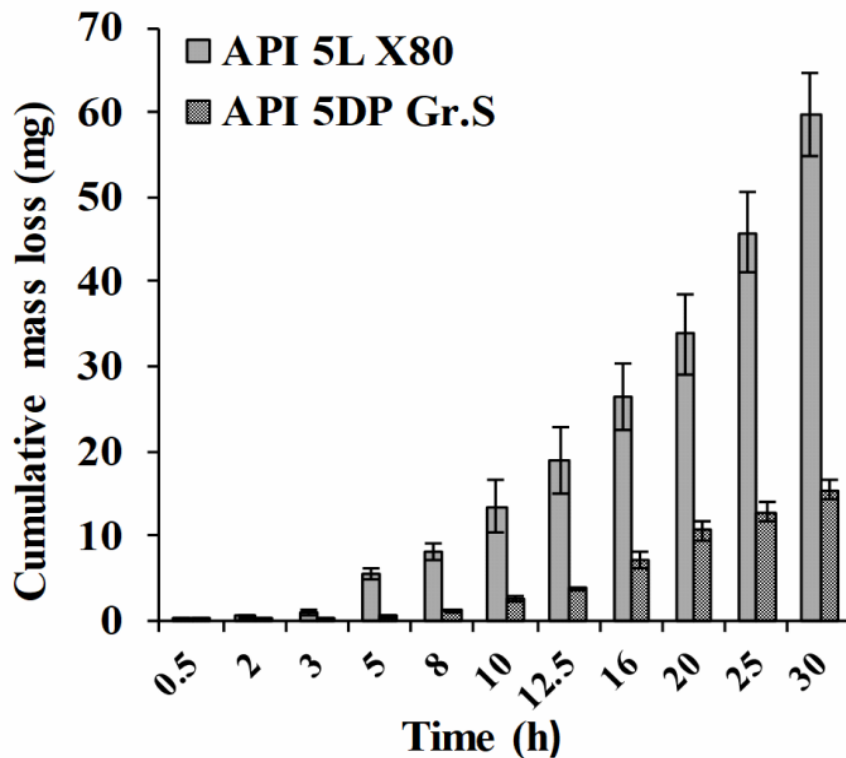


Figure 56 shows the evolution of the cavitation-erosion damage on the surface of the API 5L X80 steel. The worn surface after 1 h of testing (**Figure 56b**) confirms that, during the incubation period, a significant number of asperities were formed.

Despite the negligible mass loss during the first hour of testing, there was still a noticeable change in the surface finish. This demonstrates that the surface texture achieved after grinding can provide preferential sites for localized damage promoting cumulative degradation typical of incubation periods.

As liquid micro-jets continue to hit the surface during the acceleration stage, several craters are formed with heavily strained material around them, as shown in **Figure 56c**. Thus, fatigue becomes a significant degradation mechanism, and wear particles are detached when several micro-cracks join and grow together.

Consequently, after 8 h of testing, numerous craters and grooves with intense plastic deformation can be observed at the worn surface, as revealed in **Figure 56d**. This behavior predominates up to 30 h testing.

Figure 56 – SEM surface images of the API 5L X80 carbon steel. (a) Before the cavitation tests (surface finishing obtained by grinding with ASTM 600 emery paper); (b) after 1 h testing; (c) after 3 h testing: wear marks, plastic deformation and some craters; (d) after 8 h testing: wear marks, craters and material detachment.

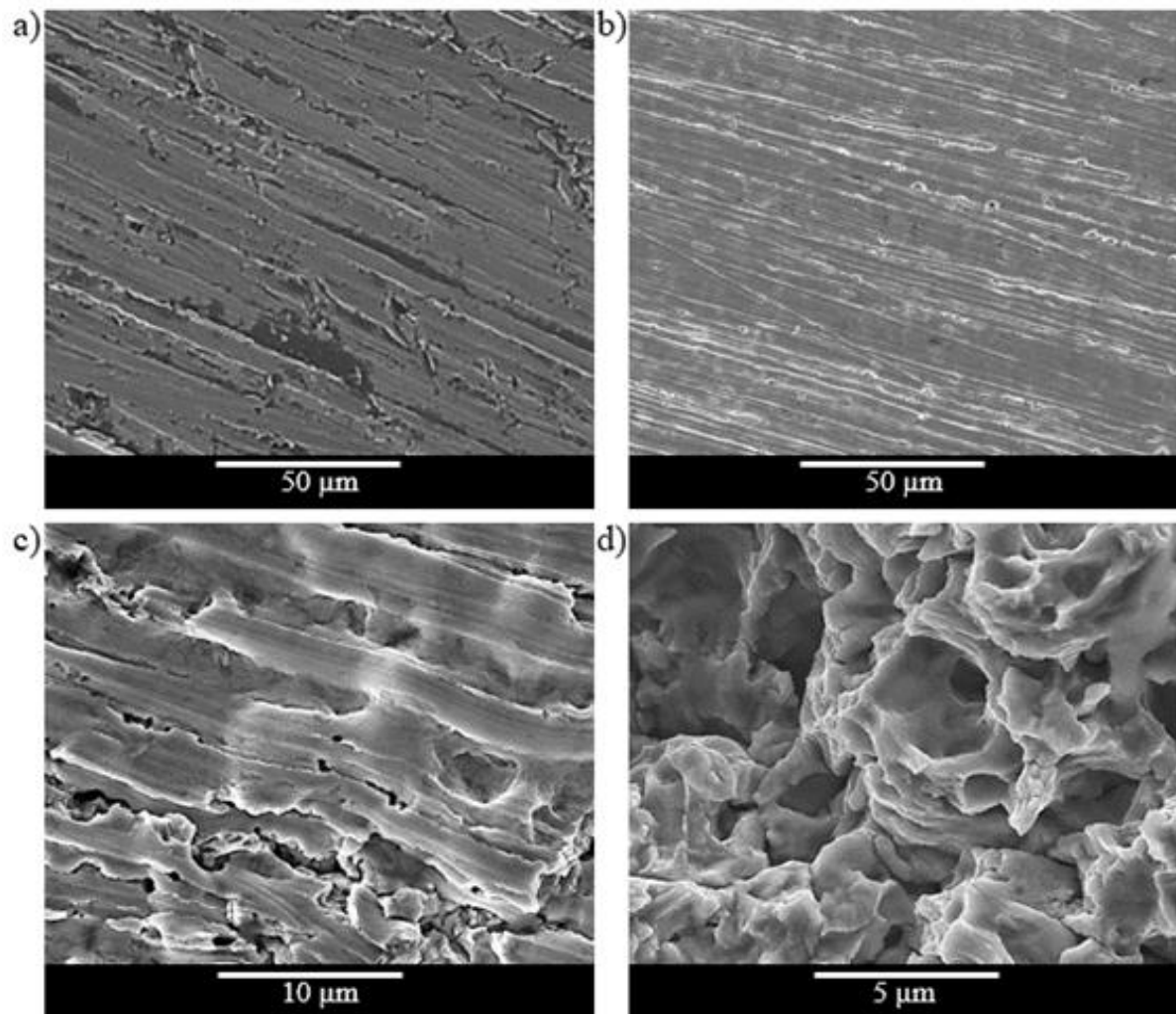


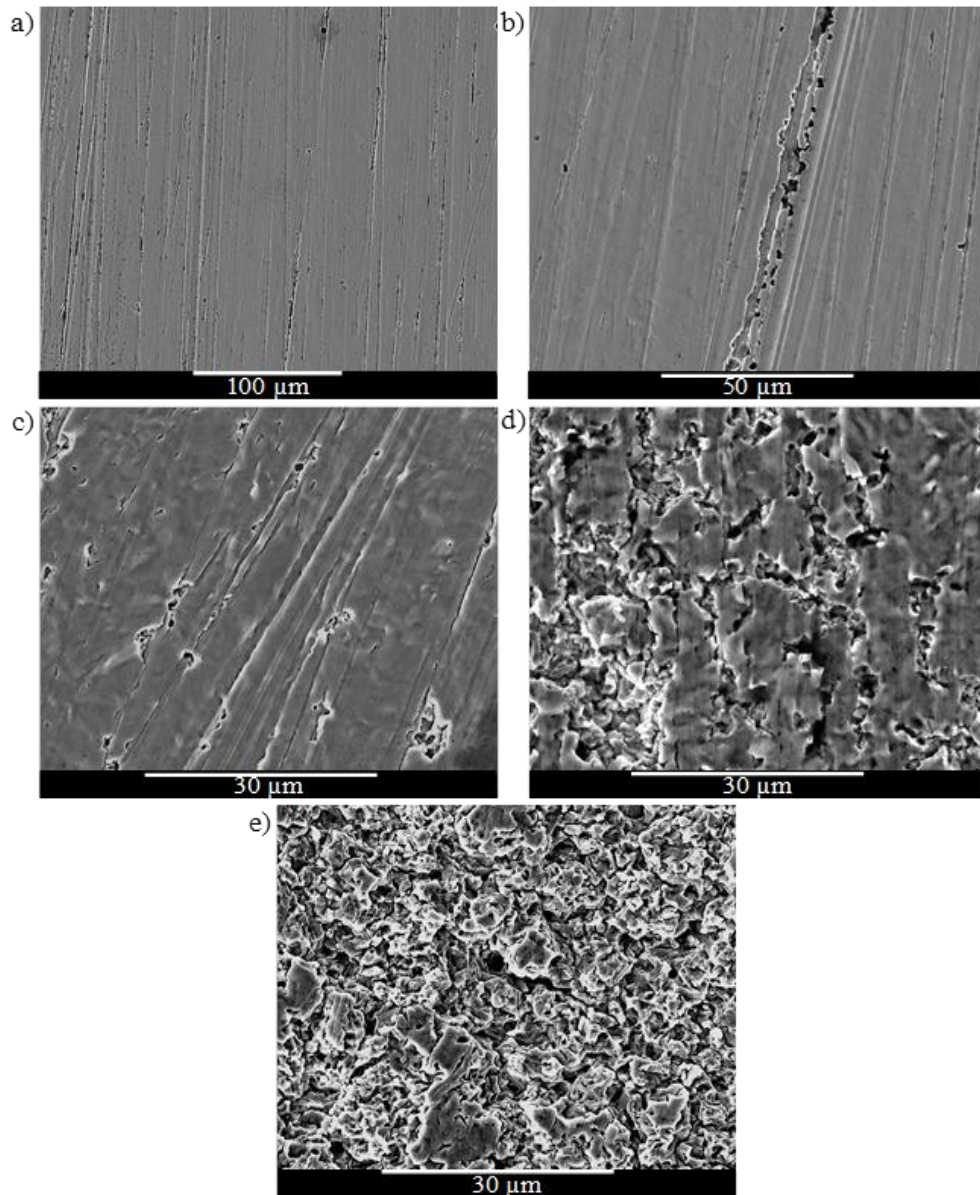
Figure 57 shows the worn surfaces of API 5DP S grade steel after the cavitation-erosion tests. **Figure 57a** to **Figure 57c** shows wear mechanisms similar to those observed for the API 5L X80 during the incubation period.

Figure 57b and **Figure 57c** show that the material detachment started preferentially at the grinding marks, creating a pattern of lines inside the smooth isolated regions of unaffected material.

Figure 57d and **Figure 57e** show the worn surfaces after the incubation period, where smooth isolated areas can be observed.

Those regions correspond to the original surface, which is about to be detached. It can be inferred from the examination of the worn surfaces that the prime removal mechanism is the detachment of large particles due to the coalescence of fatigue cracks under the surface.

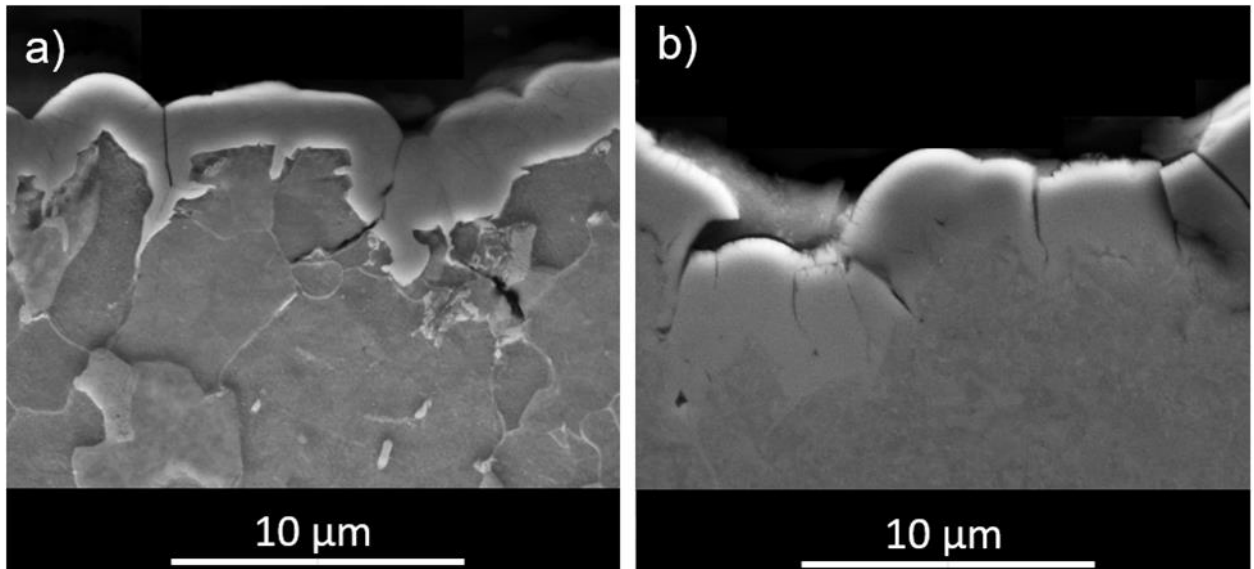
Figure 57 – SEM surface images of the API 5DP S grade. (a) Before the cavitation tests (surface finishing obtained by grinding with ASTM 600 emery paper); (b) after 2 h testing; (c) after 6 h testing: wear marks, plastic deformation and some craters; (d) after 10 h testing: wear marks, craters and material detachment and (e) after 16 h testing.



The high mass losses observed in API 5L X80 specimens can be related to the characteristics of the phases in the microstructure and their hardness. Ferrite is the weakest phase of this material and is preferentially attacked. Santa *et al.*¹⁵⁶ reported that the resistance to cavitation-erosion of ferrite is lower than that of austenite, while martensite shows the best performance. The API 5DP S steel, with a tempered martensitic microstructure, offers a hardness 55 % greater than the API X 5L X80 steel. The higher hardness of the martensitic steel contributes to the better cavitation-erosion resistance observed. Therefore, API 5L X80 ferritic + pearlitic steel, with a high-volume fraction of ferrite, should not be employed a multiphase-flow condition due to cavitation-erosion.

Figure 58a and **Figure 58b** show the micrograph of the crack in the cross-section of the worn surface after 30 h of cavitation-erosion test, demonstrating the fatigue behavior and the incipient detachment of material.

Figure 58 - Cross-sectional SEM images of worn surface of API 5L X80 (a) and API 5DP S grade (b).



4.4.3 Electrochemical Test

Static electrochemical tests were carried out to assess the corrosion without the influence of cavitation and erosion hydrodynamic factors. **Figure 59** shows the variation of the measured open-circuit potentials (OCP) for the API 5L X80 and API 5DP grade S steels during 3000 s, which indicates that both steels present the same OCP around -0.71 V vs SCE.

Figure 60 displays the potentiodynamic polarization curves of the API 5L X80 and API 5DP S steels in 15 % NaCl solution. The polarization resistance results, obtained by differentiation of the potentiodynamic curves from **Figure 60**, are summarized in **Table 24**. One can see that, for static polarization potentiodynamic test, the API 5L X80 and API 5DP S behaviors were quite similar, with polarization resistances around $32 \Omega \text{ cm}^2$ to $34 \Omega \text{ cm}^2$. Considering the above results, the dissimilar corrosion behaviors observed during multiphase-flow testing can be attributed to the pronounced cavitation-erosion processes of the API 5L X80 ferritic-pearlitic steel compared to the martensitic API 5DP S steel.

Globular carbides present in the microstructure of the martensitic steel offer less anchoring for the FeCO_3 corrosion product layer on the metal surface¹⁵⁷ favoring its complete removal from the surface of the API 5DP steel. On the contrary, the API 5L X80 steel with lamellar carbides in the pearlitic region allows anchoring the FeCO_3 corrosion products more efficiently on the surface¹⁵⁷. Although the removal of the FeCO_3 corrosion products layer from the surface of the API 5DP S steel, during corrosion multiphase flow testing, contributed to an increase in the corrosion rate, the cavitation-erosion of this martensitic steel is much less aggressive to the surface of the specimens, resulting in overall better resistance to multiphase flow corrosion during the testing. Nevertheless, the FeCO_3 layer formed on the surface of the

API 5L X80 steel protects the steel from corrosion, the lesser resistance to cavitation-erosion dominates the overall behavior, resulting in a greater corrosion rate during multiphase flow testing.

Figure 59 – OCP values of the API 5L X80 and API 5DP S grade specimens. Test conditions: 15 % of NaCl, 2 bar of CO₂ partial pressure, 40 °C.

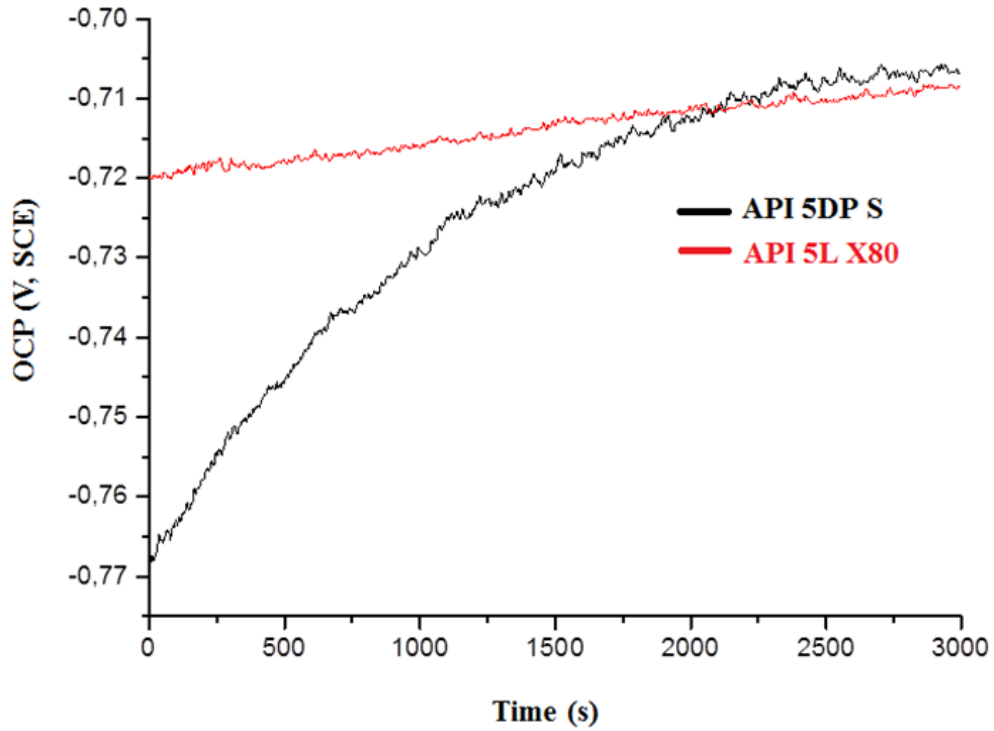


Figure 60 – Potentiodynamic linear polarization curves of the API 5L X80 and API 5DP S grade specimens.

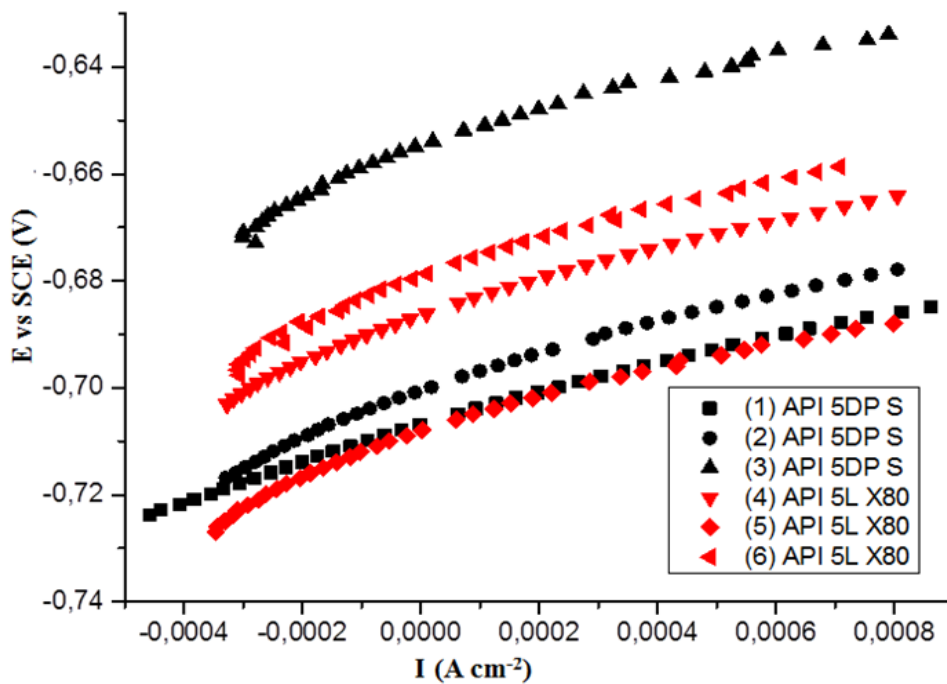


Table 24 – Polarization resistance obtained directly from **Figure 60**.

Materials	Test	Polarization resistance ($\Omega \text{ cm}^2$)	Average ($\Omega \text{ cm}^2$)	STDEV (*)
API 5L X80	1	33.8	34.8	1.6
	2	33.8		
	3	36.6		
API 5DP S	4	30.2	32.8	2.2
	5	34.1		
	6	34.2		

(*)STDEV – Standard Deviation

4.4.4 Consolidation

In the present study, corrosion multiphase flow test, standard cavitation-erosion test and electrochemical techniques were used to compare the influence of each aspect in the degradation processes of two API-steel grades, one API 5L X80 and the other API 5DP S. Based on the obtained results, the following conclusions can be drawn:

- in the multiphase flow tests, API 5DP S showed better resistance against multiphase-flow-induced corrosion than API 5L X80 ferritic-pearlitic steel. This behavior was attributed to the higher hardness of the martensitic steel, which contributes to the better cavitation-erosion resistance observed;
- although the FeCO_3 layer formed on the surface of the API 5L X80 steel contributes to protecting the steel from corrosion, the lesser resistance to cavitation-erosion dominates the overall behavior, resulting in a greater corrosion rate;
- the cavitation-erosion tests showed that during the acceleration stage, several craters are formed, indicating that fatigue is probably the primary degradation mechanism, where wear particles are detached due to the joining of micro-cracks;
- the static electrochemical test results showed that the polarization resistance of the API 5L X80 was statistically the same as the API 5DP S. This reinforced that wear damage due to cavitation-erosion dominates the overall behavior, leading to better multiphase-flow-induced corrosion resistance of the API 5DP S martensitic steel;
- the results show that assessing the corrosion resistance of alloys to be used in a multiphase flow loop, solely by using electrochemical tests can be misleading, as these testing do not indicate the real performance in the field.

4.5 Results of Autoclave Emulsion Testing

In this topic, emulsion tests were conducted with the light and the heavy crude oils used in this work to understand the significantly higher corrosion rates obtained in the multiphase-loop corrosion tests with the heavy oil. A medium crude (MO) oil was included in this study for comparison. The focus was the CO_2 environment with crude oils plus a water cut of 80 %.

The tests were performed at 40 °C under 2 bar of partial pressure of CO₂. Additionally, a characterization of the liquid phase of the multiphase-loop tests with the LO and HO was performed.

4.5.1 Results and discussion

Figure 61 shows the images obtained through a stereomicroscope examination of the (a) HO, (b) MO and (c) LO after 30 h stirring, at 40 °C, in the emulsion-test cell. From **Figure 61a**, HO, we can verify the presence of water droplets in the oil phase, indicating a W/O emulsion also known as “chocolate mousse” or “mousse” among oil spill workers²⁷. Studies show that a W/O emulsion presents the highest viscosity value at the critical water cut (60 % to 80 %), i.e., at the inversion point⁷⁹.

In **Figure 61b**, medium oil, one can observe a similar behavior with water droplets in the oil phase, indicating a W/O emulsion. For light oil, one can see drops of water inside the oil but in a different distribution mode, as shown in **Figure 61c**.

Figure 61 - Emulsion microstructures of (a) HO, (b) MO and (c) LO after the emulsion test with CO₂ partial pressure of 2.0 bar, 80 % water cut stirred (1200 rpm) for 30 h at 40 °C. Stereomicroscope (Leica Fusion Optics M205C) images with a maximum magnification of 100x in 1.0x objective lens.

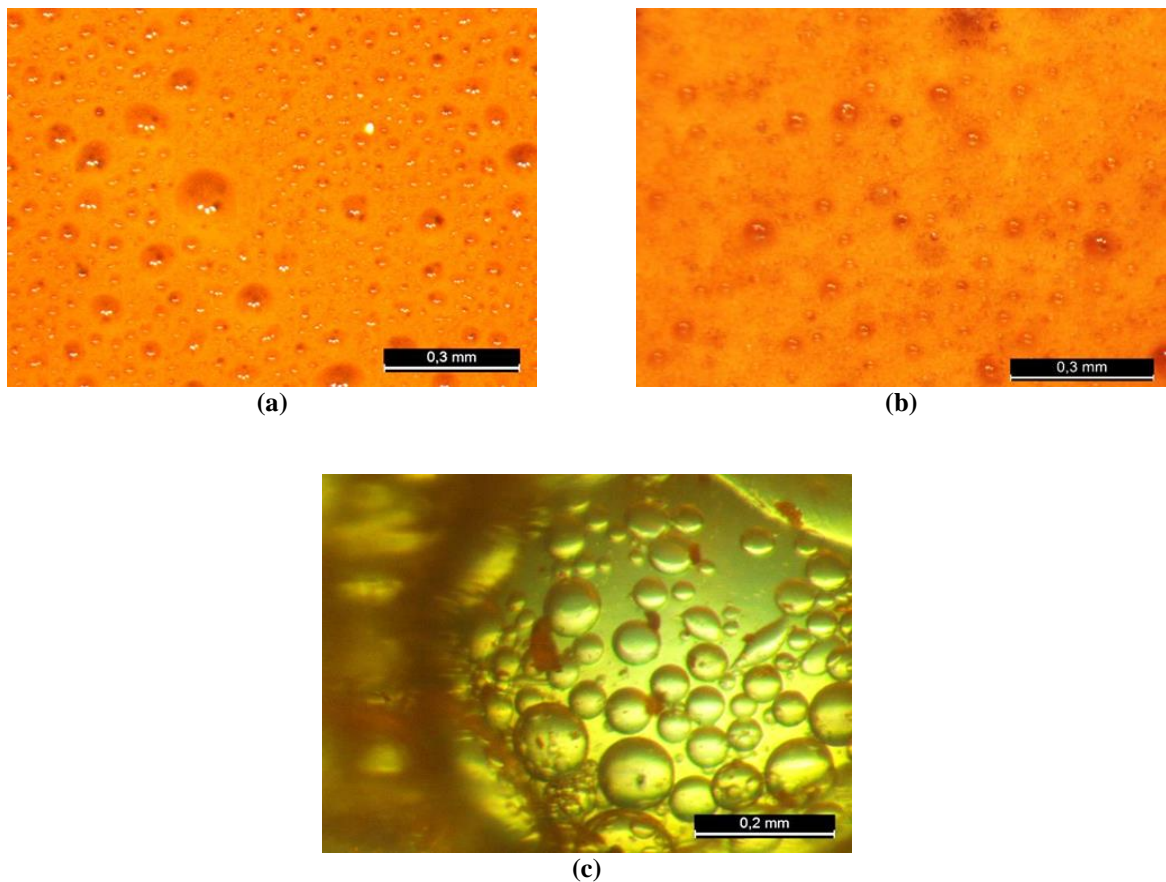
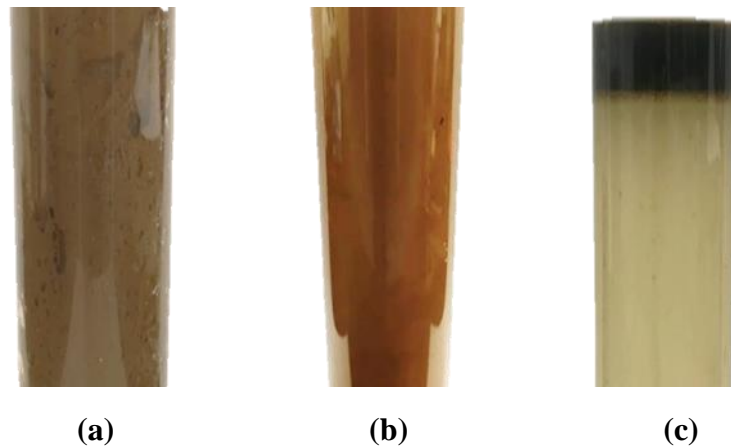


Figure 62 shows the images of the visual aspect of the oils after the emulsification tests and after the analysis in the Turbiscan, respectively: (a) and (a1) for the heavy crude oil; (b) and (b1) for the medium crude oil and (c) and (c1) for the light crude oil.

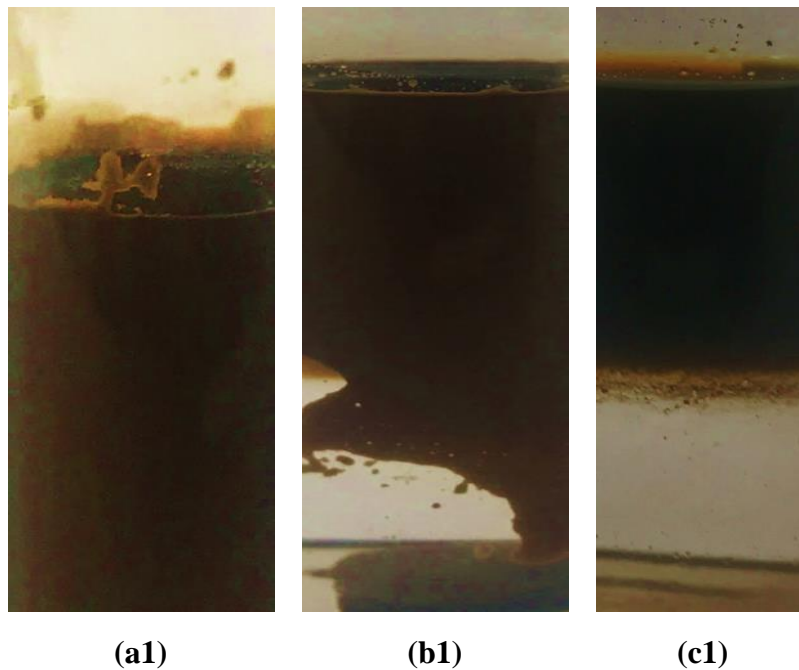
The most crucial detail of the visual observation is that the HO and MO were much more viscous and stable, with an aerated aspect and with retention of almost all water volume (**Figure 62a** and **Figure 62b**). The higher viscosity was perceived during the manipulation of the sample. The LO presented a different behavior with a quick separation soon after the sample collection, leaving the water a little whitish and the oil lighter, but without significant visible changes in viscosity and aeration (**Figure 62c**).

Figure 62 – Visual appearance of the samples after emulsification test (a) HO (b) MO (c) LO and after analysis on the Turbiscan (a1) HO (b1) MO (c1) LO.

After emulsification tests



After analysis on the turbiscan



From **Figure 62a1**, it is possible to observe that the HO presents greater stability in the form of W/O emulsion. Comparing the HO with the MO (**Figure 62b1**) and the LO (**Figure 62c1**) one can observe that the LO is more unstable. This quick phase separation behavior of the LO was already visually observed soon after the emulsification test. In the literature the corrosiveness of the W/O emulsion strongly depends on its stability and a method is suggested to avoid pipeline corrosion by keeping the emulsion stable¹³⁰. Additionally, researchers have observed in multiphase-slug-flow experimental studies that an increase in the viscosity and the flow rate (higher shear stress) promote the removal of corrosion products and thus the increase in corrosion damage⁷⁹. The emulsion stability was characterized using the Turbiscan to obtain the Stability Index (TSI). The TSI value is calculated based on **Equation 7**¹⁵⁸.

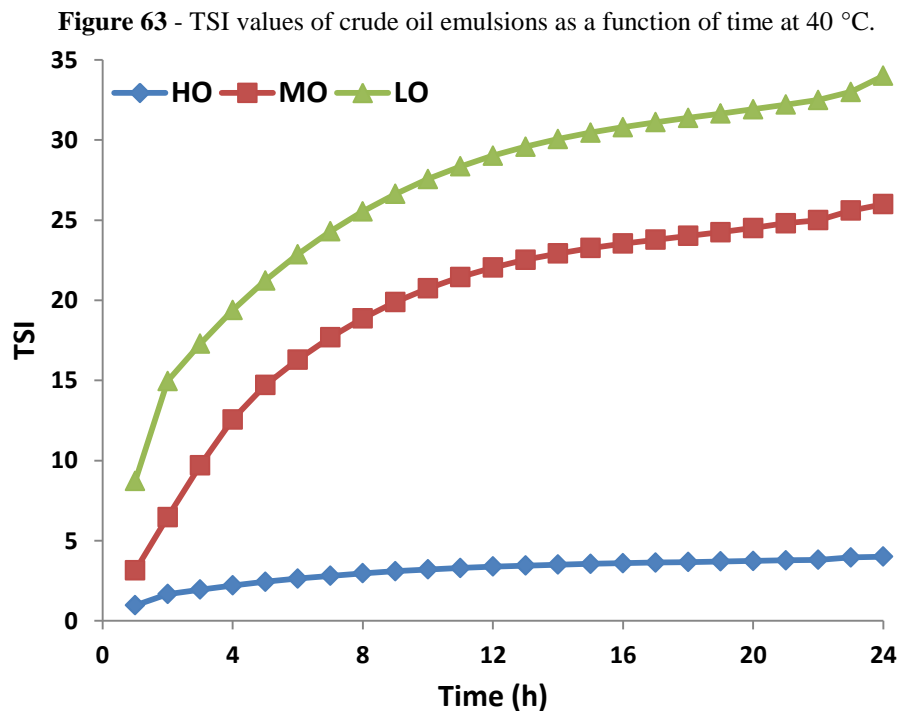
Equation 7

$$TSI = \sum_i \frac{\sum_h |scan_i(h) - scan_{i-1}(h)|}{H}$$

Where $scan_i(h)$ is the light intensity of the i -th scan at the height of h , and H is the total height of the measured sample. The combined effect of multiple instability phenomena on light intensity changes can be characterized by TSI . The larger the TSI value, the more unstable the system. **Figure 63** presents the TSI of the three crude-oil emulsions for 24 h. As can be seen from TSI , the emulsions stability results are as follows:

$$HO > MO > LO$$

It is important to mention that the measurement in the Turbiscan considers not only creaming but also the flocculation and the coalescence phenomenon.



4.5.2 Consolidation

The results of emulsion-cell tests in the laboratory with LO, MO and HO + water cut 80 %, under 2.0 bar of CO₂ pressure and 40 °C, allowed one to conclude that the behavior of the emulsion system (type and stability of emulsion) is strongly correlated with crude oil type. HO and MO formed O/W emulsion, and the LO formed W/O emulsion. Additionally, it was verified that the W/O emulsion formed with the HO was the most stable one. Therefore, it is possible to conclude that the type and the stability of the emulsion formed with HO may be correlated to the very high weight loss value obtained for this oil in the multiphase-flow loop tests.

4.6 Results of rotating cylinder electrode (RCE) testing

In this work, which gave rise to specific publications^{159,142,141,160,142,161}, carbon-steel CO₂ flow-induced corrosion was studied in a particular environment using a multiphase-flow corrosion loop and, as mentioned many times, higher weight losses were obtained for HO in CO₂-containing environments. As mentioned, according to the review of Wang and Zang⁷⁹, higher corrosion rates for heavy crude oil were not expected. Additionally, an stable emulsification process for heavy crude oil was verified.

In this topic, rotating cylinder electrode tests accompanied by electrochemical measurements were performed to finally elucidate the high weight loss of the API 5L X80 steel grade in the presence of HO and the influence of the type of emulsion formation. A short literature review was presented to understand the obtained results.

Few studies of oil/water/gas mixtures in multiphase flow conditions are found in the literature. Most published works study only water and gas multiphase flowing^{162,95,120,34}.

Wang and Zang⁷⁹ described the difficulties in monitoring the flow pattern and the emulsification process during dynamic tests of crude oil, water and gas. The researchers cited the difficulty in studying specifically heavy oil in multiphase-flow loops and the need to advance in experimental techniques. They emphasized the importance of the influence of fluid emulsification on corrosion processes, the stability of the emulsion, the entrainment of water by crude oil, and the wetting behavior in the corrosion process. According to the authors, studies of the emulsification processes should be included to understand the influence of the emulsion type on corrosion.

Waard *et al.*¹¹⁰ cited that water entrained in crude oil can be estimated by API gravity. The critical water break value (W_{break} , see also **Annex I**) can be defined as the amount of water that can be entrained into crude oil. For WC in a brine mixture below W_{break} , the aqueous phase is retained in the oil phase, preventing pipeline corrosion problems. The W_{break} is defined as¹¹⁰:

$$W_{break} = -0.0166 * API + 0.83$$

Wang and Zang⁷⁹ also mentioned the importance of crude-oil chemistry in the corrosion process. Several compounds are found in crude oils and a SARA analysis (**Annex I**) can inform the distribution of each major component: saturated (S), aromatic (A), resins (R) and asphaltenes (A). Each type of hydrocarbon gives specific properties to crude oils; for example, asphaltene is a natural emulsifier. Crude oils with significant amounts of asphaltene combined with brine and under specific operation conditions (shear stress, gas-phase rolling effect, flow pattern) can lead to an emulsification process, a common phenomenon in oil exploration.

According to Waard *et al.*¹¹⁰, in W/O emulsion, the corrosion rate of carbon steel is lower than in the presence of only water or brine. The water wettability of the steel surface controls CO₂ corrosion. The higher the water wettability, the higher the corrosion intensity. The authors concluded that the oil phase wettability prevents corrosion¹¹⁰.

Ma *et al.*¹⁶³ studied the influence of water-wetting and oil-wetting occurrence. They verified that intermittent oil/water wetting cycles make the pipeline corrosion process complex and high-frequency cycles accelerate localized corrosion of carbon steel near the oil/water/metal interface. The researchers further reported that, under dynamic conditions, shear stress and vortex turbulence determine oil film stability and intermittent wetting corrosion behavior. Additionally, a smooth surface can decrease shear stresses and the intensity of the vortex turbulence. Consequently, the life of the oil film on the surface increases and mitigates the corrosion process.

Wei *et al.*¹⁶⁴ conducted tests in an autoclave under dynamic conditions at a flow velocity of 1 m/s and partial pressure of 10 bar of CO₂ at 60 °C with WC of 10 %, 30 % and 80 %. Pipeline 3Cr, L245 and 16Mn steels were immersed in water-crude oil emulsions for seven days. The characteristics of crude oil were not mentioned.

The researchers observed lower corrosion rates for WC values below 30 % and the highest corrosion rate for the WC of 80 %. According to the authors, this occurred because for WC values lower than 30 %, the emulsion was O/W type and the steel specimens were exposed to intermittent water/oil wetting: the crude oil covered the surface of the samples, promoting a low corrosion rate. On the other hand, in the 80 % WC, the emulsion changed into the W/O type emulsion, and the specimens suffered water wetting. Consequently, the corrosion rates of the three steel specimens correspondingly increased.

Wang and Zang⁷⁹ mentioned that heavy crude oils are generally more protective against corrosion than light crude oils. They also verified that asphaltene extracted from some crude oils presents inhibitive effects due to their adsorption and persistency on carbon steel surfaces.

Nesic, Solve and Skjerve¹⁶⁵ investigated the effect of various hydrodynamic parameters on the corrosion rate of low-carbon steels in CO₂-brine solution in the presence of inhibitors. Two different flow geometries were studied simultaneously in the same electrolyte using a rotating cylinder electrode and a pipe flow loop (loop and RCE interconnected).

The authors concluded that it is possible to obtain the similar mechanism and approximately the same CO₂-corrosion rates in both RCE and loop tests since the same conditions were adopted: the same water composition and mass transfer. It is worth mentioning that these authors used equations proposed by Silverman¹⁶⁶⁻¹⁶⁸ to estimate the velocity of the RCE from the loop velocity.

Kermani and Morshed considered that performing corrosion tests without crude oil using only the brine mixture can lead to gross errors when using the test results to estimate possible corrosion problems in the field⁹³.

4.6.1. RCE Preliminary tests: CO₂-brine solution without crude oil

As mentioned in **Chapter 3**, a simple rotating electrode system was constructed. Preliminary tests without oil were performed aimed at validating the functioning of the system and establishing a standard for comparison in relation to the results of tests with crude oil.

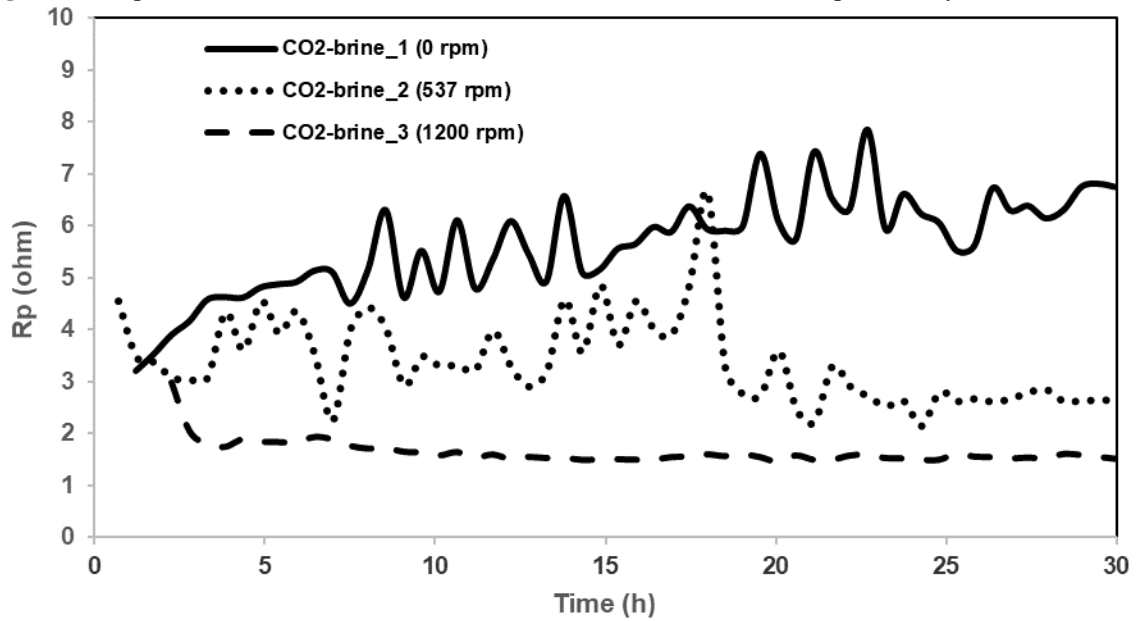
Figure 64a shows the monitoring of R_p during the CO₂-brine solution tests.

It can be seen that the values of R_p decrease with increasing rotation speed; that is, the lower the rotation speed, the higher the polarization resistance. Corrosion current densities (i_{corr}) were estimated from R_p considering the B constant value of 0.013 V. This value considers that the corrosion reaction and hydrogen evolution are governed by the activation polarization (0.04 V/decade and 0.120 V/decade, respectively)^{52,169}.

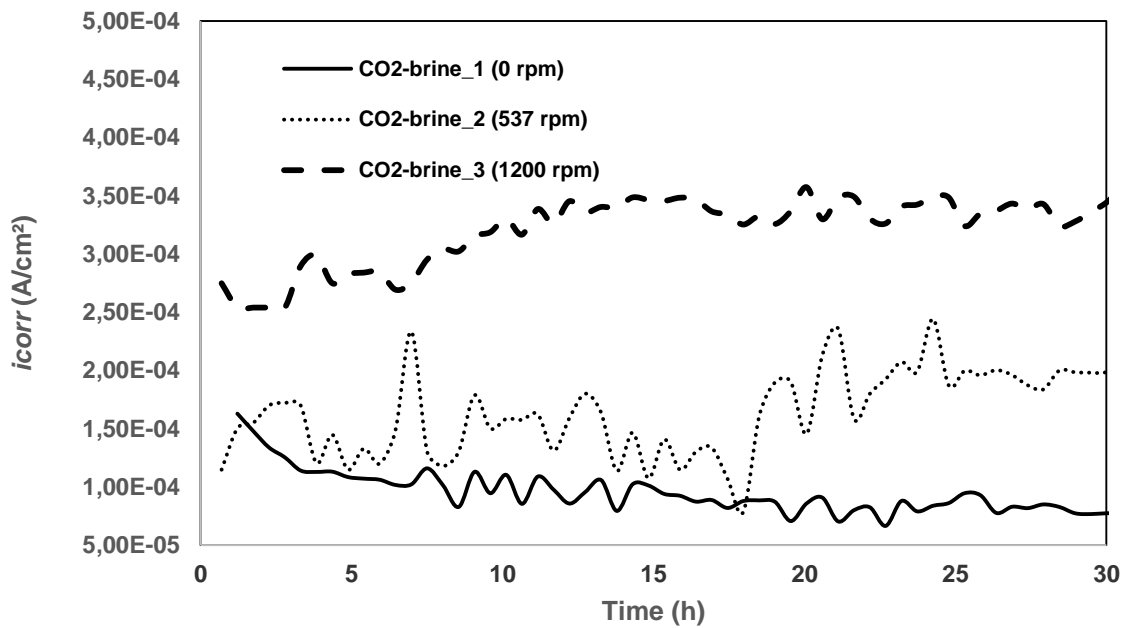
This is an approximation since, in CO₂, there is the formation of corrosion products (FeCO₃) and therefore, there is the influence of resistance polarization, both in the anodic and cathodic branches. Furthermore, the cathodic reaction is under a mixed influence (activation and concentration polarization), a fact confirmed in the literature⁵².

Figure 64b shows the plot of i_{corr} as a function of time. From the integration of i_{corr} , the corrosion rate in mm/year was estimated. These values were compared with the corrosion rates obtained from the weight loss of the working electrode after 30 h of testing in the RCE (**Figure 65**).

Figure 64 – Rp (a) and estimated i_{corr} (b) for RCE tests in CO₂-brine solution (preliminary tests without oil).



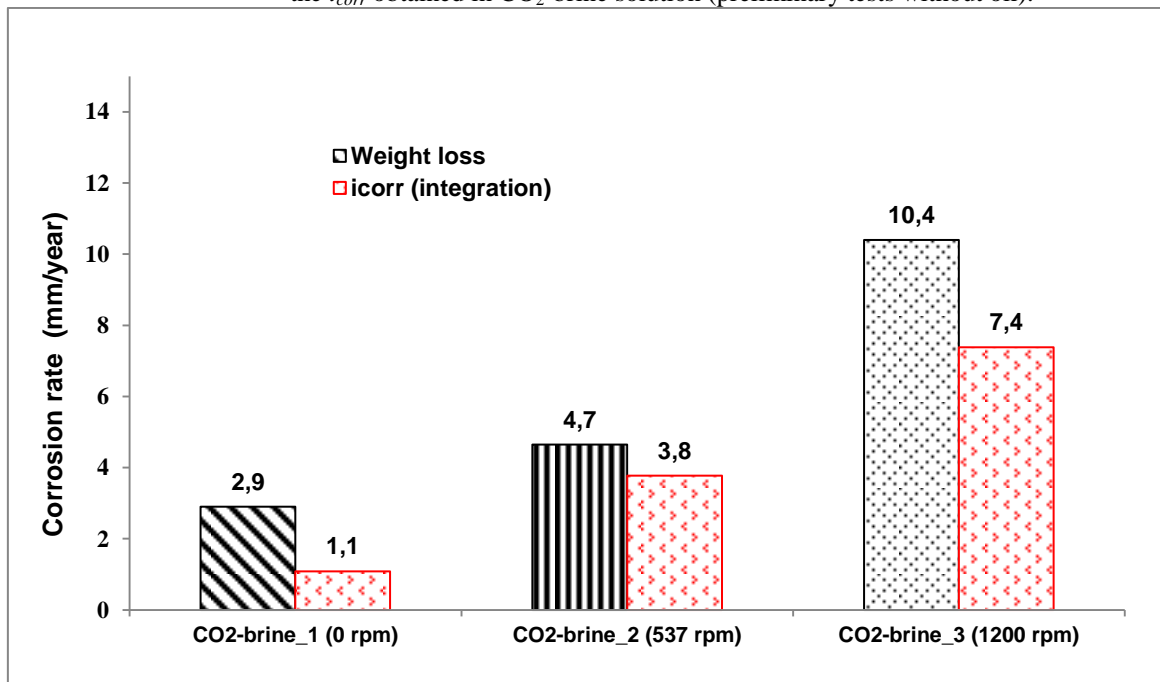
(a)



(b)

From **Figure 65**, a good correlation between the two measures can be seen, even with all the approximations made in the calculation of i_{corr} and possible errors associated with the distribution of electrical currents in the adopted experimental apparatus (for example, non-uniform distribution of current lines between the working electrode and the counter electrode). This validates corrosion monitoring through polarization resistance measurements.

Figure 65 – Corrosion rate calculated from weight loss measurement and estimated through the integration of the i_{corr} obtained in CO₂-brine solution (preliminary tests without oil).



Before the disassembly of the tests, a cathodic polarization was carried out up to 1.2 V, SCE and the limit current density was not reached. Similar results were obtained by Henriquez *et al.*⁵² in a brine solution saturated with CO₂.

To correlate rotation velocity with cathodic current, these authors determined the cathodic current density corresponding to a cathodic potential of 0.87 V, SCE for different rotation velocities and immersion times from 2 h to 15 h. With the results obtained, they plotted curves relating the densities of cathodic currents with the square root of the angular velocity.

The authors verified that regardless of the immersion time, the current densities increased with the square root of the electrode rotation speed resulting in a mean straight line that passed through the current measured with the electrode stopped. The authors mention that this measured current is not at the origin, which can be explained by the buffer effect of the acid dissociation of CO₂ in solution, contributing to an additional gain in cathodic current^{52,170}.

Figure 66 shows a plot with data from the present study similar to those of the referenced authors⁵². It can be verified that the cathodic current density increases with the square root of the angular velocity forming a mean straight line that passes through the cathodic current obtained with the electrode without agitation.

These results validate the use of R_p as a suitable electrochemical measure for monitoring the corrosion of RCE for different rotational velocities in the proposed system.

Figure 66 – Cathodic current densities for the cathodic potential of -0.87 V, SCE as a function of the square root of angular velocity (preliminary tests without crude oil).

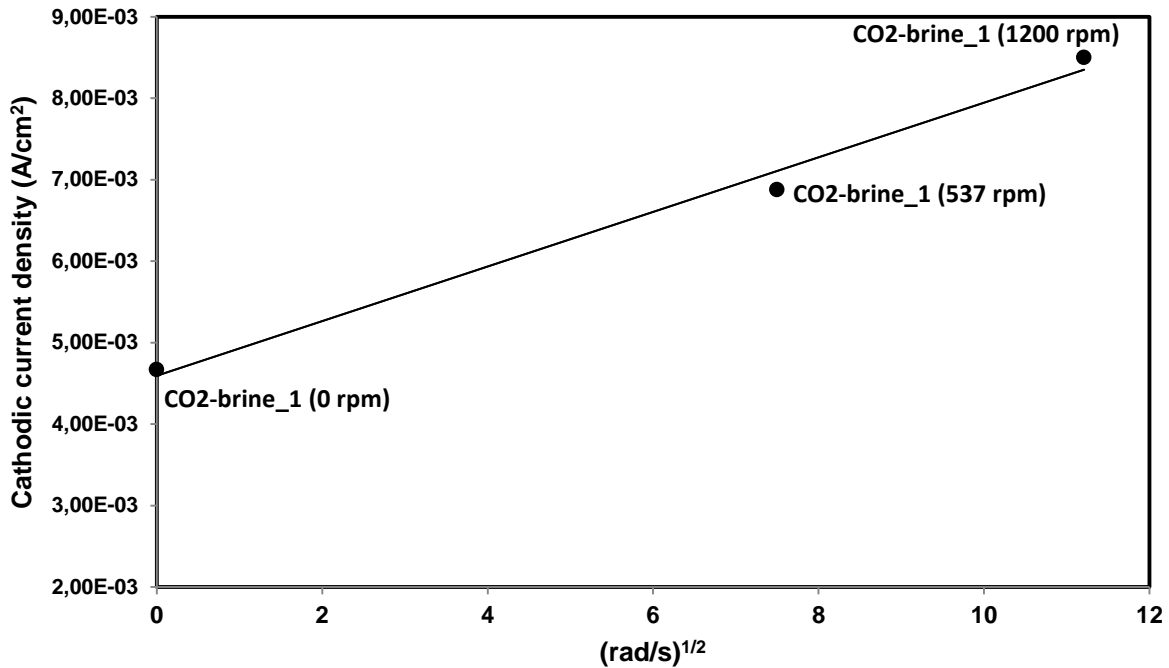


Figure 67 shows the surface of the working electrodes after 30 min of their removal from the autoclave for examination under an optical microscope (OM). We can observe reddish corrosion products resulting from the rapid oxidation of the metal after disassembly. The higher the reddish color intensity, the higher the rotation velocity. On the surface of the stationary electrode, there is also an adhered layer, probably FeCO_3 .

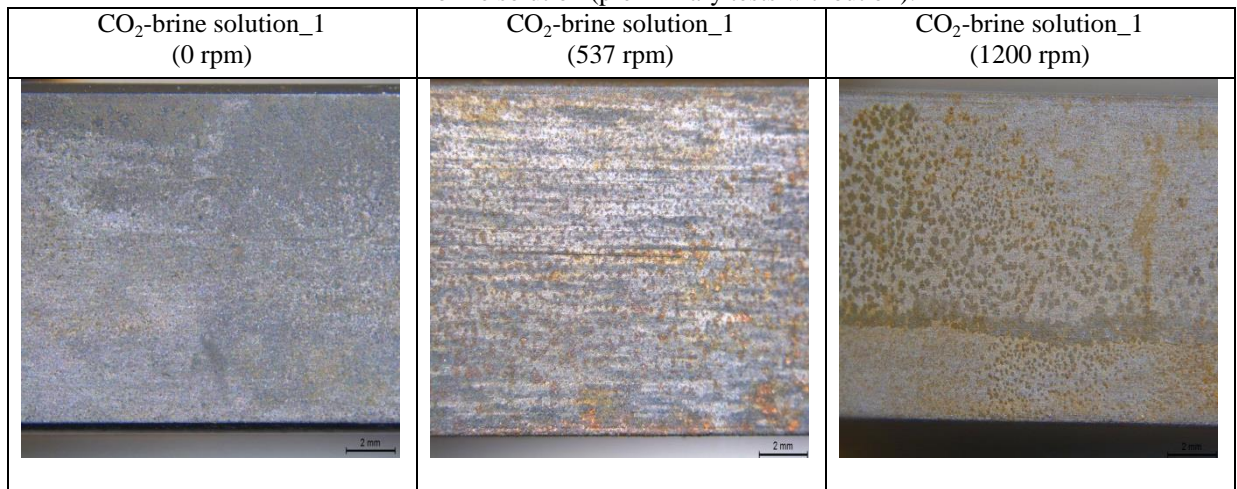
These results lead to the assumption that the FeCO_3 remained in greater quantity on the working electrode, contributing to the decrease in the active area available for the hydrogen reduction reaction during the autoclave test and to the decrease in the formation of the reddish color after the exposure of steel to air.

On the surface of the working electrodes tested at 537 rpm and 1200 rpm, the corrosion products were removed with greater intensity for the higher rotation velocity, increasing the area for the hydrogen reduction reaction in the autoclave and reducing the reddish-color formation after exposure to air.

Most likely, during the autoclave test, on the working electrode tested at 537 rpm, the FeCO_3 was formed and removed periodically, which explains the higher oscillation of R_p . In the working electrode tested at 1200 rpm, the corrosion products must have been removed quickly, leaving the surface practically unprotected, which explains the higher corrosion rate and the smaller amplitude of the R_p .

The removal of these corrosion products is an action of a mechanical nature associated with shear stresses on the surface of the working electrode. The estimated shear stress values for the CO_2 -brine solution tests at rotational velocities of 537 rpm and 1200 rpm are approximately 84 Pa and 330 Pa, respectively. The calculations are presented in **appendix II**.

Figure 67 – Optical Microscopy (OM) investigation of the surface of the specimen after the RCE tests in CO₂-brine solution (preliminary tests without oil).



4.6.2. RCE with CO₂-brine-LO and CO₂-brine-HO mixtures

For the tests with crude oil, a rotation velocity of 1200 rpm was adopted, which is the same value applied in the liquid pump used in the loop tests¹⁴².

Figure 68 shows the R_p monitoring results of the tests carried out in CO₂-brine-LO and CO₂-brine-HO, and oil-free CO₂-brine solution, all with a rotation of 1200 rpm.

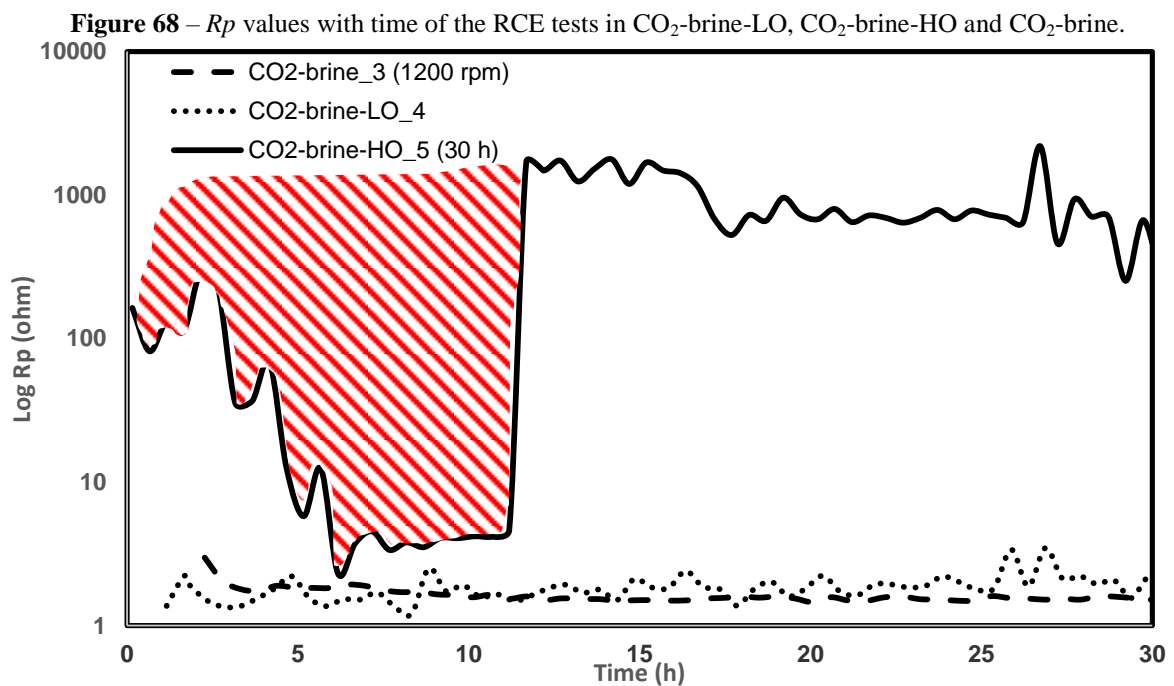
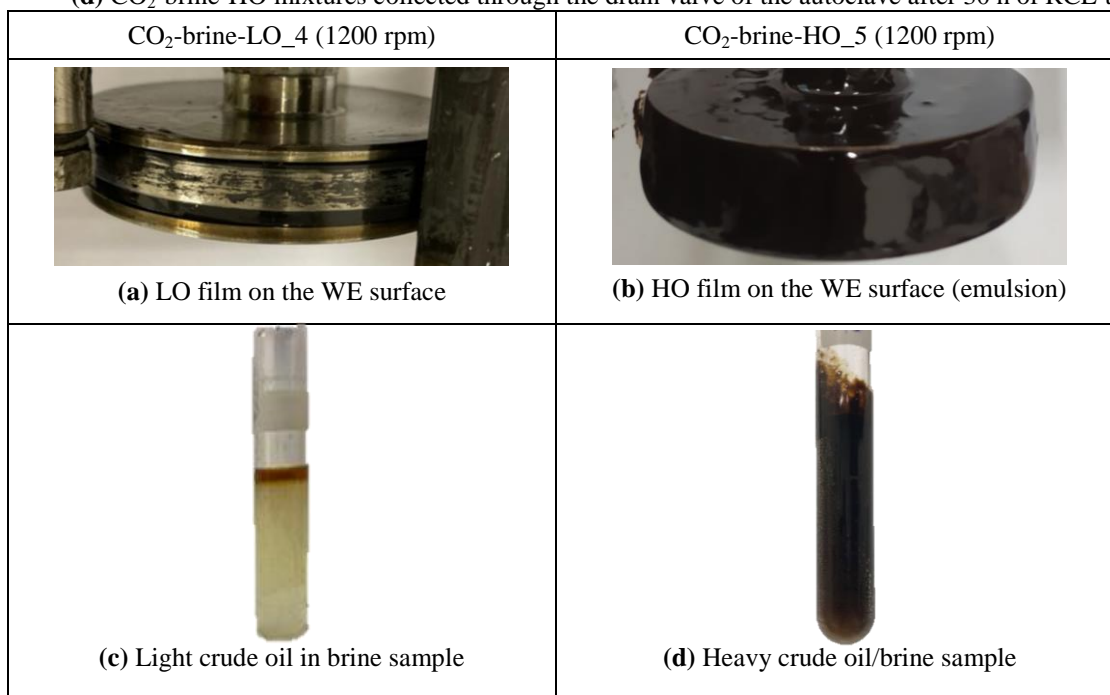


Figure 69 shows the surface of the WEs tested in the presence of crude oils after the autoclave disassembling and samples of brine-oil mixtures removed through the drain valve.

Figure 69 – Surface images of WEs without cleaning (a) LO (b) HO, and (c) sample of the CO₂-brine-LO and (d) CO₂-brine-HO mixtures collected through the drain valve of the autoclave after 30 h of RCE tests.



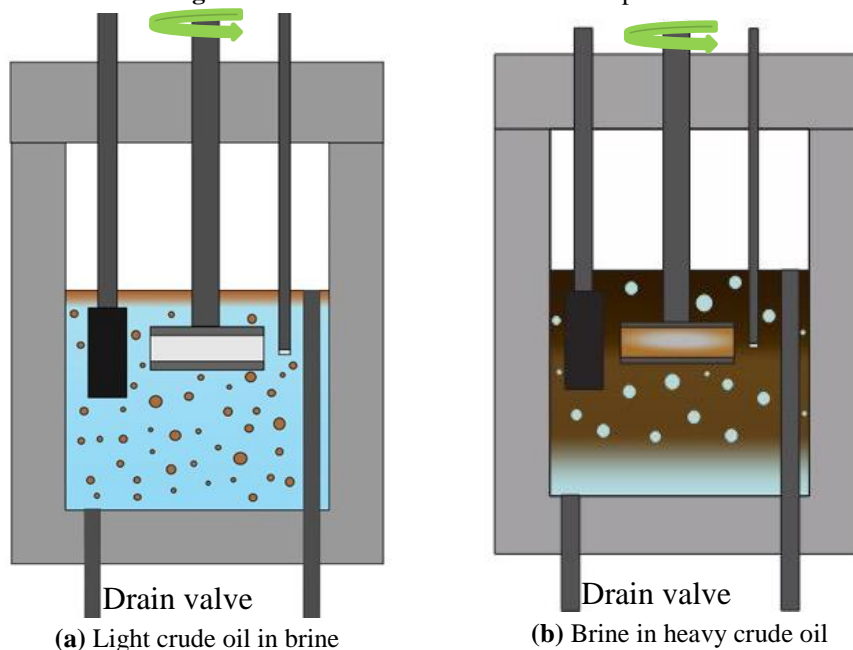
From **Figure 68**, we can observe that the R_p values in the CO₂-brine solution were very similar to values obtained in the CO₂-brine-LO mixture, which shows that the monitoring of R_p was representative and could be correlated at least qualitatively with the corrosion rates.

In the CO₂-brine-LO mixture, the R_p oscillated and, after 10 h of testing, the values were slightly higher than those obtained in the CO₂-brine solution, indicating that the presence of light crude oil had a somewhat inhibiting effect on the corrosion process (**Figure 69a**).

Oscillations in the R_p indicate an intermittent oil/water wetting occurred, as mentioned in the literature¹⁶⁴. In **item 4.5**, it was verified that LO undergoes an unstable O/W emulsion process in brine. This can be confirmed by the appearance of the sample taken just after autoclave disassembling (**Figure 69c**). The beginning of oil separation and a formation of whitish coloration due to the formation of an unstable W/O emulsion can be seen.

The schematic of the emulsification processes of the LO is shown in **Figure 70a**. It can be seen that the surface of the carbon steel working electrode is kept in contact with the CO₂-brine solution most of the time and is hit intermittently with LO droplets.

Figure 70 – Scheme of the emulsification process.



For the test with CO₂-brine-HO, the R_p did not show a good correlation with the R_p obtained in the oil-free brine, as observed in the test carried out with LO. In the first 6 h, periodic oscillations and a gradual decrease in R_p were observed. Most probably, as soon as the agitation started, the surface of the working electrode was quickly covered by the HO due to the formation of the vortex, resulting in high R_p values. Over time, the surface of the working electrode is wetted with free water, which in turn is arrested into the heavy oil. This causes a gradual decrease in free water and an increase in the viscosity of the W/O emulsion. Similar behavior was observed with tests adopting a WC of 80 % in the literature¹⁶⁴.

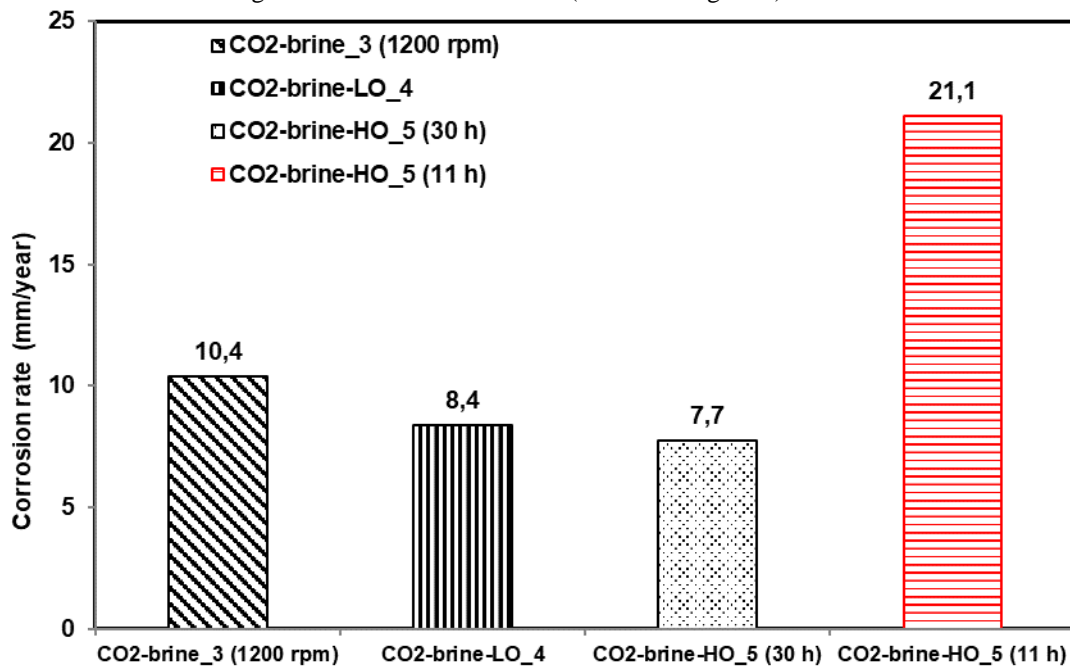
Between 8 h and 11 h, a more stable monitoring signal was observed. Most likely, the vortex effect was reduced by increasing the viscosity of the emulsion. Simultaneously, the wetted area of the surface of the working electrode slowly decreased up to the complete covering of the metal surface with the emulsion, i.e., the amount of free water decreased to the point of no longer reaching the surface of the working electrode. This caused the interruption of the electrical signal, and thus, the measurement of R_p was no longer possible. In this region (after 11 h), R_p assumed a value about three orders of magnitude higher than in the two other tests, indicating that monitoring R_p in CO₂-brine-HO was impossible because the RCE was isolated by a dense layer of an adhered W/O emulsion. A significant result of this monitoring was the indication of the exact time that the emulsion completely covered the surface of the RCE, not allowing free water access and, thus, inhibiting the corrosion process. In fact, after autoclave disassembling, the presence of a high-viscosity film on the surface of the RCE (**Figure 69b**) and the formation of a stable emulsion in the liquid phase (**Figure 69d**) were verified, confirming that an emulsification process of heavy-crude oil in brine occurred the test period.

Figure 70b shows a scheme of this emulsification process. Because of the type of emulsion (W/O), it is crucial to consider the critical water break. The calculated critical water break of the heavy crude oil was 58 % (**Annex I**). This means that 58 % of the total water enters the oil. As 80 % WC was adopted, 22 % of free brine should have remained in the lower part of the autoclave. In this way, the interruption of the electrical signal after 11 h indicates the instant in which the intermittent cycle of wettability between HO emulsion and free brine was interrupted, and the corrosion process was inhibited.

After the autoclave disassembling and cleaning the working electrodes, mass loss measurements were performed. **Figure 71** presents the results of the corrosion rates calculated from the mass loss for the tests carried out with brine without and with the presence of light and heavy crude oils.

For the CO₂-brine and CO₂-brine-LO tests, the corrosion rates were calculated using the whole 30 h of testing because the *R_p* monitoring over the test time was possible. Two corrosion rate values were obtained for the test with HO: one using the whole test time of 30 h and another using the time of 11 h. The latter was used because we considered the corrosion was negligible after the electrical signal interruption.

Figure 71 – Corrosion rates calculated from weight loss measurements. For HO two values are presented: one considering the immersion time of 11 h (brine-wetting time) and the total test time of 30 h.

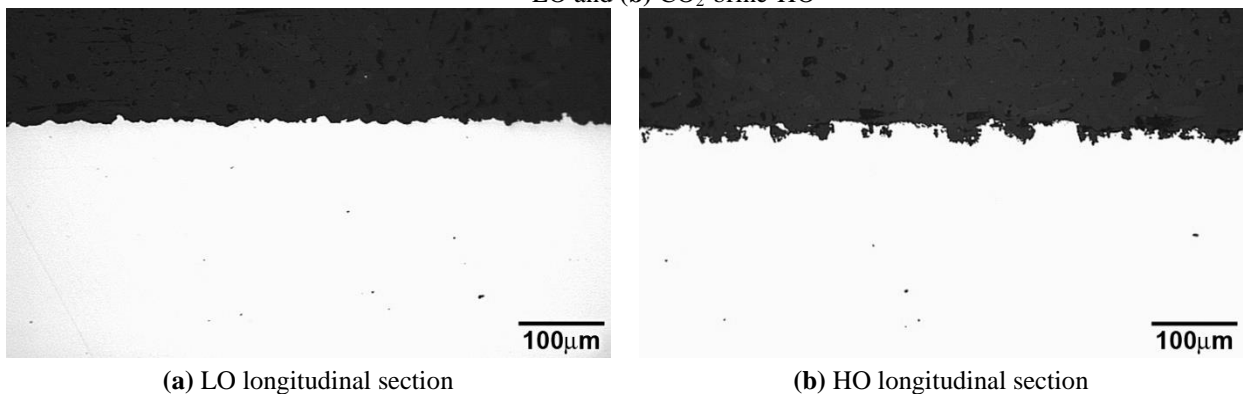


Therefore, we have three important points to be considered in **Figure 71**. The first is the result of the CO₂-brine-LO_4 test in which an O/W emulsion is formed, which shows the corrosion rate value to be slightly lower than the test without oil (CO₂-brine_3). This tendency was also observed with the results of *R_p* monitoring (**Figure 68**). The lowest intensity of corrosion in the presence of LO has been attributed to the intermittent covering of the steel surface with oil droplets.

The second point is the corrosion rate of CO₂-brine-HO calculated considering 30 h of testing. This value is very close to the result obtained in CO₂-brine-LO. However, the HO R_p values were higher than the LO R_p values (**Figure 68**), particularly after CO₂-brine (11 h): values higher than three orders of magnitude were measured. These results indicate that R_p values in CO₂-brine-HO are not associated only with the corrosion process but are strongly influenced by the W/O emulsification process over time (**Figure 69d**) which causes a considerable increase in the resistivity of the liquid phase resulting in high R_p values.

The third point is related to the corrosion rate of the HO calculated considering the first 11 h of testing in which the metal was in contact with free brine. This value is much higher than the LO corrosion rate. This result was supported by the more severe attack observed by visual examination of the WE tested in the CO₂-brine-HO. This was confirmed by observation of the longitudinal section of the WEs through an optical microscope shown in **Figure 72**. It can be seen that the WE tested in CO₂-brine-HO presents a more severe attack than the one tested in CO₂-brine-LO.

Figure 72 – Optical Microscopy (OM) analysis of the surface of the specimen after RCE test in (a) CO₂-brine-LO and (b) CO₂-brine-HO



4.6.3. Consolidation

In the RCE tests, a higher corrosion rate was also verified for HOI, which confirmed the results obtained from the multiphase-loop tests in **item 4.2**. These results, added to the results obtained in experiments carried out to verify the type of emulsion formed for each oil (**item 4.5**), allow us to assume that the causes of the greater aggressiveness of heavy oil can be attributed to the formation of a stable W/O emulsion with high viscosity associated with a relatively high amount of free brine after the emulsification process (22 %). This determined the intermittent wetting of the steel surface by free brine and emulsion. Most likely, the corrosion products formed during the contact of the aqueous phase with the steel were easily removed during contact with the high-viscosity emulsion (higher shear stress). It should be mentioned that the corrosion practically ceased when the surface of the WE was covered with the W/O emulsion.

CHAPTER 5 - GENERAL DISCUSSIONS

In this chapter, a comprehensive discussion will be carried out on each stage of the development of the study of corrosion in multiphase-flow pipelines. As mentioned earlier in this work, the impact of corrosion damages on the O&G industry goes through capital and operating expenses (CAPEX and OPEX) and reaches health, safety, and environmental issues. In this context, research and development can produce the necessary knowledge to establish material selection criteria for projects and topside or subsea structures to provide technological solutions and flow assurance.

In the O&G industry, a multidisciplinary synergy is needed in research and development projects to deal with existing problems and overcome technical and technological challenges in a way that represents, even if, on a reduced scale, the phenomena and mechanisms that occur in the field.

In this study, given the complexity of the experimental proposal for corrosion in multiphase flow, the entire conception of the loop project and the planning of the test matrix was discussed with the contracting company, other professionals from the institute where the project was developed and with the support of Interdisciplinary Nucleus of Fluid Dynamics at the Federal University of Rio de Janeiro.

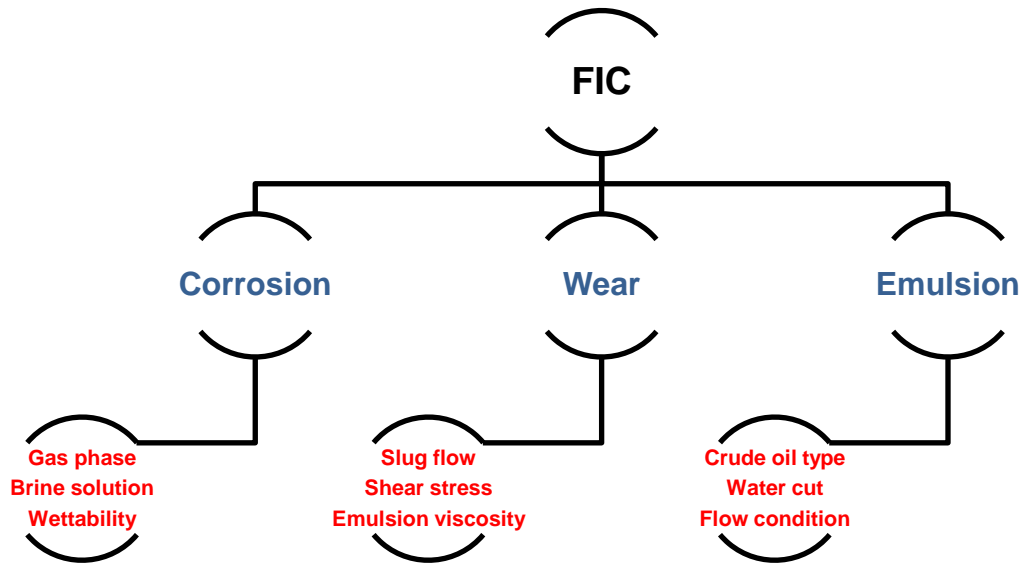
For the design of the loop, initially, it was necessary to define the main parameters of the tests to be carried out: flow pattern, salinity, water cut, and type of crude oils. These parameters were selected in discussions with the contracting company's professionals based on field data. At this stage, crude-oil inclusion in the study was one of the most challenging parameters. Specifying the equipment and instruments and keeping the liquid phase mixture (water and crude oil) adequate throughout the test period promoted a multidisciplinary learning curve. Although an investigation of the rheology of emulsion systems was not addressed in this study, the impact of system changes on the corrosion and wear process was explored.

The multiphase flow loop was designed and manufactured to promote an adequate environment that best reproduces the aforementioned operating parameters. The main challenge in this step was establishing the multiphase flow conditions, the corrosive environment (brine, oil, CO₂ and H₂S), and measuring carbon steel's corrosion rates (API 5L X80).

The study's first results allowed realizing that analyses of the observed and measured data were also challenging. After the tests, the morphology of the steel surface did not show a pure corrosion process, and the liquid phases (brine and light or heavy oil) at the end of the tests showed different appearances. In the presence of CO₂, the results showed extremely high weight loss for the HO, much higher than for the LO, which is unexpected. Thus, some hypotheses were raised. To verify the validity of these hypotheses, complementary studies were carried out through three work fronts to evaluate the impact of corrosion, cavitation, and emulsification processes in flow-induced corrosion. **Figure 73** presents the three work fronts

and the individual factors in a structured way. The proposed structure does not intend to order the interaction between the mentioned factors (gas phase, brine solution, wettability, slug flow, shear stress, crude oil type, water cut, and flow condition). However, it represents the impact of these factors on each work front.

Figure 73 – Main influencing factors on flow-induced corrosion



The proposed environments for the initial tests performed in the multiphase-flow loop were addressed to the corrosion mechanisms by CO₂ and the mixture of CO₂/H₂S establishing a sweet regime for all conditions. Based on the test results of the initially proposed matrix, it was possible to observe the greater aggressiveness of CO₂ at higher partial pressures and the inhibitory effect of H₂S, even in small proportions. It was also verified that the crude oil adding impacted the conductivity of the aqueous phase and the viscosity of the liquid phase over the test time. The former was not considered for flow-parameter measurement, and the viscosity variation measurement was not foreseen. Thus, in this study, the alterations that occurred during the loop tests were detected, but the installed instrumentation did not accurately measure them. These factors pointed out the need to improve the instrumentation of the constructed loop. On the other hand, the knowledge acquired at this stage, although it did not allow for establishing a criterion that guarantees the flow of mature wells, contributed to the development of an innovative exploratory methodology that will be useful for the adequate planning of new test matrices in future studies.

The characteristics of the surface morphology of the carbon steel at the end of the loop tests led to the hypothesis of the occurrence of wear due to cavitation. The appearance of concavities and the removal of material in the flow direction (upstream-downstream) led to a study adopting a standardized test to verify the susceptibility of carbon steel API 5L X80 to wear by cavitation. The results of this study confirmed the hypothesis of the influence of cavitation on the corrosion processes and allowed the correlation of the slug flow pattern with the observed damages. On the other hand, this investigation did not assess measurements of

the combined effect of the mechanism of wear and corrosion regarding the formation and removal of corrosion products, either by hydrodynamic effects or by shear stresses increased by the viscosity of the emulsion.

Additionally, a prediction model was built based on the data obtained in the loop tests with the support of a statistician. It was possible to observe the interaction between the viscosity of crude oil, the angle of inclination of the loop section (0° and 45°) and the partial pressures of CO_2 e H_2S in flow-induced corrosion. The statistically treated prediction model showed a good correlation with the results of the loop tests. Some conditions predicted by the model not included in the initial test matrix were graphically presented, providing a notable gain on the selection criteria of materials used in equipment that can operate under the studied conditions. The predictive model pointed to the influence of viscosity as an impacting factor on the corrosion rate, including interaction with the loop slope and the partial pressure of H_2S . These results pointed out the need to explore changes in the liquid phase as we had observed the formation of a stable emulsion with heavy oil (W/O) of high viscosity. The need to understand the emulsification process led to a specific study that included a new literature review and interaction with experts in the field.

The new literature review pointed out that, most of the time, heavy oils present higher inhibitory effects than light oils. However, in the case of the results of the loop tests, the behavior was antagonistic. Higher corrosion rates were observed in the heavy oil tests. This made the understanding of emulsification processes even more pressing. This study was divided into two stages. The first step investigated the type and stability of the emulsions for the two studied crude oil, considering a WC 80 and a 2.0 bar CO_2 partial pressure. This condition was selected because it was the one that presented the highest corrosion rate in the loop tests. In the second stage, the impact of each light or heavy crude oil on the corrosion process was evaluated using RCE.

The results of the tests carried out in the first stage corroborate the observations made in the loop tests for each oil. It was found that the visual aspect of oils and their properties changed over time due to emulsification processes, with the formation of an O/W emulsion (less stable) for the light oil and W/O (more stable) for the heavy oil. The viscosity of the emulsions was not measured during the tests. However, the visual observation of the aspect of the heavy oil after each test allowed the verification that the viscosity increase with the emulsification process (W/O) was significant when compared to the oil in the initial state. Based on these conclusions, evaluating the impact of this phenomenon on corrosion involved the development of a new methodology: the RCE test adapted for carrying out experiments with oil in an autoclave.

The methodology consisted of monitoring the system using the polarization technique to determine the polarization resistance (R_p) applied in a RCE system adapted with electrodes (WE, RE and CE) to enable tests in an autoclave in the presence of an oil mixture. We sought to reproduce the more aggressive environment adopted in the loop tests (CO_2 -brine solution and WC 80). In planning the matrix for this step, the speed on the surface of the carbon steel

API 5L X80 (WE) was calculated, which defined the degree of agitation of the rotating electrode.

The results of the RCE tests led to the recognition and discussion of some relevant points. It was possible to raise a hypothesis that explained the reason for the higher corrosion rate found in the loop tests with heavy oil, an unexpected fact according to the consulted literature, as already mentioned.

Figure 74 compares light and heavy oil corrosion rates for tests carried out under the same conditions in the RCE and the multiphase-flow corrosion loop. Corrosion rate results obtained from loop tests were about three times higher for LO and about twelve times higher for HO than those obtained from RCE tests. To explain this big difference, a proposal for the interaction between the phases during the loop tests is presented. For this purpose, a schematic slug flow 2D map was built (**Figure 75**) for the multiphase system containing the gas and liquid phase phases. The liquid phase represents the brine solution, HO, LO, W/O, and O/W.

Figure 74 - Comparison between RCE test and loop multiphase-flow results for light and heavy crude oils and brine solution, CO₂ partial pressure of 2 bar and 80 % WC + 20 %.

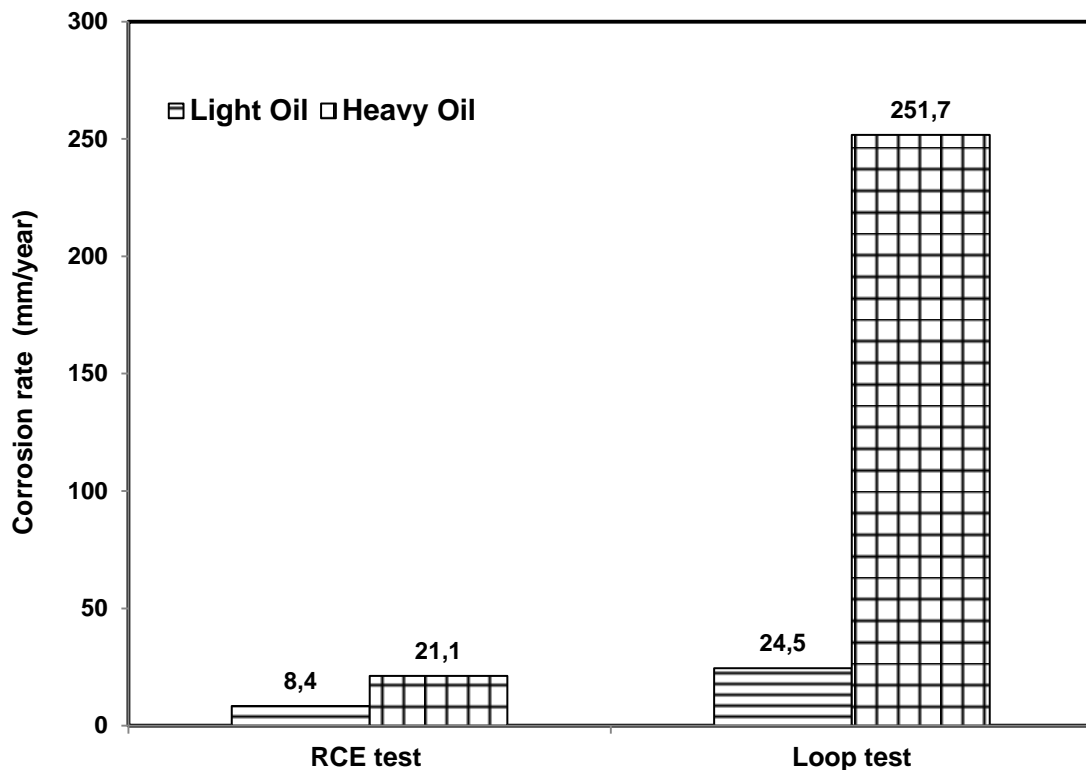


Figure 75a illustrates the slug flow proposed model in the system with LO. An O/W emulsion was formed, resulting in countless drops of LO dispersed in the aqueous solution. Over time, these drops became smaller and smaller to the point of turning the water white without significant changes in the emulsion viscosity. However, the oil in the water protected the carbon steel surface because the metal surface was submitted to wettability cycles between water and oil. The impact of this fluid property change was the inhibitory effect and a slight

reduction in the corrosion rate for the loop and RCE corrosion tests. As the slug flow pattern in the multiphase loop imposes more intense hydrodynamic effects and the RCE cannot reproduce these effects, the corrosion rate of the former was higher (**Figure 74**).

Figure 75 – Proposed multiphase slug flow 2D maps for (a) LO and (b) HO.

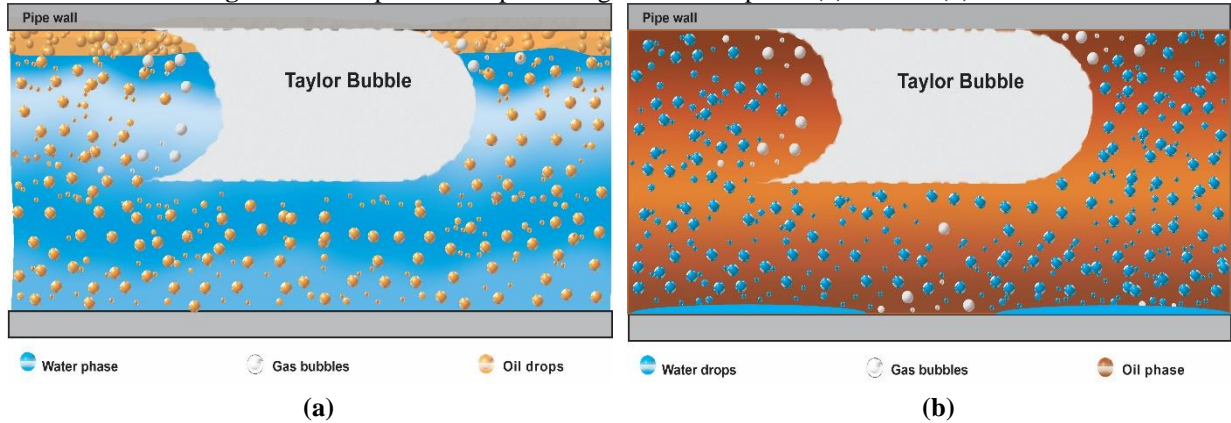


Figure 75b illustrates the slug flow proposed model in the system with HO. A W/O emulsion started forming. However, when the Water Break was reached, the water arrested into the oil ceased resulting in a liquid phase constituted by W/O emulsion and free water (22 %). During the multiphase-flow loop tests, the characteristic pulsation of a slug flow promoted an intermittent wetting of the metal surface with W/O emulsion and free water. This behavior increased the corrosion rates since the dispersed bubbles of the gaseous phase and the increase in the emulsion's viscosity promoted the removal of corrosion products formed on the carbon steel surface cyclically. In the RCE test, the surface of the steel electrode remained in contact with the W/O emulsion most of the time, and the free water remained at the bottom of the autoclave, a fact perceived by the interruption of the electrical signal of the electrochemical measurements. In this context, the slug flow reached a higher degree of severity than the RCE, not only because of the intensity of the forces involved but also because of the geometry and flow conditions.

As mentioned in **Item 4.2**, significative differences were obtained when H₂S was introduced in CO₂-containing environments. Higher weight loss values were obtained for the tests with LO. Additionally the influence of the specimen position also changed in the presence of H₂S. Both crude oils presented higher corrosion rate at the 0° position. All the differences observed in the presence of H₂S revealed that different mechanisms might act in the absence and presence of H₂S. Therefore, complementary studies are also necessary to understand the influence of H₂S. However, specific studies on this topic were not carried out in this work and will be considered for future projects

CHAPTER 6 - CONCLUSIONS

To study the corrosion in mature wells (with high WC values), a multiphase-flow loop was projected and constructed that simulated the slug regime. The challenge of manufacturing the corrosion loop led to the interaction with other research groups allowing a profitable interchange and permitting the loop construction with a low-cost investment. The first challenge was to simulate the typical hydrodynamic effects of intermittent flow. At this stage, the prototyping was carried out in a flow laboratory which allowed the definition of the appropriate parameters for developing the slug and instrumentation mesh, such as flow, pressure, and temperature meters. Using resistive flow meters brought an innovation in the study of corrosion. However, these instruments showed to be inaccurate in the multiphase-flow loop, so data obtained should be used only for comparison purposes. Another innovation implemented was using a compact separator developed on a small scale that showed efficiency in separating phases in all mixtures tested with light or heavy oil. The development of this equipment made possible the elaboration of the present research, being the only one in Brazil that allows the performance of corrosion tests in multiphase-flow conditions.

The proposed test matrix was defined to evaluate the corrosion in conditions close to the mature wells, i.e., with high water cut, and included light and heavy oils. The test gas phase represented injection conditions with CO₂ and exploration conditions with CO₂/H₂S ratios. The focus material of the research was the API 5L X80 carbon steel commonly used in rigid pipelines.

The results of the tests performed using the constructed multiphase-flow loop led to conflicting observations about the effect of flow on the corrosion process. It was observed that API 5L X80 carbon steel presented a higher corrosion intensity in CO₂-containing environments with concavities on the surface of the specimens which was attributed to the combined effect of hydrodynamics and the corrosion-erosion process. Additionally, the corrosion intensity with heavy oil was unexpectedly much more severe than in the presence of light oil, mainly at the horizontal position. After the tests with light and heavy oil, a change in the characteristics of the oils was observed, indicating the formation of emulsions that deserved attention in understanding the influence of emulsions on the corrosion process. A specific study showed that LO formed an O/W unstable emulsion and HO formed a W/O stable emulsion accompanied by a considerable amount of free water. Visual observation showed that the viscosity of the W/O emulsion (light oil) was lower than that of the O/W emulsion (heavy oil). All these observations allowed concluding that the higher corrosion intensity of the HO in a CO₂-containing environment at the horizontal position can be explained by a layer of intermittent free water at the bottom of the loop pipe where the API 5L X80 carbon steel specimens were installed. The increased corrosion intensity occurred because dispersed bubbles of the gaseous phase and the increased high viscosity of the W/O emulsion promoted the removal of corrosion products formed on the carbon steel surface cyclically.

The influence of the oil type was also noticed in the CO₂ and H₂S-contained environments, but, in this case, an apposite behavior occurred. Higher corrosion intensity was obtained for the light oil. For this oil, the influence of the specimen position also changed in the presence of H₂S. In the CO₂-containing environment, the weight losses were higher at the inclined position and, in the CO₂/SO₂-containing environment the higher values were obtained at the horizontal position. These differences revealed that different mechanisms might act in the presence of H₂S. Specific studies on this topic were not carried out in this work and will be considered for future projects

Using multiple regression and Box-Cox transformation, prediction models were obtained based on the results of the multiphase-flow loop tests. The corrosion rate model showed good correlations with the experimental test data. This model showed some important experimental conditions not explored in the experimental test matrix, demonstrating the model's predictive power. The experimental results showed that the corrosion rates, both in a CO₂-containing environment and in a CO₂/H₂S-containing environment, increased with the increase of CO₂ partial pressure. However, the response surfaces indicated areas of maximum corrosion rate and prediction of values in conditions that were not tested. Therefore, implementing this model will undoubtedly be very useful for future work.

CHAPTER 7 - FUTURE WORK SUGGESTIONS

The following suggestions are proposed to complement the study:

- improve the loop instrumentation, especially for online measurements of flow parameters, replacing it with techniques based on conductivity with tomography;
- develop a methodology to evaluate the viscosity of emulsions;
- perform a new loop test matrix varying the range of water cuts to explore the free water effect.

REFERENCES

- 1 M. B. Kermani and D. Harrop, "The Impact of Corrosion on Oil and Gas Industry," *SPE Prod. Facil.*, no. August, pp. 186–190, 1996, doi: 10.2118/29784-pa.
- 2 C. I. Ossai, B. Boswell, and I. J. Davies, "Pipeline failures in corrosive environments - A conceptual analysis of trends and effects," *Eng. Fail. Anal.*, vol. 53, pp. 36–58, 2015, doi: 10.1016/j.engfailanal.2015.03.004.
- 3 Y. Bai and Q. Bai, "Subsea Cost Estimation," in *Subsea Engineering Handbook*, Elsevier, 2019, pp. 143–172. doi: 10.1016/b978-0-12-812622-6.00006-3.
- 4 T. Y. Makogon, "Introduction," in *Handbook of Multiphase Flow Assurance*, Elsevier, 2019, pp. 1–33. doi: 10.1016/b978-0-12-813062-9.00001-4.
- 5 L. S. Furtado, E. Gonçalves, and L. A. R. Costa, "Risk and rewards dynamics: Measuring the attractiveness of the fiscal regime in the presence of exploratory risks," *Energy Policy*, vol. 132, no. April, pp. 1274–1287, 2019, doi: 10.1016/j.enpol.2019.05.059.
- 6 E. SMITH, J. DZIENKOWSKI, O. ANDERSON, J. LOWE, B. KRAMER, and J. WEAVER, *International Petroleum Transactions*. 2010.
- 7 E. Almeida, L. Losekann, Y. C. P. Braga, L. Nunes, and F. Botelho, "Custos e competitividade da atividade de E&P no Brasil," p. 36, 2016, [Online]. Available: <https://www.ibp.org.br/personalizado/uploads/2016/11/TD-custos-versão-SITE.pdf>
- 8 M. A. B. P. da Hora, B. Asrilhant, R. M. S. Accioly, R. Schaeffer, A. Szklo, and A. Hawkes, "Decision making to book oil reserves for different Brazilian fiscal agreements using dependence structure," *Energy Strateg. Rev.*, vol. 26, no. August, 2019, doi: 10.1016/j.esr.2019.100377.
- 9 R. Octavio, L. and Streeton, "Challenges and Opportunities for Subsea Multiphase Meters in the Brazilian Pre-salt," *J. Chem. Inf. Model.*, vol. 53, no. 9, pp. 1689–1699, 2013, doi: 10.1017/CBO9781107415324.004.
- 10 J. Sheffield, "World population and energy demand growth: The potential role of fusion energy in an efficient world," *Philos. Trans. R. Soc. A Math. Phys. Eng. Sci.*, vol. 357, no. 1752, pp. 377–395, 1999, doi: 10.1098/rsta.1999.0333.
- 11 X. Tang, C. Li, F. Ayello, J. Cai, and S. Nestic, "Effect of oil type on phase wetting transition and corrosion in oil-water flow," *NACE Corros.*, no. 07170, pp. 1–21, 2007, [Online]. Available: <http://www.onepetro.org/mslib/app/Preview.do?paperNumber=NACE-07170&societyCode=NACE>
- 12 M. Jerez-Carrizales, J. E. Jaramillo, and D. Fuentes, "Ingeniería y Ciencia Prediction of Multiphase Flow in Pipelines: Literature Review Prediction of Multiphase Flow in Pipelines: Literature Review," vol. 11, no. 22, pp. 213–233, 2015, doi: 10.17230/ingciencia.11.22.10.
- 13 S. Wang, K. George, and S. Nešić, "High pressure CO₂ corrosion electrochemistry and

- the effect of acid acetic,” *Nace Int.*, no. 04375, p. Paper No. 375, 2004.
- 14 B. Hu, S. Nuland, M. Langsholt, P. Andersson, and C. Lawrence, “A fast X-ray tomography system in multiphase pipe flow measurement,” 2011.
 - 15 H. Corneliussen, Sidsel; Couput, Jean-Paul; Dahl, Eivind; Dykesteen, Eivind; Frøysa, Kjell-Eivind; Malde, Erik; Moestue, Håkon; Paul Ove; Framo and Schlumberger Scheers, Lex; Tunheim, *Handbook of Multiphase Flow Metering*, vol. 2, no. March. 2005.
 - 16 S. Nešić, “Key issues related to modelling of internal corrosion of oil and gas pipelines - A review,” *Corrosion Science*, vol. 49, no. 12. pp. 4308–4338, 2007. doi: 10.1016/j.corsci.2007.06.006.
 - 17 G. Oddie, H. Shi, L. J. Durlofsky, K. Aziz, B. Pfeffer, and J. A. Holmes, “Experimental study of two and three phase flows in large diameter inclined pipes,” *Int. J. Multiph. Flow*, vol. 29, no. 4, pp. 527–558, 2003, doi: 10.1016/S0301-9322(03)00015-6.
 - 18 M. Daas, T. Golczynski, and J. Harry, “Minimum Flowrate to Unload Gas Wells: Dynamic Multiphase Modeling to Validate Existing Correlations,” *Proc. SPE Lat. Am. Caribb. Pet. Eng. Conf.*, 2012, doi: 10.2118/152597-MS.
 - 19 T. J. Hill, D. G. Wood, B. P. Exploration, and O. Co, “SPE 27960 Slug Flow : Occurrence , Coriseqimces ,” 1994.
 - 20 G. J. Zabararas, E. Shell, and P. T. Co, “SPE 56462 Prediction of Slug Frequency for Gas-Liquid Flows,” 1999, doi: 10.2118/56462-MS.
 - 21 H. Nakamura, “Slug Flow Transitions in Horizontal Gas/Liquid Two-Phase Flows (Dependence on Channel Height and System Pressure for Air/Water and Steam/Water Two-Phase Flows),” *JAERI-Research*, vol. 22, pp. 1–148, 1996.
 - 22 A. R. A. Colmanetti, M. S. de Castro, M. C. Barbosa, and O. M. H. Rodriguez, “Phase inversion phenomena in vertical three-phase flow: Experimental study on the influence of fluids viscosity, duct geometry and gas flow rate,” *Chem. Eng. Sci.*, vol. 189, pp. 245–259, 2018, doi: 10.1016/j.ces.2018.05.050.
 - 23 G. H. Al-Aithan, F. M. Al-Mutahar, R. J. Shadley, S. a Shirazi, E. F. Rybicki, and K. P. Roberts, “A Mechanistic Erosion-Corrosion Model for Predicting Iron Carbonate (FeCO₃) Scale Thickness in a CO₂ Environment with Sand,” *Corros. 2014*, no. 3854, pp. 1–15, 2014.
 - 24 E. Heitz, “Mechanistically based prevention strategies of flow-induced corrosion,” *Electrochim. Acta*, vol. 41, no. 4 SPEC. ISS., pp. 503–509, 1996, doi: 10.1016/0013-4686(95)00336-3.
 - 25 E. Trabalho, C. R. Automa, E. Trabalho, and C. R. Automa, “VCONE-NOVA TECNOLOGIA PARA MEDIÇÃO DE GÁS ÚMIDO Engenheiro Mecânico , Hirsá Sistemas de Automação,” pp. 1–9, 2005.
 - 26 J. N. M. DE SOUZA, “Modelagem e Simulação de Escoamento Multifásico em Dutos de Produção de Óleo e Gás Natural,” p. 265, 2010, [Online]. Available:

<http://tpqb.eq.ufrj.br/download/escoamento-multifasico-em-dutos-de-oleo-e-gas.pdf>

- 27 S. F. Wong, J. S. Lim, and S. S. Dol, "Crude oil emulsion: A review on formation, classification and stability of water-in-oil emulsions," *J. Pet. Sci. Eng.*, vol. 135, pp. 498–504, 2015, doi: 10.1016/j.petrol.2015.10.006.
- 28 E. Allen and A. Sturgeon, "Pipeline Corrosion – Can it always be modelled with confidence?," no. June, 2015.
- 29 M. F. Goes, M. A. Sinhoreti, S. Consani, and M. A. Silva, "Morphological effect of the type, concentration and etching time of acid solutions on enamel and dentin surfaces.," *Braz. Dent. J.*, vol. 9, no. 1, pp. 3–10, 1998, doi: 10.1088/1742-6596/755/1/011001.
- 30 E. Heitz, "Chemo-mechanical effects of flow on corrosion," *Corrosion*, vol. 47, no. 2, pp. 135–145, 1991, doi: 10.5006/1.3585229.
- 31 J. Ukpai, R. Barker, and A. Neville, "A Combined Electrochemical and Acoustic Emission Technique for Mechanistic and Quantitative Evaluation of Erosion-Corrosion and its Components," in *Corrosion 2014*, 2014, no. 4180, pp. 1–15.
- 32 C. A. S. Costa and P. M. De Oliveira, "APPLICATION OF IMAGE PROCESSING TECHNIQUES TO CHARACTERIZE INTERMITTENT FLOW INITIATION IN HORIZONTAL GAS-LIQUID FLOWS," 2017.
- 33 G. R. Magalhães, G. F. N. Gonçalves, J. B. R. Loureiro, and A. P. Silva Freire, "An experimental investigation of the effects of gas solubility on the properties of horizontal slug flow," *Int. J. Multiph. Flow*, vol. 50, no. 68503, pp. 33–40, 2013, doi: 10.1016/j.ijmultiphaseflow.2012.10.007.
- 34 J. Cai, K. J. Lee, and S. Nešić, "A MULTIPHASE FLOW AND INTERNAL CORROSION PREDICTION MODEL FOR MILD STEEL PIPELINES," *Corros. 2005*, no. 05556, pp. 1–35, 2005, [Online]. Available: <https://www.ohio.edu/engineering/sites/ohio.edu.engineering/files/sites/engineering/A-MULTIPHASE-FLOW-AND-INTERNAL-CORROSION-PREDICTION-MODEL-FOR-MILD-STEEL-PIPELINES.pdf>
- 35 M. Bonizzi and R. I. Issa, "On the simulation of three-phase slug flow in nearly horizontal pipes using the multi-fluid model," *Int. J. Multiph. Flow*, vol. 29, no. 11, pp. 1719–1747, 2003, doi: 10.1016/j.ijmultiphaseflow.2003.09.002.
- 36 J. Brady *et al.*, "SPE 166102 Performance of Multiphase Flowmeter and Continuous Water-Cut Monitoring Devices in North Slope , Alaska," 2013.
- 37 Z. Ming Wang, X. Tian Liu, X. Han, and J. Zhang, "Managing Internal Corrosion of Mild Steel Pipelines in CO₂ -Enhanced Oil Recovery Multiphase FlowConditions," 2015, doi: 10.1002/ente.201402159.
- 38 M. Daas, D. Ph, N. Munroe, and D. Ph, "Flow Assurance in Oil-Gas Pipelines," no. June, pp. 1–10, 2006.
- 39 K. Lee, "A mechanistic modeling of CO₂ corrosion of mild steel in the presence of H₂S," Ohio University, 2004. [Online]. Available:

<http://medcontent.metapress.com/index/A65RM03P4874243N.pdf%5Cnhttp://scholar.google.com/scholar?hl=en&btnG=Search&q=intitle:a+mechanistic+modeling+of+co2+corrosion+on+mild+steel+in+the+presence+of+h2s#1>

- 40 M. R. Gregg and S. Ramachandran, "Review of Corrosion Inhibitor Developments and Testing for Offshore Oil and Gas Production Systems," *Corros.* 2004, no. 04422, pp. 1–57, 2004, [Online]. Available: <http://www.onepetro.org/mslib/servlet/onepetropreview?id=NACE-04422&soc=NACE&speAppNameCookie=ONEPETRO>
- 41 "The Multiphase Flow Assurance and Innovation Centre".
- 42 T. S. Golczynski, "Defining Operating Envelopes for Multiphase Pipelines – A Flow Assurance Approach," *Geology*, pp. 1–11, 2003.
- 43 "NSFMW2011_proc".
- 44 A. Omer and R. Pal, "Pipeline flow behavior of water-in-oil emulsions with and without a polymeric additive," *Chem. Eng. Technol.*, vol. 33, no. 6, pp. 983–992, 2010, doi: 10.1002/ceat.200900297.
- 45 S. J. Svedeman, "EXPERIMENTAL STUDY OF THE EROSIONAUCORROSIONAL VELOCITY CRITERION FOR SIZING MUL TI PHASE FLOW LINES," vol. 3, 1991.
- 46 G. L. Chahine, J. Franc, and A. Karimi, *Advanced Experimental and Numerical Techniques for Cavitation Erosion Prediction*, vol. 106. 2014. doi: 10.1007/978-94-017-8539-6.
- 47 M. J. C. Diaz, "Two-Phase Slug Flow Experiments with Viscous Liquids," NTNU Norwegian University of Science and Technology Faculty of Engineering Science and Technology Department, 2016.
- 48 J. B. R. A. P. S. F. Loureiro;, "Slug flow in horizontal pipes with transpiration at the wall," *J. Phys. Conf. Ser.* 318, p. 11, 2011, doi: 10.1088/1742-6596/318/2/022014.
- 49 A. M. El-Sherik, *Trends in Oil and Gas Corrosion Research and Technologies*. Cambridge, 2017.
- 50 "Development of a Steady State Point Model for Prediction of Gas Oil and Water Oil Pipe Flow".
- 51 M. M. F. Figueiredo, J. L. Goncalves, A. M. V Nakashima, A. M. F. Fileti, and R. D. M. Carvalho, "The use of an ultrasonic technique and neural networks for identification of the flow pattern and measurement of the gas volume fraction in multiphase flows," *Exp. Therm. Fluid Sci.*, vol. 70, pp. 29–50, 2016, doi: 10.1016/j.expthermflusci.2015.08.010.
- 52 and A. V. M. Henriquez, N. Pébère, N. Ochoa, "Electrochemical Investigation of the Corrosion Behavior of API 5L-X65 Carbon Steel in Carbon Dioxide Medium," 2015. doi: <https://doi.org/10.5006/0971>.

- 53 Y. Utanohara, K. Kamahori, and A. Nakamura, "Measurement of Flow Accelerated Corrosion Rate at an Elbow Pipe and Combination Effect of an Upstream Orifice," vol. 8, pp. 1–12, 2016.
- 54 E. Barmatov, T. Hughes, and M. Nagl, "Effect of surface roughness and flow on corrosion inhibition of coiled tubing steel under matrix acidizing conditions," *Corros. 2014*, no. 4114, pp. 1–19, 2014.
- 55 P. Schempp, K. PreuB, and M. Troger, "About the correlation between crude oil corrosivity and corrosion monitoring in an oil refinery," *J. Sci. Eng.*, vol. 72, no. 6, pp. 1–47, 2016.
- 56 Y. F. Han, A. Zhao, H. X. Zhang, Y. Y. Ren, W. X. Liu, and N. D. Jin, "Differential pressure method for measuring water holdup of oil-water two-phase flow with low velocity and high water-cut," *Exp. Therm. Fluid Sci.*, vol. 72, pp. 197–209, 2016, doi: 10.1016/j.expthermflusci.2015.11.008.
- 57 J. Villarreal, D. Laverde, and C. Fuentes, "Carbon-steel corrosion in multiphase slug flow and CO₂," *Corros. Sci.*, vol. 48, no. 9, pp. 2363–2379, 2006, doi: 10.1016/j.corsci.2005.09.003.
- 58 P. Kumar, B. Smith, and D. Vedapuri, "Sand Fines Erosion in Gas Pipelines – Experiments and CFD Modeling," *Corros. 2014*, no. 3964, pp. 1–12, 2014.
- 59 M. Ishibashi and T. Morioka, "The renewed airflow standard system in Japan for 5-1000 m³/h," *Flow Meas. Instrum.*, vol. 17, no. 3, pp. 153–161, 2006, doi: 10.1016/j.flowmeasinst.2006.01.006.
- 60 C. Kang, P. P. More, J. R. Vera, P. A. Ferreira, and E. C. Bastos, "06589 - Flow Patterns and Characteristics in Multiphase Riser Pipelines," 2006.
- 61 A. Dugstad, E. Gulbrandesen, R. Nyborg, and M. Seiersten, "Paper No. 06598 CORROSION TESTING IN MULTIPHASE FLOW, CHALLENGES AND LIMITATIONS Arne," *Technology*, no. 06598, pp. 1–16, 2006.
- 62 R. E. Vieira, N. R. Kesana, S. A. Shirazi, and B. S. Mclaury, "Experiments for Sand Erosion Model Improvement for Elbows in Gas Production, Low-Liquid Loading and Annular Flow Conditions," *Corros. 2014*, no. 4325, pp. 1–20, 2014.
- 63 R. Nyborg, A. Dugstad, and T. G. Martin, "Top of Line Corrosion with High CO₂ and Traces of H₂S Rolf," in *Corrosion 2009*, 2009, no. 09283, pp. 1–11.
- 64 W. P. Vuppu, A. K.; Jepson, "Study of Sweet Corrosion in Horizontal Multiphase, Carbon Steel Pipelines," *OTC 7494*, 1994.
- 65 P. A. B. de Sampaio, J. L. H. Faccini, and J. Su, "Modelling of stratified gas-liquid two-phase flow in horizontal circular pipes," *Int. J. Heat Mass Transf.*, vol. 51, no. 11–12, pp. 2752–2761, 2008, doi: 10.1016/j.ijheatmasstransfer.2007.09.038.
- 66 C. Kang, J. Rhodes, K. Tummala, and A. A. O. Magalhae, "The Selection of Corrosion Inhibitors under Oil/Water/Gas Flow Conditions in Deep Offshore Catenary Risers," in *Corrosion 2013*, 2013, no. 2595, pp. 1–10.

- 67 M. Dugstad, Arne; Gulbrandsen, Agil; Kvarekvål, Jon; Nyborg, Rolf; Seiersten, “06598 - CORROSION TESTING IN MULTIPHASE FLOW, CHALLENGES AND LIMITATIONS,” *J. Nat. Gas Sci. Eng.*, vol. 17, no. 1, pp. 1–15, 2006, doi: 10.1016/j.jngse.2016.04.056.
- 68 J. Feyerl *et al.*, “Erosion-corrosion of carbon steels in a laboratory: Three-phase flow,” *Corrosion*, vol. 64, no. 2, pp. 175–186, 2008, doi: 10.5006/1.3280686.
- 69 S. Singer, M., Brown, B., Camacho, A., Nesic, “Combined Effect of CO₂, H₂S and Acetic Acid on Bottom of the Line Corrosion,” *Corrosion Conference and Expo*, no. 07661. p. 25, 2007.
- 70 “ANÁLISE E REVISÃO DE MODELOS DE ESCOAMENTOS MULTIFÁSICOS EMPREGADOS EM VÁLVULAS DO TIPO CHOKE,” *New York*, vol. 2, no. March, p. 880, 2011, doi: 10.1016/0142-727X(92)90041-7.
- 71 R. Nyborg, “Guidelines for prediction of CO₂ corrosion in oil and gas production systems,” *IFE Inst. Energy Technol.*, vol. 19, no. 3, pp. 1–16, 2009, doi: 10.1016/j.jngse.2016.04.056.
- 72 B. Robøle, H. K. Kvandal, and R. B. Schüller, “The Norsk Hydro Multi Phase Flow Loop. A high pressure flow loop for real three-phase hydrocarbon systems,” *Flow Meas. Instrum.*, vol. 17, no. 3, pp. 163–170, 2006, doi: 10.1016/j.flowmeasinst.2006.01.003.
- 73 A. Brown, Bruce; Schubert, “THE DESIGN AND DEVELOPMENT OF A LARGE-SCALE, MULTIPHASE FLOW LOOP FOR THE STUDY OF CORROSION IN SOUR GAS ENVIRONMENTS.,” *Corros. 2002*, no. 02502, p. 02502, 2002.
- 74 K. E. Kee, S. Richter, M. Babic, and S. Nešić, “Experimental study of oil-water flow patterns in a large diameter flow loop-the effect on water wetting and corrosion,” *Corrosion*, vol. 72, no. 4, pp. 569–582, 2016, doi: 10.5006/1753.
- 75 A. Brown, Bruce; Schubert, “02502 - THE DESIGN AND DEVELOPMENT OF A LARGE-SCALE, MULTIPHASE FLOW LOOP FOR THE STUDY OF CORROSION IN SOUR GAS ENVIRONMENTS,” *Corros. NACE Conf. expo*, vol. 2, no. March, p. 880, 2002, doi: 10.1016/0142-727X(92)90041-7.
- 76 T. Loops, “Test Loops”.
- 77 K. E. Kee, S. Richter, and M. Babic, “Flow Patterns and Water Wetting in Oil-Water Two Phase Flow – A Flow Loop Study,” *Corrosion*, no. 4068, p. 15, 2014, doi: NACE-2014-4068.
- 78 L. Hovden, C. Lawrence, and I. Wold, “Use of FACE Flow Loop Data for Validation and Improvement of Flow Simulations,” *J. Dispers. Sci. Technol.*, vol. 36, no. 10, pp. 1452–1457, 2015, doi: 10.1080/01932691.2014.996889.
- 79 Z. M. Wang and J. Zhang, “Corrosion of multiphase flow pipelines: The impact of crude oil,” *Corros. Rev.*, vol. 34, no. 1–2, pp. 17–40, 2016, doi: 10.1515/correv-2015-0053.

- 80 H. J. Zhu, Y. H. Lin, D. Z. Zeng, and R. T. Yan, “Simulations of flow induced corrosion in api drillpipe connector,” *J. Hydrodyn.*, vol. 23, no. 6, pp. 784–791, 2011, doi: 10.1016/S1001-6058(10)60177-1.
- 81 Y. Bai and Q. Bai, *Subsea Pipelines and Risers*. 2005. doi: 10.1016/b978-008044566-3.50023-3.
- 82 B. Cookingham, “Overview of Subsea Corrosion Integrity DNV GL Pipeline Services,” pp. 1–16, 2014.
- 83 M. J. Kaiser, “Offshore Overview,” in *The Offshore Pipeline Construction Industry*, Elsevier, 2020, pp. 3–38. doi: 10.1016/b978-0-12-820288-3.00001-9.
- 84 A. J. Simpson, Pete James; Lima, “Deepwater Riser Systems – Historical Review and Future Projections,” in *Offshore Technology Conference*, 2019, no. October, pp. 29–31.
- 85 Y. Bai, *PIPELINES AND RISERS*, vol. 3, no. C. 2001. doi: 10.1016/S1571-9952(01)80033-7.
- 86 M. J. Kaiser, “Offshore Pipeline Construction Cost Estimation,” in *The Offshore Pipeline Construction Industry*, Elsevier, 2020, pp. 209–228. doi: 10.1016/b978-0-12-820288-3.00009-3.
- 87 O. Bratland, *Pipe Flow 1 : Single-phase Flow Assurance*. 2013. [Online]. Available: http://scholar.google.de/scholar?q=ove+bratland+pipe+flow+assurance&btnG=&hl=de&as_sdt=0,5#1
- 88 G. P. Drumond, I. P. Pasqualino, B. C. Pinheiro, and S. F. Estefen, “Pipelines, risers and umbilicals failures: A literature review,” *Ocean Engineering*, vol. 148. Elsevier Ltd, pp. 412–425, Jan. 15, 2018. doi: 10.1016/j.oceaneng.2017.11.035.
- 89 M. N. Ilman, “Analysis of internal corrosion in subsea oil pipeline,” *Case Stud. Eng. Fail. Anal.*, vol. 2, no. 1, pp. 1–8, 2014, doi: 10.1016/j.csefa.2013.12.003.
- 90 S. Peng and Z. Zeng, “An experimental study on the internal corrosion of a subsea multiphase pipeline,” *Petroleum*, vol. 1, no. 1, pp. 75–81, 2015, doi: 10.1016/j.petlm.2015.04.003.
- 91 Y. Yang, F. Khan, P. Thodi, and R. Abbassi, “Corrosion induced failure analysis of subsea pipelines,” *Reliab. Eng. Syst. Saf.*, vol. 159, no. November 2016, pp. 214–222, 2017, doi: 10.1016/j.ress.2016.11.014.
- 92 A. B. Forero, I. S. Bott, and R. De Janeiro, “Analysis of the Corrosion Scales Formed on API 5L X70 and X80 Steel Pipe in the Presence of CO₂,” vol. 17, no. 2, pp. 461–471, 2014.
- 93 M. B. Kermani and A. Morshed, “Carbon Dioxide Corrosion in Oil and Gas Production—A Compendium,” *Corrosion*, vol. 59, no. 8, pp. 659–683, 2003, doi: 10.5006/1.3277596.
- 94 S. E. Hernandez, S. Hernandez, H. Rincon, and J. R. Vera, “Flow-induced carbon dioxide and hydrogen sulfide corrosion studies using the dynamic field tester in crude

- oil wells,” *Corrosion*, vol. 58, no. 10, pp. 881–890, 2002, doi: 10.5006/1.3287673.
- 95 B. Brown, “H₂S Multiphase Flow Loop: Co₂ Corrosion in the Presence of Trace Amounts of Hydrogen Sulfide,” 2004. [Online]. Available: https://www.ohio.edu/engineering/sites/ohio.edu.engineering/files/sites/engineering/H2S-Multiphase-Flow-Loop-CO2-Corrosion-in-the-Presence-of-Trace-Amounts-of-Hydrogen-Sulfide_B-Brown_2004_MS.pdf
 - 96 G. Bosch, M. Mueller, and G. Siegmund, “A PROBABILISTIC MODEL FOR FLOW INDUCED LOCALIZED CORROSION,” *Corrosion*, no. 00149, p. Paper No.00031, 2000, [Online]. Available: <http://www.onepetro.org/mslib/servlet/onepetroreview?id=NACE-00629>
 - 97 G. Falcone, C. Teodoriu, K. M. Reinicke, O. O. Bello, and T. U. Clausthal, “Multiphase-Flow Modeling Based on Experimental Testing: An Overview of Research Facilities Worldwide and the Need for Future Developments,” no. August 2007, pp. 11–14, 2008.
 - 98 B. F. Pots, I. G. Bromilow, and M. J. W. F. Konijn, “Severe slug flow in offshore flowline or riser systems,” in *SPE International*, 1987, vol. 2, no. 4, pp. 319–324.
 - 99 A. Kalra, A. Venkatraman, K. H. Raney, and B. Dindoruk, “Prediction and Experimental Measurements of Water-in-Oil Emulsion Viscosities During Alkaline/Surfactant Injections,” *Oil Gas Facil.*, vol. 1, no. 03, pp. 34–43, 2012, doi: 10.2118/143992-PA.
 - 100 J. Sun and W. P. Jepson, “Slug Flow Characteristics and Their Effect on Corrosion Rates in Horizontal Oil and Gas Pipelines,” *Spe*, 1992, doi: 10.2118/24787-MS.
 - 101 A. Archibong-Eso, Y. Baba, A. Aliyu, Y. Zhao, W. Yan, and H. Yeung, “On slug frequency in concurrent high viscosity liquid and gas flow,” *J. Pet. Sci. Eng.*, vol. 163, no. March 2017, pp. 600–610, 2018, doi: 10.1016/j.petrol.2017.12.071.
 - 102 J. Zhang, J. Kang, J. Fan, and J. Gao, “Study on erosion wear of fracturing pipeline under the action of multiphase flow in oil & gas industry,” *J. Nat. Gas Sci. Eng.*, vol. 32, pp. 334–346, 2016, doi: 10.1016/j.jngse.2016.04.056.
 - 103 F. Accelerated and C. Testing, “FLOW ACCELERATED CORROSION TESTING BASICS,” *Corrosion*, no. 06689, pp. 1–16.
 - 104 T. J. Hill, “Research in multiphase flow developed into new global discipline of flow assurance – an oil industry perspective,” pp. 7–20, 2018.
 - 105 M. Parsi, R. Vieira, S. K. Sajeev, B. S. McLaury, and S. A. Shirazi, “Experimental Study of Erosion in Vertical Slug/Churn Flow,” *CORROSION 2015*, no. 6086. 2015. [Online]. Available: https://www.onepetro.org/conference-paper/NACE-2015-6086?sort=&start=0&q=Sand+Erosion+in+Multiphase+Flow+For+Slug+and+Annular+Flow+Regimes&from_year=&peer_reviewed=&published_between=&fromSearchResults=true&to_year=&rows=10#
 - 106 B. Brown, K. L. Lee, and S. Nestic, “Corrosion in multiphase flow containing small amounts of H₂S,” in *Corrosion NACE conference & expo*, 2003, no. 03341, pp. 1–24.

- 107 B. F. Pots *et al.*, “Improvements on de Waard-Milliams corrosion prediction and applications to corrosion management,” in *Corrosion 2002*, 2002, no. 02235, p. 19. [Online]. Available: <http://www.onepetro.org/mslib/app/Preview.do?paperNumber=NACE-02235&societyCode=NACE>
- 108 D. P. Li, L. Zhang, J. W. Yang, M. X. Lu, J. H. Ding, and M. L. Liu, “Effect of H₂S concentration on the corrosion behavior of pipeline steel under the coexistence of H₂S and CO₂,” *Int. J. Miner. Metall. Mater.*, vol. 21, no. 4, pp. 388–394, 2014, doi: 10.1007/s12613-014-0920-y.
- 109 G. S. Das and A. S. Khanna, “Effects of small amount of H₂S ON CO₂ corrosion of pipeline steel in multiphase flow loop system,” *EUROCORR 2004 - Eur. Corros. Conf. Long Term Predict. Model. Corros.*, vol. 4, pp. 1–9, 2004.
- 110 C. De Waard, B. D. Craig, and L. M. Smith, “The influence of crude oils on well tubing corrosion rates,” in *NACE - International Corrosion Conference Series*, 2003, vol. 2003-April, no. January 2003.
- 111 O. R. M. Merlin C. E. Bandeira, Danielle Spigarollo, Rogaciano M. Moreira, “Influence of small amount of H₂S on the CO₂ corrosion of carbon steel at oil production conditions,” *INTERCORR 2016*, p. 7, 2016.
- 112 H. Wang, P. Zhou, S. Huang, and C. Yu, “Corrosion mechanism of low alloy steel in NaCl solution with CO₂ and H₂S,” *Int. J. Electrochem. Sci.*, vol. 11, no. 2, pp. 1293–1309, 2016.
- 113 Y. S. Choi, S. Nescic, and S. Ling, “Effect of H₂S on the CO₂ corrosion of carbon steel in acidic solutions,” *Electrochim. Acta*, vol. 56, no. 4, pp. 1752–1760, 2011, doi: 10.1016/j.electacta.2010.08.049.
- 114 Department of Energy Fundamentals, *Thermodynamics , Heat Transfer , and Fluid Flow Volume 1 of 3 DOE Fundamentals Handbook*, vol. 1, no. June. 1992.
- 115 O. Bratland, *Pipe Flow 2, Multiphase Flow Assurance*. 2010.
- 116 M. J. Vaze and J. Banerjee, “Effect of surface roughness and flow on corrosion inhibition of coiled tubing steel under matrix acidizing conditions,” *Int. Conf. Fluid Dyn. Thermodyn. Technol.*, vol. 33, no. Fdtt, pp. 58–63, 2012, [Online]. Available: <http://www.ipcsit.com/vol33/011-FDTT2012-F0019.pdf>
- 117 C. M. Canto Maya, “Effect of Wall Shear Stress on Corrosion Inhibitor Film Performance,” 2015.
- 118 W. Li, B. F. M. Pots, B. Brown, K. E. Kee, and S. Nescic, “A direct measurement of wall shear stress in multiphase flow-Is it an important parameter in CO₂corrosion of carbon steel pipelines?,” *Corros. Sci.*, vol. 110, pp. 35–45, 2016, doi: 10.1016/j.corsci.2016.04.008.
- 119 R. R. L. C. Roquette, “DESENVOLVIMENTO DE METODOLOGIA DE MEDIDA DE FORÇA DE ADESÃO DE INCUSTRAÇÕES PARA AVALIAÇÃO DE RECOBRIMENTOS ANTI-AEDRENTES,” UFRJ/ Escola Politécnica/ Curso de

Engenharia de Materiais, 2016.

- 120 W. Li, Y. Xiong, B. Brown, K. E. Kee, and S. Nesic, "Measurement of wall shear stress in multiphase flow and its effect on protective FeCO₃ corrosion product layer removal," in *NACE - International Corrosion Conference Series*, 2015, vol. 2015-Janua, no. September 2016. [Online]. Available: [https://www.ohio.edu/engineering/sites/ohio.edu.engineering/files/sites/engineering/conferences/C2015-5922-Measurement-of-Wall-Shear-Stress-in-Multiphase-Flow-and-Its-Effect-on-Protective-FeCO₃-Corrosion-Product-Layer-Removal-1.pdf](https://www.ohio.edu/engineering/sites/ohio.edu.engineering/files/sites/engineering/conferences/C2015-5922-Measurement-of-Wall-Shear-Stress-in-Multiphase-Flow-and-Its-Effect-on-Protective-FeCO3-Corrosion-Product-Layer-Removal-1.pdf)
- 121 W. Li, "Mechanical Effects of Flow on CO₂ Corrosion Inhibition of Carbon Steel Pipelines," 2016.
- 122 N. G193, "NACE/ASTM G193 – 20a Standard Terminology and Acronyms Relating to Corrosion," 2000. doi: 10.1520/G0193-20A.2.
- 123 ASTM G32, "Standard Test Method for Cavitation Erosion Using Vibratory Apparatus G 32," *Annu. B. ASTM Stand.*, vol. i, pp. 1–18, 2010, doi: 10.1520/G0032-10.bility.
- 124 M. Gopal, A. Kaul, and W. P. Jepson, "Mechanisms Contributing to Enhanced Corrosion in Three Phase Slug Flow in Horizontal pipes," *NACE Int. Corros.* 95, no. Paper No. 105, 1995.
- 125 L. A. Espitia, L. Varela, C. E. Pinedo, and A. P. Tschiptschin, "Cavitation erosion resistance of low temperature plasma nitrided martensitic stainless steel," *Wear*, vol. 301, no. 1–2, pp. 449–456, 2013, doi: 10.1016/j.wear.2012.12.029.
- 126 C. S. M.C. Romero, A.P. Tschiptschin, "Cavitation erosion resistance of a non-standard cast cobalt alloy: Influence of solubilizing and cold working treatments," *Wear*, vol. 427, no. September 2018, pp. 518–526, 2018, doi: 10.1016/j.wear.2018.12.044.
- 127 C.A. Silva; D.R.N. Filho; G.M.B. Nunes; G.S. Bassani; N.L. Almeida; Z. Panossian, "Corrosion in Multiphase Slug Flow Loop in Deep-water Oil and Gas exploitation," in *OTC-29720-MS*, 2019, pp. 1–28.
- 128 J. Sjöblom, *EMULSIONS AND EMULSION STABILITY*, vol. 40, no. 4. 2006. doi: 10.1353/hph.2002.0076.
- 129 M. M. Abdulredha, H. Siti Aslina, and C. A. Luqman, "Overview on petroleum emulsions, formation, influence and demulsification treatment techniques," *Arab. J. Chem.*, vol. 13, no. 1, pp. 3403–3428, 2020, doi: 10.1016/j.arabjc.2018.11.014.
- 130 Z. M. Wang, X. T. Liu, X. Han, and J. Zhang, "Managing internal corrosion of mild steel pipelines in CO₂-enhanced oil recovery multiphase flow conditions," *Energy Technol.*, vol. 3, no. 3, pp. 225–233, 2015, doi: 10.1002/ente.201402159.
- 131 T. T. Nguyen, C. Morgan, L. Poindexter, and J. Fernandez, "Application of the Hydrophilic–Lipophilic Deviation Concept to Surfactant Characterization and Surfactant Selection for Enhanced Oil Recovery," *J. Surfactants Deterg.*, vol. 22, no. 5, pp. 983–999, 2019, doi: 10.1002/jsde.12305.

- 132 J. Fritz and D. H. Russ, "H₂S MULTIPHASE FLOW LOOP: CO₂ CORROSION IN THE PRESENCE OF TRACE AMOUNTS OF HYDROGEN SULFIDE," no. November, 2004.
- 133 Z. L. Wang *et al.*, "Emulsification reducing the corrosion risk of mild steel in oil-brine mixtures," *Corros. Sci.*, vol. 86, pp. 310–317, 2014, doi: 10.1016/j.corsci.2014.06.009.
- 134 ASTM, "Standard guide for laboratory immersion corrosion testing of metals," *ASTM Int.*, vol. G31-12a, pp. 1–10, 2012, doi: 10.1520/G0031-21.2.
- 135 J. J. Ge, G. C. Zhang, P. Jiang, L. Wang, H. H. Pei, and X. L. Liu, "Study on Influencing Factors of Chemical Flooding for Heavy Oil," *J. Dispers. Sci. Technol.*, vol. 33, no. 2, pp. 278–286, 2012, doi: 10.1080/01932691.2011.561186.
- 136 T. Pérez and J. L. Nava, "Simulation of turbulent flow of a rotating cylinder electrode. influence of using plates and concentric cylinder as counter electrodes," *Int. J. Electrochem. Sci.*, vol. 8, no. 4, pp. 4690–4699, 2013, [Online]. Available: https://www.researchgate.net/publication/236030055_Simulation_of_Turbulent_Flow_of_a_Rotating_Cylinder_Electrode_Influence_of_Using_Plates_and_Concentric_Cylinder_as_Counter_Electrodes
- 137 D. R. Gabe and F. C. Walsh, "The rotating cylinder electrode: a review of development," *J. Appl. Electrochem.*, vol. 13, no. 1, pp. 3–21, 1983, doi: 10.1007/BF00615883.
- 138 F. C. Walsh, G. Kear, A. H. Nahlé, J. A. Wharton, and L. F. Arenas, "The rotating cylinder electrode for studies of corrosion engineering and protection of metals—An illustrated review," *Corros. Sci.*, vol. 123, no. November 2016, pp. 1–20, 2017, doi: 10.1016/j.corsci.2017.03.024.
- 139 R. A. Holser, G. Prentice, R. B. Pond, and R. Guanti, "Use of rotating cylinder electrodes to simulate turbulent flow conditions in corroding systems," *Corrosion*, vol. 46, no. 9, pp. 764–769, 1990, doi: 10.5006/1.3585179.
- 140 T. H. C. Pimentel, C. A. Silva, D. R. Neves, and Z. Panossian, "A novel electronic bridge for electrochemical measurements for high pressure electrochemical measures," in *21st International Corrosion Congress, ICC INTERCORR WCO 2021*, 2021, pp. 632–637. [Online]. Available: https://intercorr.com.br/anais/2021/ICC_INTERCORR_WCO_2021_453.pdf
- 141 C. A. Silva, H. B. Pereira, M. E. S. Taqueda, and Z. Panossian, "Prediction models for multiphase - flow - induced corrosion of API X80 steel in CO₂ / H₂S environment," *Mater. Corros.*, no. June, pp. 1–12, 2021, doi: 10.1002/maco.202112451.
- 142 C. A. Silva, D. R. Filho, G. M. Nunes, G. S. Bassani, N. L. Almeida, and Z. Panossian, "Corrosion in multiphase slug flow loop in deep-water oil and gas exploitation," in *Offshore Technology Conference Brasil 2019, OTCB 2019*, 2020. doi: <https://doi.org/10.4043/29720-MS>.
- 143 F. W. Breyfogle III, *IMPLEMENTING SIX SIGMA*, MENTING SI. New Jersey: John Wiley & Sons, Inc., Hoboken, 2003.

- 144 F. N. Ucla, M. Leonardo, S. Ufmg, J. Alexandre, and S. Júnior, “O Que Fazer e o Que Não Fazer Com a Regressão: pressupostos e aplicações do modelo linear de Mínimos Quadrados Ordinários (MQO),” *Rev. Política Hoje*, vol. 20, no. 1, pp. 44–99, 2011.
- 145 G. E. Box and D. R. Cox, “An analysis of transformations revisited, rebutted,” *J. Am. Stat. Assoc.*, vol. 77, no. 377, pp. 209–210, 1982, doi: 10.1080/01621459.1982.10477788.
- 146 S. Addelman, “Statistics for Experimenters,” *Technometrics*, vol. 21, no. 3, pp. 387–388, 1979. doi: 10.1080/00401706.1979.10489788.
- 147 S. N. S. and M. Joosten, “Corrosion of Carbon Steel By H₂S in CO₂ Containing Oilfield Environment,” *Corros. 2006*, no. 244, pp. 1–10, 2006, doi: 10.1016/j.japwor.2003.09.001.
- 148 P. Tang *et al.*, “Failure analysis and prediction of pipes due to the interaction between multiphase flow and structure,” *Eng. Fail. Anal.*, vol. 16, no. 5, pp. 1749–1756, 2009, doi: 10.1016/j.engfailanal.2009.01.002.
- 149 S. E. Hernandez *et al.*, “Flow-induced carbon dioxide and hydrogen sulfide corrosion studies using the dynamic field tester in crude oil wells,” *Corrosion*, vol. 58, no. 10, pp. 881–890, 2002, doi: 10.5006/1.3287673.
- 150 M. Hammer, H. Deng, L. Liu, M. Langsholt, and S. Tollak, “Upward and downward two-phase flow of CO₂ in a pipe : Comparison between experimental data and model predictions,” *Int. J. Multiph. Flow*, vol. 138, p. 103590, 2021, doi: 10.1016/j.ijmultiphaseflow.2021.103590.
- 151 J. N. E. Carneiro *et al.*, “Statistical characterization of two-phase slug flow in a horizontal pipe,” *J. Brazilian Soc. Mech. Sci. Eng.*, vol. 53, no. 9, pp. 251–258, 2019, doi: 10.1590/S1678-58782011000500007.
- 152 F. Measurement, I. Ismail, B. S. Iskandar, S. Bukhari, and W. Yang, “Tomography for multi-phase flow measurement in the oil industry,” no. April, 2005, doi: 10.1016/j.flowmeasinst.2005.02.017.
- 153 F. Farel, M. Galicia, B. Brown, S. Nestic, and H. Castaneda, “Evolution of dissolution processes at the interface of carbon steel corroding in a CO₂ environment studied by EIS,” *Corros. Sci.*, vol. 52, no. 2, pp. 509–517, 2010, doi: 10.1016/j.corsci.2009.10.007.
- 154 M. Askari, M. Aliofkhaezai, and S. Afroukhteh, “A Comprehensive Review on Internal Corrosion and Cracking of Oil and Gas Pipelines,” *J. Nat. Gas Sci. Eng.*, p. 102971, 2019, doi: 10.1016/j.jngse.2019.102971.
- 155 Z. Liu *et al.*, “Corrosion behaviour of low-alloy martensite steel exposed to vapour-saturated CO₂ and CO₂-saturated brine conditions,” *Electrochim. Acta*, vol. 213, pp. 842–855, 2016, doi: 10.1016/j.electacta.2016.08.024.
- 156 J. F. Santa, J. A. Blanco, J. E. Giraldo, and A. Toro, “Cavitation erosion of martensitic and austenitic stainless steel welded coatings,” *Wear*, vol. 271, no. 9–10, pp. 1445–1453, 2011, doi: 10.1016/j.wear.2010.12.081.

- 157 A. Dugstad, H. Hemmer, and M. Seiersten, "Effect of steel microstructure upon corrosion rate and protective iron carbonate film formation," *NACE - Int. Corros. Conf. Ser.*, vol. 2000-March, no. 4, 2000.
- 158 K. Wang, G. Li, and B. Zhang, "Opposite results of emulsion stability evaluated by the TSI and the phase separation proportion," *Colloids Surfaces A Physicochem. Eng. Asp.*, vol. 558, no. September, pp. 402–409, 2018, doi: 10.1016/j.colsurfa.2018.08.084.
- 159 C. A. Silva, L. B. Varela, F. O. Kolawole, A. P. Tschiptschin, and Z. Panossian, "Multiphase-flow-induced corrosion and cavitation-erosion damages of API 5L X80 and API 5DP grade S steels," *Wear*, vol. 452–453, no. March, p. 203282, 2020, doi: 10.1016/j.wear.2020.203282.
- 160 C. A. Silva, F. DRN, Z. MHA, and P. Z, "Impact of Crude Oil Emulsion on Pipeline Corrosion," *J. Petrochemical Eng.*, vol. 1, no. 1, pp. 11–19, 2021, doi: 10.36959/901/249.
- 161 C. A. Silva, D. R. Filho, G. M. Nunes, G. S. Bassani, N. L. Almeida, and Z. Panossian, "The Design and Development of a Small-Scale, Multiphase Flow Loop for the Study of Corrosion in Sour/Sweet Gas Environments," in *Rio Pipeline Conference and Exhibition 2019*, 2019, pp. 1–10. [Online]. Available: https://www.researchgate.net/publication/350213799_IBP1173_19_THE_DESIGN_AND_DEVELOPMENT_OF_A_SMALL-SCALE_MULTIPHASE_FLOW_LOOP_FOR_THE_STUDY_OF_CORROSION_IN_SOURSWEET_GAS_ENVIRONMENTS
- 162 S. Nešić, S. Wang, H. Fang, W. Sun, and J. K. L. Lee, "A new updated model of CO₂/H₂S corrosion in multiphase flow," in *NACE - International Corrosion Conference Series*, 2008, no. 08535, pp. 085351–0853516. [Online]. Available: <http://www.icmt.ohio.edu/documents/publications/8147.pdf>
- 163 W. Ma, H. Wang, Y. Wang, A. Neville, and Y. Hua, "Experimental and simulation studies of the effect of surface roughness on corrosion behaviour of X65 carbon steel under intermittent oil/water wetting," *Corros. Sci.*, vol. 195, p. 109947, 2022, doi: 10.1016/j.corsci.2021.109947.
- 164 W. E. I. Liang, X. Pang, and G. A. O. Kewei, "Effects of crude oil on the corrosion behavior of pipeline steel under wet CO₂ conditions," in *Materials Performance*, 2015, vol. 54, no. 5, pp. 58–62.
- 165 S. Nesic, G. T. Solvi, and S. Skjerve, "Comparison of rotating cylinder and loop methods for testing CO₂ corrosion inhibitors," *Br. Corros. J.*, vol. 32, no. 4, pp. 269–276, 1997, doi: <https://doi.org/10.1179/bcj.1997.32.4.269>.
- 166 D. C. Silverman, D. C. Silverman, "Technical note: Conditions for similarity of mass-transfer coefficients and fluid shear stresses between the rotating cylinder electrode and pipe," *Corrosion*, vol. 61, no. 6, pp. 515–518, 2005, doi: 10.5006/1.3278187.
- 167 D. C. Silverman, "ROTATING CYLINDER ELECTRODE-GEOMETRY RELATIONSHIPS FOR PREDICTION OF VELOCITY-SENSITIVE CORROSION.," *Corrosion*, vol. 44, no. 1, pp. 42–49, 1988, doi: 10.5006/1.3582024.

- 168 D. C. Silverman, "Simplified equation for simulating velocity-sensitive corrosion in the rotating cylinder electrode at higher reynolds numbers," *Corrosion*, vol. 59, no. 3, pp. 207–211, 2003, doi: 10.5006/1.3277552.
- 169 S. Nestic, J. Postlethwaite, and S. Olsen, "An Electrochemical Model for Prediction of Corrosion of Mild Steel in Aqueous Carbon Dioxide Solutions," *Corros.*, vol. 52, no. 4, pp. 280–294, 1996, doi: 10.5006/1.3293640.
- 170 E. Remita, B. Tribollet, E. Sutter, V. Vivier, F. Ropital, and J. Kittel, "Hydrogen evolution in aqueous solutions containing dissolved CO₂: Quantitative contribution of the buffering effect," *Corros. Sci.*, vol. 50, no. 5, pp. 1433–1440, 2008, doi: 10.1016/j.corsci.2007.12.007.
- 171 P. Babakhani Dehkordi, L. P. M. Colombo, E. Mohammadian, A. Shahrabadi, and A. Azdarpour, "A mechanistic model to predict pressure drop and holdup pertinent to horizontal gas-liquid-liquid intermittent flow," *Chem. Eng. Res. Des.*, vol. 149, no. July, pp. 182–194, 2019, doi: 10.1016/j.cherd.2019.07.009.

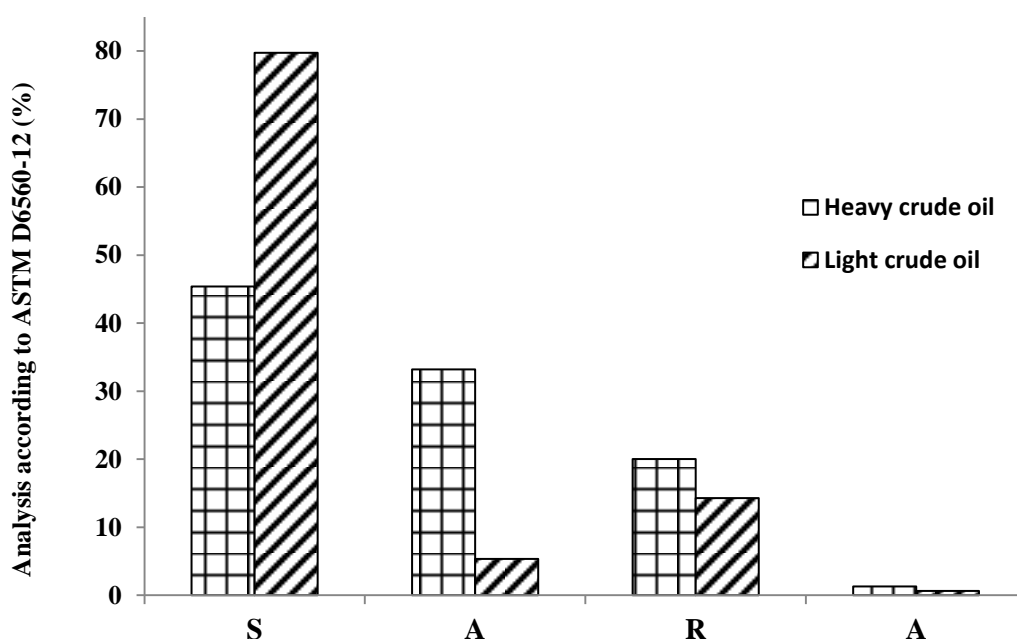
ANNEX I

a) Parameters of crude oil fluids related to corrosion

Crude oil is composed of a mixture of liquids, solids, and gases, with a predominance of hydrocarbons and organic derivatives containing oxygen, nitrogen, and sulfur. Some inorganic substances can be found in oils. The predominance of hydrocarbon families over others determines properties such as viscosity, color, and odor. Different oils are composed of the same hydrocarbons in different proportions, and these proportions are responsible for the type of oil. When the hydrocarbon chain is formed only by single bonds (paraffinic), they are named saturated hydrocarbons. Olefins are hydrocarbons that have double or single bonds. Aromatics are characterized by the presence of one or more aromatic rings in their structure. Meanwhile, asphaltenes and resins are large molecules formed by hydrocarbon skeletons that can contain sulfur, oxygen, and nitrogen⁷⁹.

b) SARA classification methodology

The characterization of light and heavy crude oil by the SARA classification methodology is presented with the separation of the saturated (S), aromatic (A), resin (R) and asphaltenes (A) fractions. The results are presented below:



Source: adapted from Repsol

c) API gravity

The density of crude oil and liquid hydrocarbons is generally reported as specific gravity (SG) or relative density, defined as the density of the liquid material divided by the density of

liquid water (999 kg/m³) at 15.6 °C. Therefore, for a hydrocarbon or an oil fraction, the SG is defined as:

$$\rho = \frac{141.5}{^{\circ}\text{API} + 131.5}$$

d) Critical water break value (W_{break}) or emulsion inversion point (EIP)

The solubility of water in oil is low, but water can be entrained in the oil in the form of a water-in-crude oil emulsion. The corrosion rate in these emulsions is lower than in the presence of water or brine. CO₂ corrosion of steel in these environments is controlled by the water wettability of the steel surface, while oil phase wettability prevents corrosion¹¹⁰.

The researchers cite that water entrained in crude oil can be estimated by API gravity. The critical water break value (W_{break}) can be defined as the amount of water that can be entrained in the crude oil. For water-cut in a brine mixture below W_{break} , the aqueous phase is retained into oil phase, preventing pipeline corrosion problems. the W_{break} is defined as¹¹⁰:

$$W_{break} = -0.0166 * \text{API} + 0.83$$

The formula simplifies the concept that heavier oils are more protective than light ones, and that very light oils give hardly any protection. Below is a table with the calculations for light and heavy oil used in this study.

Crude oil	μ (kg/ms)	ρ (kg/m ³)	$^{\circ}\text{API}$	W_{break} (%)
Heavy crude oil	0.15	0.966	15	58
Light crude oil	0.01	0.825	40	17

It is observed that the heavy oil has the capacity to carry 58 % of water against 17 % of the light oil.

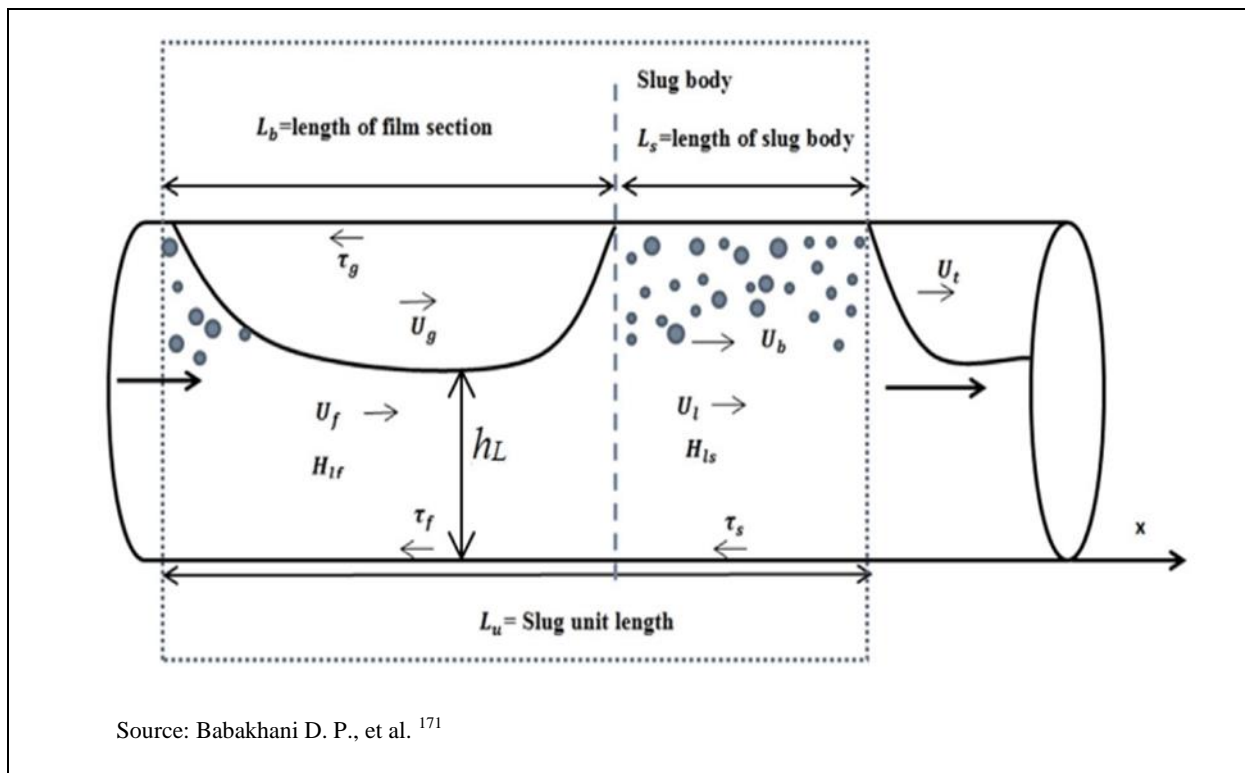
APPENDIX I

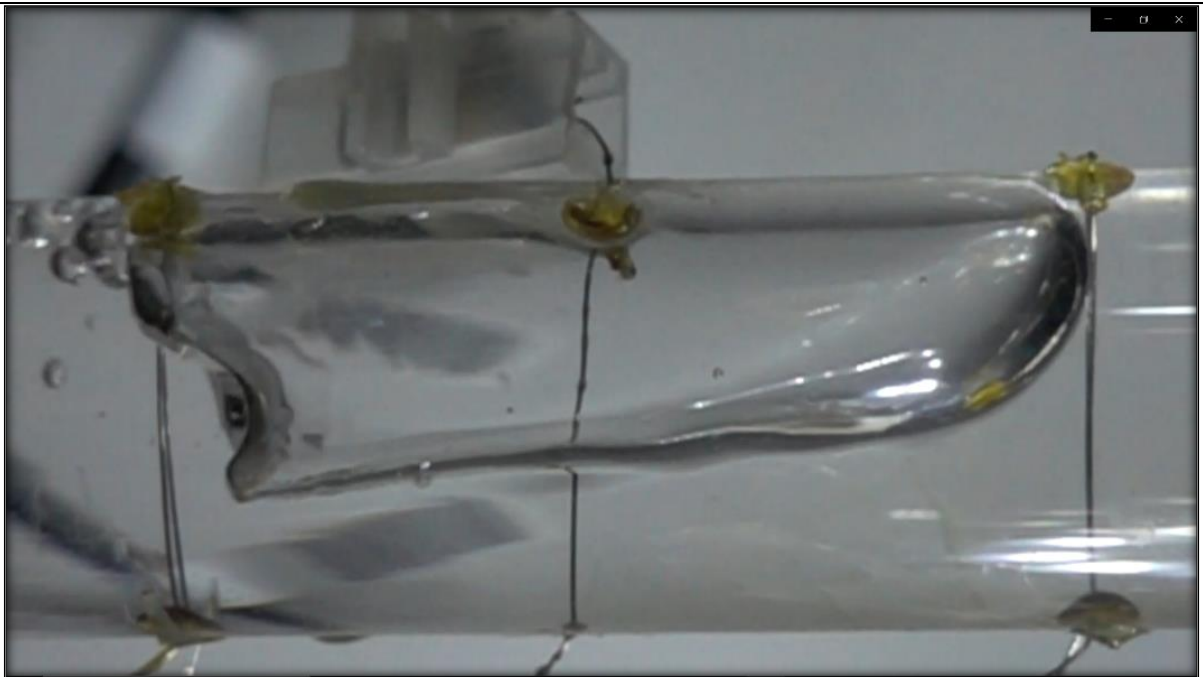
a) Multiphase-flow validation of the sensors

The simulation of the flow pattern of Taylor bubbles were produced and the validation of the sensors was carried out with similar tests measured by the particle image velocimetry (PIV) technique. Table with flow measurements

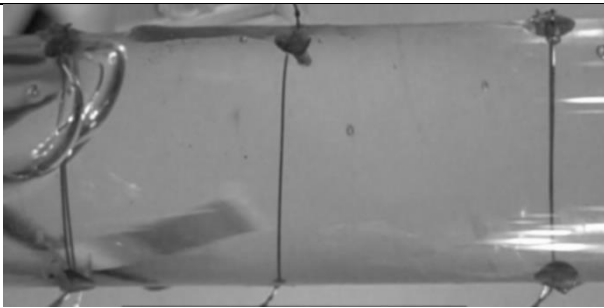
Flow parameters	Measurements (2057 bubbles)			Reference (60 bubbles)		
	Avg.	Mode	STDEV	Avg.	Mode	STDEV
Bubble velocity (m/s)	0.24	0.24	0.02	0.25	0.25	0.02
Bubble frequency (Hz)	1.27	1.17	0.14	1.24	1.16	0.46
Bubble size (mm)	76	66	14	77	63	26
Liquid-slug size (mm)	146	138	40	145	143	41

b) Image of slug flow in the test of validation

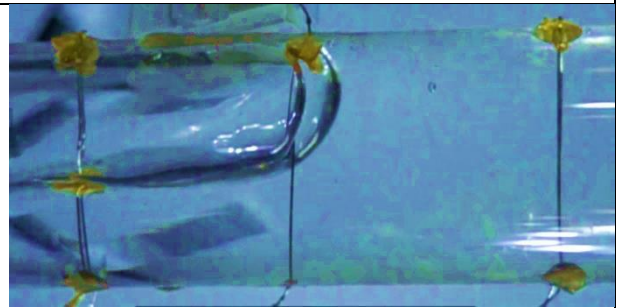




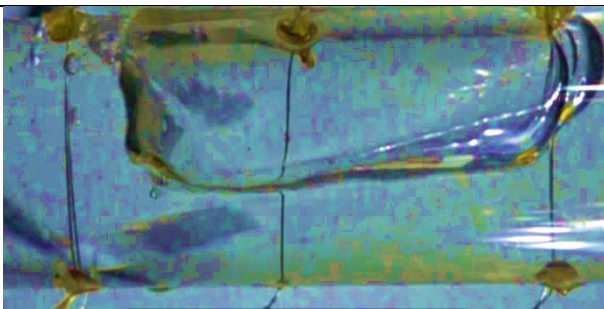
Taylor Bubble



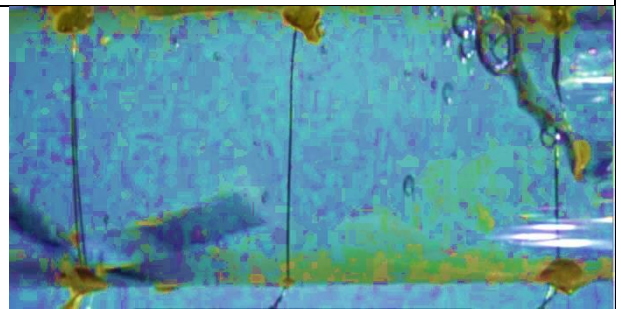
1s



5s

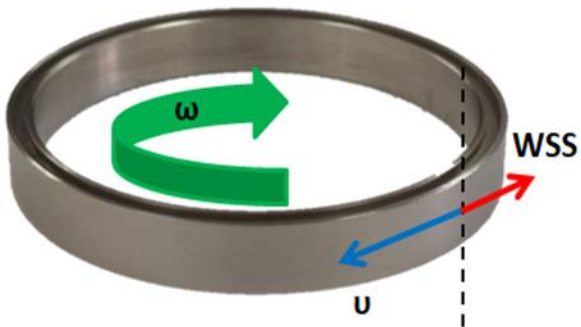


10s



15s

APPENDIX II

Calculation Memorial					
<p>Working Electrode (WE) dimensions: Outside cylinder diameter (d_c): 80 mm Working width (WW): 10 mm</p>		<p>Representation of angular velocity (ω), linear velocity (\mathbf{v}) and wall shear stress (WSS)</p> 			
Equations adopted					
<p>a) $\omega = 2\pi f$, where f = frequency in Hz or rpm</p> <p>b) $v = \omega r$, where $r = d_c/2$ ¹⁶⁵</p> <p>c) $Re = \rho_{H_2O} v d_c / \mu$ ^{165 166}</p> <p>d) $WSS = 0.079 Re^{-0.3} \rho \omega^2 r^2$ ¹³⁸</p> <p>e) friction factor (F) then $F = 0.158 Re^{-0.3}$ ¹⁶⁵ or $F = 2WSS / \rho v^2$ ¹⁶⁶</p> <p>f) $W_{break} = -0.0166 API + 0.83$ ¹¹⁰</p>					
Input data		Output data defined by Rotating Cylinder Electrode (RCE)			
Water density (ρ_{H_2O})	997 kg/m ³	ω (rad/s)	v (m/s)	WSS (Pa)	Rotation (rpm)
Slug-bubble velocity (SBV) of multiphase-flow loop ¹⁴¹	2.2 m/s	56.2	2.2	84.0	537 (8.9 Hz)
Rotation of the centrifugal pump of ¹²⁷	1200 rpm	125.7	5.0	329.7	1200 (20 Hz)